Plasmonic properties of supported nanoparticles

Sunniva Indrehus

THÈSE DE DOCTORAT
SORBONNE UNIVERSITÉ

Spécialité

Physique

École doctorale 397 Physique et chimie des matériaux

réalisée aux laboratoires

Surface du Verre et Interfaces, UMR 125 CNRS/Saint-Gobain
Institut des NanoSciences de Paris, CNRS/Sorbonne Université

présentée par

Sunniva INDREHUS

pour obtenir le grade de

DOCTEUR DE SORBONNE UNIVERSITÉ

Sujet de la thèse

Plasmonic properties of supported nanoparticles

soutenue publiquement le 18 septembre 2020

devant le jury composé de :

M. Lionel Simonot	Maître de Conférence HDR, Université Poitiers	Rapporteur
M. Gabriel Soriano	Maître de Conférence HDR, Instute Fresnel	Rapporteur
M^{me} Nathalie Destouches	Professeure, Université Lyon	Examinatrice
M^{me} Agnès Maître	Professeure, Sorbonne Université	Examinatrice
M. Ingve Simonsen	Professeur, SGR Paris et NTNU Norvège	Directeur de thése
M. Rémi Lazzari	Directeur de recherche CNRS, INSP	Codirecteur de thése
M^{me} Iryna Gozhyk	Ingénieure R&D, SGR Paris	Encadrante invitée

Plasmonic properties of supported nanoparticles

Keywords: GranFilm, excess field formalism, supported nanoparticles, quasi-static approximation, plasmonics.

Abstract

The GranFilm toolbox aims at linking the morphology to the optical properties of granular thin films with particle islands in the form of truncated spheres or spheroids of sub-wavelength sizes. By exploiting the excess field formalism in the non-retarded limit all the linear Fresnel coefficients of the film can be calculated from the polarizability tensor of the particles. The tensor is obtained through a multipole expansion of the scalar potential that can describe the anisotropic response in the directions normal and parallel to the substrate. While already used to understand *in situ* growth from the plasmonic response of equally sized particles, the introduction of pair correlation functions of islands randomly distributed on the lattice extends the toolbox's capabilities. Systems of polydisperse particles can now be described with GranFilm, a more realistic situation from an experimental point of view.

CONTENTS

Acknowledgment

If I have seen further it is by
standing on the shoulders of Giants

Isaac Newton, 1675

A PhD is certainly not a one-woman task. I would never have succeeded without the help of some great people.

I would like to express my deepest appreciation and gratitude to my three supervisors Ingve, Rémi, and Iryna. Thank you for giving me the opportunity to work with your project and the countless hours you have spent discussing, teaching, correcting, questioning, and guiding me through the processes leading to this manuscript. You have given me the space to perform mistakes and learn from them. When I can use the Greek alphabet like Ingve, reason around the physics in a plot like Rémi, and understand cultural differences like Iryna, I would consider myself a successful scientist. Especially, I'm deeply grateful for the fast and successful long-distance-communication during the last couple of months. Not even the Covid-19 pandemic stopped you.

The three last years with 'la vie qoutidien' in Paris has been both fantastic and hard. I would not have made it through the daily battles on the RER-B, the selection process at the boulangerie, or through the French administration system without the fantastic support and care from the extended SVI-family. I could not have dreamed of a warmer welcome in the French working life. It has been a pleasure to be a part of the team.

Gratitude is extended towards my three dear Quentins, for deep LaTeX-discussions, guidence through the jungle of French flats, and teaching me 'les petits et grands mots'.

I gratefully thank my parents and sister for the unconditional support and encouragement they have given me through all of my studies.

Finally, Johan, my dear husband, you are simply the best.

Abbreviations

2D two-dimensional.
3D three-dimensional.

BC boundary condition.
BV Bedeaux-Vlieger.

CDF cumulative distribution function.

DDA Discrete Dipole Approximation.

EF excess field.
EM electromagnetic.

FCM finite coverage monodisperse.
FCP finite coverage polydisperse.
FT fourier transformation.

IM interaction mean.

LCM low coverage monodisperse.
LCP low coverage polydisperse.
LM Levenberg-Marquardt.
LSPR localized surface plasmon resonance.
LU lower-upper.

MC Monte Carlo.
ME Maxwell's equations.
MF mean field.
MFT Mean Field Theory.

MI mean interaction.

NP nanoparticle.

PDF probability density function.

RDF radial distribution function.

SDRS Surface Differential Reflectivity Spectroscopy.
SH spherical harmonics.
SPR surface plasmon resonances.

Notation

This chapter gives an overview of the notation used in the manuscript.

The use of the bold and *italic* font

In the text. In the text, like here, the bold font is used to give the title of a paragraph. Italic is used to emphasize a word, *i.e.* the first time we introduce a new parameter or variable.

In expressions and equations. Tensors are written in boldface. A component of a tensor and variables are presented in italic. To differentiate a second-order tensor (a dyadic) from a vector a double arrow will be added over the tensor, *e.g.* $\overleftrightarrow{\boldsymbol{A}}$. Matrices are written in the blackboard bold font, *e.g.* $\mathbb{A}$. Mathematical operators are upright.

The multiplication of a tensor of any rank are (most) unmistakably in index notation with the summation convention. We will use both the 'tensor' and the 'matrix' notation through this manuscript, depending on the problem at hand. Equivalent operations in the two notations are commented on below

$$A_{ij} = v_i w_j, \quad \overleftrightarrow{\boldsymbol{A}} = \mathbf{v} \otimes \mathbf{w} \tag{1a}$$

$$v_i = A_{ij} w_j, \quad \mathbf{v} = \overleftrightarrow{\boldsymbol{A}} \circ \mathbf{w}. \tag{1b}$$

(1a) The product of two vectors yields a second-rank tensor, also known as the outer product or the tensor product.

(1b) Multiplication of a second-rank tensor and a vector yields another vector. In index notation a sum over the repeated index j is indicated, in tensor notation this operation is also called a 'single contraction', represented with $\circ$.

Mathematical symbols

Symbol	Explanation
$\perp$	a subscript, associated with the perpendicular direction of the substrate
$\parallel$	a subscript, associated with the parallel direction of the substrate
∞	a condition in infinity
$\star$	the optimized values of a parameter
$\neq$	is not equal to
$\approx$	is approximately equal to
$\equiv$	equivalence, identical to
$\pm$	plus or minus
$<$	smaller than
$\leq$	smaller or equal than
$>$	greater than
$\geq$	greater or equal than
$\sim$	similar to
$[\ ,\ ,\ ]$	a vector in matrix notation
$\{\ ,\ ,\ \}$	a set
$*$	the complex conjugate
$\forall$	for all
$\in$	is a member of
$\notin$	is not a member of
$\leftrightarrow$	symbol for a second-order tensor, a dyad $\overleftrightarrow{\boldsymbol{A}}$
$\bigcirc_s$	the whole spherical surface s
$\cap_s$	the whole spherical surface s, above the substrate
$\cup_s$	the whole spherical surface s, below the substrate
$\langle\cdot\rangle$	the average over a quantity

Operators

Symbol	Explanation
$\frac{\partial a}{\partial b}$	partial derivative of a with respect to b
$\boldsymbol{\nabla} \equiv \left[\frac{\partial}{\partial x}, \frac{\partial}{\partial y}, \frac{\partial}{\partial z}\right]$	the 3D-gradient operator in cartesian coordinates
$\boldsymbol{\nabla}_{\parallel} \equiv \left[\frac{\partial}{\partial x}, \frac{\partial}{\partial y}\right]$	the 2D-gradient operator in cartesian coordinates
$\boldsymbol{\nabla}_p \equiv \left[\frac{\partial}{\partial p_i}, ..., \frac{\partial}{\partial p_N}\right]$	the first order partial derivatives with respect to a model parameter for $i = 1, ..., N$.
$\boldsymbol{\nabla}\cdot$	the divergence operator
$\boldsymbol{\nabla}\times$	the curl operator
∇^2	the Laplace operator
$\otimes$	the tensor product
$\circ$	single contraction, defines the multiplication of a second ordered tensor with a vector

Greek alphabet

Symbol	Explanation
α	two uses; (i) with subscript α_i,$i = \parallel / \perp$, the parallel/perpendicular component of the single particle polarizability (ii) with tilde $\tilde{\alpha}$, a component of the polarizability renormalized for the island-island interaction
$\overleftrightarrow{\boldsymbol{\alpha}}$	The (full) polarizability tensor
β	the first order (dipolar order) surface susceptibility, associated with the direction perpendicular to the substrate
γ	the first order (dipolar order) surface susceptibility, associated with the direction parallel to the substrate
Γ	the damping frequency in a material, with subscript Γ_∞, the damping frequency in the bulk material
δ	three uses; (i) the second order (quadrupolar) surface susceptibility, (ii) the Dirac delta function, (iii) the Kronecker delta
Δ	indicates a the change in a parameter/quantity
ε	three uses; (i) the complex dielectric function of a material, (ii) with subscript $\varepsilon_1/\varepsilon_2$ the real/imaginary part of the dielectric function, (iii) the levi-civita tensor
ζ	with sub- and superscipts $\zeta^m_{\ell\ell'}$, a constant terms in the SH.
η	two uses; (i) a spheroidal coordinate, (ii) collective denoting the dimensionless position of the multipole (μ) or the image multipole ($\bar{\mu}$)
θ	two uses; (i) the polar angle of incidence, (ii) the heaviside step function
Θ	the surface coverage of particles in a lattice
κ	scaling factor of the imaginary part of the experimental bulk dielectric function
λ	three uses; (i) the wavelength of an electromagnetic field, (ii) with subscripts $\lambda_{\nu\nu'}$ a parameter in the scaling approximation (iii) the eigenvalues in a matrix equation

μ	three uses; (i) indicating either the dimensonless direct multipole position, (ii) with subindices, $\mu_{R_\parallel}, \mu_{R_\perp}$, or μ_{t_r}, the mean of a truncated normal distribution, (iii) the vacuum permeability
$\bar{\mu}$	the dimensonless image multipole position
ξ	two uses; (i) the surface density, (ii) specifies the surface of a spheroidal object, (iii) with subscript ξ_i geometrical type of particle i
ρ	three uses; (i) the surface density, (ii) the excess current density of the free charges, (iii) the distance from a point to the intersections of the ring of foci in the spheroidal oblate coordinate system
σ	two uses; (i) the standard deviation of a random variable, (ii) with subscript σ_f the free charge density
Σ	two uses; (i) the summation symbol, (ii) a geometry dependent constant used in the surface correction
τ	the second order (quadrupolar) surface susceptibility
ϕ	two uses; (i) azimuthal angle of incidence, (ii) the normal distribution
Φ	CDF for the normal distribution
χ	three uses; (i) a component of the radius ratio to define the thickness of a spherical layer, (ii) the minimization criteria in a parameter optimization, (iii) the electric susceptibility
ψ	the electrostatic potential
ω	the angular frequency of an electromagnetic field, with subscript, ω_p, the so-called plasma frequency of the free electron gas
Ω	two uses; (i) control volume, (ii) with subscript Ω_N the set of predefined particle geometries

Latin alphabet

Symbol	Explanation
a	two uses; (i) the amplitude at $r = D_0$ for the exponential pair-correlation function model, (ii) radius of the ring of foci for oblate spheroidal coordinates

A	the surface area of a particle
$A_{\ell m}^{(i)}$	multipole coefficient outside a region of interest i related to the direct dipole
$\bar{A}_{\ell m}^{(i)}$	multipole coefficient outside a region of interest i related to the image dipole
$\mathcal{A}$	set of lower limits of a set distributed parameters
$\mathbf{A}$	three uses; (i) could be any of the electromagnetic fields, (ii) with subscript $\mathbf{A}_{ex}$, could be any of the electromagnetic excess fields , (iii) with sub- and superscript $\mathbf{A}_{ex}^{s}$, could be any of the the total excess fields
B	two uses; (i) with sub- and superscipt $B_{\ell m}^{(i)}$ multipole coefficient inside a region of interest i related to the direct dipole, (ii) material dependent constant used in the surface correction
$\overline{B}_{\ell m}^{(i)}$	multipole coefficient inside a region of interest i related to the image dipole
$\mathcal{B}$	set of upper limits of a set distributed parameters
$\mathbf{B}$	the magnetic flux density
c	the speed of light in vacuum
C	two uses; (i) a normalization constant, (ii) a cross-section
$\mathbb{C}$	the covariance matrix
d	two uses; (i) the distance from the center of a particle to the substrate, (ii) with subscript $\mu\overline{\mu}$, $d_{\mu\overline{\mu}}$ the distance from the direct to the image multipole in a particle
d	an infinitesimal of a variable
D	two uses; (i) with subscript D_{eff}, the effective oscillation length of the s-electrons in spheroidal nanoparticles, (ii) with subscript D_0, the apparent diameter of a particle
$\mathbf{D}$	the electric displacement field
e	the exponential function, sometimes also denoted exp{}
$\mathbf{E}$	the electric field
f	two uses; (i) a factor used for determining if a surface is truncated by the substrate or not (ii) the truncated normal distribution
$g(r)$	two uses; (i) the RDF in a monodisperse system, (ii) with subscript $g_{\nu\nu'}(r)$, the RDF in a polydisperse system

$h(r)$	the pair correlation function
$\hbar$	Planck's reduced constant, $\hbar = \frac{h}{2\pi}$
$\mathbf{H}$	the magnetic field
$\mathbb{H}$	the Hessian matrix
i	an index
I	two uses; (i) with subscripts $I_{20}/\bar{I}_{20}$, the distribution integral to incorporate the island-island interaction between an island and the direct/image multipoles of it's neighbors for particles organized in a random array, (ii) with sub- and superscipt $I^m_{\ell\ell}$, an identity for the integral of a Legendre polynomial
$\mathbf{I}$	the density or the free current
$\mathbb{I}$	the unit dyad
j	an index, used to indicate a different state than the index i
J	with sub- and superscipt $J^m_{\ell\ell}$ an identity for an integral of the derivative of the Legendre polynomial
$\mathbb{J}$	the Jacobian matrix
$\tilde{k}$	the imaginary part of the refractive index
$\mathbf{k}$	the wave vector of an electromagnetic field
$\mathbf{K}_f$	the free surface current density
ℓ	four uses; (i) a given term in the multipole expansion $\ell = 0, ..., \infty$, (ii) with subscripts the lower/upper limit, $\ell^{\min}/\ell^{\max}$ for a bounded parameter $\bar{\mathcal{P}}$ (iii) with subscript, δ, ℓ_δ the skin depth of an electromagnetic field, (iv) with subscript ℓ_∞ the mean free path of the electrons in a bulk material
L	three uses; (i) the distance between two neighboring particles, the lattice constant, (ii) with subscript L_z, the total size (height) of an excess region, (iii) with subscript L_i, the geometrical depolarization factor for a spheroidal object in the directon i
m	two uses; (i) a term in the multipole expansion, defined as $m = -\ell, ..., \ell$ (ii) with subscript m_e, the electron mass
M	two uses; (i) the number of multipoles in a linear set of equation, (ii) with sub- and superscipt $M^{m(i)}_{\ell\ell,S}$ matrix element for a region i and surface s
$\mathbf{M}$	the magentization field
$\mathbb{M}$	a matrix containing the frequency dependent part of the linear system of equations containing the multipole coefficients

n	two uses; (i) the number of particles in a spherical shell of radius $r_\parallel$, (ii) the complex refractive index
$\tilde{n}$	the real part of the refractive index
$\hat{\mathbf{n}}$	vector normal to the interface
N	two uses; (i) the total number of a variable, (ii) with sub- and superscipt $N_{\ell\ell,S}^{m(i)}$ matrix element for a region i and surface s
$\mathcal{N}$	the set of individual islands in a distribution
p_i	a bounded model parameter
$\bar{p}_i$	an unbounded model parameter
$\mathbf{p}$	with subscript $\mathbf{p}_i/\bar{\mathbf{p}}_i$ dipole moment due to direct/image dipole in position i
P	two uses; (i) a point of observation, (ii) with indices $P_{\ell m}$, the associated Legendre polynomial
$\mathcal{P}$	set distributed parameters
$\boldsymbol{\mathcal{P}}$	two uses; (i) the set of a vector of bounded model parameters, (ii) with an overline, $\overline{\boldsymbol{\mathcal{P}}}$, the set of a vector of unbounded parameters. With superscripts $\boldsymbol{\mathcal{P}}^\star$, the set of optimized model parameters, $\boldsymbol{\mathcal{P}}^0$ the set guessed model parameters
r	two uses; (i) with subscripts r_s/r_p, the complex reflection amplitude in s/p-polarization, (ii) with subscript $r_\parallel^{(i)}/\bar{r}_\parallel^{(i)}$, the radial in plane distance between the direct-direct/direct-image neighboring particles
$\mathbf{r}$	two uses; (i) the residual array in a χ^2-optimization, (ii) with subscript $\mathbf{r}_{\mu/\bar{\mu}}$, the position from a direct/image multipole to a point,
R	two uses; (i) the radius in a particle; with subscripts $R_{\parallel/\perp}$, the radius of the particle parallel/perpendicular to the substrate, with superscript $R^{(s)}$, the radius of the surface s of a coated particle, (ii) with subscripts R_p/R_p the reflectivity, reflection amplitude in s/p-polarization
s	a given surface in a particle

S	two uses; (i) the total number of surfaces in an island, (ii) with subscripts $S_{20}/\bar{S}_{20}$ the lattice sum to incorporate the island-island interaction between an island and the direct/image multipoles of it's neighbors for particles organized in an ordered array
$\mathcal{S}$	a coordinate system
t	three uses; (i) the time variable, (ii) with subscripts t_s/t_p, the complex transmission amplitude in s/p-polarization, (iii) with subscript t_r, the truncation ratio, derived parameter to denote an island's degree of truncation
T	with subscripts T_s/T_p the transmissivity, transmission amplitude in s/p-polarization
$\mathbf{T}$	a transformation from bounded to unbounded model parameters
$\overleftrightarrow{\boldsymbol{T}}$	with subscript and bar $\overleftrightarrow{\boldsymbol{T}}_{ij}/\overleftrightarrow{\overline{\boldsymbol{T}}}_{ij}$ dipole-dipole/dipole-image interaction tensor between particle i and j
v_f	the Fermi velocity of the s-electrons
V	the volume of the particle above the substrate
$\mathbf{V}$	a vector containing the terms of the field which excites the LSPR oscillations in a system
$\overleftrightarrow{\boldsymbol{V}}$	with subscript $\overleftrightarrow{\boldsymbol{V}}_{ij}$ dyad containing dipole-dipole and dipole-image interaction tensor between particle i and j
x	abscissa
$\hat{\mathbf{x}}$	the unit vector in the x-direction
X_ℓ^m	radial function in oblate spheroidal coordinates
$\mathbf{X}$	column vector containing unknown multipole coefficients
y	ordinate
Y	with indices Y_ℓ^m, the spherical harmonic of order ℓm
$\hat{\mathbf{y}}$	the unit vector in the y-direction
$\hat{\mathbf{z}}$	the unit vector in the z-direction
z	with subscript $z_{mp}/z_{\overline{mp}}$ the position of the direct/image multipole $mp/\overline{mp}$ relative to the center of a reference island
Z_ℓ^m	radial function for oblate spheroidal coordinates

Chapter 1

Light scattering in complex systems

Nowadays, plasmonics is involved in a broad range of applications and scientific fields. In plasmonics, one studies the interaction between an *electromagnetic* (EM)-field and a metal object that can be of more or less complex form (rough surfaces, particles, etc...). The free electrons of the metal will react to the external EM-field and oscillate in phase with it. This collective movement is called a plasmon. This chapter provides a qualitative explanation of the tunability of the EM response of supported metallic *nanoparticle*s (NP)s.

Contents

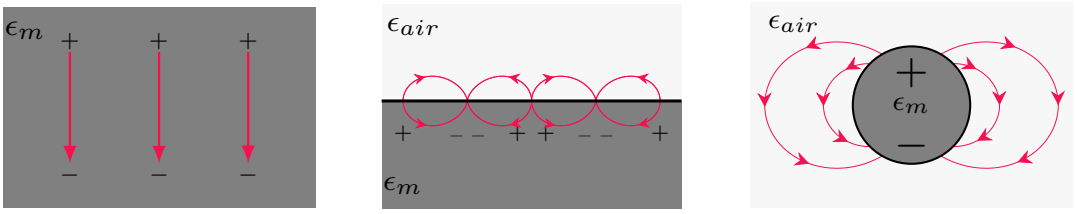

(a) **(b)** **(c)**

Figure 1.1 Examples of plasmon resonances in a bulk metal (a), at an interface between air and a metal (b), and in a metallic NP surrounded by air (c).

Today, we typically use the word *plasmonics* about a scientific and applied field that aims to control the interaction between an EM-field and a metallic object. The advent of nanotechnology has given us the ability to structure matter at the nanoscale and, therefore, to finely tune the interaction of light and matter. The understanding of the plasmonic properties of NPs can provide us with design rules for more complex nanostructures with targeted optical response [1, 2]. There is a wide range of potential applications of plasmonics in fields like medicine, engineering, space science and biology [3].

One typically divides the type of plasmons into three main categories: bulk plasmons encountered in the metallic bulk phase [Fig. 1.1(a)], *surface plasmon resonances* (SPR) which can be excited at the interface between a dielectric and a metal, relevant for the response from a continuous thin metal film [4] [Fig. 1.1(b)], and the *localized surface plasmon resonance* (LSPR) typically observed in metallic NPs [Fig. 1.1(c)].

In this work, we are mainly interested in the latter type of excitations, namely the LSPRs in metallic NPs. We start this chapter with a brief introduction to EM theory and the interaction between metal and light. Then we will explain the observed resonances in metallic particles placed in a homogeneous background. Next, the case of truncated particles on a substrate is treated. Both in terms of analytical models and computational tools that can be used to model their optical response.

1.1 A brief introduction to electromagnetic theory

A surface may be regarded as a discontinuity between two media of different dielectric and magnetic properties. Herein we are mainly interested in the study of the interaction between light and a non-sharp surface containing metallic NP. As our results are built from the *Bedeaux-Vlieger* (BV)-theory of excess fields and surface susceptibilities, we have chosen to follow their choice of the c.g.s unit system for the field equations, rather than the SI-units. This is a practical choice for our analysis because the electric fields, the displacement fields, and the polarization densities all have the same dimension. The experimental relevant formulas are always used in a form where the choice of unit systems does not matter. The conversion of the field equations to the SI-system is easily done by adding the appropriate powers of the electric permittivity and the magnetic permeability of vacuum.

This section aims to give the reader a feeling of the required tools to understand the

basic theory applied in this work. Thus, the discussion has to start with *Maxwell's equations* (ME).

1.1.1 Maxwell's equations

The theoretical framework to describe the response of matter to an external EM-field is given by the fundamental ME which in the *c.g.s*-unit system read [5]:

$$\boldsymbol{\nabla} \cdot \mathbf{D}(\mathbf{r}, t) = \rho(\mathbf{r}, t) \tag{1.1a}$$

$$\boldsymbol{\nabla} \times \mathbf{E}(\mathbf{r}, t) = -\frac{1}{c}\frac{\partial \mathbf{B}(\mathbf{r}, t)}{\partial t} \tag{1.1b}$$

$$\boldsymbol{\nabla} \cdot \mathbf{B}(\mathbf{r}, t) = 0 \tag{1.1c}$$

$$\boldsymbol{\nabla} \times \mathbf{H}(\mathbf{r}, t) = \frac{1}{c}\mathbf{I}(\mathbf{r}, t) + \frac{1}{c}\frac{\partial \mathbf{D}(\mathbf{r}, t)}{\partial t} \tag{1.1d}$$

where the four macroscopic fields are denoted $\mathbf{D}$ (the dielectric displacement field), $\mathbf{B}$ (the magnetic induction or the flux density), $\mathbf{E}$ (the electric field), $\mathbf{H}$ (the magnetic field), $\boldsymbol{\rho}$ (the external charge), and $\mathbf{I}$ (the density or free current), and c is the speed of light.

Boundary conditions

In general, the fields given in Eq. (1.1) are not continuous over a boundary. They will change according to the properties of the media on each side of the interface. With the divergence and Stokes's theorem, Eq. (1.1) can be written in integral form. A set of *boundary condition*s (BC)s can then be derived for the EM-fields [6]:

$$D^1_\perp(\mathbf{r}, t) - D^2_\perp(\mathbf{r}, t) = \sigma_f(\mathbf{r}, t) \tag{1.2a}$$

$$\mathbf{E}^1_\parallel(\mathbf{r}, t) - \mathbf{E}^2_\parallel(\mathbf{r}, t) = 0 \tag{1.2b}$$

$$B^1_\perp(\mathbf{r}, t) - B^2_\perp(\mathbf{r}, t) = 0 \tag{1.2c}$$

$$\mathbf{H}^1_\parallel(\mathbf{r}, t) - \mathbf{H}^2_\parallel(\mathbf{r}, t) = \mathbf{K}_f(\mathbf{r}, t) \times \hat{\mathbf{n}}, \tag{1.2d}$$

where $\sigma_f(\mathbf{r}, t)$ is the free charge density at the boundary, $\mathbf{K}_f(\mathbf{r}, t)$ is the free surface current density, and $\hat{\mathbf{n}}$ is the unit vector perpendicular to the surface. Furthermore, the subscript $i = \perp, \parallel$ indicates a parallel or a perpendicular component of the relevant field and the superscripts 1 and 2 indicate the relevant medium.

The Fourier transform of Maxwell's equations

In the following, we will need the temporal *fourier transformation* (FT) which we defined as[1]

$$\mathbf{A}(\mathbf{r}, \omega) = \int_{-\infty}^{\infty} \mathrm{d}t \quad \mathrm{e}^{i\omega t}\mathbf{A}(\mathbf{r}, t), \tag{1.3}$$

[1] We will use the physicist's convention where the expression $\mathrm{e}^{i(\mathbf{k}\cdot\mathbf{r}-\omega t)}$ describes a plane wave traveling in direction $\mathbf{k}$.

where $\mathbf{A}(\mathbf{r},t)$ may denote any of the EM-fields given in Eq. (1.1). By assuming all the EM-fields to be time-harmonic, the EM-fields in Eq. (1.1) can readily be transformed into the temporal *Fourier domain*. For instance, the FT of the time derivative of a vector field $\frac{\partial}{\partial t}\mathbf{A}(\mathbf{r},t)$ yields

$$\begin{aligned}\frac{\partial}{\partial t}\mathbf{A}(\mathbf{r},t) &= \frac{\partial}{\partial t}\mathrm{Re}\left\{\mathrm{e}^{-i\omega t}\hat{\mathbf{A}}(\mathbf{r})\right\}\\ &= -i\omega\mathrm{Re}\left\{\mathrm{e}^{-i\omega t}\hat{\mathbf{A}}(\mathbf{r})\right\}\\ &= -i\omega\mathbf{A}(\mathbf{r},\omega).\end{aligned} \tag{1.4}$$

Thus, the temporal FT of the ME in Eq. (1.1) results in

$$\boldsymbol{\nabla}\cdot\mathbf{D}(\mathbf{r},\omega) = \rho(\mathbf{r},\omega) \tag{1.5a}$$
$$\boldsymbol{\nabla}\times\mathbf{E}(\mathbf{r},\omega) = i\frac{\omega}{c}\mathbf{B}(\mathbf{r},\omega) \tag{1.5b}$$
$$\boldsymbol{\nabla}\cdot\mathbf{B}(\mathbf{r},\omega) = 0 \tag{1.5c}$$
$$\boldsymbol{\nabla}\times\mathbf{H}(\mathbf{r},\omega) = \frac{1}{c}\mathbf{I}(\mathbf{r},\omega) - i\frac{\omega}{c}\mathbf{D}(\mathbf{r},\omega). \tag{1.5d}$$

The constitutive relations in matter

To relate the behavior of the EM-fields in various materials it is common to introduce the macroscopic polarization, $\mathbf{P}(\mathbf{r},\omega)$ and magnetization densities $\mathbf{M}(\mathbf{r},\omega)$, related to the EM-fields through the constitutive relations

$$\mathbf{D}(\mathbf{r},\omega) = \varepsilon(\omega)\mathbf{E}(\mathbf{r},\omega) + \mathbf{P}(\mathbf{r},\omega) \tag{1.6a}$$
$$\mathbf{B}(\mathbf{r},\omega) = \mu(\omega)\left[\mathbf{H}(\mathbf{r},\omega) + \mathbf{M}(\mathbf{r},\omega)\right], \tag{1.6b}$$

where the permittivity of the material is denoted $\varepsilon(\omega)$, and the permeability of the material $\mu(\omega)$. In the further analysis we will focus only on the relations for the electric-field.

For a linear, isotropic and homogeneous medium the macroscopic polarization is linked to the electric field through the electric susceptibility

$$\mathbf{P}(\mathbf{r},\omega) = \chi(\omega)\mathbf{E}(\mathbf{r},\omega), \tag{1.7}$$

thus, with the relations in Eqs. (1.6)-(1.7) one can show that the electric susceptibility is related to the permittivity of the material like

$$\varepsilon(\omega) = \chi(\omega) + 1. \tag{1.8}$$

Helmholtz equation in simple materials

In a source free and non-conducting material, one can obtain the Helmholtz equation by substituting the relations connecting the polarizability and magnetization density given in Eq. (1.6) together with the curl equations in Eq. (1.1a) and Eq. (1.1d) and the vector identity

$$
\begin{aligned}
\boldsymbol{\nabla} \times (\boldsymbol{\nabla} \times \mathbf{A}(\mathbf{r},\omega)) &= \varepsilon_{i,j,k}\partial_j \varepsilon_{k,l,m}\partial_l A_m \\
&= \varepsilon_{i,j,k}\varepsilon_{k,l,m}\partial_j\partial_l A_m \\
&\overset{①}{=} \delta_{i,l}\delta_{j,m} - \delta_{i,m}\delta_{j,l}\left(\partial_j\partial_l A_m\right) \\
&= \delta_{i,l}\delta_{j,m}\partial_j\partial_l A_m - \delta_{i,m}\delta_{j,l}\partial_j\partial_l A_m \\
&= \partial_j\partial_i A_j - \partial_j\partial_j A_i \\
&\overset{②}{=} \partial_i\partial_j A_j - \partial_j\partial_j A_i \\
&= \boldsymbol{\nabla}\left(\boldsymbol{\nabla}\cdot\mathbf{A}(\mathbf{r},\omega)\right) - \nabla^2\mathbf{A}(\mathbf{r},\omega),
\end{aligned}
\tag{1.9}
$$

① Property of the double levi-cevita tensor: $\varepsilon_{i,j,k}\varepsilon_{k,l,m} = \delta_{i,l}\delta_{j,m} - \delta_{i,m}\delta_{j,l}$.
② Independent order of the partial derivative: $\partial_i\partial_j A_j = \partial_j\partial_i A_j$.

so the Helmholtz equation for the FT electric-field is

$$
\varepsilon(\omega)\mu(\omega)\frac{\omega^2}{c^2}\mathbf{E}(\mathbf{r},\omega) - \nabla^2\mathbf{E}(\mathbf{r},\omega) = 0. \tag{1.10}
$$

As discussed in any book on electromagnetism [6], for the field in a homogeneous and isotropic medium Eq. (1.10) have plane-wave solutions in the FT domain in the form

$$
\mathbf{E}(\mathbf{r},\omega) = \mathbf{E}_0 \mathrm{e}^{i(\mathbf{k}\cdot\mathbf{r})} 2\pi\delta(\omega-\omega_0), \tag{1.11a}
$$

and as a function of position and time as

$$
\mathbf{E}(\mathbf{r},t) = \mathbf{E}_0 \mathrm{e}^{i(\mathbf{k}\cdot\mathbf{r}-\omega t)}, \tag{1.11b}
$$

where $\mathbf{k}$ is the wave vector of the field, describing the direction of the propagation of of the field, and $\omega = 2\pi\nu$ is its angular frequency of the wave.

Furthermore, the plane wave solutions in Eq. (1.10) must satisfy the dispersion relation of the fields

$$
\left[\frac{n(\omega)\omega}{c}\right]^2 = \mathbf{k}^2, \tag{1.12}
$$

where the complex refractive index of the medium is defined as $n(\omega) = \sqrt{\varepsilon(\omega)\mu(\omega)}$.

1.1.2 The complex refractive index

The complex refractive index, $n(\omega) = \tilde{n}(\omega) + i\tilde{k}(\omega)$, relates the phase velocity and attenuation of plane waves in matter.

The physical meaning of the refraction index

The term *evanescent* is derived from the Latin word *evanescere*, and means vanishing from notice [7]. Evanescent fields are described by having a non-vanishing and positive imaginary part of the wave vector leading to an exponential decay along the propagation direction.

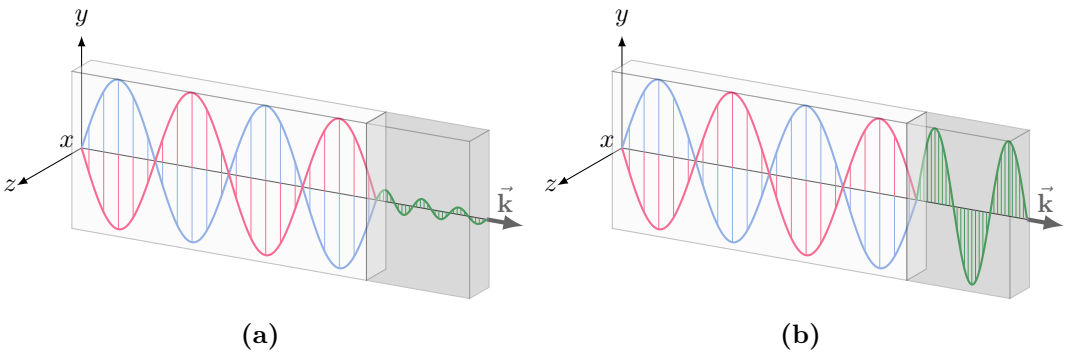

(a) (b)

Figure 1.2 An EM-wave traveling from one medium (white rectangle) towards another (gray rectangle). At the interface, the incoming wave (in blue) is partly reflected (in red) and transmitted (in green). For a conducting material, the wave is damped evanescently (a), whereas for a non-conducting material (b) the wave vector is changed, but the propagation continues through the material without being damped.

A plane wave traveling in the positive x-direction can be described by the refractive index on the form $\mathbf{E}(x,t) = E_0 e^{i[\omega\tilde{n}(\omega)x/c-\omega t]} e^{-(\omega\tilde{k}(\omega)x/c)}$, which are related to the length of the wave vector (the wave number) through the dispersion relation in Eq. (1.12), $k = 2\pi/\lambda$. Thus, the imaginary part of the refractive index, $\tilde{k}(\omega)$ determines the optical absorption of an EM-wave propagating through a medium [8].

The skin depth, $\ell_\delta = 1/b$, for such an EM-wave is related to the imaginary part of the complex refractive index as $b = 4\pi\hat{k}(\omega)/\lambda$.

Electromagnetic fields traveling between media

An EM-wave traveling from medium 1 to medium 2 with different dielectric properties will be partly reflected and transmitted at the interface. An illustration of the different behaviors at the interface of a conducting and non-conducting material is given in Fig. 1.2. In the case of a non-conducting material the transmitted part of the wave is not damped, *i.e.* the refractive index of the material is purely real.

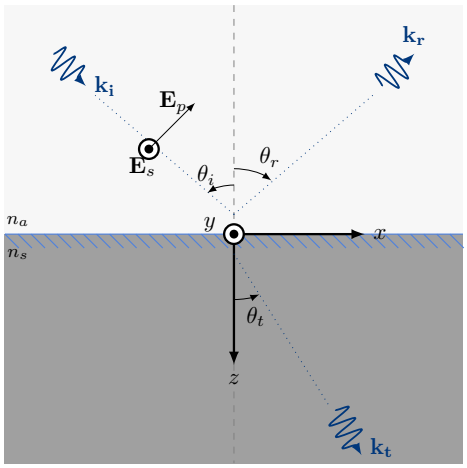

Figure 1.3 An illustration of the optical response for a flat surface on an interface between the two media n_a and n_s. The light beam is partly reflected and partly transmitted. Notice the positive z-axis pointing downwards and the two different polarizations of the electric-field.

1.1.3 The Fresnel coefficients for a flat substrate

Applying the BC given in Eq. (1.2) on the EM-fields given as plane waves on a single interface between two bulk media leads to the well-known Fresnel amplitudes [7, 9]:

$$r_p(\omega) = \frac{n_s(\omega)\cos\theta_i - n_s(\omega)\cos\theta_t}{n_a(\omega)\cos\theta_t + n_s(\omega)\cos\theta_i}, \tag{1.13a}$$

$$t_p(\omega) = \frac{2n_a(\omega)\cos\theta_i}{n_a(\omega)\cos\theta_t + n_s(\omega)\cos\theta_t}, \tag{1.13b}$$

$$r_s(\omega) = \frac{n_a(\omega)\cos\theta_i - n_s(\omega)\cos\theta_t}{n_a(\omega)\cos\theta_i + n_s(\omega)\cos\theta_t}, \tag{1.13c}$$

$$t_s(\omega) = \frac{2n_a(\omega)\cos\theta_i}{n_a(\omega)\cos\theta_i + n_s(\omega)\cos\theta_t}, \tag{1.13d}$$

where θ_x, $x = i, t$ denotes the angle of incidence or transmission, and n_j, $j = a, s$ is the reflection index of the ambient medium or the substrate, respectively. The terms r_ν, and t_ν, $\nu = s, p$ is, respectively, the reflection and transmission amplitude in s- or p-polarization.

The s- or p-polarizations are used to denote the two possible orientations of the incident electric field. If the polarization is orthogonal to the plane of incidence, we say the light is s-polarized, where s comes from the German word for orthogonal *senkrecht*. This polarization is also known as a transverse electric wave. The opposite possibility is given by p-polarization or a transverse magnetic wave where p stands for parallel.

With known forms of the reflection and transmission amplitudes one can also express the Fresnel coefficients. At normal incidence, $\theta_i = 0°$, they read

$$R(\omega) = \frac{[n_a(\omega) - n_s(\omega)]^2}{[n_a(\omega) + n_s(\omega)]^2}, \tag{1.14a}$$

$$T(\omega) = \frac{4n_a(\omega)n_s(\omega)}{[n_a(\omega) + n_s(\omega)]^2}, \tag{1.14b}$$

where R denotes the reflection coefficient and T the transmission coefficient. Because of energy conservation $R + T = 1$.

Generally, the reflection and transmission by macroscopic planes and slabs are more conveniently described by n. The microscopic mechanisms, *e.g.* absorption and scattering by small particles, are generally better described by *the complex dielectic function* [10].

1.2 The complex dielectric function

In the limit of a linear and isotropic medium for which $\mu(\omega) \approx 1$ (non-magnetic medium), the complex refraction index and the dielectric function are related by

$$\varepsilon(\omega) = n(\omega)^2, \tag{1.15}$$

where $\varepsilon(\omega) = \varepsilon_1(\omega) + i\varepsilon_2(\omega)$.

In a metal, the dielectric function models the macroscopic behavior of the conduction electrons. We have already seen that the complex dielectric function is needed in the constitutive relations given in Eq. (1.6). Even though more precise theoretical models for this function exist in the literature, the semi-classical derivation of the complex dielectric function given by the *Drude model* is good enough to catch the plasmonic properties of metals qualitatively.

1.2.1 The Drude Model

The Drude model is a semi-classical model that describes the coupling between electrons and ions with a mechanical analog where the mass of the nucleus is assumed to be much higher than that of the electrons $m_e \ll m_{nucleus}$.

Following Maier in Ref. 8, a semi-classical derivation of the complex dielectric function starts with writing an equation of motion for an electron in the plasma sea in a material under the influence of an external electric field. The equation of motion for the position of the electrons reads

$$m_e \frac{\partial^2 \mathbf{x}(t)}{\partial t^2} + m_e \Gamma_\infty \frac{\partial \mathbf{x}(t)}{\partial t} = -e\mathbf{E}(t), \tag{1.16}$$

where the displacement of the electron is given by the position vector $\mathbf{x}(t)$, m_e is the mass of the electrons, $\mathbf{E}(t)$ as the external electric field, the term Γ_∞ is the damping constant in the bulk material due to frictional forces and finally the charge carriers in the material is denoted by e.

Assuming a time harmonic field and again performing the temporal FT, a solution to Eq. (1.16) is

$$\mathbf{x}(\omega) = \frac{e\mathbf{E}(\omega)}{m_e \left[\omega^2 + i\Gamma_\infty \omega\right]}. \tag{1.17}$$

The displacement of the electrons will contribute to the macroscopic polarization as follows

$$\begin{aligned} \mathbf{P}(\omega) &= -ne\mathbf{x}(\omega) \\ &= -\frac{\omega_p^2}{\omega^2 + i\Gamma_\infty \omega}\mathbf{E}(\omega), \end{aligned} \tag{1.18}$$

where n is the total number of electrons, and the introduced term ω_p in the last line of Eq. (1.18) is the so-called Drude plasma frequency which is defined as

$$\omega_p = \sqrt{\frac{ne^2}{m_e}}. \tag{1.19}$$

From the constitutive relations for the polarization $\mathbf{P}(\omega)$ and the electric susceptibility in Eq. (1.6a) and Eq. (1.8), respectively, the displacement field $\mathbf{D}(\omega)$ is given by

$$\begin{aligned} \mathbf{D}(\omega) &= \varepsilon(\omega)\mathbf{E}(\omega) + \mathbf{P}(\omega) \\ &= \left[1 - \frac{\omega_p^2}{\omega^2 + i\Gamma_\infty \omega}\right] \mathbf{E}(\omega) \end{aligned} \tag{1.20}$$

from which the complex dielectric function of the material can be defined as

$$\begin{aligned}\varepsilon(\omega) &= 1 - \frac{\omega_p^2}{\omega^2 + i\Gamma_\infty\omega} \\ &= \varepsilon_1(\omega) + i\varepsilon_2(\omega).\end{aligned} \tag{1.21}$$

For alkaline metals and noble metal (like silver or gold), the Drude model satisfactorily describes the behavior of the conduction s-electrons. Already with noble metal, not speaking about transition metals, an extension of the dielectric function involves the band-to-band transitions involving *d*-electrons [8]. Thus, the dielectric function is often corrected by the screening they induce accordingly to an extra-term

$$\varepsilon(\omega) = \varepsilon_\infty - \frac{\omega_p^2}{\omega^2 + i\Gamma_\infty\omega}. \tag{1.22}$$

More complex expressions for the dielectric function exist to include interband transitions as sum of oscillators. Otherwise, one may resort to functions determined experimentally and tabulated as done herein for silver.

1.2.2 Optical properties of a Drude metal

Because of the link between the refractive index and the dielectric function, given in Eq. (1.15), simple analysis can give us some intuition about the expected optical behavior of the material. In metals with small damping for the electrons $\omega \gg \Gamma_\infty$, the dielectric function becomes

$$\varepsilon_1 \approx 1 - \frac{\omega_p^2}{\omega^2} \tag{1.23}$$

$$\varepsilon_2(\omega) \approx \frac{\omega_p^2\Gamma_\infty}{\omega^3}, \tag{1.24}$$

thus leading to vanishing real part of the dielectric function [$\varepsilon_1 = 0$] at $\omega = \omega_p$, the well-known condition for the excitation of the so-called bulk plasmon.

Figure 1.4 illustrates the connection between the bulk dielectric function for a Drude metal and the connected optical properties of this material at normal incidence ($\theta = 0°$). The conductive behavior ($\varepsilon_1 < 0$, illustrated as the gray region in Fig. 1.4) of this theoretical metal is lost when the real part of the dielectric function becomes positive [solid blue line in Fig. 1.4(a)]. When $\varepsilon_1 > 0$ the imaginary part of the complex refractive index (the term connected to absorption in the material) approaches zero, $\tilde{k} \to 0$ [solid red line in Fig. 1.4(c)] and the refractive index becomes purely real.

For a light wave traveling from air to the same theoretical Drude metal at normal incidence, the transmission coefficient goes to 100% [solid red line in Fig. 1.4(b)] at the same energy value where the real part of the dielectric function becomes positive and the metal behaves like a dielectric.

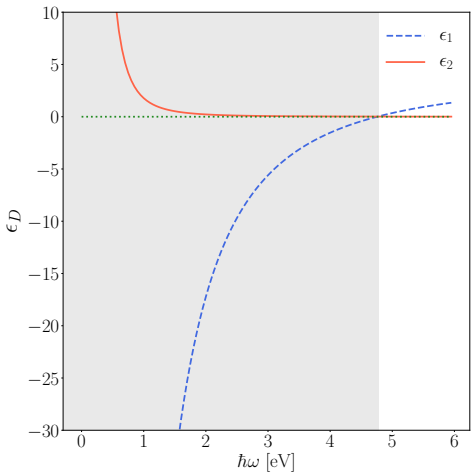

Variable	Value
$\hbar\omega_p$ [eV]	9.2
$\hbar\Gamma_\infty$ [eV]	0.045
ε_∞	3.7
θ_0	0°

(a) The dielectric function of a Drude metal.

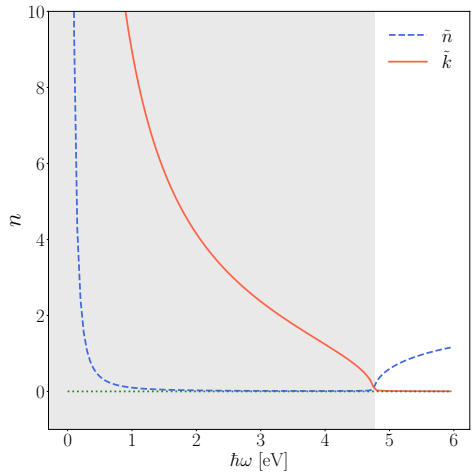

(b) The complex refractive index. index.

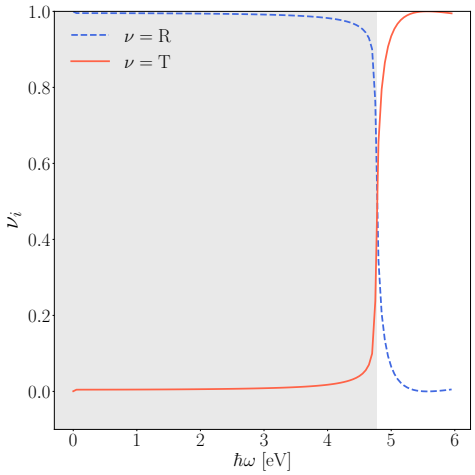

(c) Reflection and transmission coefficients of an EM-wave traveling from air to the Drude metal at normal incidence.

Figure 1.4 The dielectric function (a), reflection (b) and refractive index (c) at normal incidence for a theoretical Drude metal. The parameters used in the simulations are retrieved from [11] and described the free electrons in silver. They are indicated in the upper right corner of the figure.

1.2.3 The dielectric function of real metals

The dielectric properties of real materials are only approximately described by a Drude dielectric function since the interband transitions are not properly accounted for in this model. In the literature, a corrective term is often added to describe the later [12]

$$\begin{aligned}\varepsilon_B(\omega) &= \varepsilon_D(\omega) + \varepsilon_I(\omega) \\ &= 1 - \frac{\omega_p^2}{\omega(\omega + i\Gamma_\infty)} + \varepsilon_I(\omega),\end{aligned} \tag{1.25}$$

$\varepsilon_B(\omega)$ denotes the total bulk permittivity of the metal as a function of frequency consisting of a Drude and an interband transition part, respectively denoted by $\varepsilon_D(\omega)$ and $\varepsilon_I(\omega)$.

Even for silver, which is one of the most used plasmonics materials with almost Drude-like behavior, the interband transitions of the electrons above $\hbar\omega > 3.8\,\text{eV}$ complicate the dielectric function of the material considerably. The energy interval where the metal behaves as conducting, and could possibly excite plasmons, is less then what we would expect from the Drude-model.

In Fig. 1.5(a) the decomposition in Drude- and interband components is shown for silver. Even though the imaginary Drude part of the dielectric function approaches zero from above as the real part of the Drude dielectric function approaches zero from below, the contribution of the intraband electrons makes the behavior of the total dielectric function more complicated than what we saw for the theoretical Drude metal in Fig. 1.4(a) modeled with Eq. (1.22). As a consequence, the actual energy interval where the plasmons can be excited are smaller than what we expect from Fig. 1.4(a).

For materials like gold [Fig. 1.5(b)], chromium [Fig. 1.5(c)] and zinc [Fig. 1.5(d)], the intraband transitions are progressively shifted towards lower energies making the energy interval were the plasmon can be excited even smaller.

1.3 Plasmonics of metallic nanoparticles: a starter

Already the Romans were fascinated by the optical properties created by metal particles in the glass matrix. One of the most famous examples is the Lycurgus cup, illustrated in Fig. 1.6. The gold NPs in this object make its color changing from green to red, depending on whether it is seen with reflected or transmitted light, respectively [13, 14].

The first structured and scientific works on the investigations of the optical properties of metallic particles are credited to Maxwell-Garnett and Frölich. In 1904, Maxwell-Garnett gave the first explanation of the coloration of glasses doped by a metal precursor [15]. A more detailed description of light scattering by a spherical particle was given by Mie in 1908 [16].

For metallic NPs, the main effect of an incoming EM wave is to polarize the electronic gas of the metal and to excite a collective motion of the electrons, known as the LSPR.

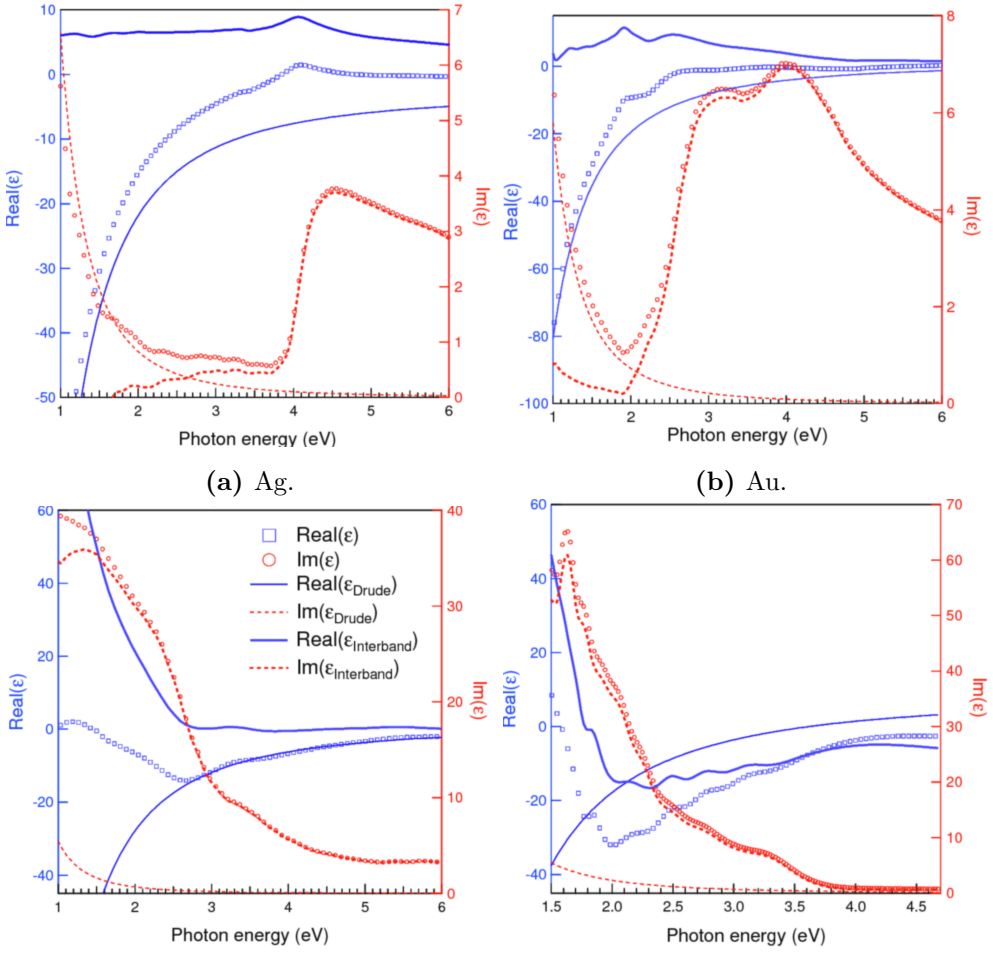

(a) Ag. **(b)** Au.

(c) Cr. **(d)** Zn.

Figure 1.5 Actual bulk dielectric functions for silver (a), gold (b), chromium (c), and zinc (d). Each function is decomposed into its Drude and interband components. Courtesy of R Lazzari.

(a) (b)

Figure 1.6 The Lycurgus cup seen in reflected (a) and transmitted (b) light. Gold nanoparticles embedded in the glass cause the apparent color change of the object. Figures are given with permission of ©Trustees of the British Museum.

For a time-varying field the polarization process of the electrons in the NP leads to a dipole like behavior of the free electrons in the metal. The restoring force acting on electrons is due to the positive background of charge of the nuclei.

A sketch of the oscillations of the electron cloud in a metallic NP with and without the impact of an external EM-field is given in Fig. 1.7. As the wave is propagating the movement of the free electrons in the metallic NP shift their direction, and thus the particle behavior can be seen as dipole-like.

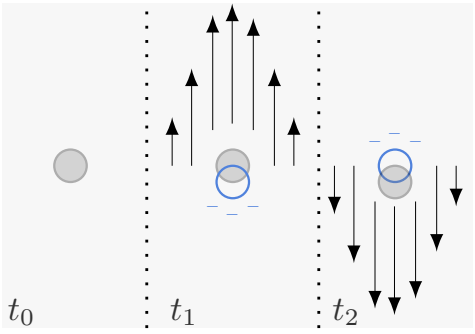

Figure 1.7 Sketch of a metal sphere without ($t = t_0$) and with ($t = t_1$ and $t = t_2$) the influence of an external electrical field. The oscillating electron cloud is indicated in blue.

The quasi-static regime

If the size of the particles is much smaller than the wavelength of the incoming field, *i.e.* $2R \ll \lambda$ where R is the radius of the particles and λ the optical wavelenght, the

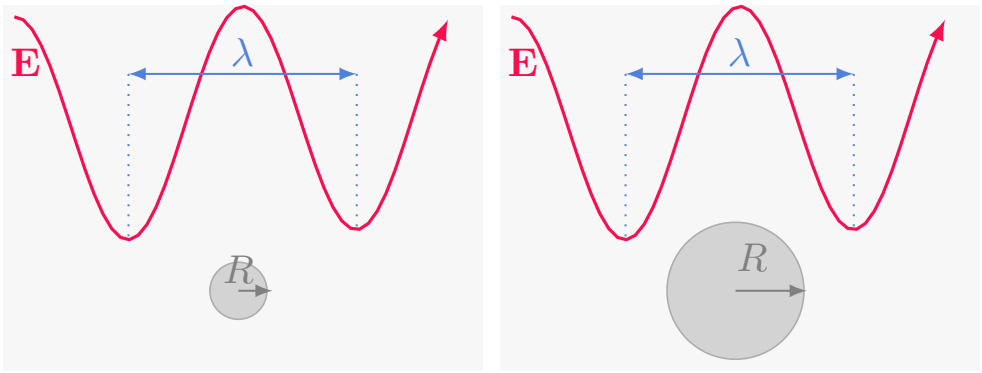

(a) $2R \ll \lambda$. **(b)** $2R \not\ll \lambda$.

Figure 1.8 A valid (a) and a non-valid case (b) case of the quasi static-approximation.

NP experiences a nearly uniform field but with a time-dependence. This size regime of is known as the *quasi-static regime* (see Fig. 1.8).

In the quasi-static regime the scattering cross-section of a metallic sphere is given as [10]

$$C_{sca} = \frac{k^4}{6\pi} |\alpha(\omega)|^2 = \frac{8\pi}{3} k^2 R^6 \left| \frac{\varepsilon(\omega) - \varepsilon_a}{\varepsilon(\omega) + 2\varepsilon_a} \right|^2, \tag{1.26a}$$

and the absorption cross-section is

$$C_{abs} = k\mathrm{Im}\left\{\alpha(\omega)\right\} = 4\pi k R^3 \mathrm{Im}\left\{ \frac{\varepsilon(\omega) - \varepsilon_a}{\varepsilon(\omega) + 2\varepsilon_a} \right\}, \tag{1.26b}$$

where k is a relevant component of the wave-vector, R the radius of the NP, and $\alpha(\omega)$ its polarizability. Furthermore, here $\varepsilon(\omega)$ is the frequency-dependent dielectric function of the metallic particle and ε_a denotes the constant dielectric function of the surrounding medium. The polarizability is an example of a response function, telling us how the polarization of a particle is changed under the influence of an applied electric field. It links the induced dipole in the particle to the incident field.

The extinction cross-section has a scattering component proportional to $(\lambda/2R)^4$ and an absorption component proportional $(\lambda/2R)$. Thus, in the quasi-static regime $2R \ll \lambda$, the interaction between the field and the particle will be dominated by absorption. Absorption (and scattering) will be resonant for a frequency ω for which $\varepsilon(\omega) = -2\varepsilon_a$. For a Drude metal, this leads to an oscillator-like behavior for the absorption called the LSPR. But more generally, the resonance condition will depend intimately on the shape of the object and the dielectric function $\varepsilon(\omega)$ of the metal, or in other words on its polarizability $\alpha(\omega)$. This quantity will be central throughout this thesis.

The two main geometries considered all along this thesis are spheres or spheroids. Together with simple analytical models, we will present plots of the particles polarizabilities with the same model of Drude metal for the dielectric function [given in

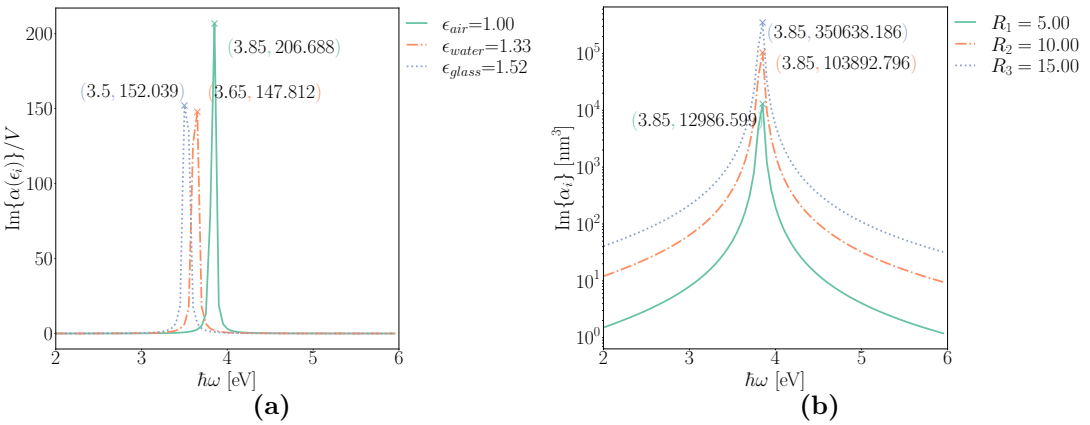

Figure 1.9 Imaginary part of the polarizability of a silver sphere in a homogeneous medium of different dielectric function Fig. 1.9a with different radius Fig. 1.9b. The resonance peaks are tagged with (energy, amplitude).

Eq. (1.22), and displayed in Fig. 1.4(a)]. All the graphs in the following sections keep the same energy scale so the reader can quickly compare plots. Furthermore, the resonance peaks are marked by (energy, amplitude) tags.

Spheres

The famous formula for the polarizability of a metal sphere in a homogeneous medium of dielectric constant ε_a reads [8]

$$\alpha_s(\omega) = 4\pi R^3 \frac{\varepsilon(\omega) - \varepsilon_a}{\varepsilon(\omega) + 2\varepsilon_a}. \tag{1.27}$$

As mentioned earlier, the resonance condition of Eq. (1.27) is found at the pole of the function on the right-hand side, *i.e.* when $\varepsilon(\omega) + 2\varepsilon_a = 0$.

For a metal with a small or slowly varying imaginary part of the dielectric function, the resonance condition simplifies to

$$\begin{aligned} \mathrm{Re}\{\varepsilon(\omega)\} + 2\varepsilon_a &= 0 \\ \varepsilon_1(\omega) &= -2\varepsilon_a. \end{aligned} \tag{1.28}$$

In the literature the condition in Eq. (1.28) is often referred to as *the Frölich condition* of the metal particle. The associated mode is known as the metal particle *dipole surface plasmon* or *the Frölich mode* [8, 10]. For an ambient medium of constant dielectric function ε_a, and for a Drude metal sphere with a small damping, *i.e.* $\Gamma \ll \omega$ (small absorption), the resonance frequency is given by $\omega = \frac{\omega_p}{\sqrt{2\varepsilon_a+1}}$. Thus, the energy position of the resonance changes with ε_a [see Fig. 1.9(a) and Fig. 1.9(b)]. Higher values of the dielectric function ε_a, red-shifts (a shift towards lower energies) the resonance. The particle radius, as long as the quasi-static regime holds, will only change peak amplitude without impacting peak position. Notice that the intensity of the resonance scales with the particle volume.

Ellipsoids

An ellipsoid has three symmetry axis given by the relation

$$\frac{x^2}{a_1^2}+\frac{y^2}{a_2^2}+\frac{z^2}{a_3^2}=1, \tag{1.29}$$

where a_1, a_2, and a_3 define the radius of the ellipsoid along the x-, y-, and z-directions, respectively. As a consequence of the different spacial symmetries, the polarizability of an ellipsoidal in a homogeneous medium becomes direction dependent and is given as [8]:

$$\alpha_i(\omega)=4\pi\varepsilon_a a_1 a_2 a_3 \frac{\varepsilon(\omega)-\varepsilon_a}{3\varepsilon_a+3L_i\left(\varepsilon(\omega)-\varepsilon_a\right)}, \quad i=1,2,3 \tag{1.30a}$$

where the so-called depolarization factor is defined as

$$L_i=\frac{a_1 a_2 a_3}{2}\int_0^\infty \frac{dq}{\left(a_i^2+q\right)\sqrt{\left(a_1^2+q\right)\left(a_2^2+q\right)\left(a_3^2+q\right)}}, \tag{1.30b}$$

and is a geometrical factor dependent of the direction (specified by i) of the exciting electric field. Notice that $\sum_i L_i=1$ and that in the special case of a sphere, for which $L_1=L_2=L_3=1/3$, the expression for the polarizability Eq. (1.27) is recovered.

The resonance condition of an ellipsoidal is given by

$$\mathrm{Re}\{\varepsilon(\omega)\}+\varepsilon_a\left(\frac{1}{L_i}-1\right)=0, \tag{1.31}$$

in the limit of a non-absorbing ambient medium. For an ellipsoid in a homogeneous medium with constant dielectric function ε_a and a Drude metal with small damping $\Gamma \ll \omega$, the resonance frequency is found when $\omega = \omega_p/\sqrt{L_i}$.

The polarizability of an ellipsoid is illustrated in the case of oblates[3] and prolates[4] in Fig. 1.10(a) and Fig. 1.10(c), respectively. For both cases, the resonances are compared with a sphere of the same volume. The first observation is a peak splitting due to the change of particle shape. A smaller value of the radius yields a higher value of the geometrical factor (L_i) and consequently a red-shift compared to the spherical case. In the opposite case, a smaller value of the geometrical factor will shift the polarizability to higher values (blue-shift) as compared to the sphere. For both the configurations, the resonance along the major axis ($R_\parallel^o$ and $R_\perp^p$) is blue-shifted, and along the minor axis ($R_\perp^o$ and $R_\parallel^p$) is red-shifted as compared to the sphere of the same volume.

Coated spheres

Spheres or spheroids coated with concentric layer(s) of different materials are geometries of interest in plasmonics [17]. The polarizability of a coated spherical NP in a homogeneous background is given as [10, 12, 18, 19]:

$$\alpha(\omega)=4\pi(R_2)^3\frac{[\varepsilon_2(\omega)-\varepsilon_a][\varepsilon_1(\omega)+2\varepsilon_2(\omega)]+f[\varepsilon_1(\omega)-\varepsilon_2(\omega)][\varepsilon_a+2\varepsilon_2(\omega)]}{[\varepsilon_2(\omega)+2\varepsilon_a][\varepsilon_1(\omega)+2\varepsilon_2(\omega)]+2f[\varepsilon_2(\omega)-\varepsilon_a][\varepsilon_1(\omega)-\varepsilon_2]}, \tag{1.32}$$

[3] $a_1=a_2\neq a_3, a_1>a_3$, often illustrated as squeezed sphere in the literature.
[4] $a_1=a_2\neq a_3, a_1<a_3$ often illustrated as dragged sphere in the literature.

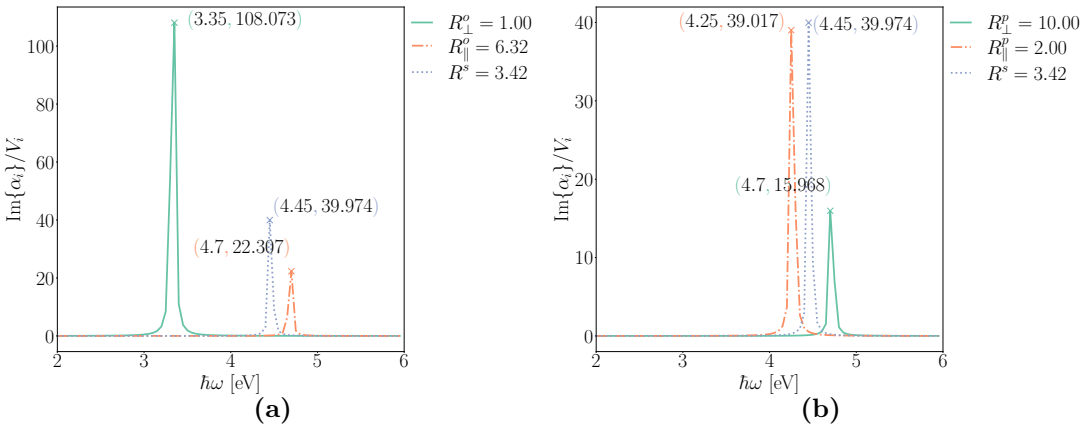

Figure 1.10 The shift in the plasmonic peak of an oblate (a) and a prolate (c) ellipsoid compared to a spherical particle of the same volume calculated with the expression for the polarizability Eq. (1.30). The resonance peaks are marked with (energy, amplitude).

where the outer radius of the NP is denoted R_2, the inner radius R_1, and the number $f = (R_1/R_2)^3$ is the fraction of the total particle volume occupied by the inner sphere. The dielectric function of the inner and outer materials are denoted $\varepsilon_1(\omega)$ and $\varepsilon_2(\omega)$, respectively. The dielectric function of the non-absorbing embedding medium is again denoted by ε_a.

Figure 1.11 displays the imaginary part of the polarizability and therefore the resonance conditions for a coated particle in a homogeneous medium for $R_2 = 10\,\mathrm{nm}$. The two systems we will consider consist of either a thick [$f = 0.4$, $R_1 = 4\,\mathrm{nm}$, Fig. 1.11(a)] or thin [$f = 0.4$, $R_1 = 8\,\mathrm{nm}$, Fig. 1.11(b)] coating layer of a dielectric material on a metallic core (D/M) or a metallic coating on a dielectric core (M/D). The resonance frequency of the corresponding non-coated sphere of the same volume calculated with Eq. (1.27) is shown for comparison. The metallic layer/core is modeled by a Drude-metal given in Fig. 1.4(a), while the value of the dielectric layer/core is taken to $\varepsilon_D = 1.52$.

Choosing a dielectric coating layer (dashed orange lines in the plot), the resonance is red-shifted in energy as compared to the non-coated sphere (blue dotted lines in the plot). The amplitudes of the resonances are also changed. The effects of the shifts in the energy positions of the resonances are most prominent for the thicker dielectric coating [Fig. 1.11(b)]. For the metallic shell, we observe two resonances (green solid lines), one which is red-shifted, and one which is blue-shifted as compared to the corresponding full sphere. The shifts in the energy position of the two peaks are more prominent for the thin metallic shell configuration.

A qualitative explanation of the oscillation peaks observed for a NP coated with a dielectric layer and with a metallic core, or a metallic layer on dielectric core is given in Fig. 1.12. The dielectric layer is mainly shielding the metallic core [Fig. 1.12(a)], whereas in the metallic layer there are two valid patters for the polarization charges [Figs. 1.12(b)-(c)], in accordance with the *hybridization model* [17].

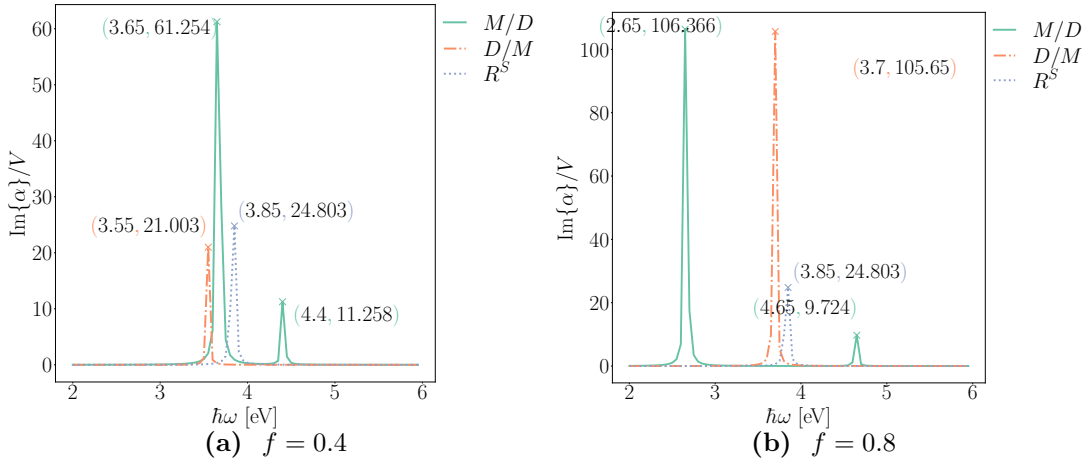

(a) $f = 0.4$ **(b)** $f = 0.8$

Figure 1.11 The shift in the plasmonic peak for a particle with a metallic (M/D) or dielectric (D/M) thick (b) and thin (a) coating layer as compared to the response of an uncoated sphere. The homogeneous material is air $\varepsilon_{air} = 1 + i0$, and the dielectric material is $\varepsilon_D = 1.52 + i0$. The resonance peaks are marked with (energy, amplitude).

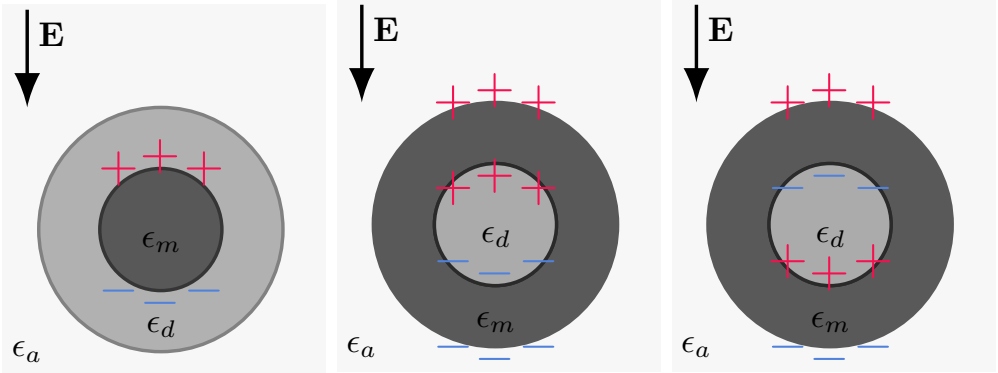

(a) **(b)** **(c)**

Figure 1.12 The polarization pattern for the electric charges in a metallic particle coated with a dielectric (a) and for a dielectric particle coated with a metallic layer (b)/(c).

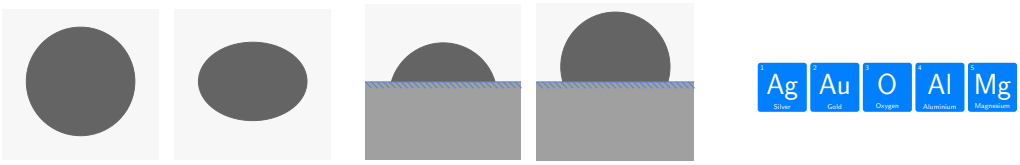

(a) Geometries. **(b)** Environment. **(c)** Material.

Figure 1.13 The most important factors controlling the optical properties of supported nanoparticle films: shape (a), environment (b) and material (c) of the particles.

1.4 Plasmonic resonances in supported and truncated nanoparticles

The understanding of the connection between the optical properties of granular thin films and the plasmonic properties of truncated and supported NPs is essential for the study of the growth process of metallic nanocomposite thin films [1, 20]. The analytical expressions for the polarizabilities of NPs in a homogeneous medium serve as general guidelines to understanding the trends of the optical properties of thin films made out of particles. Shape, environment, and dielectric functions are of paramount importance for the understanding of the plasmonic response [21–23] (see Fig. 1.13). However, the presence of the substrate and the truncation of the particles induced by the partial wetting of the substrate and the break of symmetries as compared to the case of the free-standing particles previously described. As already seen for the metallic shell, a complex mode of polarization can be excited in such supported objects. No analytical model exists for truncated and supported spheres or spheroids. The forthcoming chapters will describe how to handle such situations. Another important issue, not treated up till now, is the presence of a collection of objects that may interact electromagnetically. But before entering into complex modeling, this section aims at highlighting with basic concepts/models the role of the substrate and the presence of the neighboring particles.

Role of the substrate and the concept of image charges

When a metallic NP is placed in the vicinity of a substrate, the original symmetry of the system is broken. Even for a fully symmetrical particle like a sphere, the presence of the substrate complicates the situation in the quasi-static regime. The incident field polarizes the particle and creates a dipole. This dipole is mirrored in the substrate in a so-called image dipole. This latter dipole creates an inhomogeneous field on the particle that may excite a quadrupole in the particle. In turn, it gives rise to an image quadrupole and so on. The polarization of the particle can be seen as a cascade of direct and image multipoles. As a result, the optical response of the particle will become anisotropic and will depend on the direction of the exciting electric field parallel and perpendicular to the substrate and on the angle of incidence. The image response effect will introduce a lift of degeneracy in the polarizability parallel and perpendicular to the substrate, denoted $\alpha_{\parallel} \neq \alpha_{\perp}$. The electrostatic coupling with the

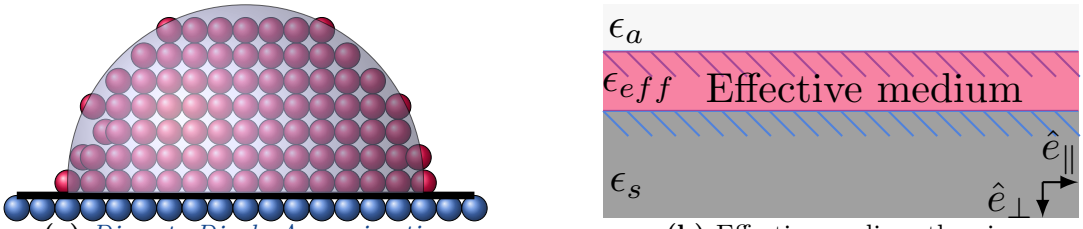

(a) *Discrete Dipole Approximation* (DDA).

(b) Effective medium theories (Maxwell-Garnet)

Figure 1.14 A computational expensive [(a)], and inexpensive [(b)] methods to study the EM-interactions with metallic NPs and light.

substrate can be analyzed in the framework of the *method of images* [1, 6, 22].

Modeling the response of supported and truncated nanoparticles

There exists a broad collection of computational methods capable of modeling the plasmonic response of truncated and supported NPs. Using the static-approximation, the method of image charges and multipoles will be used later to obtain the polarizabilities of truncated supported sphere/spheroid.

Solving the full set of MEs is typically a hard task that requires much computational effort. Methods that are used for this task are often based on a discretization of the domain of interest. Some of these methods are the *Discrete Dipole Approximation* (DDA) [24, 25] and the T-matrix method [26]. Such methods are typically not restricted to a specific particle shape but sufficiently good discretization schemes are required to obtain accurate results. Furthermore, for the DDA-method the electric field close to the particle surfaces are inaccurate [27].

Another class of computational methods is *effective medium theories* [28], where one tries to find the dielectric function of an equivalent continuous layer containing the NPs [see Fig. 1.14(b)]. Effective medium theories, like the *Maxwell Garnett* or *Buggerman model* treat the particle interaction with the substrate by embedding them in an *effective medium*, of which the dielectric constant is chosen between that of vacuum and the substrate. *Maxwell Garnett* [29], successfully describes the colors of glass with metallic particles and their dependence on volume fraction, but fails to account for the break of symmetry induced by the substrate. Improvements along various directions have been attempted to account for the interaction with the substrate, and also for the interactions between objects at dipolar order.

A dipolar description of the anisotropic response in the quasi-static regime was first given by Yamaguchi *et al.* [30]. They tried to explain the anomalous absorption in thin silver films by replacing each particle by a point-dipole and its image in the substrate [31].

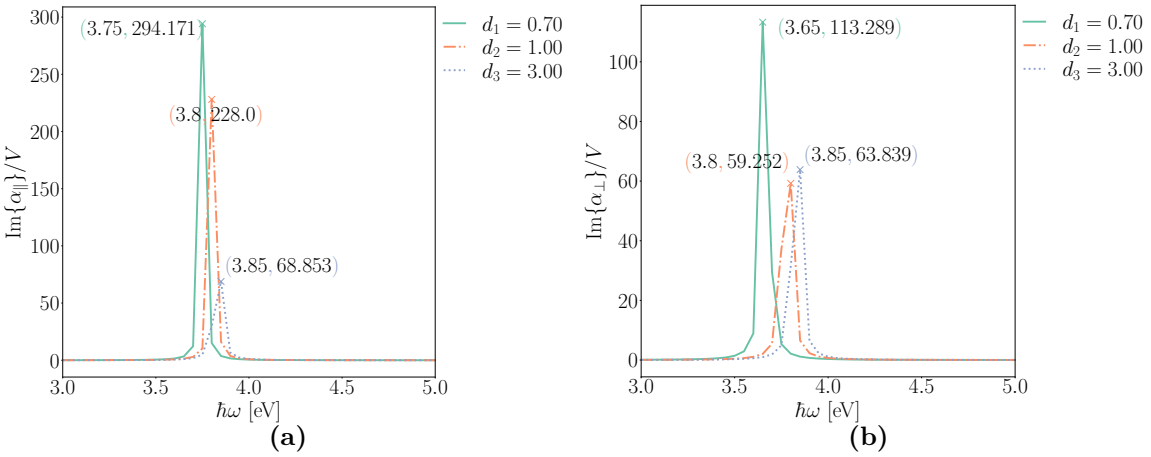

Figure 1.15 Dipolar Yamaguchi model : effect of the difference in the parallel (a) perpendicular (b) component of the imaginary and normalized polarizability when bringing a Drude silver particle close to a substrate of glass (distance indicated in figure). The dielectric function of the substrate was $\varepsilon_s = \varepsilon_D = 1.52$, the ambient media was air $\varepsilon_{air} = 1$. The peaks are marked with (energy, amplitude).

1.4.1 The substrate effect at the dipolar level

In the Yamaguchi model, the direction-dependent polarizabilities of a polarizable sphere is given by [5]:

$$\alpha_i(0) = 4\pi R^3 \frac{\varepsilon_a \left[\varepsilon(\omega) - \varepsilon_a\right]}{\varepsilon_a + L_i \left[\varepsilon(\omega) - \varepsilon_a\right]}, \qquad i = \perp, \parallel \tag{1.33a}$$

with

$$L_\perp = \frac{1}{3} + \frac{1}{12} \frac{\varepsilon_a - \varepsilon_s}{\varepsilon_a + \varepsilon_s} \left(\frac{R}{d}\right)^3 \tag{1.33b}$$

$$L_\parallel = \frac{1}{3} + \frac{1}{24} \frac{\varepsilon_a - \varepsilon_s}{\varepsilon_a + \varepsilon_s} \left(\frac{R}{d}\right)^3 , . \tag{1.33c}$$

Here d describes the distance from the particle to the substrate, R is the particle radius, and ε_s, and ε_a are the dielectric constants of the substrate and the ambient, respectively. The well-known result for the polarizability of a sphere in a homogeneous medium given in Eq. (1.27) is recovered in the limit of infinite distance $\lim_{d\to\infty} \alpha_i = \alpha$, as it should. The induced dipoles caused by the incoming field give the expected break of degeneracy of the parallel and perpendicular direction to the substrate.

A plot of the normalized imaginary part of the direction dependent polarizabilities for a Drude-like metal sphere in the Yamaguchi dipolar model Eq. (1.33a) is shown in Fig. 1.15. Far away from the substrate the effect of the image dipole is negligible and $\alpha_\perp \approx \alpha_\parallel$. As the sphere is brought closer to the substrate, the splitting between the two directions becomes more apparent, while both resonances are shifted towards lower energies.

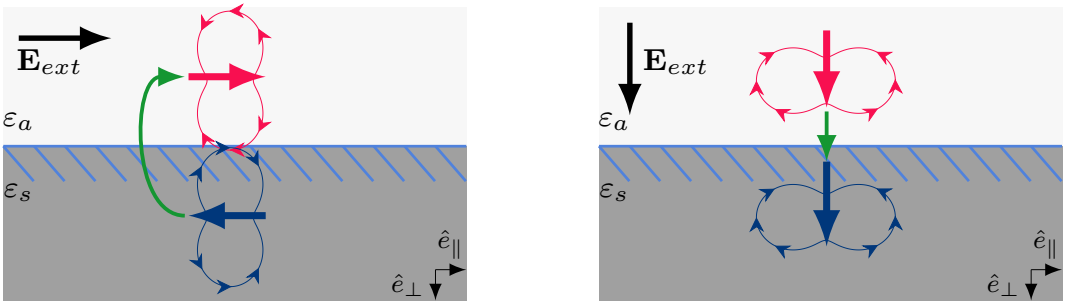

(a) Parallel response. **(b)** Perpendicular response.

Figure 1.16 Qualitative illustration of the direction of the depolarization field in the parallel (a) and perpendicular (b) directions caused by the presence of the surface. The considered dipole is marked in red.

A qualitative explanation of the red-shifts caused by the presence of the substrate is presented in Fig. 1.16. For both directions, the image dipole will create a depolarization field in the particle, proportional to the dipole itself, that will be added to the excitation field. As a result, the restoring force due the positive nuclei acting on the electrons is reduced. A softening of the resonance frequency and a red-shift compared to the free-standing particle is therefore observed.

From the literature, it is known that the inclusion of mutltipolar interactions between the particle and the substrate give rise to additional resonances other than the dipolar one [1]. The dipolar Yamaguchi-model can not account for these higher order terms. Also, the model does not incorporate an accurate description of the particle shape (truncation). The BV-theory describes both the EM-interaction along the surface and the interaction with the substrate. It is based on a direct/image multipole series expansion of the electrostatic potential and a correct matching of the BCs of the potential and its normal derivative at the surface of the particle. It is suitable for cases of truncated and supported particles (see Chs. 2-4 for a proper description of the BV-theory applied to truncated NPs). Because BV-theory takes the geometry of the particles into account it gives better results than the Yamaguchi model [5, 32], even at dipolar order.

1.4.2 The neighbor effect at dipolar order

In a system where the neighboring particles are sufficiently close to feel their neighbors' EM response, the island-island interaction must also be included in order to describe the optical response of the system accurately. In principle, both the island-substrate and the island-island interaction should be accounted for in the same system at high multipolar order [1, 5]. However, as soon as the quasi-static approximation is valid (for particle spacing much smaller than the wavelength), the dipolar coupling leads to similar results as for quadrupolar coupling given that the surface coverage is smaller than 50 % [33,34]. For a lattice of particles, the dipolar correction of the polarizabilities

due to inter-particle coupling reads [5, Eqs. (7.34)–(7.37),Ch. 7]

$$\alpha_i(\omega) = 4\pi R^3 \frac{\varepsilon_a \left[\varepsilon(\omega) - \varepsilon_a\right]}{\varepsilon_a + L_i \left[\varepsilon(\omega) - \varepsilon_a\right]}, \qquad i = \perp, \parallel, \tag{1.34a}$$

with

$$L_\perp = \frac{1}{3}\left\{1 - 4\left(\frac{R}{L}\right)^3 \left[S_{20} - \frac{\varepsilon_a - \varepsilon_s}{\varepsilon_a + \varepsilon_s}\overline{S}_{20}\right]\sqrt{\pi/5}\right\} \tag{1.34b}$$

$$L_\parallel = \frac{1}{3}\left\{1 + 2\left(\frac{R}{L}\right)^3 \left[S_{20} + \frac{\varepsilon_a - \varepsilon_s}{\varepsilon_a + \varepsilon_s}\overline{S}_{20}\right]\sqrt{\pi/5}\right\}, \tag{1.34c}$$

where S_{20} and $\overline{S}_{20}$ denotes the lattice sums over the 2D array of dipoles and their images[5], and L is the lattice constant (determining the distance between two particles).

Again, in the *low coverage limit* and when the distance between the particles (lattice constant) is sufficiently long so the interaction between the particles can be ignored, we recover the Yamaguchi model at dipolar order. In other words, when $S_{20} \to 0$ and $2\overline{S}_{20}\sqrt{\pi/5} \to (L/2d)^3$, the direction-dependent depolarization factors become equal to the case of an isolated object in interaction with the substrate [Eq. (1.34b) → Eq. (1.33b), and Eq. (1.34c) → Eq. (1.33c)].

Plots of the imaginary part of the polarizabilities for a Drude like metal particles including the island-island interaction at dipolar order Eq. (1.34) are presented in Fig. 1.17. The peaks in the response along the parallel and perpendicular directions shift in opposite directions as the lattice constant is decreased. Also, the amplitudes of the resonances are affected.

The underlying reason for the shift of the resonance frequencies is similar to what was given previously for the image effect on a dipole. Along the perpendicular direction [see Fig. 1.18(b)], neighbors create a depolarization field that acts in the opposite direction to the excitation field. This depolarizaton field, proportional to the dipole itself, strengthens the restoring force acting on the electronic cloud, and therefore increases the apparent oscillator frequency (blue-shift). Along the parallel direction [see Fig. 1.18(a)], the situation is less obvious since some neighbors create a depolarization field in the same direction as the excitating field, others in the opposite direction. But due the angular variation of the dipolar term, the ones that soften the resonances win.

1.5 Conclusion

This chapter has given a short overview of the theory needed to describe the plasmonic properties of nanoparticles. In the quasi-static approximation, the absorption dominates over scattering and is driven by the particle polarizability. The analytical models for the polarizability of spheres, spheroids, and coated spheres in homogeneous media have been compared. The case of particles interacting with the substrate and their neighbors only at dipolar order have been described. These basic models allowed for the extraction of important trends of the LSPR. These resonances are sensitive to

[5] An algorithm for the calculation of these lattice sums are given in [5, App. A,Ch. 7]

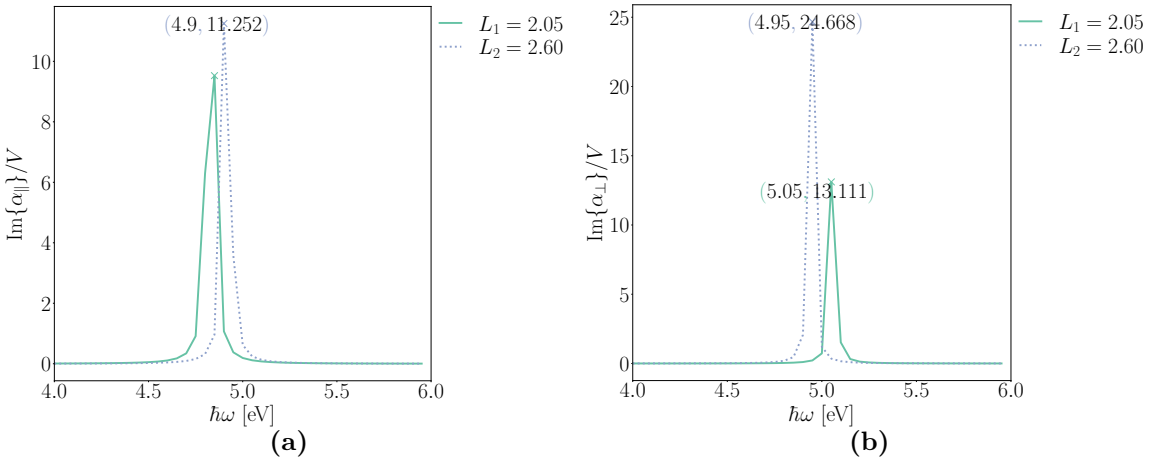

Figure 1.17 Particle-particle coupling at dipolar order: parallel (a) and perpendicular (b) components of the polarizability for a sphere of radius $R = 1$, touching the substrate in one point $d = 1$. Calculations are done for a Drude metal particle in front of a glass substrate by varying the distance between the particles. The dielectric function of the substrate is $\varepsilon_D = 1.52$ and that of the ambient media is $\varepsilon_{air} = 1$. The peaks are marked with (energy, amplitude).

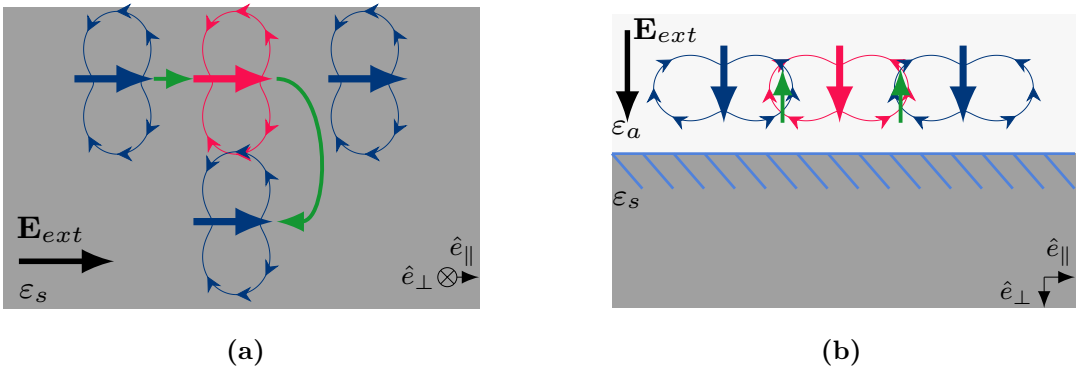

Figure 1.18 Qualitative illustration of the depolarization field induced by neighboring dipoles in parallel (a) and perpendicular (b) directions. The considered dipole is marked in red.

- the dielectric function of the particle,
- the volume of the particle,
- the dielectric constant of the surroundings,
- the distance of the particle to the substrate through the induced image,
- the neighbors through the depolarization field they induce.

Analytical models for the polarizabilities only serve as general guidelines, to properly describe the interaction with the substrate and the neighboring particles, and to predict the effect of the truncated shape of the particles, more complex models are required.

1.6 Organization of the manuscript

In this chapter, basic concepts about the LSPR have been introduced and the complexity induced by the break of symmetry due to the substrate's presence and the truncation of the particle have been discussed.

Chapter 2 will present the theoretical framework of the BV-formalism. It will explain how the *excess fields* (EFs) can be used to describe the EM properties of non-sharp interfaces. The *surface susceptibilities* are the formalism's key concepts and allow to derive all the Fresnel coefficients of the system. These quantities represent the link between the micro- and macroscopic properties of the system.

As will be shown, the surface susceptibilities depend on the polarizabilities of the particles. In Ch. 3, we will give the general system of equations used to derive the polarizabilities of truncated spherical or spheroidal islands interaction at multipolar order with the substrate. To this end, the image charge technique and multipolar expansion of the electrostatic potential (quasi-static approximation) will be used to solve the Laplace equation with appropriate boundary conditions. This chapter ends with a discussion of the island-island interactions and how they influence the optical properties of island films containing supported particles.

Chapter 4 is devoted to a detailed description of GranFilm, a software written in Fortran 90, where the equations from Chs. 2-3 have been implemented. We will here give a detailed description of the powerful features of this software and we will comment on some of the new functionality it has, among them, the GranFilm Python interface. Simulation results for typical system geometries will be presented to illustrate the capabilities of GranFilm.

The break of symmetry represented by the introduction of the substrate and the truncation of the particles allow for the the excitation of several eigenmodes of polarization in the NPs. The notion of eigenmodes of oscillations in truncated and potentially coated NPs will be presented in Ch. 5 and the methodology to identify them will be introduced. The geometries of non-coated truncated silver spheres, coated particles with a metallic core/shell, and a dielectric shell/core will all be discussed. The calculation of 'dispersion' maps will help to rationalize the effect of truncation and coating thickness. Contour plots of the spatial variation of the potential will help to visualize the corresponding pattern of polarization.

In Ch. 6, we address the so-called *experimental broadening* of the plasmon resonances, observed in experimental results, by introducing a dispersion, either in size or shape of the particles. Both the low- and finite-coverage limit of a polydisperse system will be considered. The former consists of a 'simple' average of the polarizabilities over the shape and size distribution of the partiels in the system. The finite-coverage limit will be handled within the mean-field approximation to account for fluctuations of the depolarization fields induced by neighbors of varying size and shape.

Finally, in Ch. 7 we present a summary of the main results obtained during the work with this thesis. Furthermore, we also here put forward the take-home messages and perspectives on the work. We also present the general conclusions.

Chapter 2

Effective boundary conditions for non-sharp interfaces

The macroscopic optical response of a system containing only sharp (or planar) interfaces can be described using the Fresnel amplitudes. However the EM properties of non-sharp interfaces, like island films or rough surfaces, can not be described by these amplitudes alone. This chapter focuses on the BV-formalism, accounted for in detail in the book *Optical properties of surfaces* [5] by Bedeaux and Vlieger. The key concept of the BV-formalism is the introduction of the so-called *excess quantities* and the *surface susceptibilities*. These quantities serve as a link between the microscopic structure of the system and its macroscopic optical response.

Contents

2.1 The definition of the excess fields

Albano *et al.* introduced a position dependent *excess field* (EF) to enable the description of the properties of a boundary layer between two bulk media without considering the exact structure of the layer along the surface normal [35, 36]. For an arbitrary time-dependent EM-field, $\mathbf{A}(\mathbf{r},t)$, its associated EF is defined as

$$\mathbf{A}_{ex}(\mathbf{r},t) = \mathbf{A}(\mathbf{r},t) - \mathbf{A}^{-}(\mathbf{r},t)\theta(-z) - \mathbf{A}^{+}(\mathbf{r},t)\theta(z), \tag{2.1}$$

where $\theta(z)$ denotes the *Heaviside step function*[1]. In writing the expression in Eq. (2.1), we have assumed a *dividing surface* to be located at $z = 0$ (inside the excess region) and we have defined the quantities $\mathbf{A}^{\pm}(\mathbf{r},t)$ which denote the *far fields* extrapolated into the regions just above and below the dividing surface. In principle, the vector $\mathbf{A}(\mathbf{r},t)$, can represent any of the EM-related quantities[2]. For instance, it can be the electric displacement field $\mathbf{D}(\mathbf{r},t)$; the electric field $\mathbf{E}(\mathbf{r},t)$; the magnetic flux density $\mathbf{B}(\mathbf{r},t)$; the magnetic field $\mathbf{H}(\mathbf{r},t)$; the excess or free current density $\mathbf{I}(\mathbf{r},t)$; or, finally, the excess or free charge density $\rho(\mathbf{r},t)$.

Due to the terms $\mathbf{A}^{\pm}(\mathbf{r},t)\theta(\pm z)$ that appear on the right-hand side of Eq. (2.1), the EFs are only significant in the excess region (around the dividing surface) since $\mathbf{A}(\mathbf{r},t) = \mathbf{A}^{\pm}(\mathbf{r},t)$ when $z \to \pm\infty$. An illustration of a system with an excess region is given in Fig. 2.1.

The validity of the BV-formalism is based on the assumption that the integral of the EF along the entire z-axis essentially can be approximated as

$$\int_{-\infty}^{\infty} \mathrm{d}z \mathbf{A}_{ex}(\mathbf{r},t) \approx \int_{-\frac{L_z}{2}}^{\frac{L_z}{2}} \mathrm{d}z \delta(z) \mathbf{A}_{ex}(\mathbf{r},t), \tag{2.2}$$

where L_z denotes the full width (height) of the excess region and $\delta(z)$ the Dirac delta function. An illustration of cases where the excess regions are much smaller, and of the same order of magnitude as the wavelength of the incoming field, is given in Fig. 2.2.

2.2 Maxwell equations for the excess fields

By starting from the original ME given in Eq. (1.1) and the definition of the EF given in Eq. (2.1) it is possible to derive the following new sets of equations describing the

[1] Defined as $\theta(z) \equiv 0, z < 0$ and $\theta(z) \equiv 1, z > 0$.

[2] In the following, $\mathbf{A}(\mathbf{r},t)$ will be used to collectively denote any of these quantities in order to avoid having to repeat similar equations multiple times.

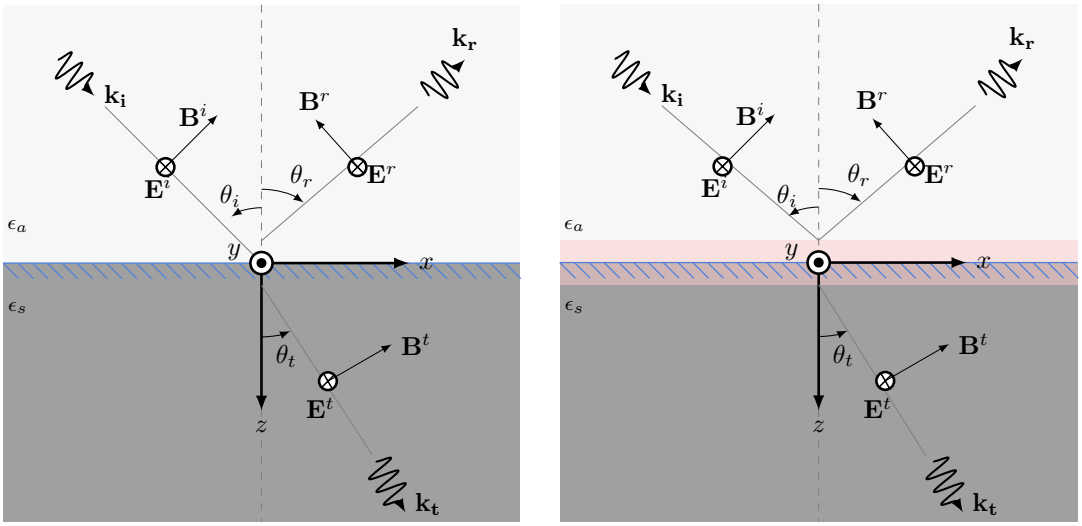

(a) **(b)**

Figure 2.1 Two bulk materials divided by a sharp interface respectively without (a) and with (b) an excess region (show in pink). Notice the choice of the z-axis with positive direction pointed downwards. This convention follows the one assumed by Bedaux and Vlieger [5].

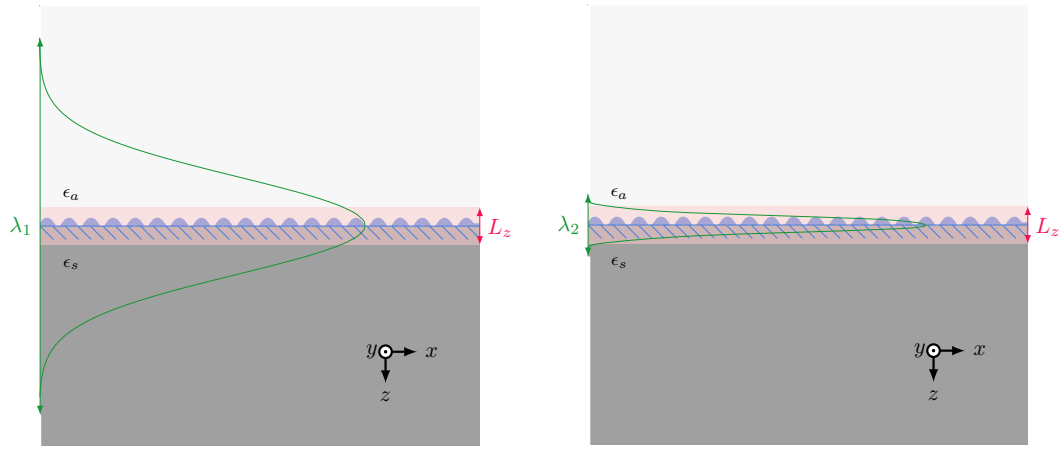

(a) $L_z \ll \lambda_1$. **(b)** $L_z \not\ll \lambda_2$.

Figure 2.2 The width of the excess region, L_z, much smaller (a) and of the same order of magnitude (b) as the wavelength λ_i of an incoming EM-field.

jumps of the EM fields on the planar dividing surface at $z = 0$

$$\boldsymbol{\nabla}\cdot\mathbf{D}_{ex}(\mathbf{r},t) + \left[D_z^+(\mathbf{r},t) - D_z^-(\mathbf{r},t)\right]_{z=0}\delta(z) = \rho_{ex}(\mathbf{r},t) \tag{2.3a}$$

$$\boldsymbol{\nabla}\times\mathbf{E}_{ex}(\mathbf{r},t) + \hat{\mathbf{z}}\times\left[\mathbf{E}_{\parallel}^+(\mathbf{r},t) - \mathbf{E}_{\parallel}^-(\mathbf{r},t)\right]_{z=0}\delta(z) = -\frac{1}{c}\frac{\partial\mathbf{B}_{ex}(\mathbf{r},t)}{\partial t} \tag{2.3b}$$

$$\boldsymbol{\nabla}\cdot\mathbf{B}_{ex}(\mathbf{r},t) + \left[B_z^+(\mathbf{r},t) - B_z^-(\mathbf{r},t)\right]_{z=0}\delta(z) = 0 \tag{2.3c}$$

$$\boldsymbol{\nabla}\times\mathbf{H}_{ex}(\mathbf{r},t) + \hat{\mathbf{z}}\times\left[\mathbf{H}_{\parallel}^+(\mathbf{r},t) - \mathbf{H}_{\parallel}^-(\mathbf{r},t)\right]_{z=0}\delta(z) = \frac{1}{c}\mathbf{I}_{ex}(\mathbf{r},t) + \frac{1}{c}\frac{\partial\mathbf{D}_{ex}(\mathbf{r},t)}{\partial t}. \tag{2.3d}$$

Here $\mathbf{A}_{\parallel}(\mathbf{r},t) = [A_x(\mathbf{r},t), A_y(\mathbf{r},t)]$ represents the in-plane or parallel component of the field $\mathbf{A}(\mathbf{r},t)$ when projected onto the xy-plane ($z = 0$), and the term $A_z(\mathbf{r},t)$, is the normal component of the corresponding quantity. Moreover, $\hat{\mathbf{x}} = [1,0,0]$, $\hat{\mathbf{y}} = [0,1,0]$, and $\hat{\mathbf{z}} = [0,0,1]$ are the unit vectors pointing along the positive x-, y- and z-directions, respectively. The delta function, $\delta(z)$, is present to ensure that the term $\left[\mathbf{A}_{\parallel}^+(\mathbf{r},t) - \mathbf{A}_{\parallel}^-(\mathbf{r},t)\right]$ is zero away from the dividing surface. As usual, $\boldsymbol{\nabla} = \left[\frac{\partial}{\partial x}, \frac{\partial}{\partial y}, \frac{\partial}{\partial z}\right]$ denotes the *three-dimensional* (3D) nabla operator.

Boundary conditions

To see how the EFs modify the BCs given in Eq. (2.3), it is useful to FT the EFs with respect to the z-coordinate. Such a FT over the spatial component of $\mathbf{A}_{ex}(\mathbf{r},t)$ we define as

$$\mathbf{A}_{ex}(\mathbf{r}_{\parallel},k_z,t) = \int_{-\infty}^{\infty}\mathrm{d}z\mathrm{e}^{-ik_z z}\mathbf{A}_{ex}(\mathbf{r},t). \tag{2.4}$$

At the location $z = 0$ one can show that the spatial FT of the EF given in Eq. (2.3) can be written [35,36]:

$$\begin{aligned}&\boldsymbol{\nabla}_{\parallel}\cdot\mathbf{D}_{ex,\parallel}(\mathbf{r}_{\parallel},k_z,t) + ik_z D_{ex,z}(\mathbf{r}_{\parallel},k_z,t)\\ &+\left[D_z^+(\mathbf{r}_{\parallel},z=0,t) - D_z^-(\mathbf{r}_{\parallel},z=0,t)\right] = \rho_{ex}(\mathbf{r}_{\parallel},k_z,t)\end{aligned} \tag{2.5a}$$

$$\begin{aligned}&\boldsymbol{\nabla}_{\parallel}\times\mathbf{E}_{ex}(\mathbf{r}_{\parallel},k_z,t) + ik_z\hat{\mathbf{z}}\times\mathbf{E}_{ex,\parallel}(\mathbf{r}_{\parallel},k_z,t)\\ &+\hat{\mathbf{z}}\times\left[\mathbf{E}_{\parallel}^+(\mathbf{r}_{\parallel},z=0,t) - \mathbf{E}_{\parallel}^-(\mathbf{r}_{\parallel},z=0,t)\right] = -\frac{1}{c}\frac{\partial}{\partial t}\mathbf{B}_{ex}(\mathbf{r}_{\parallel},k_z t)\end{aligned} \tag{2.5b}$$

$$\begin{aligned}&\boldsymbol{\nabla}_{\parallel}\cdot\mathbf{B}_{ex,\parallel}(\mathbf{r}_{\parallel},k_z,t) + ik_z B_{ex,z}(\mathbf{r}_{\parallel},k_z,t)\\ &+\left[B_z^+(\mathbf{r}_{\parallel},z=0,t) - B_z^-(\mathbf{r}_{\parallel},z=0,t)\right] = 0\end{aligned} \tag{2.5c}$$

$$\begin{aligned}&\boldsymbol{\nabla}_{\parallel}\times\mathbf{H}_{ex}(\mathbf{r}_{\parallel},k_z,t) + ik_z\hat{\mathbf{z}}\times\mathbf{H}_{ex,\parallel}(\mathbf{r}_{\parallel},k_z,t)\\ &+\hat{\mathbf{z}}\times\left[\mathbf{H}_{\parallel}^+(\mathbf{r}_{\parallel},z=0,t) - \mathbf{H}_{\parallel}^-(\mathbf{r}_{\parallel},z=0,t)\right] = \frac{1}{c}\mathbf{I}_{ex}(\mathbf{r}_{\parallel},k_z,t) + \frac{1}{c}\frac{\partial}{\partial t}\mathbf{D}_{ex}(\mathbf{r}_{\parallel},k_z,t),\end{aligned} \tag{2.5d}$$

where $\boldsymbol{\nabla}_{\parallel} = \left[\frac{\partial}{\partial x}, \frac{\partial}{\partial y}\right]$ denotes the *two-dimensional* (2D) nabla operator.

To obtain an expression for the jumps in the fields in a simpler form, one can set $k_z = 0$ and simplify the notation further by introducing the *total excess* of the quantities

$$\mathbf{A}^s_{\parallel}(\mathbf{r}_{\parallel}, t) \equiv \hat{\mathbf{A}}_{ex,\parallel}(\mathbf{r}_{\parallel}, k_z = 0, t) = \int_{-\infty}^{\infty} \mathrm{d}z \mathrm{e}^{-ik_z z} \mathbf{A}_{ex,\parallel}(\mathbf{r}_{\parallel}, z, t) \tag{2.6a}$$

$$A^s_z(\mathbf{r}_{\parallel}, t) \equiv \hat{A}_{ex,z}(\mathbf{r}_{\parallel}, k_z = 0, t) = \int_{-\infty}^{\infty} \mathrm{d}z \mathrm{e}^{-ik_z z} A_{ex,z}(\mathbf{r}_{\parallel}, z, t), \tag{2.6b}$$

where the superscript s denotes the total excess quantity of the actual field evaluated at $k_z = 0$.

Applying these simplifications in notation, we can now recast Eq. (2.5) in component form with the jumps of the bulk fields extrapolated at the surface. In this way we obtain

$$D^+_z(\mathbf{r}_{\parallel}, z = 0, t) - D^-_z(\mathbf{r}_{\parallel}, z = 0, t) = -\boldsymbol{\nabla}_{\parallel} \cdot \mathbf{D}^s_{\parallel}\left(\mathbf{r}_{\parallel}, t\right) + \rho^s(\mathbf{r}_{\parallel}, t) \tag{2.7a}$$

$$E^+_x(\mathbf{r}_{\parallel}, z = 0, t) - E^-_x(\mathbf{r}_{\parallel}, z = 0, t) = \frac{\partial}{\partial x} E^s_z(\mathbf{r}_{\parallel}, t) - \frac{1}{c}\frac{\partial}{\partial t} B^s_y(\mathbf{r}_{\parallel}, t) \tag{2.7b}$$

$$E^+_y(\mathbf{r}_{\parallel}, z = 0, t) - E^-_y(\mathbf{r}_{\parallel}, z = 0, t) = \frac{\partial}{\partial y} E^s_z(\mathbf{r}_{\parallel}, t) + \frac{1}{c}\frac{\partial}{\partial t} B^s_x(\mathbf{r}_{\parallel}, t) \tag{2.7c}$$

$$B^+_z(\mathbf{r}_{\parallel}, z = 0, t) - B^-_z(\mathbf{r}_{\parallel}, z = 0, t) = -\boldsymbol{\nabla}_{\parallel} \cdot \mathbf{B}^s_{\parallel}\left(\mathbf{r}_{\parallel}, t\right) \tag{2.7d}$$

$$\begin{aligned} H^+_x(\mathbf{r}_{\parallel}, z = 0, t) - H^-_x(\mathbf{r}_{\parallel}, z = 0, t) = {} & \frac{\partial}{\partial x} H^s_z(\mathbf{r}_{\parallel} t) + \frac{1}{c} I^s_y(\mathbf{r}_{\parallel}, t) \\ & + \frac{1}{c}\frac{\partial}{\partial t} D^s_y(\mathbf{r}_{\parallel}, t) \end{aligned} \tag{2.7e}$$

$$\begin{aligned} H^+_y(\mathbf{r}_{\parallel}, z = 0, t) - H^-_y(\mathbf{r}_{\parallel}, z = 0, t) = {} & \frac{\partial}{\partial y} H^s_z(\mathbf{r}_{\parallel}, t) - \frac{1}{c} I^s_x(\mathbf{r}_{\parallel}, t) \\ & - \frac{1}{c}\frac{\partial}{\partial t} D^s_x(\mathbf{r}_{\parallel}, t). \end{aligned} \tag{2.7f}$$

2.3 Surface polarization and magnetization

As explained in Sec. 1.1.1, it is convenient to introduce surface polarization and magnetization for the solutions of the MEs. With the total excess of the fields we introduce the concepts of *generalized surface* polarization and magnetization densities, denoted $\mathbf{P}^s(\mathbf{r}_{\parallel}, t)$ and $\mathbf{M}^s(\mathbf{r}_{\parallel}, t)$, respectively. In the case when a boundary layer is present the definition for these quantities are not as straightforward as in the bulk case. Here, we follow Bedeaux and Vlieger and define them as [37]:

$$\mathbf{P}^s(\mathbf{r}_{\parallel}, t) \equiv \left[\mathbf{D}^s_{\parallel}(\mathbf{r}_{\parallel}, t), -E^s_z(\mathbf{r}_{\parallel}, t)\right] \tag{2.8a}$$

$$\mathbf{M}^s(\mathbf{r}_{\parallel}, t) \equiv \left[\mathbf{B}^s_{\parallel}(\mathbf{r}_{\parallel}, t), -H^s_z(\mathbf{r}_{\parallel}, t)\right], \tag{2.8b}$$

where again the superscript s stands for the total excess of the corresponding quantity [*c.f.* Eq. (2.6)].

2.3.1 The choice of zero fields

It is often convenient to introduce zero fields in the mathematical analysis. This choice should not affect the global optical properties of the system. Again, following Ref. 37 we chose the following zero fields

$$D_z^s(\mathbf{r}_\parallel,t)\equiv\mathbf{E}_\parallel^s(\mathbf{r}_\parallel,t)\equiv B_z^s(\mathbf{r}_\parallel,t)\equiv\mathbf{H}_\parallel^s(\mathbf{r}_\parallel,t)\equiv I_z^s(\mathbf{r}_\parallel,t)\equiv 0. \tag{2.9}$$

The interfacial polarization and magnetization densities in Eq. (2.8) can then be rewritten as

$$\mathbf{P}^s(\mathbf{r}_\parallel,t)=\mathbf{D}^s(\mathbf{r}_\parallel,t)-\mathbf{E}^s(\mathbf{r}_\parallel,t) \tag{2.10a}$$
$$\mathbf{M}^s(\mathbf{r}_\parallel,t)=\mathbf{B}^s(\mathbf{r}_\parallel,t)-\mathbf{H}^s(\mathbf{r}_\parallel,t). \tag{2.10b}$$

Bear in mind, that in contrast to the definitions of the surface polarization and magnetization densities given in Eq. (2.8), the interfacial polarization and magnetization densities are now expressed with the total vector fields. Our definition is only true for a certain choice of zero fields. In general,

$$\mathbf{A}_\parallel^s(\mathbf{r}_\parallel,t)\neq\hat{\mathbf{A}}_{ex,\parallel}(\mathbf{r}_\parallel,k_z=0,t) \tag{2.11a}$$
$$A_z^s(\mathbf{r}_\parallel,t)\neq\hat{A}_{ex,z}(\mathbf{r}_\parallel,k_z=0,t), \tag{2.11b}$$

where the left-hand side of Eq. (2.11) is zero by definition, but the right-hand side maybe different from zero.

2.3.2 The planar surface as an example

The polarization and magnetization density for the planar surface can be obtained by integrating Eq. (2.4) along the entire z-axis with $k_z=0$

$$\mathbf{P}^s(\mathbf{r}_\parallel,t)=\int_{-\infty}^{\infty}\mathrm{d}z\left[\mathbf{D}_\parallel^s(\mathbf{r}_\parallel,z,t),-E_z^s(\mathbf{r}_\parallel,z,t)\right] \tag{2.12a}$$
$$\mathbf{M}^s(\mathbf{r}_\parallel,t)=\int_{-\infty}^{\infty}\mathrm{d}z\left[\mathbf{B}_\parallel^s(\mathbf{r}_\parallel,z,t),-H_z^s(\mathbf{r}_\parallel,z,t)\right]. \tag{2.12b}$$

The BCs [given in Eq. (2.7)] for the jumps in the fields can be reexpressed in terms of the interfacial polarization and magnetization densities defined in Eq. (2.8). When

this is done, the results is:

$$D_z^+(\mathbf{r}_\parallel, z=0,t) - D_z^-(\mathbf{r}_\parallel, z=0,t) = -\boldsymbol{\nabla}_\parallel \cdot \mathbf{P}_\parallel^s\left(\mathbf{r}_\parallel, t\right) + \rho^s(\mathbf{r}_\parallel, t) \tag{2.13a}$$

$$E_x^+(\mathbf{r}_\parallel, z=0,t) - E_x^-(\mathbf{r}_\parallel, z=0,t) = -\frac{\partial}{\partial x} P_z^s(\mathbf{r}_\parallel, t) - \frac{1}{c}\frac{\partial}{\partial t} M_y^s(\mathbf{r}_\parallel, t) \tag{2.13b}$$

$$E_y^+(\mathbf{r}_\parallel, z=0,t) - E_y^-(\mathbf{r}_\parallel, z=0,t) = -\frac{\partial}{\partial y} P_z^s(\mathbf{r}_\parallel, t) + \frac{1}{c}\frac{\partial}{\partial t} M_x^s(\mathbf{r}_\parallel, t) \tag{2.13c}$$

$$B_z^+(\mathbf{r}_\parallel, z=0,t) - B_z^-(\mathbf{r}_\parallel, z=0,t) = -\boldsymbol{\nabla}_\parallel \cdot \mathbf{M}^s\left(\mathbf{r}_\parallel, t\right) \tag{2.13d}$$

$$\begin{aligned} H_x^+(\mathbf{r}_\parallel, z=0,t) - H_x^-(\mathbf{r}_\parallel, z=0,t) = &-\frac{\partial}{\partial x} M_z^s(\mathbf{r}_\parallel, t) + \frac{1}{c} I_y^s(\mathbf{r}_\parallel, t) \\ &+ \frac{1}{c}\frac{\partial}{\partial t} P_y^s(\mathbf{r}_\parallel, t) \end{aligned} \tag{2.13e}$$

$$\begin{aligned} H_y^+(\mathbf{r}_\parallel, z=0,t) - H_y^-(\mathbf{r}_\parallel, z=0,t) = &-\frac{1}{c}\frac{\partial}{\partial y} M_z^s(\mathbf{r}_\parallel, t) - \frac{1}{c} I_x^s(\mathbf{r}_\parallel, t) \\ &- \frac{\partial}{\partial t} P_x^s(\mathbf{r}_\parallel, t). \end{aligned} \tag{2.13f}$$

If the surface polarization and magnetization densities, as well as all the charge and current densities are set to zero in Eq. (2.13), the resulting BCs reduce, as they should, to the familiar expressions given in Eq. (1.2).

2.4 The generalized electric displacement field

A common and convenient technique for working with problems of time dependence is to define a generalized electric displacement field, $\mathbf{D}'(\mathbf{r}, \omega)$. An additional advantage in the description of surfaces is that to describe charge conservation, it is necessary to take the normal component of the excess electric displacement field and the excess electric current density to zero [37, Chapter 3].

In the following, as we did in Ch. 1, we will again use the temporal FT which we defined as

$$\mathbf{A}(\mathbf{r}, \omega) = \int_{-\infty}^{\infty} \mathrm{d}t \quad \mathrm{e}^{i\omega t} \mathbf{A}_{ex}(\mathbf{r}, t). \tag{2.14}$$

If one introduces the general electrical displacement field, it is necessary to put only the normal component of the EF to zero; thus we have a less restrictive formulation. We define the general displacement field is defined as

$$\mathbf{D}'(\mathbf{r}, \omega) \equiv \mathbf{D}(\mathbf{r}, \omega) + \frac{i}{\omega}\mathbf{I}(\mathbf{r}, \omega), \tag{2.15}$$

where the FT over time has been performed [$t \to \omega$]. Furthermore, we may use the definition of the generalized displacement field given in Eq. (2.15) and charge

conservation[3] to rewrite Eq. (1.5)

$$\boldsymbol{\nabla}\cdot\mathbf{D}'(\mathbf{r},\omega)=0 \tag{2.16a}$$

$$\boldsymbol{\nabla}\times\mathbf{E}(\mathbf{r},\omega)=i\frac{\omega}{c}\mathbf{B}(\mathbf{r},\omega) \tag{2.16b}$$

$$\boldsymbol{\nabla}\cdot\mathbf{B}(\mathbf{r},\omega)=0 \tag{2.16c}$$

$$\boldsymbol{\nabla}\times\mathbf{H}(\mathbf{r},\omega)=-i\frac{\omega}{c}\mathbf{D}'(\mathbf{r},\omega). \tag{2.16d}$$

The choice of absorbing the electric current density into the generalized electric displacement field is convenient for time independent problems. In the context of this thesis, our interest is mainly optical problems. Thus, this choice is not a restriction for us.

Using these definitions and of the temporal FT [*c.f.* Eq. (2.14)], the polarization and magnetization densities become

$$\mathbf{P}'^{s}(\mathbf{r}_\parallel,\omega)\equiv\left[\mathbf{D}'^{s}_\parallel(\mathbf{r}_\parallel,\omega),-E^s_z(\mathbf{r}_\parallel,\omega)\right] \tag{2.17a}$$

$$\mathbf{M}^s(\mathbf{r}_\parallel,\omega)\equiv\left[\mathbf{B}^s_\parallel(\mathbf{r}_\parallel,\omega),-H^s_z(\mathbf{r}_\parallel,\omega)\right]. \tag{2.17b}$$

Again, following Ref. 37 the choices for the singular behavior of the fields are

$$\begin{aligned}&\mathbf{E}^s_\parallel(\mathbf{r}_\parallel,\omega)=0, \qquad D'^{s}_z(\mathbf{r}_\parallel,\omega)\equiv D^s_z(\mathbf{r}_\parallel,\omega)+\frac{i}{\omega}I^s_z(\mathbf{r}_\parallel,\omega)=0\\ &\mathbf{H}^s_\parallel(\mathbf{r}_\parallel,\omega)=0, \qquad B^s_z(\mathbf{r}_\parallel,\omega)=0.\end{aligned} \tag{2.18}$$

The interfacial polarization and magnetization densities are again given by the total fields

$$\mathbf{P}'^{s}(\mathbf{r}_\parallel,\omega)=\mathbf{D}'^{s}(\mathbf{r}_\parallel,\omega)-\mathbf{E}^s(\mathbf{r}_\parallel,\omega) \tag{2.19a}$$

$$\mathbf{M}^s(\mathbf{r}_\parallel,\omega)=\mathbf{B}^s(\mathbf{r}_\parallel,\omega)-\mathbf{H}^s(\mathbf{r}_\parallel,\omega). \tag{2.19b}$$

Performing the replacements $\mathbf{D}\to\mathbf{D}'$, $\mathbf{P}^s\to\mathbf{P}^{s,\prime}$ and setting $\rho=0$ and $\mathbf{I}=0$ in Eq. (2.13), the singular behavior of the time harmonic fields on the dividing surface with generalized displacement fields becomes

$$D^+_z(\mathbf{r}_\parallel,z=0,\omega)-D^-_z(\mathbf{r}_\parallel,z=0,\omega)=-\boldsymbol{\nabla}_\parallel\cdot\mathbf{P}'^{s}_\parallel\left(\mathbf{r}_\parallel,\omega\right) \tag{2.20a}$$

$$\mathbf{E}^+_\parallel(\mathbf{r}_\parallel,z=0,\omega)-\mathbf{E}^-_\parallel(\mathbf{r}_\parallel,z=0,\omega)=-\boldsymbol{\nabla}_\parallel P'^{s}_z(\mathbf{r}_\parallel,\omega)-i\frac{\omega}{c}\hat{\mathbf{z}}\times\mathbf{M}^s_\parallel(\mathbf{r}_\parallel,\omega) \tag{2.20b}$$

$$B^+_z(\mathbf{r}_\parallel,z=0,\omega)-B^-_z(\mathbf{r}_\parallel,z=0,\omega)=-\boldsymbol{\nabla}_\parallel\cdot\mathbf{M}^s_\parallel\left(\mathbf{r}_\parallel,\omega\right) \tag{2.20c}$$

$$\mathbf{H}^+_\parallel(\mathbf{r}_\parallel,z=0,\omega)-\mathbf{H}^-_\parallel(\mathbf{r}_\parallel,z=0,\omega)=-\boldsymbol{\nabla}_\parallel M^s_z(\mathbf{r}_\parallel,\omega)+i\frac{\omega}{c}\hat{\mathbf{z}}\times\mathbf{P}'^{s}_\parallel(\mathbf{r}_\parallel,\omega). \tag{2.20d}$$

With our choices for the fields, it is sufficient to set the normal component of the generalized field $\mathbf{D}'^{s}_z(\mathbf{r}_\parallel,\omega)$ to zero, and not separately the displacement field $\mathbf{D}^s_z(\mathbf{r},\omega)$ and the free current density $\frac{i}{\omega}\mathbf{I}^s_z(\mathbf{r},\omega)$. In order to simplify the notation, we will from now onward suppress the explicit use of primes on the generalized displacement field and related quantities. In what follows, we will let $\mathbf{D}'\to\mathbf{D}$ and $\mathbf{P}'\to\mathbf{P}$.

[3] Charge conservation yields: $i\omega\rho(\mathbf{r},\omega)=\boldsymbol{\nabla}\cdot\mathbf{I}(\mathbf{r},\omega)\to\boldsymbol{\nabla}\cdot\mathbf{D}'(\mathbf{r},\omega)=\boldsymbol{\nabla}\cdot\left[\mathbf{D}(\mathbf{r},\omega)+\frac{i}{\omega}\mathbf{I}(\mathbf{r},\omega)\right]$.

2.5 Constitutive relations

To make practical use of the BCs given by Eq. (2.20) the interfacial polarization and magnetization densities, $\mathbf{P}^s(\mathbf{r}_\parallel,\omega)$ and $\mathbf{M}^s(\mathbf{r}_\parallel,\omega)$, characterizing the actual surface need to be linked to the bulk fields extrapolated onto the (dividing) surface [35, 36].

2.5.1 Isotropic interfaces without spatial dispersion

Given that the source-observer symmetry is satisfied, as we will assume here, the constitutive coefficients that relate the interfacial polarization and magnetization densities to the various components of the EM-fields, will be symmetric tensors (matrices).

In the absence of spatial dispersion, the most general constitutive relation is defined by the multiplication of a second-rank tensor and a vector

$$\mathbf{P}^s(\mathbf{r}_\parallel,\omega) = \overleftrightarrow{\boldsymbol{\xi}}^s_e(\omega) \circ \Big[\mathbf{E}_{\parallel,\Sigma}(\mathbf{r}_\parallel,\omega), D_{z,\Sigma}(\mathbf{r}_\parallel,\omega)\Big] \tag{2.21a}$$

$$\Big[\mathbf{M}^s(\mathbf{r}_\parallel,\omega)\Big]_i = \overleftrightarrow{\boldsymbol{\xi}}^s_m(\omega) \circ \Big[\mathbf{H}_{\parallel,\Sigma}(\mathbf{r}_\parallel,\omega), B_{z,\Sigma}(\mathbf{r}_\parallel,\omega)\Big]\,, \tag{2.21b}$$

where the subscript Σ on a EM-field quantity indicates that its associated extrapolated fields on both side of the dividing surface are an average; the formal definition is $\mathbf{A}_\Sigma(\mathbf{r}_\parallel,\omega) = \frac{1}{2}\Big[\mathbf{A}^-(\mathbf{r}_\parallel,\omega) + \mathbf{A}^+(\mathbf{r}_\parallel,\omega)\Big]$, the $\circ$-symbol denotes the multiplication between a second order tensor and a vector[4]. The terms $\overleftrightarrow{\boldsymbol{\xi}}^s_e$ and $\overleftrightarrow{\boldsymbol{\xi}}^s_m$ that appear in Eq. (2.21), are dependent on the actual geometry and properties of the surface. We call them the constitutive coefficients. In this sense, we can therefore say that the features and characteristics of the excess region are encoded into these two quantities. As a consequence, they will be of primary importance when we later on address the optical properties of surfaces with a non-trivial excess region.

In this thesis, the surface is always assumed to be isotropic. In the Cartesian coordinate system the constitutive coefficients can be represented as matrices with nine components. For an isotropic surface without spatial dispersion[5], only the diagonal elements of these matrices will be different from zero

$$\overleftrightarrow{\boldsymbol{\xi}}^s_i(\omega) = \begin{bmatrix} \gamma_i(\omega) & 0 & 0 \\ 0 & \gamma_i(\omega) & 0 \\ 0 & 0 & \beta_i(\omega) \end{bmatrix} \tag{2.22}$$

where β_i and γ_i (with $i = e, m$) denote the first order *surface susceptibilities*. These first order surface susceptibilities have the dimension of length. They can be interpreted as an effective optical thickness d, that can be obtained by *Surface Differential Reflectivity Spectroscopy* (SDRS) or ellipsometry experiments.

[4] This operation is also called *single contraction* in tensor notation [38].
[5] *i.e.* the dielectric function has no dependence of the wave vector $\mathbf{k}$.

Combining Eq. (2.21) and Eq. (2.22) one obtains

$$\mathbf{P}^s_{\parallel}(\mathbf{r}_{\parallel},\omega) = \gamma_e(\omega)\mathbf{E}^s_{\parallel,\Sigma}(\mathbf{r}_{\parallel},\omega) \tag{2.23a}$$

$$P^s_z(\mathbf{r}_{\parallel},\omega) = \beta_e(\omega)D^s_{z,\Sigma}(\mathbf{r}_{\parallel},\omega) \tag{2.23b}$$

$$\mathbf{M}^s_{\parallel}(\mathbf{r}_{\parallel},\omega) = \gamma_m(\omega)\mathbf{H}^s_{\parallel,\Sigma}(\mathbf{r}_{\parallel},\omega) \tag{2.23c}$$

$$M^s_z(\mathbf{r}_{\parallel},\omega) = \beta_m(\omega)B^s_{z,\Sigma}(\mathbf{r}_{\parallel},\omega). \tag{2.23d}$$

2.5.2 Isotropic interfaces with spatial dispersion

For a spatially dispersive surface, polarization and magnetization densities are no longer related to the fields in a spatially local manner. To relate the constitutive relations to the extrapolated bulk fields one must introduce two new second order surface susceptibilities. Bedeaux and Vlieger [5] denote them τ and δ, and we will do the same. It can be shown that the constitutive relations for the ME to first order in the non-locality take the form [37, Chapter 3.7]

$$\mathbf{P}^s_{\parallel}(\mathbf{r}_{\parallel},\omega) = \gamma_e(\omega)\mathbf{E}^s_{\parallel,\Sigma}(\mathbf{r}_{\parallel},\omega) - \delta_e(\omega)\boldsymbol{\nabla}_{\parallel}D^s_{z,\Sigma}(\mathbf{r}_{\parallel},\omega) + i\frac{\omega}{c}\tau(\omega)\hat{\mathbf{z}}\times\mathbf{H}^s_{\parallel,\Sigma}(\mathbf{r}_{\parallel},\omega) \tag{2.24a}$$

$$P^s_z(\mathbf{r}_{\parallel},\omega) = \delta_e(\omega)\,\boldsymbol{\nabla}_{\parallel}\cdot\mathbf{E}^s_{\parallel,\Sigma}(\mathbf{r}_{\parallel},\omega) + \beta_e(\omega)D^s_{z,\Sigma}(\mathbf{r}_{\parallel},\omega) \tag{2.24b}$$

$$\mathbf{M}^s_{\parallel}(\mathbf{r}_{\parallel},\omega) = \gamma_m(\omega)\mathbf{H}^s_{\parallel,\Sigma}(\mathbf{r}_{\parallel},\omega) - \delta_m(\omega)\boldsymbol{\nabla}_{\parallel}B^s_{z,\Sigma}(\mathbf{r}_{\parallel},\omega) + i\frac{\omega}{c}\tau(\omega)\hat{\mathbf{z}}\times\mathbf{E}^s_{\parallel,\Sigma}(\mathbf{r}_{\parallel},\omega) \tag{2.24c}$$

$$M^s_z(\mathbf{r}_{\parallel},\omega) = \delta_m(\omega)\,\boldsymbol{\nabla}_{\parallel}\cdot\mathbf{H}^s_{\parallel,\Sigma}(\mathbf{r}_{\parallel},\omega) + \beta_m(\omega)B^s_{z,\Sigma}(\mathbf{r}_{\parallel},\omega). \tag{2.24d}$$

The second order surface susceptibilities δ and τ give the contributions to the derivatives of the magnetic dipole polarization and the electric excess fields. They have the dimension of length squared and are therefore a factor of optical thickness divided by the wavelength d/λ smaller than the first order surface susceptibilities. In Ch. 3 it will become clear that the second order surface susceptibilities are linked to the direction dependent quadrupolar polarizabilities, $\alpha^{10}_{\parallel}$ and $\alpha^{10}_{\perp}$, for a non-sharp interface containing island particles.

2.5.3 Example geometries

The expressions of the surface susceptibilities will depend on the geometry of the boundary layer. For a thin film that is parallel to the surface of the substrate, the first order surface susceptibilities are [39]

$$\gamma = d\,(\varepsilon_f - \varepsilon_a) \tag{2.25a}$$

$$\beta = d\frac{(\varepsilon_f - \varepsilon_a)}{\varepsilon_f\varepsilon_a}, \tag{2.25b}$$

where d is the thickness of the film, and ε_a and ε_f denote the relative permittivity of the ambient medium and the film, respectively. The result in Eq. (2.25) is well-known

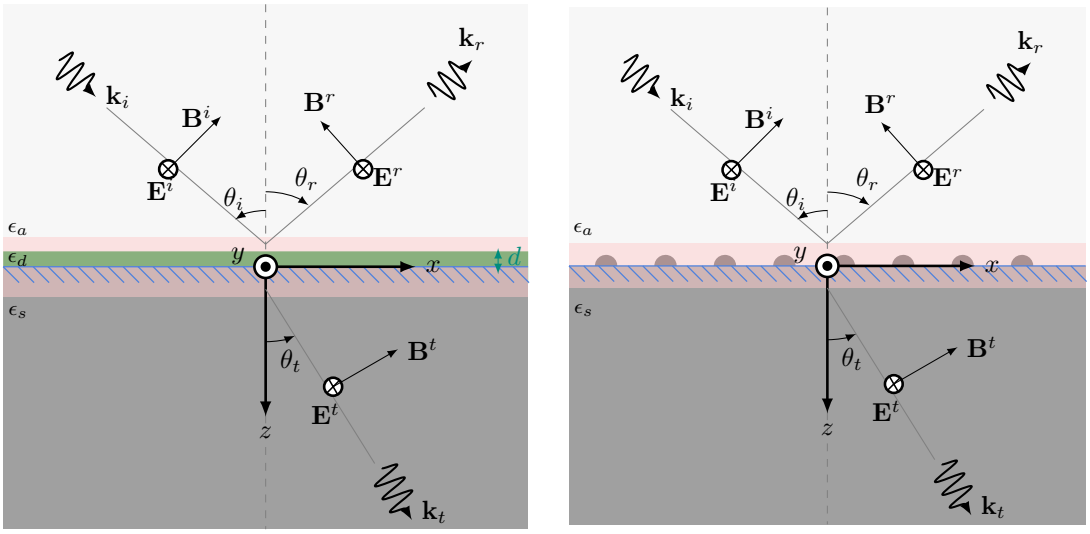

Figure 2.3 Illustration of the 'excess' regions for a boundary layer containing a parallel thin film (a) and spherical particles (b).

from thin film theory and is an illustrative and simple example to use to check that the BV-formalism can reproduce this result correctly. Figure 2.3(a) display the relevant geometry in such a system.

A less trivial illustration of practical use is a geometry where the boundary layer consists of spherical particles. In this case, the first order surface susceptibilities are given by [5]

$$\gamma = \rho\langle\alpha_{\parallel}\rangle \tag{2.26a}$$

$$\beta = \rho\frac{\langle\alpha_{\perp}\rangle}{\varepsilon_a^2}, \tag{2.26b}$$

where ρ denotes the density of particles, ε_a is the relative permittivity of the substrate, α_i is the direction dependent polarizabilities, and the term $\langle\cdot\rangle$ denotes the average. A thin film containing truncated particles in the boundary region defined by the EFs is illustrated in Fig. 2.3(b).

Since the polarizability scales with the volume of the particle, the surface susceptibilities γ and β are both proportional to the amount of matter in the film. They describe how the interface polarizes the light that is reflected or trasmitted from it. An explicit calculation of the polarizabilities $\alpha_{\parallel}$ and $\alpha_{\perp}$ in the case of supported and truncated spherical or spheroidal particles will be given in detail in Ch. 3.

2.6 Modified Fresnel coefficients

It is a standard exercise in optics to calculate the Fresnel amplitudes of light reflected or transmitted from a plane and uniform interface between two bulk media. This is

done by expressing the EM-fields as a superposition of the incoming and the reflected fields on one side of the boundary and the transmitted field on the opposite side of the boundary. These expressions are then used to satisfy the BCs of the fields on the surface.

The relevant geometries considered in this thesis are not sharp interfaces, but following a similar way of thinking a set of *modified Fresnel coefficients* can be obtained. How this can be done is detailed in Ref. [5]. When doing this, one starts from the modified BCs in Eq. (2.20d) and the constitutive relations in Eq. (2.21).

By inserting the plane wave solutions, defined in Eq. (1.11), for the bulk extrapolated fields into Eq. (2.23), assuming non-magnetic media such that $n_i = \sqrt{\varepsilon_i(\omega)}$, where $i = a, s$ are the refractive indices of the ambient and substrate, respectively, and defining the surface polarization in accordance with Eq. (2.20), one can derive the following complex reflection and transmission amplitudes for s- and p-polarized light of angular frequency[6] ω:

$$r_s = \frac{n_a \cos\theta_i - n_s \cos\theta_t + i\frac{\omega}{c}\gamma}{n_a \cos\theta_i + n_s \cos\theta_t - i\frac{\omega}{c}\gamma} \tag{2.27a}$$

$$t_s = \frac{2n_a \cos\theta_i}{n_a \cos\theta_i + n_s \cos\theta_t - i\frac{\omega}{c}\gamma} \tag{2.27b}$$

$$r_p = \frac{\kappa_- - i\frac{\omega}{c}\left[\gamma \cos\theta_i \cos\theta_t - \beta\varepsilon_s n_a n_s \sin^2\theta_i\right]}{\kappa_+ - i\frac{\omega}{c}\left[\gamma \cos\theta_t \cos\theta_i + n_a n_s \varepsilon_s \beta \sin^2\theta_i\right]} \tag{2.27c}$$

$$t_p = \frac{2n_a \cos\theta_i \left[1 + \frac{\omega^2}{4c^2}\varepsilon_a \gamma\beta \sin^2\theta_i\right]}{\kappa_+ - i\frac{\omega}{c}\left[\gamma \cos\theta_i \cos\theta_t + n_s n_a \varepsilon_a \beta \sin^2\theta_t\right]}, \tag{2.27d}$$

with

$$\kappa_\pm = \left[n_s \cos\theta_i \pm n_a \cos\theta_t\right]\left[1 - \frac{\omega^2}{4c^2}\varepsilon_a \gamma\beta \sin^2\theta_i\right]. \tag{2.27e}$$

Here θ_i and θ_t denote the polar angle of incidence/reflection and transmitted, respectively, and $c = \sqrt{\varepsilon_0\mu_0}$ is the speed of light in vacuum. In the limit when γ and β are set equal to zero in Eq. (2.27), the familiar Fresnel amplitudes, Eq. (1.13), are obtained.

Notice that the reflection and transmission amplitudes for s-polarized light in Eq. (2.27) only depend on the surface susceptibility parallel to the surface. This is so since the electric field for this polarization only has a component parallel to the surface. On the other hand, for p-polarized light the Fresnel reflection and transmission amplitudes both dependent on the parallel and perpendicular surface susceptibility. In this case the electric field has both parallel and perpendicular components.

In passing it should be remarked that similar, but more complicated, relations to those given in Eq. (2.27) can be derived that will include also the second order surface susceptibilities *i.e.* including δ and τ. We will not do so here, but the interested reader is directed to Ref. [40] for details. These second order terms are crucial for a

[6] In the following, the explicit dependence of the frequency for all the amplitudes, r_s, r_p, t_s, t_p, the refractive index, n_i, and the first order surface susceptibilities, γ and β, are considered to be implicit.

proper understanding of the optical properties of systems consisting of, for instance, non-absorbing (dielectric) particles in the excess region or rough surfaces.

2.6.1 The role of the position of the dividing surface on reflectivity and transmissivity

The somewhat arbitrary choice of the vertical position of the dividing surface, here we defined $z = 0$, should not have any physical significance for measurable quantities. One should notice that the modified Fresnel amplitudes defined in Eq. (2.27) depend on the vertical position of the dividing surface because the surface susceptibilities dependent on this choice. However, one can define a new set of *invariant* quantities, *i.e.* a combination of surface susceptibilities γ, β, δ, and τ that do not depend on the location of the dividing surface. For instance, this was done in Ref. [37, Chapter 3.8]. It can be shown that Eq. (2.27) can be expressed in terms of these invariants multiplied by a noninvariant complex phase factor. This phase factor, is of no physical importance for a given polarization $\nu = \{s, p\}$ because it disappears in the calculation of the Fresnel (intensity) coefficients defined as

$$R_\nu = \left|\frac{r_\nu}{r_i}\right|^2 \tag{2.28a}$$

$$T_\nu = \left|\frac{t_\nu}{r_i}\right|^2 \frac{n_s \cos\theta_t}{n_a \cos\theta_i}, \tag{2.28b}$$

where n_a and n_s again denoted the refraction index for the bulk materials, θ_i and θ_t denotes the angle for the incoming and transmitted field, and the term r_i is the amplitude if the incident field, and finally R_ν and T_ν are the reflectivity and transmisivty coefficients[7].

2.6.2 Differential reflectivity

The GranFilm software is designed to perform fast calculations of the optical response of systems containing a boundary layer of metallic particles obtained, *e.g.* during the deposition process in a SDRS experiment. In this context, it is especially useful to define the *differential reflectivity* for a given polarization, $\nu = s$ or p. This quantity is defined as

$$\frac{\Delta R_\nu}{R_\nu} = \frac{|r_\nu|^2 - |r_{\nu,0}|^2}{|r_{\nu,0}|^2}, \tag{2.29}$$

where r_ν is the reflection amplitude of the substrate *with* metal particles, and $r_{\nu,0}$ denotes the Fresnel reflection amplitude of the 'bare' substrate, before the deposit starts.

In the long wavelength approximation, (*i.e.* when $2\pi/\lambda\gamma \ll 1$ and $2\pi/\lambda\beta \ll 1$), it can be shown that the differential reflectivity signal is directly proportional to the

[7] For homogeneous and semi-infinite materials separated by a planar surface, as in this work, the reflectance/transmittance and the reflectivity/transmissivity are the same. For systems where both *specular* and *diffuse* reflection of the incident light beam take place, as is the case in the scattering from a random surface, one has to distinguish these quantities.

imaginary parts of the surface susceptibilities, and therefore the absorption in the layer [20, 41, 42]. With the excess field formalism the formulas for the differential reflectivity on a non-absorbing dielectric substrate ε_s are

$$\frac{\Delta R_s}{R_s} = 4\frac{\omega}{c}\frac{n_a \cos\theta_i}{\varepsilon_s - \varepsilon_a}\mathrm{Im}\{\gamma\} \tag{2.30a}$$

$$\frac{\Delta R_p}{R_p} = 4\frac{\omega}{c}\frac{n_a \cos\theta_i}{(\varepsilon_s - \varepsilon_a)(\varepsilon_a \sin^2\theta_i - \varepsilon_s \cos^2\theta_i)}\left[(\varepsilon_s - \varepsilon_a \sin^2\theta_i)\mathrm{Im}\{\gamma\} - \varepsilon_a \varepsilon_s^2 \sin^2\theta_i \mathrm{Im}\{\beta\}\right]. \tag{2.30b}$$

The same type of formulas have been derived by Bagchi *et al.* for the reflectivity of a surface with a non-local surface dielectric tensor [43].

2.7 Conclusion

This chapter has explained how the BV-formalism may be used to describe the EM properties of non-sharp interfaces. A detailed description of the formalism is given in the book *Optical properties of surfaces* [5] by Bedeaux and Vlieger. The definitions of the so called *excess quantities* and the *surface susceptibilities* were the key concepts of the formalism.

Chapter 3

The polarizabilities of supported islands

In Ch. 2 the BV-formalism was introduced to describe the EM properties of so-called boundary layers. We saw that the *surface susceptibilities* of a generic boundary layer fully determines the optical properties of the considered system. This chapter details the procedure to calculate the polarizabilities defined in Eq. (2.25) for a truncated spherical particle in the *quasi-static approximation*. The polarization of an isolated island is expressed by a multipolar expansion of the electrostatic potential with the introduction of image multipoles in the substrate. Then we will outline how the single particle polarizability is corrected for the interactions with its neighbors.

Contents

3.1 The linear response of an island

Considering a single island surrounded by an ambient material the island's response generated by an incoming EM-field may be characterized by the dipole, quadrupolar, and higher-order multipolar polarizabilities [6]. The general linear response of an island of arbitrary shape to an incident electric field may be written in the form [37, Eq. (5.2), Ch. 5.2]

$$P_i(\mathbf{r},t) = \int \mathrm{d}\mathbf{r}'\mathrm{d}t'\alpha_{ij}(\mathbf{r},t|\mathbf{r}',t')E_j(\mathbf{r}',t'), \tag{3.1}$$

where $P_i(\mathbf{r},t)$ is a component of the polarization vector of the island, $\alpha_{ij}(\mathbf{r},t|\mathbf{r}',t')$ a component of the island's polarizability tensor at coordinates $\mathbf{r}$,t induced by a component of the incoming electric field at coordinates $\mathbf{r}'$,t', $E_j(\mathbf{r}',t')$. The Einstein summation convention has been assumed [44]. Thus, the repeated indices in Eq. (3.1) should be summed over.

As the incoming field is real, the polarization is real, and by source observer symmetry

$$\overleftrightarrow{\boldsymbol{\alpha}}(\mathbf{r},t|\mathbf{r}',t') = \left[\overleftrightarrow{\boldsymbol{\alpha}}(\mathbf{r},t|\mathbf{r}',t')\right]^* \tag{3.2a}$$

$$\alpha_{ij}(\mathbf{r},t|\mathbf{r}',t') = \alpha_{ji}(\mathbf{r}',t'|\mathbf{r},t), \tag{3.2b}$$

where $*$ denotes the complex conjugate. The systems treated in the following are always stationary, $\overleftrightarrow{\boldsymbol{\alpha}}(\mathbf{r},t|\mathbf{r}',t') = \overleftrightarrow{\boldsymbol{\alpha}}(\mathbf{r},t-t'|\mathbf{r}',0) \equiv \overleftrightarrow{\boldsymbol{\alpha}}(\mathbf{r},t|\mathbf{r}')$, so the FT of the time dependence can be defined as

$$\overleftrightarrow{\boldsymbol{\alpha}}(\mathbf{r},\omega|\mathbf{r}') = \int_{-\infty}^{\infty} \mathrm{d}t\overleftrightarrow{\boldsymbol{\alpha}}(\mathbf{r},t|\mathbf{r}')\mathrm{e}^{i\omega t}. \tag{3.3}$$

With similar definitions for the FT of the electric field and polarization density we can recast Eq. (3.1) to

$$P_i(\mathbf{r},\omega) = \int \mathrm{d}\mathbf{r}'\alpha_{ij}(\mathbf{r},\omega|\mathbf{r}')E_j(\mathbf{r}',\omega). \tag{3.4}$$

Moreover, the polarizability of an island equals zero outside the island. Thus,

$$\overleftrightarrow{\boldsymbol{\alpha}}(\mathbf{r},\omega|\mathbf{r}') = 0 \text{ if } \{\mathbf{r},\mathbf{r}'\} \notin V, \tag{3.5}$$

where V is the volume occupied by the island. If the field, due to the polarization of the particle, is calculated far away from the island it is convenient to give the polarizability tensor as a multipole expansion. The series expansion of the i,j-component of the polarizability tensor up to quadrupolar order reads

$$\begin{aligned}\alpha_{ij}(\mathbf{r},\omega|\mathbf{r}') \approx{}& \alpha^{00}_{ij}(\omega)\delta(\mathbf{r})\delta(\mathbf{r}') - \alpha^{10}_{kij}(\omega)\frac{\partial}{\partial r_k}\delta(\mathbf{r})\delta(\mathbf{r}') \\ &- \alpha^{01}_{ijk}(\omega)\delta(\mathbf{r})\frac{\partial}{\partial r'_k}\delta(\mathbf{r}') + \alpha^{11}_{\ell ijk}(\omega)\frac{\partial}{\partial r_\ell}\delta(\mathbf{r})\frac{\partial}{\partial r'_k}\delta(\mathbf{r}'),\end{aligned} \tag{3.6}$$

where $\delta(\mathbf{r})$ denotes the 3D delta-function and the different components of the polarizability tensor are

$$\alpha^{00}_{ij}(\omega) = \int \mathrm{d}\mathbf{r} \int \mathrm{d}\mathbf{r}' \alpha_{ij}(\mathbf{r}, \omega|\mathbf{r}') \tag{3.7a}$$

$$\alpha^{10}_{kij}(\omega) = -\int \mathrm{d}\mathbf{r} \int \mathrm{d}\mathbf{r}' r_k \alpha_{ij}(\mathbf{r}, \omega|\mathbf{r}') \tag{3.7b}$$

$$\alpha^{01}_{ijk}(\omega) = -\int \mathrm{d}\mathbf{r} \int \mathrm{d}\mathbf{r}' \alpha_{ij}(\mathbf{r}, \omega|\mathbf{r}') r'_k \tag{3.7c}$$

$$\alpha^{11}_{\ell ijk}(\omega) = \int \mathrm{d}\mathbf{r} \int \mathrm{d}\mathbf{r}' r_\ell \alpha_{ij}(\mathbf{r}, \omega|\mathbf{r}') r'_k \tag{3.7d}$$

By combining Eq. (3.6) and the polarization vector written as in Eq. (3.4) an expansion of the polarization up quadrupolar order yields

$$\begin{aligned}
P_i(\mathbf{r}, \omega) &= \int \mathrm{d}\mathbf{r}' \alpha_{ij}(\mathbf{r}, \omega|\mathbf{r}') E_j(\mathbf{r}', \omega) \\
&\approx \int \mathrm{d}\mathbf{r}' \Big[\alpha^{00}_{ij}(\omega)\delta(\mathbf{r})\delta(\mathbf{r}') - \alpha^{10}_{kij}(\omega)\frac{\partial}{\partial r_k}\delta(\mathbf{r})\delta(\mathbf{r}') \\
&\qquad + \alpha^{01}_{ijk}(\omega)\delta(\mathbf{r})\frac{\partial}{\partial r'_k}\delta(\mathbf{r}') - \alpha^{11}_{\ell ijk}(\omega)\frac{\partial}{\partial r_\ell}\delta(\mathbf{r})\frac{\partial}{\partial r'_k}\delta(\mathbf{r}') \Big] E_j(\mathbf{r}', \omega) \\
&\overset{①}{=} \alpha^{00}_{ij}(\mathbf{r}, \omega|\mathbf{r}')\delta(\mathbf{r}) E_i(\mathbf{r}', \omega)\,\Big|_{\mathbf{r}'=\mathbf{0}} - \alpha^{01}_{ij}(\mathbf{r}, \omega|\mathbf{r}') r'_k \delta(\mathbf{r}) \left[\frac{\partial}{\partial r'_k} E_i(\mathbf{r}', \omega)\right]_{\mathbf{r}'=\mathbf{0}} \\
&\qquad + r_k \alpha^{10}_{ij}(\mathbf{r}, \omega|\mathbf{r}')\frac{\partial}{\partial r_k}\delta(\mathbf{r}) E_j(\mathbf{r}', \omega)\,|_{\mathbf{r}'=\mathbf{0}} \\
&\qquad - r_\ell \alpha^{11}_{ij}(\mathbf{r}, \omega|\mathbf{r}') r'_k \frac{\partial}{\partial r_\ell}\delta(\mathbf{r}) \left[\frac{\partial}{\partial r'_k} E_i(\mathbf{r}', \omega)\right]_{\mathbf{r}'=\mathbf{0}},
\end{aligned} \tag{3.8}$$

① By definition of the delta function $\left[\frac{\mathrm{d}}{\mathrm{d}x}\delta(x-a)\right] f(x) = -\delta(x-a)f'(x)$.

where $\mathbf{0} = (0, 0, 0)$ is the null-vector. Letting D_i and Q_{ij} denote, respectively the dipole and quadrupole moments of the polarization, we define

$$\begin{aligned}
D_i(\omega) &= \int \mathrm{d}\mathbf{r} P_i(\mathbf{r}, \omega) \\
&= \alpha^{00}_{ij}(\omega) E_j(\mathbf{r}', \omega)\,\Big|_{\mathbf{r}'=\mathbf{0}} + \alpha^{01}_{ijk}(\omega)\left[\frac{\partial}{\partial r'_k} E_j(\mathbf{r}', \omega)\right]_{\mathbf{r}'=\mathbf{0}}
\end{aligned} \tag{3.9a}$$

$$\begin{aligned}
Q_{ij}(\omega) &= \int \mathrm{d}\mathbf{r} r_i P_j(\mathbf{r}, \omega) \\
&= \alpha^{10}_{ijk}(\omega) E_k(\mathbf{r}', \omega)\,|_{\mathbf{r}'=\mathbf{0}} + \alpha^{11}_{ijk\ell}(\omega)\left[\frac{\partial}{\partial r'_\ell} E_k(\mathbf{r}', \omega)\right]_{\mathbf{r}'=\mathbf{0}}.
\end{aligned} \tag{3.9b}$$

Thus, the problem at hand is to identify the terms in the dipole and quadrupolar moments of the island's polarizability. Bringing a particle towards a dielectric substrate

will modify the moments of the polarization tensor in Eq. (3.9) due to the charge distribution induced in the substrate [45]. As this is the relevant geometry for a film containing supported NPs we will now detail how such a calculation can be done for the first order terms in the polarizability tensor, in the case of a rotationally symmetric field around an axis perpendicular to the substrate and a known form of the incoming field, can be done. Such a derivation will be performed within the *quasi-static approximation*.

3.2 Laplace's equation and the relevant boundary conditions

The BV-formalism described in Ch. 2 was based on the assumption that the characteristic distances in the excess region are much smaller than the wavelength of the incoming field. If the size of the considered islands are small compared to the wavelength of the incoming field, we can safely neglect retardation effects inside and around the island and work in the so-called quasi-static approximation. For non-magnetic materials, the relevant ME are

$$\boldsymbol{\nabla} \cdot \mathbf{D}(\mathbf{r}, \omega) = 0 \tag{3.10a}$$

$$\boldsymbol{\nabla} \times \mathbf{E}(\mathbf{r}, \omega) = 0. \tag{3.10b}$$

Furthermore, in the quasi-static approximation, the electric field can be defined only with the electrostatic scalar potential $\psi(\mathbf{r}|\omega)$

$$\mathbf{E}(\mathbf{r}, \omega) = -\boldsymbol{\nabla}\psi(\mathbf{r}|\omega)\,. \tag{3.11}$$

Combining Eq. (3.10a) and the fact that materials are defined by a local dielectric function $\mathbf{E}(\mathbf{r}) = \mathbf{D}(\mathbf{r})/\varepsilon(\omega)$, where $\varepsilon(\omega)$ is the dielectric function[2] of the considered region, the well-known Laplace's equation is obtained

$$\nabla^2\psi(\mathbf{r}|\omega) = 0, \tag{3.12}$$

where ∇^2 is the Laplace operator. Equation (3.12) has an infinite set of solutions that can be restricted by the appropriate BCs. At the boundary between two surfaces, a text-book analysis of ME shows that the continuity of the potential itself and the normal components of the displacement field should be continuous [6, 46]

$$\psi_i(\mathbf{r}|\omega)\,|_{\mathbf{r}=\mathbf{r}_s} = \psi_j(\mathbf{r}|\omega)\,|_{\mathbf{r}=\mathbf{r}_s} \tag{3.13a}$$

$$\varepsilon_i(\omega)\partial_n\psi_i(\mathbf{r}|\omega)\,|_{\mathbf{r}=\mathbf{r}_s} = \varepsilon_j(\omega)\partial_n\psi_j(\mathbf{r}|\omega)\,|_{\mathbf{r}=\mathbf{r}_s}, \tag{3.13b}$$

where i and j denote different media, the term $\mathbf{r}_s$ is any point on the surface, and the term $\partial_n = \hat{\mathbf{n}} \cdot \boldsymbol{\nabla}$ denotes the normal derivative of the potential on the surface evaluated in the point $\mathbf{r}_s$. Furthermore, the potential must be finite everywhere *i.e.*

$$|\psi(\mathbf{r}|\omega)| < \infty, \quad \forall \mathbf{r}. \tag{3.14}$$

When constructing a meaningful solution to Eq. (3.12), one should pay special attention to the value of the electrostatic potential at the origin, $\lim_{\mathbf{r}\to 0}$, and infinity, $\lim_{\mathbf{r}\to\infty}$.

[2] See Ch. 1, Sec. 1.2 for a reminder of the properties of the dielectric function of a material.

A general solution of Laplace's equation

In this work we study truncated NPs of spherical shape. In spherical coordinates, Eq. (3.12) takes the form

$$\nabla^2\psi(\mathbf{r}|\omega) = \frac{1}{r^2}\frac{\partial}{\partial r}\left(r^2\frac{\partial\psi(\mathbf{r}|\omega)}{\partial r}\right) + \frac{1}{r^2\sin\theta}\left[\frac{\partial}{\partial\theta}\left(\sin\theta\frac{\partial\psi(\mathbf{r}|\omega)}{\partial\theta}\right) + \frac{1}{\sin\theta}\left(\frac{\partial^2\psi(\mathbf{r}|\omega)}{\partial^2\phi}\right)\right] = 0, \tag{3.15}$$

where the spherical polar coordinates are defined by; $r \in [0,\infty)$ the radial distance from the origin, $\theta \in [0,\pi]$ the polar angle from the z-axis, and $\phi \in [0,2\pi)$ the azimuthal angle around from the x-axis. A general solution of Eq. (3.15) is found with the technique of separation of variables and is given by the classical multipole expansion in terms of the *spherical harmonics* (SH) [47]

$$\psi(\mathbf{r}|\omega) = \sum_{\ell=0}^{\infty}\sum_{m=-\ell}^{\ell}\left(A_{\ell m}(\omega)r^{-(\ell+1)} + B_{\ell m}(\omega)r^{\ell}\right)Y_\ell^m(\theta,\phi), \tag{3.16}$$

where the unknown multipole coefficients are denoted $A_{\ell m}(\omega)$ and $B_{\ell m}(\omega)$. Following the definition of Refs. 5, 37, the SH $Y_\ell^m(\theta,\phi)$ are found by the following relation

$$Y_\ell^m(\theta,\phi) = \sqrt{\frac{(2\ell+1)(\ell-m)!}{(4\pi)(\ell+m)!}}P_\ell^m(\cos\theta)(-1)^m e^{im\phi}, \tag{3.17}$$

where the Condon-Shortly phase factor is assumed. The associated Legendre Polynomials are defined as

$$P_\ell^m(x) = \begin{cases} \frac{1}{2^\ell\ell!}(1-x^2)^{m/2}\left(\frac{d}{dx}\right)^{\ell+m}(x^2-1)^\ell & \text{for } 0 \le m \\ (-1)^m\frac{(\ell+m)!}{(\ell-m)!}P_\ell^{-m}(x) & \text{for } m < 0, \end{cases} \tag{3.18}$$

with $x = \cos\theta$. If follows from Eq. (3.18) that $Y_\ell^{-m}(\theta,\phi) = (-1)^m\left[Y_\ell^m(\theta,\phi)\right]^*$, where the superscript $*$ again denotes the complex conjugate. The orthogonality relations of the SH over all angles yields

$$\int_{-1}^{1}\mathrm{d}(\cos\theta)\int_0^{2\pi}\mathrm{d}\phi Y_\ell^m(\theta,\phi)\left[Y_{\ell'}^{m'}(\theta,\phi)\right]^* = \delta_{\ell\ell'}\delta_{mm'}, \tag{3.19}$$

which means that the SH form a complete set of functions. As a reminder, a shortlist of the first few SH is given in Table 3.1.

The relation between the multipole coefficients and the polarizability

An electrostatic potential in the form given in Eq. (3.16) must be finite valued for all values of r. Hence, the first term containing $r^{-(\ell+1)}$ gives the field due to sources inside a region of interest R_s ($r < R_s$), and the second term r^ℓ, gives the field due to sources outside the region of interest ($r > R_s$). The position of the expansion point (the origin) should be chosen somewhere close to the island. An obvious choice for the origin is the center of the island. Consequnetly, the region of interest R_s will be defined as the radius of the smallest sphere which contains the island (see the next sections).

Table 3.1 The first few SHs.

SH	Mathematical Expression
$Y_0^0(\theta,\phi)$	$\frac{1}{2\sqrt{\pi}}$
$Y_1^{-1}(\theta,\phi)$	$\frac{1}{2}\sqrt{\frac{3}{2\pi}}\sin\theta e^{-i\phi}$
$Y_1^0(\theta,\phi)$	$\frac{1}{2}\sqrt{\frac{3}{\pi}}\cos\theta$
$Y_1^1(\theta,\phi)$	$-\frac{1}{2}\sqrt{\frac{3}{2\pi}}\sin\theta e^{i\phi}$

Since the amplitudes of the multipole fields in Eq. (3.16) are given in terms of the incident field, we can express the multipole coefficients with a polarizability matrix

$$A_{\ell m}(\omega) = -\sum_{\ell' m'} \alpha_{\ell m,\ell' m'}(\omega) B_{\ell' m'}(\omega), \quad \ell \neq 0 \tag{3.20}$$

where $\ell' = 1, ..., \infty$, and $m' = -\ell', ..., \ell'$. The A_{1m} coefficient is zero because the island has no net charge. The B_{1m} coefficient is given from the incident field which is regarded as constant, and B_{0m} may, therefore, be chosen arbitrarily.

If we choose the island to be symmetric around the z-axis, all matrix elements with different m-elements are zero and Eq. (3.20) reduces to

$$A_{\ell m}(\omega) = -\sum_{\ell' m'}{}' \delta_{mm'} \alpha_{\ell m,\ell' m'}(\omega) B_{\ell' m'}(\omega). \tag{3.21}$$

To conclude, once the expression for the electrostatic potential is known for a given incident field, one can determine the polarizabilities of the supported islands, and thus the surface susceptibilities from the expansion coefficients of the potential.

In the following, we derive the polarizabilities up to the second order for the geometry of a truncated and supported sphere.

3.3 The polarizability of supported truncated spherical particles

Figure 3.1(a) displays a sketch of a truncated spherical particle placed on a substrate. Figure 3.1(b) presents a sketch of relevant quantities needed to describe the particle geometry. Here R denotes the radius of the particle. The z-coordinate of the position of the surface of the substrate is denoted d.

The degree of truncation of the particles is defined by the *truncation ratio* $t_r = d/R$ ($-1 < t_r \leq 1$). The value $t_r = 1$ corresponds to a full sphere touching the substrate at one point, while $t_r = 0$ corresponds to a hemisphere lying on the surface. For the configuration $t_r < 0$ the particle will be a spherical cap. The center of the sphere is then located below the surface of the substrate. The dielectric functions of the ambient material, the substrate and the particle are respectively denoted ε_a, ε_s, and ε_p. A natural choice for the origin of the multipolar expansion in Eq. (3.16) is somewhere inside the particle.

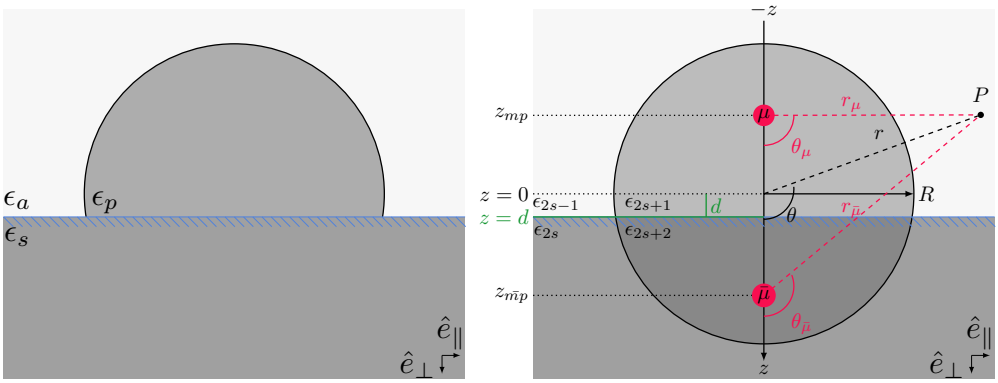

(a) Sketch of a truncated particle placed on a substrate.

(b) Coordinate system for the center of the sphere $\mathcal{S}$, the direct multipole $\mathcal{S}_\mu$ and the image multipole $\mathcal{S}_{\bar{\mu}}$.

Figure 3.1 A sketch of a truncated particle placed on a substrate (a) with relevant coordinate systems used in the calculations (b).

In the original derivation by Wind *et al.* [48,49], the expansion point was placed in the center of the spherical particle. The cases where the center of the sphere lies above or below the substrate must then be treated differently. In the original work, only symmetry arguments were used to obtain the $t_r < 0$ case from the solutions for the $t_r > 0$. The actual expressions for the potentials in the case of $t_r < 0$ was given later in Ref. 37.

Simonsen and co-workers moved the position of the multipoles away from the center of the sphere along the axis normal to the substrate surface, but always keeping the expansion point above the surface [46]. This method provides the same expression for the potentials in the cases for $t_r > 0$ and $t_r < 0$ and improves the convergence of the numerical implementation.

In the following, we will comply with the formalism made in Ref. 46. The multipole expansion point will lie somewhere on the z-axis, but always inside the particle and above the substrate surface.

3.3.1 The island geometry

Figure 3.1(b) also presents a sketch of the relevant coordinate systems needed to evaluate the potential in Eq. (3.16) in a point P for a system containing a truncated and supported particle.

The main spherical coordinate system $\mathcal{S}$ has it's origin placed in the center of the sphere. It's position vector $\mathbf{r} = (x, y, z)$ is defined so the positive z-axis is downwards, as we did in Ch. 2. The direct and image multipole expansion points are placed in the positions $\mathbf{r}_{mp} = z_{mp}\hat{\mathbf{z}}$ and $\mathbf{r}_{\overline{mp}} = z_{\overline{mp}}\hat{\mathbf{z}}$, marked with red filled circles in Fig. 3.1(b). The image point is placed so the distance from the plane $z = d$ are equal to the distance of the direct multipole, *i.e* $z_{\overline{mp}} = 2d - z_{mp}$. If the direct multipole is placed in the center of the sphere, as originally done by Wind *et al.* [48, 49], its position is

$\mathbf{r}_{mp} = 0$. The position vector of the image multipole would then be $\mathbf{r}_{\overline{mp}} = 2d\hat{\mathbf{z}}$.

The distance to a multipole expansion point

For later convenience, we introduce the dimensionless quantities $\mu = z_{mp}/R$ and $\bar{\mu} = z_{\overline{mp}}/R$ used to denote the direct or image multipole, respectively. To evaluate the potentials in Eq. (3.16) in a point P we define two new coordinate systems $\mathcal{S}_\mu$ and $\mathcal{S}_{\bar{\mu}}$. Their origins are placed in the positions of the direct and image multipole expansion points, respectively. The position vectors in the two coordinate systems are

$$\mathbf{r}_\mu(\mathbf{r}) = \mathbf{r} - z_{mp}\hat{\mathbf{z}} \tag{3.22a}$$

$$\mathbf{r}_{\bar{\mu}}(\mathbf{r}) = \mathbf{r} - z_{\overline{mp}}\hat{\mathbf{z}}. \tag{3.22b}$$

In spherical coordinates the position vectors in the different coordinate systems $\mathcal{S}$, $\mathcal{S}_\mu$, and $\mathcal{S}_{\bar{\mu}}$ are respectively given as $\mathbf{r} = (r, \theta, \phi)$, $\mathbf{r}_\mu = (r_\mu, \theta_\mu, \phi_\mu)$, and $\mathbf{r}_{\bar{\mu}} = (r_{\bar{\mu}}, \theta_{\bar{\mu}}, \phi_{\bar{\mu}})$. Because of the common direction of the z-axis $\phi = \phi_\mu = \phi_{\bar{\mu}}$.

Relating the coordinate systems to each other

Using the transformation relation between the two coordinate systems in Eq. (3.22) $\mathcal{S}_\mu$ and $\mathcal{S}$ are linked by

$$r_\mu(\mathbf{r}) = \left[r^2 + z_{mp}^2 - 2rz_{mp}\cos\theta\right]^{1/2} \tag{3.23a}$$

$$\cos\theta_\mu(\mathbf{r}) = \hat{\mathbf{r}}_\mu \cdot \hat{\mathbf{z}} = \frac{r\cos\theta - z_{mp}}{\left[r^2 + z_{mp}^2 - 2rz_{mp}\cos\theta\right]^{1/2}} \tag{3.23b}$$

$$\phi_\mu = \phi, \tag{3.23c}$$

where the law of cosines[3] and the relation $\hat{\mathbf{r}} \cdot \hat{\mathbf{z}} = \cos\theta$ have been used. For later use, also the derivatives of Eqs. (3.23a)-(3.23b) are given

$$\partial_r r_\mu(\mathbf{r}) = \frac{r - z_{mp}\cos\theta}{\left[r^2 + z_{mp}^2 - 2rz_{mp}\cos\theta\right]^{1/2}} \tag{3.24a}$$

$$\partial_r\left[\cos\theta_\mu(\mathbf{r})\right] = \frac{\cos\theta}{\left[r^2 + z_{mp}^2 - 2rz_{mp}\cos\theta\right]^{1/2}} - \frac{(r - z_{mp}\cos\theta)(r - z_{mp}\cos\theta)}{\left[r^2 + z_{mp}^2 - 2rz_{mp}\cos\theta\right]^{3/2}}. \tag{3.24b}$$

Corresponding relations between the coordinates of the systems $\mathcal{S}_{\bar{\mu}}$ and $\mathcal{S}$ are found by replacing z_{mp} and μ in Eqs. (3.23)-(3.24) with $z_{\overline{mp}}$ and $\bar{\mu}$.

The numbering convention of surfaces and regions

Core-shell particles are of interest in nanoscience due to the new optical properties arising from the interaction of the elementary plasmons supported by the individual

[3]The law of cosines yields: $c^2 = a^2 + b^2 - 2ab\cos\theta$.

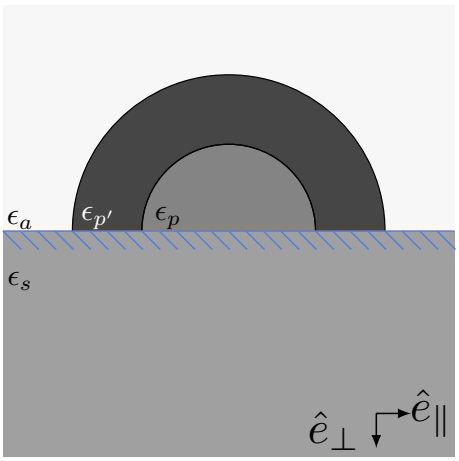

(a) Sketch of a coated truncated spherical particle placed on a substrate.

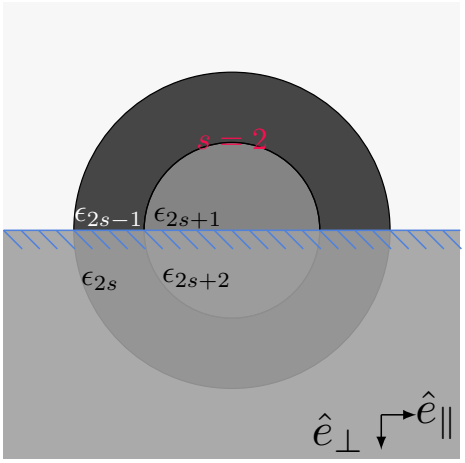

(b) Numbering convention for the surface $s = 2$ in a coated truncated spherical particle.

Figure 3.2 A sketch of a coated truncated spherical particle placed on a substrate (a) with the chosen numbering convention to name the regions around the surface $s = 2$ (b).

geometries of the spheres and cavities [21]. Thereby, we extend our formalism to include geometries of coated and supported NPs. To tackle this kind of systems one has to keep track of the number of surfaces and regions of different materials in the particle.

To fully describe the geometry of a system with coated particles, we would need to introduce the *radius ratio*, and truncation ratio for each surface s. These quantities are defined as $\chi^{(s)} = R^{(s)}/R^{(1)}$ and $t_r^{(s)} = t_r^{(1)}/\chi^{(s)}$, respectively. For the outer surface of the particle, $s = 1$, we have $R^{(1)} \equiv R$ and $t_r^{(1)} \equiv t_r$. Since the radii of potential inner surfaces must be smaller than the radius of the outer surface, we must have $R^{(s)} < R^{(1)}$, $s = 2, 3, ..., S$, $S \geq 2$.

A special case of coated particle geometry is found in the case where one or several of the inner layers, $s > 1$, are non-truncated and 'floating' either above or below the substrate. Thus, for this special case $t_r^{(s)} > 1$ for a particle above the surface and $t_r^{(s)} < 1$ for a particle embedded in the substrate. The total number of regions in the system N, must satisfy $N \leq 2S + 2$, dependent on the value of the truncation ratios for the possible inner surfaces. If $N = 2S + 2$ all the surfaces in the particle are truncated. If $N < 2S + 2$ some of the inner surfaces s will be non-truncated.

Only one spherical surface $s = 1$ is shown in Fig. 3.1(b), but the numbering convention of the surrounding regions is chosen such that the generalization to a system where the total number of surfaces $S > 1$ will be straightforward. Figure 3.2(a) displays a sketch of the system of interest containing a coated truncated spherical particle. An example of how our numbering convention will number the regions around the surface $s = 2$ is given in Fig. 3.2(b).

For the case of a uncoated particle where the total number of surfaces $S = s = 1$, the chosen naming convention results in the following regions: the region with the ambient material dielectric function is labeled $\varepsilon_a = \varepsilon_1 = \varepsilon_{2s-1}$. The region outside the particle in the substrate is labeled $\varepsilon_s = \varepsilon_2 = \varepsilon_{2s}$. The regions of different materials inside the particle above the substrate are labeled $\varepsilon_3 = \varepsilon_{2s+1}$ and below the substrate $\varepsilon_4 = \varepsilon_{2s+2}$.

For a general geometry, any material with an odd index will be placed above the substrate, and any material with an even index will be placed below the substrate. Furthermore, one can notice the two regions below the substrate inside and outside the particle are given different labels. This is done for mathematical convenience only. In the end all dielectric functions in the regions with an even numbered index are set equal to ε_2.

To conclude, a convention consistent with the case of a particle with coating(s) is used to name the different regions for the geometry considered in Fig. 3.1(b) and Fig. 3.2(b).

3.3.2 The electrostatic potential in different regions around and inside the particle

The challenge is now to express the electrostatic potential in the regions inside and outside the islands. From the previous sections, we saw that there are two main types of regions. Those located above and below the substrate. For a region above the substrate, *i.e.* $i = \{1, 3, ..., 2S + 1\}$, the general expression for the potential yields

$$\psi_i(\mathbf{r}|\omega) = \psi_{inc}^{(i)}(\mathbf{r}|\omega)\,\delta_{1,i} + \psi_0^{(i)}(\omega) + \sum_{\ell=1}^{\infty}\sum_{m=-\ell}^{\ell}\left[A_{\ell m}^{(i)}(\omega) r_\mu^{-\ell-1} + B_{\ell m}^{(i)}(\omega) r_\mu^{\ell}\right] Y_\ell^m(\theta_\mu, \phi_\mu) + \sum_{\ell=1}^{\infty}\sum_{m=-\ell}^{\ell}\left[\bar{A}_{\ell m}^{(i)}(\omega) r_{\bar{\mu}}^{-\ell-1} + \overline{B}_{\ell m}^{(i)}(\omega) r_{\bar{\mu}}^{\ell}\right] Y_\ell^m(\theta_{\bar{\mu}}, \phi_{\bar{\mu}}), \tag{3.25a}$$

where the set $\{A_{\ell m}^{(i)}(\omega), B_{\ell m}^{(i)}(\omega)\}$ contains the unknown multipole coefficients related to the direct multipole expansion point placed at $\mathbf{r}_\mu = (r_\mu, \theta_\mu, \phi_\mu)$. Similarly, the set $\{\bar{A}_{\ell m}^{(i)}(\omega), \overline{B}_{\ell m}^{(i)}(\omega)\}$ is related to the image multipole expansion point placed at $\mathbf{r}_{\bar{\mu}} = (r_{\bar{\mu}}, \theta_{\bar{\mu}}, \phi_{\bar{\mu}})$. The term $\delta_{1,i}$ makes sure that the incoming potential is only present in the region $i = 1$. Furthermore, $\psi_0^{(i)}(\omega)$ are the constant potentials in the considered region.

If a region i is not bounded by the substrate, *i.e.* for a layer of coating where the surface is hovering entirely above the substrate, there are no contributions from the image terms in Eq. (3.25a). Meaning that the coefficients $\bar{A}_{\ell m}^{(i)}(\omega) \equiv 0$ and $\overline{B}_{\ell m}^{(i)}(\omega) \equiv 0$.

For a region below the substrate $i + 1$, the general electrostatic potential is

$$\psi_{i+1}(\mathbf{r}|\omega) = \psi_{tr}^{(i+1)}(\mathbf{r}|\omega)\,\delta_{2,i+1} + \psi_0^{(i+1)}(\omega) + \sum_{\ell=1}^{\infty}\sum_{m=-\ell}^{\ell}\left[A_{\ell m}^{(i+1)}(\omega) r_\mu^{-\ell-1} + B_{\ell m}^{(i+1)}(\omega) r_\mu^{\ell}\right] Y_\ell^m(\theta_\mu, \phi_\mu). \tag{3.25b}$$

Our target is to express the unknown multipole coefficients in Eq. (3.25) so we can identify the polarizabilities with the scaling relation stated in Eq. (3.21). To do so, we will express the incoming field and satisfy the BCs on the surfaces of the substrate and sphere.

The electrostatic potential associated with the incoming field

Considering an incident field given by a plane wave

$$\mathbf{E}_0(\mathbf{r}|\omega) = E_0(\omega)\left[\sin\theta_0\cos\phi_0, \sin\theta_0\sin\phi_0, \cos\theta_0\right], \tag{3.26}$$

where θ_0 is the polar angle of incidence between $\mathbf{E}_0$ and the negative z-axis[4] and ϕ_0 the angle between the projection of $\mathbf{E}_0$ on the substrate and the positive x-axis. As any vector $\mathbf{r}$ expressed in spherical coordinates is

$$\mathbf{r} = \left[r\sin\theta\cos\phi, r\sin\theta\sin\phi, r\cos\theta\right], \tag{3.27}$$

the electrostatic potential at the coordinate $\mathbf{r}$ associated with the incident field (corresponding to the incoming plane wave) reads

$$\begin{aligned}\psi_{inc}(\mathbf{r}|\omega) &= -\mathbf{r}\cdot\mathbf{E}_0(\mathbf{r}|\omega)\\ &= -rE_0(\omega)\sqrt{\frac{2\pi}{3}}\left\{\sqrt{2}\cos\theta_0 Y_1^0(\theta,\phi) - \sin\theta_0\left[\mathrm{e}^{-i\phi_0}Y_1^1(\theta,\phi) - \mathrm{e}^{i\phi_0}Y_1^{-1}(\theta,\phi)\right]\right\},\end{aligned} \tag{3.28a}$$

where the definitions of the SH in Table 3.1 have been used. The incident field is partly transmitted into the substrate. The corresponding transmitted potential is

$$\begin{aligned}\psi_{tr}(\mathbf{r}|\omega) = a_0 - rE_0(\omega)\sqrt{\frac{2\pi}{3}}\Big\{&a_1\sqrt{2}\cos\theta_0 Y_1^0(\theta,\phi)\\ &- \sin\theta_0\left[a_2\mathrm{e}^{-i\phi_0}Y_1^1(\theta,\phi) - a_3\mathrm{e}^{i\phi_0}Y_1^{-1}(\theta,\phi)\right]\Big\},\end{aligned} \tag{3.28b}$$

where a_0, a_1, a_2, and a_3 are constants to be determined by the BCs across the substrate (see Appendix 3.A for a detailed explanation).

The electrostatic potential in different regions of a truncated spherical island

Appendix 3.A demonstrates that with the image formulation and the BCs at the surface of the substrate we can rewrite the potentials in the different regions i on a form only containing the set $\{A_{\ell m}^{(i)}(\omega), B_{\ell m}^{(i)}(\omega)\}$.

For a system with one surface, $s = 1$ [see Fig. 3.1(b)], the potential in the four different

[4] This choice is consistent with the coordinate system defined in Ch. 2.

regions is a special case of the general form in Eq. (3.53) expressed as

$$\psi_1(\mathbf{r}|\omega) = \psi_{inc}(\mathbf{r}|\omega) + \sum_{\ell=1}^{\infty}\sum_{m=-\ell}^{\ell} A_{\ell m}^{(1)}(\omega)\left[r_\mu^{-\ell-1}Y_\ell^m(\theta_\mu,\phi_\mu) + (-1)^{\ell+m}\frac{\varepsilon_1(\omega)-\varepsilon_2(\omega)}{\varepsilon_1(\omega)+\varepsilon_2(\omega)}r_{\bar{\mu}}^{-\ell-1}Y_\ell^m(\theta_{\bar{\mu}},\phi_{\bar{\mu}})\right] \tag{3.29a}$$

$$\psi_2(\mathbf{r}|\omega) = \psi_{tr}(\mathbf{r}|\omega) + \sum_{\ell=1}^{\infty}\sum_{m=-\ell}^{\ell} A_{\ell m}^{(1)}(\omega)\frac{2\varepsilon_1(\omega)}{\varepsilon_1(\omega)+\varepsilon_2(\omega)}r_\mu^{-\ell-1}Y_\ell^m(\theta_\mu,\phi_\mu) \tag{3.29b}$$

$$\psi_3(\mathbf{r}|\omega) = \psi_0^{(3)}(\omega) + \sum_{\ell=1}^{\infty}\sum_{m=-\ell}^{\ell} B_{\ell m}^{(3)}(\omega)\left[r_\mu^{\ell}Y_\ell^m(\theta_\mu,\phi_\mu) + (-1)^{\ell+m}\frac{\varepsilon_3(\omega)-\varepsilon_4(\omega)}{\varepsilon_3(\omega)+\varepsilon_4(\omega)}r_{\bar{\mu}}^{\ell}Y_\ell^m(\theta_{\bar{\mu}},\phi_{\bar{\mu}})\right] \tag{3.29c}$$

$$\psi_4(\mathbf{r}|\omega) = \psi_0^{(3)}(\omega) + \sum_{\ell=1}^{\infty}\sum_{m=-\ell}^{\ell} B_{\ell m}^{(3)}(\omega)\frac{2\varepsilon_3(\omega)}{\varepsilon_3(\omega)+\varepsilon_4(\omega)}r_\mu^{\ell}Y_\ell^m(\theta_\mu,\phi_\mu)\,. \tag{3.29d}$$

To find the set of the remaining unknown coefficients[5] $\{A_{\ell m}^{(1)}(\omega), B_{\ell m}^{(3)}(\omega)\}$, the BCs Eq. (3.13) at the spherical surface will be exploited through a so-called a weak formulation of the BCs.

The weak formulation of the boundary conditions

The BCs at the spherical surface given in Eq. (3.13) requires the continuity of the potential and the normal derivative times the dielectric function *at every point* on the spherical surface. A so-called strong formulation of the BCs. For our purpose, it is more convenient to adopt the so-called *weak formulation* of the BCs.

This formulation is obtained by multiplying the point-wise BCs by the complex conjugated of the SH, $\left[Y_{\ell'}^{m'}(\theta,\phi)\right]^*$, and then integrate over the full solid angle. The weak boundary formulation is necessary, but not sufficient conditions. To verify the quality of the obtained expressions for the multipole coefficients one should always check the continuity of the potential in the end [46].

To find the unknown expansion coefficients in Eq. (3.29) we will take advantage of the orthogonality relations of the SH given in Eq. (3.19) and the BCs evaluated at the spherical surface given in Eq. (3.13). Distinguishing the regions above and below the substrate we obtain

$$\int_{\bigcirc_s} \mathrm{d}\Omega = \int_{\cap_s} \mathrm{d}\Omega + \int_{\cup_s} \mathrm{d}\Omega, \tag{3.30}$$

where the symbol $\bigcirc_s$ denotes the whole spherical surface s, the symbols $\cap_s$ and $\cup_s$ are, respectively, the parts of the spherical surface which is placed above and below the substrate surface, and $\mathrm{d}\Omega = \sin\theta \mathrm{d}\theta\mathrm{d}\phi$ the full solid angle.

[5] The $\psi_0^{(3)}(\omega)$ coefficient is still unknown, but it is only needed to check the BCs and/or map the potential. The expression for this coefficient is given elsewhere [46].

The weak formulation of the BCs for the different regions in Eq. (3.29) on the spherical surface $r = R_s$ are

$$\begin{aligned}&\int_{\cap_s} \mathrm{d}\Omega\, [\psi_{2s-1}(\mathbf{r}|\omega) - \psi_{2s+1}(\mathbf{r}|\omega)]|_{r=R_s} \left[Y_{\ell'}^{m'}(\theta,\phi)\right]^* \\ &+ \\ &\int_{\cup_s} \mathrm{d}\Omega\, [\psi_{2s}(\mathbf{r}|\omega) - \psi_{2s+2}(\mathbf{r}|\omega)]|_{r=R_s} \left[Y_{\ell'}^{m'}(\theta,\phi)\right]^* = 0 \end{aligned} \tag{3.31a}$$

which follows from the continuity of the electrostatic potential Eq. (3.13a), and

$$\begin{aligned}&\int_{\cap_s} \mathrm{d}\Omega\, [\varepsilon_{2s-1}(\omega)\partial_n\psi_{2s-1}(\mathbf{r}|\omega) - \varepsilon_{2s+1}(\omega)\partial_n\psi_{2s+1}(\mathbf{r}|\omega)]|_{r=R_s} \left[Y_{\ell'}^{m'}(\theta,\phi)\right]^* \\ &+ \\ &\int_{\cup_s} \mathrm{d}\Omega\, [\varepsilon_{2s}(\omega)\partial_n\psi_{2s}(\mathbf{r}|\omega) - \varepsilon_{2s+2}(\omega)\partial_n\psi_{2s+2}(\mathbf{r}|\omega)]|_{r=R_s} \left[Y_{\ell'}^{m'}(\theta,\phi)\right]^* = 0. \end{aligned} \tag{3.31b}$$

as a consequence of the continuity of the dielectric function times the normal derivative of the potential Eq. (3.13b).

3.3.3 A linear set of equations

In Appendix 3.B we have given the derivation of the linear system of equations for a truncated and potentially coated sphere. They are obtained after some straightforward algebra by inserting the expressions from Eq. (3.29) into Eq. (3.31).

In the case of the uncoated truncated spherical particle, the number of surfaces in the system is $S = 1$. The relevant unknown expansion coefficients are then $A_{\ell m}^{(1)}(\omega)$ and $B_{\ell m}^{(3)}(\omega)$. They can be obtained from the relations

$$\begin{aligned}&\sum_{\substack{\ell'=|m|\\ \ell'\neq 0}} \zeta_{\ell\ell'}^m R_s^{-\ell'-2} \left[M_{\ell\ell';1}^{m;(1)}[-\ell'-1](t_r)\, A_{\ell' m}^{(1)}\right] + \sum_{\substack{\ell'=|m|\\ \ell'\neq 0}} \zeta_{\ell\ell'}^m R_s^{\ell'-1} \left[-M_{\ell\ell';1}^{m;(3)}[\ell'](t_r)\, B_{\ell' m}^{(3)}\right] \\ &\quad = \delta_{\ell 0}\delta_{m0}\frac{\sqrt{4\pi}}{R_s}\psi_0^{(3)} \\ &\qquad + E_0 \left\{\delta_{m0}\sqrt{\frac{4\pi}{3}}\cos\theta_0 \left[\frac{\varepsilon_2-\varepsilon_1}{\varepsilon_2}\left\{\sqrt{3}t_r\left[\delta_{\ell 0} - \zeta_{\ell 0}^0 I_{\ell 0}^0[0|0](t_r)\right] + \zeta_{\ell 1}^0 I_{\ell 1}^0[0|0](t_r)\right\} + \delta_{\ell 1}\frac{\varepsilon_1}{\varepsilon_2}\right]\right. \\ &\qquad\qquad \left. + \delta_{\ell 1}\sqrt{\frac{2\pi}{3}}\sin\theta_0\left[\delta_{m,-1}\exp(\mathrm{i}\phi_0) - \delta_{m1}\exp(-\mathrm{i}\phi_0)\right]\right\} \end{aligned} \tag{3.32a}$$

and

$$\sum_{\substack{\ell'=|m|\\ \ell'\neq 0}} \zeta^m_{\ell\ell'} R_s^{-\ell'-2} \left[N^{m;\,(1)}_{\ell\ell';\,1}[-\ell'-1](t_r)\, A^{(1)}_{\ell' m}\right] + \sum_{\substack{\ell'=|m|\\ \ell'\neq 0}} \zeta^m_{\ell\ell'} R_s^{\ell'-1} \left[-N^{m;\,(3)}_{\ell\ell';\,1}[\ell'](t_r)\, B^{(3)}_{\ell' m}\right]$$

$$\begin{aligned} &= E_0 \Bigg\{ \delta_{\ell 1}\delta_{m0}\sqrt{\frac{4\pi}{3}}\varepsilon_1 \cos\theta_0 \\ &\quad - \sqrt{\frac{2\pi}{3}}\,(\varepsilon_2-\varepsilon_1)\sin\theta_0 \left[\delta_{m,-1}\exp(\mathrm{i}\phi_0)\zeta^{-1}_{\ell 1} I^{-1}_{\ell 1}[0|0](t_r) - \delta_{m1}\exp(-\mathrm{i}\phi_0)\zeta^{1}_{\ell 1} I^{1}_{\ell 1}[0|0](t_r)\right] \\ &\quad + \delta_{\ell 1}\sqrt{\frac{2\pi}{3}}\varepsilon_2 \sin\theta_0 \left[\delta_{m,-1}\exp(\mathrm{i}\phi_0) - \delta_{m1}\exp(-\mathrm{i}\phi_0)\right] \Bigg\}, \end{aligned} \tag{3.32b}$$

where $\ell = 0, 1, \ldots$; $m = 0, \pm 1, \ldots, \pm\ell$; $s = 1$. The terms $M^{m;\,(1)}_{\ell\ell';\,2}$, $N^{m;\,(1)}_{\ell\ell';\,1}$, $I^m_{\ell\ell'}[0|0](t_r)$, $\psi^{(3)}_0$, and $\zeta^m_{\ell\ell'}$ are explicitly defined in Appendix 3.B. Again, for a more compact notation the explicit dependence of the frequency ω of the multipole coefficients, the field, the constant potential, and the dependence of the direct and image terms in the matrix elements M and N have been dropped.

Because of the rotational symmetry of the system around the z-axis the different ms do not couple to each other. Hence, the equation system can be solved separately for the different values of m. One should note that the right-hand side of Eq. (3.32) are non-zero only for the values $m = 0$ and $m = \pm 1$.

Furthermore, by comparing the set of equations for $m = -1$ and $m = 1$ one realizes that the expansion coefficients are related like

$$A^{(i)}_{\ell' 1}\mathrm{e}^{(i\phi_0)} = -A^{(i)}_{\ell' -1}\mathrm{e}^{-(i\phi_0)} \tag{3.33a}$$

$$B^{(i)}_{\ell' 1}\mathrm{e}^{(i\phi_0)} = -B^{(i)}_{\ell' -1}\mathrm{e}^{-(i\phi_0)}. \tag{3.33b}$$

Accordingly, only the terms where $m = 0$ and $m = 1$ are considered for the solutions of Eq. (3.32).

3.3.4 The island polarizabilities

For particles which are symmetric around the z-axis one may show that the elements of the polarizability tensor given in Eq. (3.21) can be written as [5, 48]

$$A_{10} = -\sum_{0\ell'}^{M} \alpha_{10,\ell' 0} B_{\ell' 0} = -\frac{\alpha^{00}_{\perp}}{4\pi\varepsilon_1} B_{10} \tag{3.34a}$$

$$A_{11} = -\sum_{1\ell'}^{M} \alpha_{11,\ell' 1} B_{\ell' 1} = \alpha_{1-1,1-1} = -\frac{\alpha^{00}_{\parallel}}{4\pi\varepsilon_1} B_{11} \tag{3.34b}$$

$$A_{20} = -\sum_{0\ell'}^{M} \alpha_{20,\ell' 0} B_{\ell' 0} = \alpha_{2-1,1-1} = -3\frac{\alpha^{10}_{\parallel}}{4\pi\varepsilon_1\sqrt{5}} B_{10} \tag{3.34c}$$

$$A_{21} = -\sum_{1\ell'}^{M} \alpha_{21,\ell' 0} B_{\ell' 1} = \frac{3}{5}\alpha_{10,20} = -\frac{\alpha^{10}_{\perp}}{2\pi\varepsilon_1\sqrt{5/3}} B_{11}, \tag{3.34d}$$

where $\ell' = 1, ..., M$, and the terms α_i^{00} and α_i^{10} denotes the direction dependent dipole and quadrupolar polarizabilities, respectively, where $i = \{\parallel, \perp\}$ are the direction parallel or perpendicular to the substrate. In the following we will omit the subscript 00 in the direction dependent first order polarizabilities.

With the expressions of the constant incoming and transmitted scalar potential in Eq. (3.53c) and Eq. (3.28a) and the identities for the $B_{\ell m}$ coefficients in Eq. (3.34) one can write the dipole and quadrupolar polarizabilities of the truncated sphere modified by the presence of the substrate as

$$\alpha_\perp = \frac{2\pi\varepsilon_1 A_{10}}{E_0\sqrt{\pi/3}\cos\theta_0} \tag{3.35a}$$

$$\alpha_\perp^{10} = \frac{\pi\varepsilon_1 A_{20}}{E_0\sqrt{\pi/5}\cos\theta_0} \tag{3.35b}$$

$$\alpha_\parallel = -\frac{4\pi\varepsilon_1 A_{11}}{E_0\sqrt{2\pi/3}\sin\theta_0 \mathrm{e}^{-i\phi_0}} \tag{3.35c}$$

$$\alpha_\parallel^{10} = -\frac{4\pi\varepsilon_1 A_{21}}{E_0\sqrt{6\pi/5}\sin\theta_0 \mathrm{e}^{-i\phi_0}}. \tag{3.35d}$$

Notice that the direction dependent polarizabilities in this formulation only are scaled by the angles of incidents θ_0 and ϕ_0.

As discussed in Ch. 2, it is the surface susceptibilities that drives all the optical response of a film containing metallic NPs. These can, finally, be expressed from the polarizabilities in Eq. (3.35). For a substrate placed at $z = d$ the electric surface susceptibilities to dipolar (γ, β) and quadrupolar (τ, δ) order are [37]

$$\gamma(d) = \rho\alpha_\parallel(d) \tag{3.36a}$$

$$\beta(d) = \frac{\rho}{\varepsilon_1^2}\alpha_\perp(d) \tag{3.36b}$$

$$\tau(d) = -\rho\alpha_\parallel^{10}(d) \tag{3.36c}$$

$$\delta(d) = -\frac{\rho}{\varepsilon_1}\left[\alpha_\perp^{10}(d) + \alpha_\parallel^{10}(d)\right]. \tag{3.36d}$$

Thus, all the macroscopic optical properties of the system can be obtained from the relations given in Eq. (2.27). If the particles in the film show a slight dispersion in size and/or shape, the polarizabilities that appear in Eq. (3.36) must be replaced by an average over the distribution characterizing the size and/or shape dispersion (see Ch. 6 for details).

Since the polarizabilities are determined from the coefficients A_{00},A_{10},A_{20}, and A_{21} alone, it is tempting to set $M = 2$ in Eq. (3.32). However, this is not recommended since the convergence of these coefficients depends critically on the size of the matrix system. A more stringent and accurate test of convergence is given by the degree of fulfillment of the BCs for $\psi(\mathbf{r})$ over the spherical surface for a given truncation of the matrix system at M [46]. We recall that the BCs on the planar surface of the substrate by construction always are satisfied for any value of M.

3.4 The polarizability of a truncated spheroidal particle

Solving Laplace's equation, given in Eq. (3.12), in spherical coordinates is just a matter of convenience related to the object's spherical symmetry. As long as one can find a complete set of functions for which each function also is a solution of Laplace's equation, any coordinate system may be used. For particles of spheroidal shapes where the axis of rotation is normal to the surface of the substrate, either oblate [Figs. 3.3(a)-(b)] or prolate [Figs. 3.3(c)-(d)] spheroids can be considered.

Detailed derivations for the expressions of the polarizabilities of a spheroidal particle geometries can be found in Refs. 5, 50, 51. For oblate and prolate spheroidal particles it is most convenient to work in terms of oblate and prolate spheroidal coordinates, respectively. A multipole expansion of the solutions to the Laplace's equation is also possible in these coordinate system and one talks about *oblate* and *prolate spheroidal multipole expansions*. Such expansions are facilitated by the so-called oblate and prolate spheroidal harmonics which form complete sets of functions on the surface of the oblate and prolate spheroids, respectively.

In the context of relevant experimental systems, the truncated oblate spheroidal particles are especially interesting. Therefore, we will only report the relevant results for the oblate spheroidal particles.

The island geometry

The spheroidal coordinate systems convenient to use for oblate and prolate spheroids are different. For an oblate spheroid, an *oblate spheroidal coordinate system* is used. The coordinates (ξ, η, ϕ) in this system are defined in the range $0 \leq \xi < \infty$, $-1 \leq \eta \leq 1$, and $0 \leq \phi \leq 2\pi$.

Furthermore, the radius parallel to the surface is defined as $R_{\parallel} = a\sqrt{\xi_0^2 + 1}$ and the radius perpendicular to the substrate as $R_{\perp} = a\xi_0$. The constant $\xi = \xi_0$ defines the surface of the spheroid and the term a denotes the radius of the ring of foci [see Fig. 3.3(b)]. The limit case $\xi_0 \to \infty$, $a \to 0$ where $a\xi_0 = R$ is a constant, corresponds a sphere with radius R.

The relations between the Cartesian and the oblate spheroidal coordinate system, as defined by Morse and Feshbach in Ref. 52, are

$$\xi = \left[\left(\frac{\rho_1 + \rho_2}{2a}\right) - 1\right]^{1/2} \tag{3.37a}$$

$$\eta = \pm\left[\left(1 - \frac{\rho_1 - \rho_2}{2a}\right)\right]^{1/2} \tag{3.37b}$$

$$\phi = \arctan\left(\frac{y}{x}\right) \tag{3.37c}$$

with

$$\rho_1 = \left[z^2 + (x + a\cos\phi)^2 + (y + a\sin\phi)^2\right]^{(1/2)} \tag{3.37d}$$

$$\rho_2 = \left[z^2 + (x - a\cos\phi)^2 + (y - a\sin\phi)^2\right]^{(1/2)}, \tag{3.37e}$$

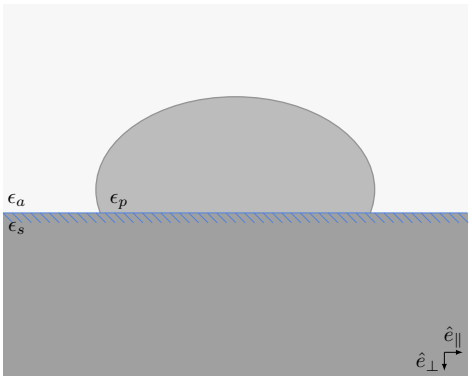

(a) Truncated oblate spheroidal particle.

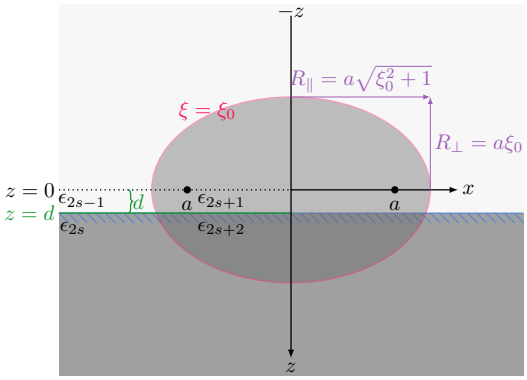

(b) Relevant quantities for the spheroidal oblate coordinate system.

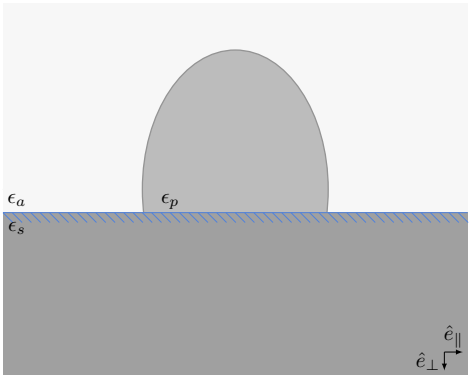

(c) Truncated prolate spheroidal particle.

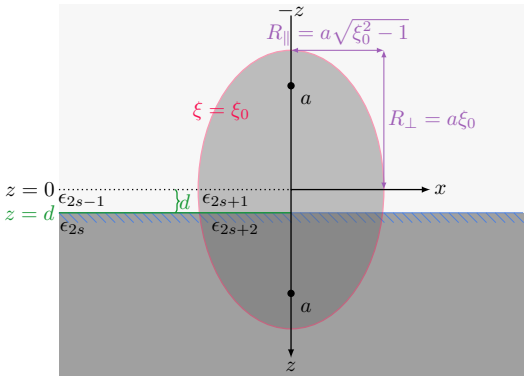

(d) Relevant quantities for the spheroidal prolate coordinate system.

Figure 3.3 A sketch of a truncated oblate (a) and prolate (c) spheroidal particle with relevant quantities for the actual coordinate systems, for the oblate in (b) and for the prolate in (d). The particle is generated by the rotation of an ellipse around it's large (prolate) or small (oblate) axis. The radius of the ring of foci is denoted a. The surface of the spheroid corresponds to $\xi = \xi_0$.

where ρ_1 and ρ_2 are the distances from a point P in the (x, y, z)-coordinates to the intersections of the ring of foci $2a$ with the plane through (x, y, z) and the z-axis. The term ϕ defines the angle of this place with respect to the xz-plane. The positive sign in Eq. (3.37b) should be used for $z \geq 0$ and the negative sign if $z < 0$.

The inverse transformation from oblate spheroidal coordinates to Cartesian coordinates is given by

$$x = a\left[(\xi^2+1)(1-\eta^2)\right]^{1/2}\cos\phi \tag{3.38a}$$

$$y = a\left[(\xi^2+1)(1-\eta^2)\right]^{1/2}\sin\phi \tag{3.38b}$$

$$z = a\xi\eta. \tag{3.38c}$$

A solution of Laplace's equation in spheroidal harmonics

In oblate spheroidal coordinates, Laplace's equation can be written in the form of a product between radial functions (ξ) and the oblate spheroidal harmonics

$$\psi(\mathbf{r}|\omega) = \sum_{l=0}^{\infty}\sum_{m=-\ell}^{\ell}\left[A_{\ell m}Z_\ell^m(\xi,a) + B_{\ell m}X_\ell^m(\xi,a)\right]Y_\ell^m\left(\arccos\eta,\phi\right), \tag{3.39}$$

where summation indices again are $\ell = 0, 1, ..., \infty$ and $m = -\ell, -\ell+1, ..., \ell-1, \ell$, the angular part of the spheroidal harmonics is given by the $Y_\ell^m\left(\arccos\eta,\phi\right)$ term, and, again, the unknown multipole coefficients are denoted $A_{\ell m}$ and $B_{\ell m}$. The functions $Z_\ell^m(\xi,a)$ and $X_\ell^m(\xi,a)$ are defined for oblate coordinates as in [51]:

$$Z_\ell^m(\xi,a) = i^{\ell+1}\frac{(2\ell+1)!!}{(\ell+m)!}a^{-\ell-1}Q_\ell^m(i\xi), \tag{3.40a}$$

$$X_\ell^m(\xi,a) = i^{m-\ell}\frac{(\ell-m)!}{(2\ell+1)!!}a^{\ell}P_\ell^m(i\xi) \tag{3.40b}$$

where $P_\ell^m(i\xi)$ and $Q_\ell^m(i\xi)$ are the associated Legendre functions of degree ℓ and order m of the first and second kind, respectively [51]. The term $(n)!!$ is defined as $(n)!! \equiv 1\times3\times...\times(n-2)\times n$, for odd values of n and $(n)!! \equiv 2\times4\times...\times(n-2)\times n$ for even numbers of n. By definition $(-1)!! \equiv 1$.

In the limit $\xi \to \infty$ the asymptotic behavior of the functions in Eq. (3.40) are

$$\lim_{\xi\to\infty} X_\ell^m(\xi,a) \approx r^{(\ell)} \tag{3.41a}$$

$$\lim_{\xi\to\infty} Z_\ell^m(\xi,a) \approx r^{-(\ell+1)}, \tag{3.41b}$$

and we recover the spherical case.

To finally determine the polarizabilities of a truncated oblate spheroidal islands on a substrate one would (again) have to express the electrostatic potential in all regions outside and inside the particle and impose the relevant BCs. This will not be done here, see Refs. 5, 51 for a full discussion.

3.5 The polarizabilities of a film of truncated particles

The calculations in the previous sections did not account for the potential island-island interaction between neighboring particles. The polarizabilities given by Eq. (3.35) are calculated taking the electrostatic interaction with the substrate (or the image multipoles) into account to the multipolar order M. In an ensemble of particles, each particle may create a local field on its neighbors that will locally modify the electric field. If particles are sufficiently far apart this phenomenon, where the leading term is of dipolar character, may be safely neglected. We call this organization of particles for the *low coverage* regime [Fig. 3.4(a)]. In this case the particle is only polarized by the incoming field. If the distances between the particles are decreased, at some point, the island-island interaction between the particles and their respective images will be of importance and the polarization field of a particle will be modified by the presence of its neighbors [5, 40, 53, 54]. This limit corresponds to what is called herein as the *finite coverage* regime [Fig. 3.4(b)].

In principle, one should take into account all interactions, island-substrate and island-island, to high order and fulfill the required BCs over all the interfaces. The calculations of island-island interactions are more complex than the island-substrate interactions. Fortunately, because of the fast decrease of the higher-order terms in the island-island interaction between particles, the problem can be limited to include only the low-order terms like the dipolar or quadrupolar ones [40].

The limit where the island-island interaction can not be ignored will depend on the chosen system (*i.e.* dielectric function of the materials and the distance between the particles). Calculations performed by Letnes and co-workers for a lattice of supported full silver spheres on an alumina substrate have shown that in the case where the spacing between the particles is greater than four times the sphere diameter, the finite coverage regime can be ignored. The system could then be regarded as a collection of independent non-interacting objects [34]. Their simulations were performed in the quasi-static regime where the radii of the particles were $R = 10\,\text{nm}$.

The overlap between the experimental result of lithographically produced arrays of gold nanoparticles and the theoretical predictions for the case of a square lattice with gold nanoparticles in the form of oblate islands with the polarizabilities corrected for the island-island interaction have been found [55]. The size of the island diameters and lattice constant were, respectively, $D = 13 - 35\,\text{nm}$ and $L = 50\,\text{nm}$ in this work.

Organization of the particles in an island film

As a matter of convenience, two types of organizations of particles are considered in the present formalism. The so-called regular array (square or hexagonal) with only one particle per unit cell (Fig. 3.5), and a random array defined by its pair correlation function. The calculation of the correction terms for the island-island interactions are known to dipolar and quadrupolar order in our framework [40]. In the polarizable dipole models all amplitudes where $\ell \neq \ell' \neq 1$ are set to zero. In the quadrupole model all the amplitudes with $\ell = \ell' > 2$ are set to zero. A detailed derivation for the island-island correction term is reported in [37, 53]. Here, only the final result at

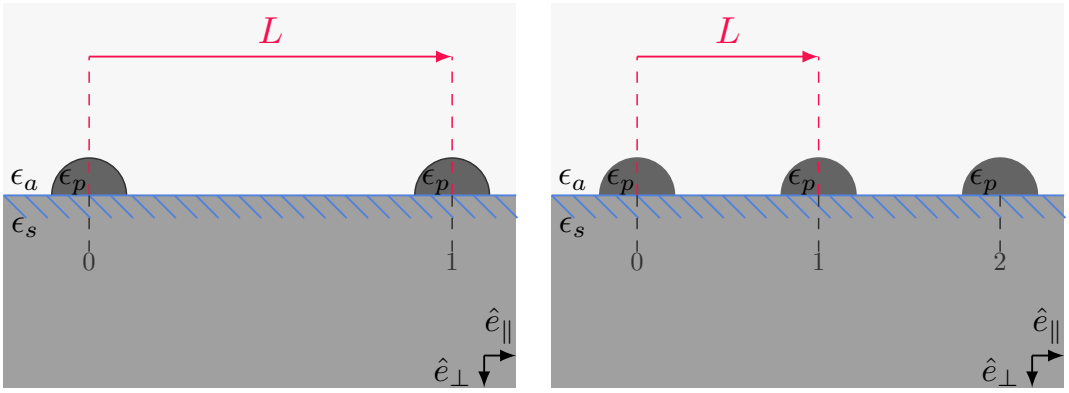

(a) Low coverage. **(b)** Finite coverage.

Figure 3.4 A schematic illustration of the islands in the low (a), or finite(b) coverage regime.

dipolar order will be commented on.

3.5.1 The dipolar approximation

In the case of particles arranged in a regular array, the direction dependent polarizabilities corrected for the interaction between neighboring particles reads

$$\hat{\alpha}_\perp = \alpha_\perp \left\{ 1 - \frac{\alpha_\perp}{2\pi\varepsilon_1 L^3} \left[S_{2,0} - \left(\frac{\varepsilon_1 - \varepsilon_2}{\varepsilon_1 + \varepsilon_2} \right) \bar{S}_{2,0} \right] \right\}^{-1} \tag{3.42a}$$

$$\hat{\alpha}_\parallel = \alpha_\parallel \left\{ 1 + \frac{\alpha_\parallel}{4\pi\varepsilon_1 L^3} \left[S_{2,0} + \left(\frac{\varepsilon_1 - \varepsilon_2}{\varepsilon_1 + \varepsilon_2} \right) \bar{S}_{2,0} \right] \right\}^{-1}, \tag{3.42b}$$

where the quantity L denotes the lattice constant and the direct/image lattice sums are denoted $S_{2,0}/\bar{S}_{2,0}$. The expressions for the lattice sums are taken from [56]

$$S_{2,0} = \sum_{i \neq 0} \left(\frac{L}{r} \right)^3_{r=R_\parallel^{(i)}} Y_\ell^m(\theta, \phi) \tag{3.43a}$$

$$\bar{S}_{2,0} = \sum_{i \neq 0} \left(\frac{L}{r} \right)^3_{r=\bar{R}_\parallel^{(i)}} Y_\ell^m(\theta, \phi), \tag{3.43b}$$

where $R_\parallel^{(i)}$ and $\bar{R}_\parallel^{(i)}$ denotes, respectively, the radial distance in the plane of the substrate between the direct and image dipoles of the neighbors. The index runs from $i = 1$ because the interaction of the considered particle and it's image is already taken into account when calculating the single particle response. The lattice sums are calculated according to the method described in Ref. 5. The expressions for the lattice sums are dependent on whenever the particles are arranged in a square or hexagonal lattice. In the limit where the distance between the set of direct and image multipoles are far from each other $\{R_\parallel^{(i)}, \bar{R}_\parallel^{(i)}\} \gg L$, the results in the finite and low coverage regime approach each other.

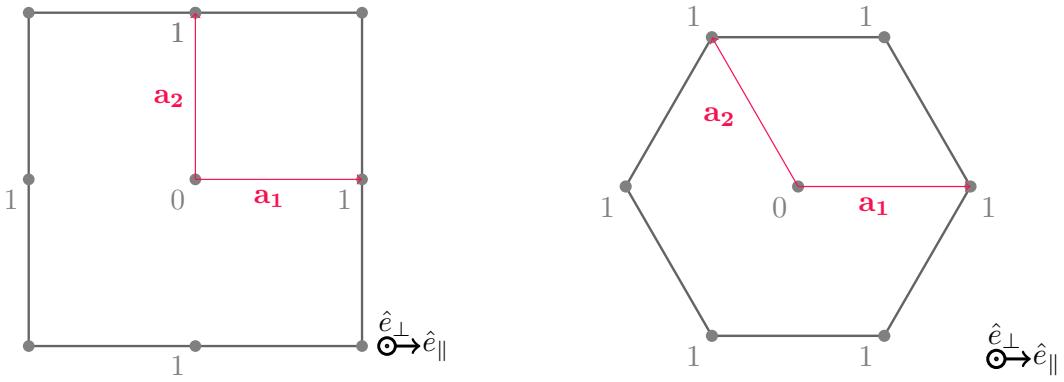

(a) Square lattice. **(b)** Hexagonal lattice.

Figure 3.5 Illustration of permitted organization of the ensemble of the particles on a regular lattice accounted for within our framework. Particles placed in a square (a) or hexagonal (b) structure, as seen from above. The considered particle is marked 0 whereas the first order neighbors are labeled with 1s.

If, on the other hand, the particles are organized in a random array the multiparticle correlations are described by pair correlation functions [53]. For the random array configuration Eq. (3.42) are valid if the normalization term L^{-3} is replaced with $\rho^{3/2}$, where ρ is the surface density of particles and the set of lattice sums $\{S_{20}, \bar{S}_{20}\}$ become continuous distribution integrals $\{I_2, \bar{I}_2\}$ given as

$$I_2 = 2\pi\rho^{-1/2} \int_0^\infty dr_\parallel g(r_\parallel) r_\parallel^{-2} P_2^0(0) \sqrt{5/4\pi} \tag{3.44a}$$

$$\bar{I}_2 = 2\pi\rho^{-1/2} \int_0^\infty dr_\parallel g(r_\parallel) r_\parallel (r_\parallel^2 + d_{\mu\bar{\mu}}^2)^{-3/2} P_2^0(d_{\mu\bar{\mu}}/(r_\parallel^2 + d_{\mu\bar{\mu}}^2)^{1/2}) \sqrt{5/4\pi}, \tag{3.44b}$$

where $d_{\mu\bar{\mu}}$ denotes the distance from the expansion point to its image multipole, and the integration variable $r_\parallel$ is taken in the plane of the substrate, P_2^0 again denotes the associated Legendre-polynomial, and $g(r_\parallel)$ is the pair-correlation. Appendix B discusses the considered form of the pair-correlation function in our formalism.

Similar, but more complex expressions can be derived at quadrupolar order [37].

3.5.2 The surface coverage parameter

We define the surface coverage of particles in a system by the dimensionless parameter Θ. It is given by the fraction of the surface area covered by islands, as seen from above. The area of the bottom part of a single island touching the substrate is given by $A_{bottom} = \pi R_{app}^2$, where R_{app} is the apparent radius of the island defined like

$$R_{app} = \begin{cases} R_\parallel^{(1)} & t_r^{(1)} > 0 \\ R_\parallel^{(1)} \sqrt{1 - (t_r^{(1)})^2} & t_r^{(1)} \leq 0. \end{cases} \tag{3.45}$$

Thus, we define the surface coverage for the different types of ordered arrays as

$$\Theta(R_{app}) = \pi R_{app}^2 \rho = \begin{cases} \pi(\frac{R_{app}}{L})^2 & \text{Square lattice,} \\ \frac{2\pi}{\sqrt{3}}(\frac{R_{app}}{L})^2 & \text{Hexagonal lattice.} \end{cases} \tag{3.46}$$

The distribution of the particles in a random array are not ordered. To be able to compare the optical response in ordered and random arrays we define the coverage of a random array by the equivalent coverage of particles as if the system was organized in a square or hexagonal array

$$\Theta_{rand}(R_{app}) = \pi R_{app}^2 \rho_{rand} = \begin{cases} \pi(\frac{R_{app}}{L})^2 & \text{Equivalent to a square lattice,} \\ \frac{2\pi}{\sqrt{3}}(\frac{R_{app}}{L})^2 & \text{Equivalent to a hexagonal lattice.} \end{cases} \tag{3.47}$$

Even though the maximal coverage theoretically is given as $L = 2R_{app}$ the actual lattice sums can only be taken to dipolar or quadrupolar order. Thus, it is not expected that the lattice sums or the distribution integrals to this order are sufficient to describe the inter-island couplings [5].

It has been demonstrated that the difference between the two correction terms for truncated spheres organized in an ordered or random array is negligible up to a coverage of particles which is higher than experimentally relevant (a surface coverage of particles of about 40%) [53].

3.6 Conclusion

This chapter has illustrated how the polarizabilities, to the second order, of truncated and supported particles can be obtained in the quasi-static approximation. More generally, the calculation method described in the previous sections is valid for particles which are symmetric along the z-axis. The analysis was detailed primarily for the case of a truncated sphere. Guidelines to the generalization to coated objects as well as spheroidal particles were given.

Laplace's equation was solved by separation of variables and a multipole series expansion containing a direct and an image term. The multipole expansion point was allowed to move freely along the z-axis, but kept inside the island. The appropriate BCs at the surface of the substrate were naturally handled by the method of images. On the spherical surfaces, a weak formulation of the BCs based on the completeness of the SHs was used. A linear system of equations was obtained to determine the expressions of the multipolar coefficients. The lower order multipole coefficients are used to define the dipolar and quadrupolar polarizabilities, which are closely related to the surface susceptibilities, the main ingredients in the BV-formalism.

Finally, the chapter ended with a discussion of the island-island interactions and how they influence the optical properties of island films containing supported particles. Expressions for the polarizabilities renormalized by the island-island interactions were introduced for particles organized in a regular or random array.

The theory described in this chapter has been implemented in the GranFilm software. The organization and capabilities of the code will be the topic of Chapter 4. Our discussion of the direction dependent polarizabilities was restricted to the case of identical particles in the system. The cases where the particles exhibit dispersion in size and shape will be detailed in Chapter 6.

3.A Fulfillment of the boundary conditions on the planar surface of the substrate

In this appendix, we will demonstrate how one can simplify the expressions of the electrostatic potential given in Eq. (3.16) by fulfilling the BCs, Eqs. (3.13)-(3.14), at the planar surface of the substrate with the use of the method of images.

We start from the general expressions of the potentials that were given in Eq. (3.25). For a region above the substrate $i = \{1, 3, ..., 2S + 1\}$ the general expression for the potential yields

$$\psi_i(\mathbf{r}|\omega) = \psi_{inc}^{(i)}(\mathbf{r}|\omega)\,\delta_{1,i} + \psi_0^{(i)}(\omega) + \sum_{\ell=1}^{\infty}\sum_{m=-\ell}^{\ell}\left[A_{\ell m}^{(i)}(\omega) r_\mu^{-\ell-1} + B_{\ell m}^{(i)}(\omega) r_\mu^{\ell}\right] Y_\ell^m(\theta_\mu, \phi_\mu) + \sum_{\ell=1}^{\infty}\sum_{m=-\ell}^{\ell}\left[\bar{A}_{\ell m}^{(i)}(\omega) r_{\bar{\mu}}^{-\ell-1} + \overline{B}_{\ell m}^{(i)}(\omega) r_{\bar{\mu}}^{\ell}\right] Y_\ell^m(\theta_{\bar{\mu}}, \phi_{\bar{\mu}}), \tag{3.48a}$$

where the set $\{A_{\ell m}^{(i)}(\omega), B_{\ell m}^{(i)}(\omega)\}$ is related to the unknown multipole coefficients linked to the direct multipole expansion point placed at $\mathbf{r}_\mu = (r_\mu, \theta_\mu, \phi_\mu)$. Similarly, the set $\{\bar{A}_{\ell m}^{(i)}(\omega), \overline{B}_{\ell m}^{(i)}(\omega)\}$ is related to the image multipole expansion point placed at $\mathbf{r}_{\bar{\mu}} = (r_{\bar{\mu}}, \theta_{\bar{\mu}}, \phi_{\bar{\mu}})$. The term $\delta_{1,i}$ makes sure that the incoming potential is only present in the region $i = 1$. Furthermore, $\psi_0^{(i)}(\omega)$ are the constant potentials in the region.

For a region below the substrate $i + 1$, the general electrostatic potential is

$$\psi_{i+1}(\mathbf{r}|\omega) = \psi_{tr}^{(i+1)}(\mathbf{r}|\omega)\,\delta_{2,i+1} + \psi_0^{(i+1)}(\omega) + \sum_{\ell=1}^{\infty}\sum_{m=-\ell}^{\ell}\left[A_{\ell m}^{(i+1)}(\omega) r_\mu^{-\ell-1} + B_{\ell m}^{(i+1)}(\omega) r_\mu^{\ell}\right] Y_\ell^m(\theta_\mu, \phi_\mu) \tag{3.48b}$$

Our target is to express the unknown multipole coefficients in Eq. (3.48) so we can identify the polarizabilities with the scaling relation stated in Eq. (3.21). To do so we will express the incoming field, and satisfy the BCs on the substrate and sphere surfaces. At the surface of the substrate, $z = d$ we can write the continuity of the potentials $\psi_i(\mathbf{r}|\omega)$ and $\psi_{i+1}(\mathbf{r}|\omega)$ with the general form given in Eq. (3.48) and the expressions for the incoming and transmitted field given in Eqs. (3.28a)-(3.28b) as

$$
\begin{aligned}
&\psi_i(\mathbf{r}|\omega) - \psi_{i+1}(\mathbf{r}|\omega) = \\
&\quad \psi_{inc}^{(i)}(\mathbf{r}|\omega)\,\delta_{1,i} + \psi_0^{(i)}(\omega) + \sum_{\ell=1}^{\infty}\sum_{m=-\ell}^{\ell}\left[A_{\ell m}^{(i)}(\omega) r_\mu^{-\ell-1} + B_{\ell m}^{(i)}(\omega) r_\mu^{\ell}\right] Y_\ell^m\left(\theta_\mu, \phi_\mu\right) \\
&\quad + \sum_{\ell=1}^{\infty}\sum_{m=-\ell}^{\ell}\left[\bar{A}_{\ell m}^{(i)}(\omega) r_{\bar{\mu}}^{-\ell-1} + \overline{B}_{\ell m}^{(i)}(\omega) r_{\bar{\mu}}^{\ell}\right] Y_\ell^m\left(\theta_{\bar{\mu}}, \phi_{\bar{\mu}}\right) \\
&- \\
&\quad \left\{\psi_{tr}^{(i+1)}(\mathbf{r}|\omega)\,\delta_{2,i+1} + \psi_0^{(i+1)}(\omega) + \sum_{\ell=1}^{\infty}\sum_{m=-\ell}^{\ell}\left[A_{\ell m}^{(i+1)}(\omega) r_\mu^{-\ell-1} + B_{\ell m}^{(i+1)}(\omega) r_\mu^{\ell}\right] Y_\ell^m\left(\theta_\mu, \phi_\mu\right)\right\}.
\end{aligned}
$$

By the symmetry of the system, the coordinates for the direct and image points at $z = d$ are related

$$
\begin{aligned}
r_{\bar{\mu}} &= r_\mu \\
\theta_{\bar{\mu}} &\overset{①}{=} \pi - \theta_\mu \\
\phi_{\bar{\mu}} &= \phi_\mu.
\end{aligned}
\tag{3.49}
$$

① $\cos\theta_{\bar{\mu}} = \cos(\pi - \theta_\mu) = (-1)\cos\theta_\mu \implies Y_\ell^m\left(\theta_{\bar{\mu}}, \phi_{\bar{\mu}}\right) = (-1)^m Y_\ell^m\left(\theta_\mu, \phi_\mu\right)$.

Similarly, the BC of the dielectric function times the normal derivative of the potential on the boundary is

$$
\begin{aligned}
&\varepsilon_i(\omega)\partial_n\psi_i(\mathbf{r}|\omega) - \varepsilon_{i+1}(\omega)\partial_n\psi_{i+1}(\mathbf{r}|\omega) = \\
&\varepsilon_i(\omega)\frac{\partial}{\partial r}\frac{\partial r}{\partial n}\left\{\psi_{inc}^{(i)}(\mathbf{r}|\omega)\,\delta_{1,i} + \psi_0^{(i)}(\omega) + \sum_{\ell=1}^{\infty}\sum_{m=-\ell}^{\ell}\left[A_{\ell m}^{(i)}(\omega)r_\mu^{-\ell-1} + B_{\ell m}^{(i)}(\omega)r_\mu^{\ell}\right]Y_\ell^m\left(\theta_\mu,\phi_\mu\right)\right. \\
&\quad\left. + \sum_{\ell=1}^{\infty}\sum_{m=-\ell}^{\ell} f_i\left[\bar{A}_{\ell m}^{(i)}(\omega)r_{\bar{\mu}}^{-\ell-1} + \overline{B}_{\ell m}^{(i)}(\omega)r_{\bar{\mu}}^{\ell}\right]Y_\ell^m\left(\theta_{\bar{\mu}},\phi_{\bar{\mu}}\right)\right\} \\
&- \\
&\quad\varepsilon_{i+1}(\omega)\frac{\partial}{\partial r}\frac{\partial r}{\partial n}\left\{\psi_{tr}^{(i+1)}(\mathbf{r}|\omega)\,\delta_{2,i+1} + \psi_0^{(i+1)}(\omega)\right. \\
&\quad\left. + \sum_{\ell=1}^{\infty}\sum_{m=-\ell}^{\ell}\left[A_{\ell m}^{(i+1)}(\omega)r_\mu^{-\ell-1} + B_{\ell m}^{(i+1)}(\omega)r_\mu^{\ell}\right]Y_\ell^m\left(\theta_\mu,\phi_\mu\right)\right\} \\
&\overset{①}{=} \\
&\quad\varepsilon_i(\omega)\left\{-E_0(\omega)\sqrt{\frac{2\pi}{3}}\left(\sqrt{2}\cos\theta_0 Y_1^0\left(\theta,\phi\right) - \sin\theta_0\left[\mathrm{e}^{-i\phi_0}Y_1^1\left(\theta,\phi\right) - \mathrm{e}^{i\phi_0}Y_1^{-1}\left(\theta,\phi\right)\right]\right)\right. \\
&\quad + \sum_{\ell=1}^{\infty}\sum_{m=-\ell}^{\ell}\left[A_{\ell m}^{(i)}(\omega)(-\ell-1)r_\mu^{-\ell-2} + B_{\ell m}^{(i)}(\omega)\ell r_\mu^{\ell-1}\right]Y_\ell^m\left(\theta_\mu,\phi_\mu\right) \\
&\quad\left. + \sum_{\ell=1}^{\infty}\sum_{m=-\ell}^{\ell}\left[\bar{A}_{\ell m}^{(i)}(\omega)(-\ell-1)(-1)^\ell r_{\bar{\mu}}^{-\ell-2} + \overline{B}_{\ell m}^{(i)}(\omega)(-1)^\ell\ell r_{\bar{\mu}}^{\ell-1}\right]Y_\ell^m\left(\theta_{\bar{\mu}},\phi_{\bar{\mu}}\right)\right\} \\
&- \\
&\quad\varepsilon_{i+1}(\omega)\left\{-E_0(\omega)\sqrt{\frac{2\pi}{3}}\left(\sqrt{2}a_1\cos\theta_0 Y_1^0\left(\theta,\phi\right) - \sin\theta_0\left[a_2\mathrm{e}^{-i\phi_0}Y_1^1\left(\theta,\phi\right) - a_3\mathrm{e}^{i\phi_0}Y_1^{-1}\left(\theta,\phi\right)\right]\right)\right. \\
&\quad\left. + \sum_{\ell=1}^{\infty}\sum_{m=-\ell}^{\ell}\left[A_{\ell m}^{(i+1)}(\omega)(-\ell-1)r_\mu^{-\ell-2} + B_{\ell m}^{(i+1)}(\omega)\ell r_\mu^{\ell-1}\right]Y_\ell^m\left(\theta_\mu,\phi_\mu\right)\right\}.
\end{aligned}
$$

① Note the different sign for the direct and image mutipole due to the opposite direction of the normal derivative $\frac{\partial r_\mu}{\partial n} = 1$, $\frac{\partial r_{\bar{\mu}}}{\partial n} = -1$.

Since Eq. (3.49) and Eq. (3.50) are verified for any point along the surface, the equality should hold term by term. Thus, for the continuity of the potential Eq. (3.49) the

following relations must be fulfilled

$$A_{\ell m}^{(i)}(\omega) + (-1)^{\ell+m}\bar{A}_{\ell m}^{(i)}(\omega) - A_{\ell m}^{(i+1)}(\omega) = 0 \tag{3.50a}$$

$$B_{\ell m}^{(i)}(\omega) + (-1)^{\ell+m}\overline{B}_{\ell m}^{(i)}(\omega) - B_{\ell m}^{(i+1)}(\omega) = 0 \tag{3.50b}$$

$$\psi_0^{(i)} - \psi_0^{(i+1)} = 0 \tag{3.50c}$$

$$\begin{aligned} &- rE_0(\omega)\sqrt{\frac{2\pi}{3}}\left(\sqrt{2}\cos\theta_0 Y_1^0(\theta,\phi) - \sin\theta_0\left[\mathrm{e}^{-i\phi_0}Y_1^1(\theta,\phi) - \mathrm{e}^{i\phi_0}Y_1^{-1}(\theta,\phi)\right]\right) - a_0 \\ &+ \\ &\quad rE_0(\omega)\sqrt{\frac{2\pi}{3}}\left(\sqrt{2}a_1\cos\theta_0 Y_1^0(\theta,\phi) - \sin\theta_0\left[a_2\mathrm{e}^{-i\phi_0}Y_1^1(\theta,\phi) - a_3\mathrm{e}^{i\phi_0}Y_1^{-1}(\theta,\phi)\right]\right) = 0. \end{aligned} \tag{3.50d}$$

For the dielectric function times the normal derivative of the potential Eq. (3.50) we can write

$$\varepsilon_i(\omega)\left[A_{\ell m}^{(i)}(\omega) + (-1)^{\ell+m}\bar{A}_{\ell m}^{(i)}\right] - \varepsilon_{i+1}(\omega)A_{\ell m}^{(i+1)}(\omega) = 0 \tag{3.51a}$$

$$\varepsilon_i(\omega)\left[B_{\ell m}^{(i)}(\omega) + (-1)^{\ell+m}\overline{B}_{\ell m}^{(i)}(\omega)\right] - \varepsilon_{i+1}(\omega)B_{\ell m}^{(i+1)}(\omega) = 0 \tag{3.51b}$$

$$\begin{aligned} &\varepsilon_i(\omega)\left\{-E_0(\omega)\sqrt{\frac{2\pi}{3}}\left(-\sin\theta_0\left[\mathrm{e}^{-i\phi_0}Y_1^1(\theta,\phi) - \mathrm{e}^{i\phi_0}Y_1^{-1}(\theta,\phi)\right]\right)\right\} \\ &\quad - \varepsilon_{i+1}(\omega)\left\{-\sin\theta_0\left[a_2\mathrm{e}^{-i\phi_0}Y_1^1(\theta,\phi) - a_3\mathrm{e}^{i\phi_0}Y_1^{-1}(\theta,\phi)\right]\right\} = 0 \end{aligned} \tag{3.51c}$$

$$\varepsilon_{i+1}(\omega)E_0(\omega)\sqrt{\frac{2\pi}{3}}\left(\sqrt{2}a_1\cos\theta_0 Y_1^0(\theta,\phi)\right) - \varepsilon_i(\omega)E_0(\omega)\sqrt{\frac{2\pi}{3}}\left(\sqrt{2}\cos\theta_0 Y_1^0(\theta,\phi)\right) = 0 \tag{3.51d}$$

Rearranging and inserting Eq. (3.50) into Eq. (3.51), one finds the following relations for the unknown coefficients

$$a_0 = E_0(\omega)\cos\theta_0 d(a_1 - 1), \tag{3.52a}$$

$$a_1 = \frac{\varepsilon_i(\omega)}{\varepsilon_{i+1}(\omega)}, \tag{3.52b}$$

$$a_2 = a_3 = 1, \tag{3.52c}$$

$$A_{\ell m}^{(i+1)}(\omega) = \frac{2\varepsilon_i(\omega)}{\varepsilon_i(\omega) + \varepsilon_{i+1}(\omega)}A_{\ell m}^{(i)}(\omega), \tag{3.52d}$$

$$\bar{A}_{\ell m}^{(i)}(\omega) = f_i(-1)^{\ell+m}\frac{\varepsilon_i(\omega) - \varepsilon_{i+1}(\omega)}{\varepsilon_i(\omega) + \varepsilon_{i+1}(\omega)}A_{\ell m}^{(i)}(\omega) \tag{3.52e}$$

$$B_{\ell m}^{(i+1)}(\omega) = \frac{2\varepsilon_i(\omega)}{\varepsilon_i(\omega) + \varepsilon_{i+1}(\omega)}B_{\ell m}^{(i)}(\omega), \tag{3.52f}$$

$$\overline{B}_{\ell m}^{(i)}(\omega) = f_i(-1)^{\ell+m}\frac{\varepsilon_i(\omega) - \varepsilon_{i+1}(\omega)}{\varepsilon_i(\omega) + \varepsilon_{i+1}(\omega)}B_{\ell m}^{(i)}(\omega). \tag{3.52g}$$

To have a general formalism in the cases where a region i is not bounded by the planar surface, we have multiplied the right-hand side of Eq. (3.52e) and Eq. (3.52g) by the

factor f_i. This quantity is relevant for the cases when some of the particle surfaces are not truncated by the substrate. It is defined $f_i = 1$ when a region is bounded by the surface of the substrate and $f_i = 0$ otherwise. If $f_i = 0$ in a region i means that the region $i+1$ does not exist in the geometry of interest. The expansion of the potential $\psi_{i+1}(\mathbf{r}|\omega)$ is then irrelevant.

The relations between the unknown coefficients in Eq. (3.52) can now be used to simplify the expressions of the electrostatic potential given in Eq. (3.48). The potential in the regions i and $i+1$, $\{1, 3, ..., 2S+1\}$ can then be written only in form of the (still) unknown set of coefficients $\{A^{(i)}_{\ell m}(\omega), B^{(i)}_{\ell m}(\omega)\}$

$$\begin{aligned}\psi_i(\mathbf{r}|\omega) = \psi^{(i)}_{inc}(\mathbf{r}|\omega)\,\delta_{1,i} + \psi^{(i)}_0(\omega) \\ + \sum_{\ell=1}^{\infty}\sum_{m=-\ell}^{\ell} A^{(i)}_{\ell m}(\omega)\left[r_\mu^{-\ell-1}Y_\ell^m(\theta_\mu,\phi_\mu) + f_i(-1)^{\ell+m}\frac{\varepsilon_i(\omega)-\varepsilon_{i+1}(\omega)}{\varepsilon_i(\omega)+\varepsilon_{i+1}(\omega)}r_{\bar\mu}^{-\ell-1}Y_\ell^m(\theta_{\bar\mu},\phi_{\bar\mu})\right] \\ + \sum_{\ell=1}^{\infty}\sum_{m=-\ell}^{\ell} B^{(i)}_{\ell m}(\omega)\left[r_{\bar\mu}^{-\ell-1}Y_\ell^m(\theta_\mu,\phi_\mu) + f_i(-1)^{\ell+m}\frac{\varepsilon_i(\omega)-\varepsilon_{i+1}(\omega)}{\varepsilon_i(\omega)+\varepsilon_{i+1}(\omega)}r_{\bar\mu}^{\ell}Y_\ell^m(\theta_{\bar\mu},\phi_{\bar\mu})\right],\end{aligned} \tag{3.53a}$$

For a region below the substrate $i+1$, the general electrostatic potential is

$$\begin{aligned}\psi_{i+1}(\mathbf{r}|\omega) = \psi^{(i+1)}_{tr}(\mathbf{r}|\omega)\,\delta_{2,i+1} + \psi^{(i+1)}_0(\omega) \\ + \frac{2\varepsilon_i(\omega)}{\varepsilon_i(\omega)+\varepsilon_{i+1}(\omega)}\sum_{\ell=1}^{\infty}\sum_{m=-\ell}^{\ell}\left[A^{(i)}_{\ell m}(\omega)r_\mu^{-\ell-1} + B^{(i)}_{\ell m}(\omega)r_\mu^{\ell}\right]Y_\ell^m(\theta_\mu,\phi_\mu),\end{aligned} \tag{3.53b}$$

where the constants in the expressions of $\psi_{inc}(\mathbf{r}|\omega)$ also have been determined

$$\begin{aligned}\psi_{inc}(\mathbf{r}|\omega) = -rE_0(\omega)\sqrt{\frac{2\pi}{3}}\left\{\frac{\varepsilon_1}{\varepsilon_2}\sqrt{2}\cos\theta_0 Y_1^0(\theta,\phi)\right. \\ \left. - \sin\theta_0\left[e^{-i\phi_0}Y_1^1(\theta,\phi) - e^{i\phi_0}Y_1^{-1}(\theta,\phi)\right]\right\} + E_0(\omega)\cos\theta_0 d(\frac{\varepsilon_1}{\varepsilon_2}-1)\end{aligned} \tag{3.53c}$$

Furthermore, to fulfill the restriction that the potential should be finitely valued for any values of r, we set the coefficients

$$B^{(1)}_{\ell m}(\omega) = 0, \qquad A^{(i)}_{\ell m}(\omega) = 0, i \in \{3, 5, ..., 2S+1\}, \tag{3.53d}$$

and chooses (without the loss of generality) that the constant potentials

$$\psi^{(1)}_0 = \psi^{(2)}_0 = 0. \tag{3.53e}$$

With the potential on the form Eqs. (3.53a)-(3.53b), and the extra restrictions of the coefficients given in Eqs. (3.53d)-(3.53e) the potential automatically satisfy the proper BCs at the surface of the substrate $z = d$.

3.B Fulfillment of the boundary conditions on the spherical surface(s)

Writing the potentials in the different regions as we did in Eq. (3.53) still leaves the set of the expansion coefficients $\{A_{\ell m}^{(i)}(\omega), B_{\ell m}^{(i)}(\omega)\}$, $i \in \{1, 3, ..., 2S+1\}$ unknown. In this appendix we will impose the remaining BCs of the potential itself and the derivatives of the normal component times the dielectric functions that were given in Eq. (3.13). By deploying a so-called *weak formulation of the boundary conditions*. This formulation follows from the former, but the opposite is not true, we will arrive at an infinitely dimensional linear system of equations that can determine the multipole expansion coefficients.

We will do the derivation for the general case of a truncated spherical particle which may contain coatings. To keep the notation manageable the explicit dependence of the frequency ω in the multipole coefficients, the electric field, and the scalar potential will be suppressed.

Useful relations

To evaluate the relations between the potentials for a surface s evaluated at the the spherical surface $r = R_s$ that were given in Eq. (3.31) we rewrite the expressions that where given in Eqs. (3.23)-(3.24) to yield

$$[r_\eta(\mathbf{r})]|_{r=R_s} = R_s \left[1 + \eta_s^2 - 2\eta_s \cos\theta\right]^{1/2} \tag{3.54a}$$

$$[\cos\theta_\eta(\mathbf{r})]|_{r=R_s} = \frac{\cos\theta - \eta_s}{[1 + \eta_s^2 - 2\eta_s \cos\theta]^{1/2}} \tag{3.54b}$$

where η_s collectively denotes the set $\{\mu_s = z_{mp}/R_s, \bar{\mu}_s = z_{\overline{mp}}/R_s\}$. Similarly, derivatives of the relations in Eq. (3.54) becomes

$$[\partial_r r_\eta(\mathbf{r})]|_{r=R_s} = \frac{1 - \eta_s \cos\theta}{[1 - 2\eta_s \cos\theta + \eta_s^2]^{\frac{1}{2}}} \tag{3.54c}$$

$$[\partial_r \{\cos\theta_\eta(\mathbf{r})\}]|_{r=R_s} = \frac{1}{R_s\,[1 - 2\eta_s \cos\theta + \eta_s^2]^{\frac{1}{2}}} \left[\cos\theta - \frac{(\cos\theta - \eta_s)(1 - \eta_s\cos\theta)}{1 - 2\eta_s\cos\theta + \eta_s^2}\right]. \tag{3.54d}$$

Furthermore, we will define the quantities

$$\zeta_{\ell\ell'}^{mm'} = \frac{1}{2}\left(\frac{(2\ell+1)(2\ell'+1)(\ell-m)!(\ell'-m')!}{(\ell+m)!(\ell'+m')!}\right)^{1/2}. \tag{3.55}$$

and the matrix elements

$$M_{\ell\ell';\,s}^{m;\,(i)}[\nu](\hat{t}_r^{(s)}) = \frac{\varepsilon_i - \varepsilon_{i+1}}{\varepsilon_i + \varepsilon_{i+1}}\left[-I_{\ell\ell'}^m[\nu|\mu_s](\hat{t}_r^{(s)}) + f_i(-1)^{\ell'+m} I_{\ell\ell'}^m[\nu|\bar{\mu}_s](\hat{t}_r^{(s)})\right] + \frac{2\varepsilon_i}{\varepsilon_i + \varepsilon_{i+1}} I_{\ell\ell'}^m[\nu|\mu_s](1) \tag{3.56a}$$

and

$$N^{m;\,(i)}_{\ell\ell';\,s}[\nu](\hat{t}^{(s)}_r) = \varepsilon_i \frac{\varepsilon_i - \varepsilon_{i+1}}{\varepsilon_i + \varepsilon_{i+1}} \left[J^m_{\ell\ell'}[\nu|\mu_s](\hat{t}^{(s)}_r) + f_i(-1)^{\ell'+m}\, J^m_{\ell\ell'}[\nu|\bar{\mu}_s](\hat{t}^{(s)}_r) \right] + \varepsilon_{i+1} \frac{2\varepsilon_i}{\varepsilon_i + \varepsilon_{i+1}} J^m_{\ell\ell'}[\nu|\mu_s](1), \tag{3.56b}$$

where $i = 2s \pm 1$ and ν are integers. The quantity f_i is again used to determine if a term should be included or not, depending on if the surface is truncated or not. The explicit dependence of the matrix elements on μ_s and $\bar{\mu}_s$ have been suppressed, again to keep the notation compact. Since we are working with the general truncated sphere we have defined the term $\hat{t}^{(s)}_r$ as

$$\hat{t}^{(s)}_r = \min(t^{(s)}_r, 1). \tag{3.57}$$

Moreover, we assume that $t^{(s)}_r > -1$ for all the spherical surfaces s, because this is the most interesting geometry for us. In this way, we make sure that the limits of the integrals Eq. (3.58) in the case of a non-truncated particle surface hovering above the substrate is correctly treated.

Furthermore, the following integrals are defined in the definitions of the matrix elements in Eq. (3.56):

$$I^m_{\ell\ell'}[\nu|\eta_s](\hat{t}^{(s)}_r) = \int_{-1}^{\hat{t}^{(s)}_r} \mathrm{d}u\, P^m_\ell(u) P^m_{\ell'}\left(\frac{u - \eta_s}{\sqrt{1 - 2\eta_s u + \eta_s^2}} \right) \left[1 - 2\eta_s u + \eta_s^2\right]^{\nu/2} \tag{3.58a}$$

and

$$J^m_{\ell\ell'}[\nu|\eta_s](t^{(s)}_r) = \int_{-1}^{t^{(s)}_r} \mathrm{d}u P^m_\ell(u) \left\{ \frac{\partial}{\partial \tilde{r}_s} \left[P^m_{\ell'}\left(\frac{\tilde{r}_s u - \eta_s}{\sqrt{\tilde{r}_s^2 - 2\eta_s \tilde{r}_s u + \eta_s^2}} \right) \times \left[\tilde{r}_s^2 - 2\eta_s \tilde{r}_s u + \eta_s^2\right]^{\nu/2} \right] \right\} \Big|_{\tilde{r}_s = 1}. \tag{3.58b}$$

In both cases, η_s denotes either μ_s or $\bar{\mu}_s$ and $\tilde{r}_s = r/R_s$.

The integrals in Eq. (3.58) are results from the BCs in Eq. (3.13). The distance vectors $\mathbf{r}_\mu$ and $\mathbf{r}_{\bar{\mu}}$ that appear in the integrands of these integrals have been expressed as in Eq. (3.54), in terms of the main coordinates of system $\mathcal{S}$.

Derivation of the linear system

Substituting the multipole expansions for the potentials as given in the form in Eq. (3.53) into the weak formulation of the BCs given in Eq. (3.31a) we define the following useful relations

$$\int_{\cap_s} \mathrm{d}\Omega\ [Y^m_\ell(\theta,\phi)]^* \left[r^\nu_\eta\, Y^{m'}_{\ell'}(\theta_\eta, \phi_\eta) \right] \Big|_{r=R_s} = \delta_{mm'} \zeta^m_{\ell\ell'} R^\nu_s\, I^m_{\ell\ell'}[\nu|\eta_s](\hat{t}^{(s)}_r) \tag{3.59a}$$

$$\int_{\cup_s} \mathrm{d}\Omega\ [Y^m_\ell(\theta,\phi)]^* \left[r^\nu_\eta\, Y^{m'}_{\ell'}(\theta_\eta, \phi_\eta) \right] \Big|_{r=R_s} = \delta_{mm'} \zeta^m_{\ell\ell'} R^\nu_s \left[I^m_{\ell\ell'}[\nu|\eta_s](1) - I^m_{\ell\ell'}[\nu|\eta_s](\hat{t}^{(s)}_r) \right], \tag{3.59b}$$

with $\ell = 1, 2, \ldots$; $m = 0, \pm 1, \ldots, \pm\ell$, $\ell' = 1, 2, \ldots$; $m' = 0, \pm 1, \ldots, \pm\ell'$. The symbols $\cap_s$ and $\cup_s$ denotes, respectively the parts of the spherical surface s above and below the substrate placed in $z = d$. The constants $\zeta^m_{\ell\ell'}$ are given by Eq. (3.55), and the integrals $I^m_{\ell\ell'}[\nu|\eta_s](t_r^{(s)})$ are defined as in Eq. (3.58a).

These results are obtained in the following manner: first the definition of the spherical harmonics Eq. (3.17) is substituted into the left-hand side of Eq. (3.59). Next we use relation that $\phi_\eta = \phi$ [Eq. (3.23c)] and apply the orthogonality relation

$$\int_0^{2\pi} \mathrm{d}\phi \;\; \exp\left[-i(m - m')\phi\right] = 2\pi\, \delta_{mm'}. \tag{3.60}$$

Then the results from Eqs. (3.54a)-(3.54b) are used. After making the change of variable $u = \cos\theta$, we obtain the expressions that appear on the right-hand side of Eq. (3.59).

Similarly, for the boundary conditions for the normal derivative times the dielectric function in Eq. (3.31b) substituted with the final form of the potential in Eq. (3.53) the resulting equation will contain terms of the following form

$$\int_{\cap_s} \mathrm{d}\Omega \;\; [Y^m_\ell(\theta,\phi)]^* \left[\partial_r \left\{ r^\nu_\eta Y^{m'}_{\ell'}(\theta_\eta, \phi_\eta) \right\}\right]\Big|_{r=R_s} = \delta_{mm'} \zeta^m_{\ell\ell'} R_s^{\nu-1}\, J^m_{\ell\ell'}[\nu|\eta_s](t_r^{(s)}) \tag{3.61a}$$

$$\int_{\cup_s} \mathrm{d}\Omega \;\; [Y^m_\ell(\theta,\phi)]^* \left[\partial_r \left\{ r^\nu_\eta Y^{m'}_{\ell'}(\theta_\eta, \phi_\eta) \right\}\right]\Big|_{r=R_s} = \delta_{mm'} \zeta^m_{\ell\ell'} R_s^{\nu-1} \left[J^m_{\ell\ell'}[\nu|\eta_s](1) - J^m_{\ell\ell'}[\nu|\eta_s](t_r^{(s)})\right], \tag{3.61b}$$

where $\ell = 1, 2, \ldots$; $m = 0, \pm 1, \ldots, \pm\ell$, and $\ell' = 1, 2, \ldots$; $m' = 0, \pm 1, \ldots, \pm\ell'$.

The right-hand sides of Eq. (3.61) are derived in an analogous way to the right-hand sides of Eq. (3.59). The only difference is that the relations were obtained with the derivatives of the distance vectors as given in Eqs. (3.54c)-(3.54d) for the distance vectors.

To evaluate the derivative of the Legendre polynomial that appears implicitly in Eq. (3.61) we have used the recurrence relation [56]

$$\frac{\partial P^m_\ell(w)}{\partial w} = \frac{1}{w^2 - 1}\left[w\ell P^m_\ell(w) - (\ell + m) P^m_{\ell-1}(w)\right]. \tag{3.62}$$

Explicit form of the equations

Combining the form of the multipole expansion in Eq. (3.53) with the weak formulation of the BCs for the potential and normal derivative of the potential (times the dielectric

function) on the form of Eq. (3.59) and Eq. (3.61) we obtain respectively

$$\begin{aligned}
&\sum_{\ell'=|m|}^{\ell'\neq 0} \zeta_{\ell\ell'}^{m} R_s^{-\ell'-1} \left[M_{\ell\ell';\,s}^{m;\,(2s-1)}[-\ell'-1](t_r^{(s)})\, A_{\ell' m}^{(2s-1)} - M_{\ell\ell';\,s}^{m;\,(2s+1)}[-\ell'-1](t_r^{(s)})\, A_{\ell' m}^{(2s+1)} \right] \\
&+ \sum_{\ell'=|m|}^{\ell'\neq 0} \zeta_{\ell\ell'}^{m} R_s^{\ell'} \left[M_{\ell\ell';\,s}^{m;\,(2s-1)}[\ell'](t_r^{(s)})\, B_{\ell' m}^{(2s-1)} - M_{\ell\ell';\,s}^{m;\,(2s+1)}[\ell'](t_r^{(s)})\, B_{\ell' m}^{(2s+1)} \right] \\
&\qquad = -\delta_{\ell 0}\delta_{m0}\sqrt{4\pi}\left[\psi_0^{(2s-1)} - \psi_0^{(2s+1)}\right] \\
&\qquad\quad - \delta_{2s-1,1}\left[\int_{\cap_1} \mathrm{d}\Omega\, [Y_\ell^m(\theta,\phi)]^*\, \psi_{\mathrm{inc}}(\mathbf{r})|_{r=R_1} + \int_{\cup_1} \mathrm{d}\Omega\, [Y_\ell^m(\theta,\phi)]^*\, \psi_{\mathrm{tr}}(\mathbf{r})|_{r=R_1}\right]
\end{aligned} \tag{3.63a}$$

and

$$\begin{aligned}
&\sum_{\ell'=|m|}^{\ell'\neq 0} \zeta_{\ell\ell'}^{m} R_s^{-\ell'-2} \left[N_{\ell\ell';\,s}^{m;\,(2s-1)}[-\ell'-1](t_r^{(s)})\, A_{\ell' m}^{(2s-1)} - N_{\ell\ell';\,s}^{m;\,(2s+1)}[-\ell'-1](t_r^{(s)})\, A_{\ell' m}^{(2s+1)} \right] \\
&+ \sum_{\ell'=|m|}^{\ell'\neq 0} \zeta_{\ell\ell'}^{m} R_s^{\ell'-1} \left[N_{\ell\ell';\,s}^{m;\,(2s-1)}[\ell'](t_r^{(s)})\, B_{\ell' m}^{(2s-1)} - N_{\ell\ell';\,s}^{m;\,(2s+1)}[\ell'](t_r^{(s)})\, B_{\ell' m}^{(2s+1)} \right] \\
&\qquad = -\delta_{2s-1,1}\left[\int_{\cap_1} \mathrm{d}\Omega\, [Y_\ell^m(\theta,\phi)]^*\, \varepsilon_1 \partial_r \psi_{\mathrm{inc}}(\mathbf{r})|_{r=R_1} \right. \\
&\qquad\qquad \left. + \int_{\cup_1} \mathrm{d}\Omega\, [Y_\ell^m(\theta,\phi)]^*\, \varepsilon_2 \partial_r \psi_{\mathrm{tr}}(\mathbf{r})|_{r=R_1}\right],
\end{aligned} \tag{3.63b}$$

where $\ell = 0, 1, \ldots$; $m = 0, \pm 1, \ldots, \pm\ell$; and $s = 1, 2, \ldots, S$.

The first term on the right-hand side of Eq. (3.63a) was obtained by realizing that $\psi_0^{(2s\pm1)}$ are constant potentials. Thus, with the orthonormality condition for the SH given in Eq. (3.19) we have

$$\int_{\bigcirc_s} \mathrm{d}\Omega\; [Y_\ell^m(\theta,\phi)]^* \psi_0^{(2s\pm1)} = \delta_{\ell 0}\delta_{m0} \frac{\psi_0^{(2s\pm1)}}{Y_0^0(\theta,\phi)} = \delta_{\ell 0}\delta_{m0}\sqrt{4\pi}\psi_0^{(2s\pm1)}, \tag{3.64}$$

where the symbol $\bigcirc_s$ denotes the whole spherical surface s [$\bigcirc_s = \cap_s + \cup_s$]. In the last transmission of this equation we have used that $Y_0^0(\theta,\phi) = 1/\sqrt{4\pi}$, as stated in Table 3.1.

The linear system of equations given in Eq. (3.63) for the determination of the set of expansion coefficients $\{A_{\ell m}^{(i)}, B_{\ell m}^{(i)}\}$ is valid for any form of the incident field. However, an explicit form of the incident field is needed to have a well-defined system of equations. Also, the constants $\psi_0^{(2s\pm1)}$, must be determined.

Determining the constant potential

In Eqs. (3.28a)-(3.28b) we found that with a plane wave illumination of the incident electric field the corresponding incoming potential was

$$\psi_{\mathrm{inc}}(\mathbf{r}) = -rE_0\sqrt{\frac{2\pi}{3}}\left\{\sqrt{2}\cos\theta_0 Y_1^0(\theta,\phi) + \sin\theta_0\left[\exp(\mathrm{i}\phi_0)Y_1^{-1}(\theta,\phi) - \exp(-\mathrm{i}\phi_0)Y_1^1(\theta,\phi)\right]\right\}, \tag{3.65a}$$

and the potential of transmission was

$$\begin{aligned}\psi_{\mathrm{tr}}(\mathbf{r}) = E_0 \Bigg[& d\left(\frac{\varepsilon_1}{\varepsilon_2} - 1\right)\cos\theta_0 \\ & -r\sqrt{\frac{2\pi}{3}}\left\{\sqrt{2}\frac{\varepsilon_1}{\varepsilon_2}\cos\theta_0 Y_1^0(\theta,\phi)\right. \\ & \left. +\sin\theta_0\Big[\exp(\mathrm{i}\phi_0)Y_1^{-1}(\theta,\phi) - \exp(-\mathrm{i}\phi_0)Y_1^1(\theta,\phi)\Big]\right\}\Bigg]. \end{aligned} \tag{3.65b}$$

To do the calculations of the right-hand sides in Eq. (3.63) we recall that for the surface $s = 1$ we have $R^{(s)} = R \equiv R^1$ and $t_r^{(s)} = t_r \equiv t_r^{(1)}$. We can then define the relations

$$\begin{aligned}&\int_{\cap_1} \mathrm{d}\Omega\ [Y_\ell^m(\theta,\phi)]^*\,\psi_{\mathrm{inc}}(\mathbf{r})|_{r=R} + \int_{\cup_1} \mathrm{d}\Omega\ [Y_\ell^m(\theta,\phi)]^*\,\psi_{\mathrm{tr}}(\mathbf{r})|_{r=R} \\ &\quad = -\delta_{m0}\sqrt{\frac{4\pi}{3}}E_0 R\cos\theta_0\left[\frac{\varepsilon_2-\varepsilon_1}{\varepsilon_2}\left\{\sqrt{3}t_r\left[\delta_{\ell 0} - \zeta_{\ell 0}^0 I_{\ell 0}^0[0|0](t_r)\right] + \zeta_{\ell 1}^0 I_{\ell 1}^0[0|0](t_r)\right\}\right. \\ &\qquad\qquad \left. +\delta_{\ell 1}\frac{\varepsilon_1}{\varepsilon_2}\right] \\ &\quad -\delta_{\ell 1}\sqrt{\frac{2\pi}{3}}E_0 R\sin\theta_0\left[\delta_{m,-1}\exp(\mathrm{i}\phi_0) - \delta_{m1}\exp(-\mathrm{i}\phi_0)\right] \end{aligned} \tag{3.66a}$$

and

$$\begin{aligned}&\int_{\cap_1} \mathrm{d}\Omega\ [Y_\ell^m(\theta,\phi)]^*\,\varepsilon_1\partial_r\psi_{\mathrm{inc}}(\mathbf{r})|_{r=R} + \int_{\cup_1} \mathrm{d}\Omega\ [Y_\ell^m(\theta,\phi)]^*\,\varepsilon_2\partial_r\psi_{\mathrm{tr}}(\mathbf{r})|_{r=R} \\ &\quad = -\delta_{\ell 1}\delta_{m0}\sqrt{\frac{4\pi}{3}}E_0\varepsilon_1\cos\theta_0 \\ &\qquad +\sqrt{\frac{2\pi}{3}}E_0(\varepsilon_2-\varepsilon_1)\sin\theta_0\Big[\delta_{m,-1}\exp(\mathrm{i}\phi_0)\zeta_{\ell 1}^{-1}I_{\ell 1}^{-1}[0|0](t_r) \\ &\qquad\qquad -\delta_{m1}\exp(-\mathrm{i}\phi_0)\zeta_{\ell 1}^1 I_{\ell 1}^1[0|0](t_r)\Big] \\ &\qquad -\delta_{\ell 1}\sqrt{\frac{2\pi}{3}}E_0\varepsilon_2\sin\theta_0\left[\delta_{m,-1}\exp(\mathrm{i}\phi_0) - \delta_{m1}\exp(-\mathrm{i}\phi_0)\right], \end{aligned} \tag{3.66b}$$

where again the orthogonality conditions of the SH in Eq. (3.19) and the predefined integrals from the last section have been used.

In the limit, $t_r \to 1$, where the particles are starting to just touch the substrate's surface, it is readily demonstrated that the right-hand sides of Eqs. (3.66a)-(3.66b) are independent of ε_2, as they should. This is shown with the identity $I_{\ell\ell'}^m[0|0](1) = \delta_{\ell\ell'}/\zeta_{\ell\ell'}^m$, which is a consequence of Eq. (3.19).

The expressions obtained in Eq. (3.66) are identical to the expressions obtained when the particles are hovering above the surface of the substrate (so that the spherical surface $s = 1$ is not truncated). To automatically also deal with the situation where the particles are located a certain distance above the substrate's surface the term, t_r should be replaced by $\hat{t}_r = \min(t_r, 1)$ in Eq. (3.66).

The constant potentials $\psi_0^{(2s\pm1)}$ that appear in Eq. (3.63a) are generally obtained with the relations

$$\begin{aligned}
&\psi_0^{(2s-1)} - \psi_0^{(2s+1)} = \\
&\frac{1}{\sqrt{4\pi}} \Bigg\{ \sum_{\ell'=|m|}^{\ell'\neq 0} \zeta_{0\ell'}^0 R_s^{-\ell'-1} \left[M_{0\ell';\,s}^{0;\,(2s-1)}[-\ell'-1](t_r^{(s)})\, A_{\ell'0}^{(2s-1)} - M_{0\ell';\,s}^{0;\,(2s+1)}[-\ell'-1](t_r^{(s)})\, A_{\ell'0}^{(2s+1)} \right] \\
&\qquad + \sum_{\ell'=|m|}^{\ell'\neq 0} \zeta_{0\ell'}^0 R_s^{\ell'} \left[M_{0\ell';\,s}^{0;\,(2s-1)}[\ell'](t_r^{(s)})\, B_{\ell'0}^{(2s-1)} - M_{0\ell';\,s}^{0;\,(2s+1)}[\ell'](t_r^{(s)})\, B_{\ell'0}^{(2s+1)} \right] \\
&\qquad + \delta_{2s-1,1} \left[\int_{\cap_1} \mathrm{d}\Omega\, [Y_0^0(\theta,\phi)]^*\, \psi_{\mathrm{inc}}(\mathbf{r})|_{r=R_1} + \int_{\cup_1} \mathrm{d}\Omega\, [Y_0^0(\theta,\phi)]^*\, \psi_{\mathrm{tr}}(\mathbf{r})|_{r=R_1} \right] \Bigg\}.
\end{aligned} \tag{3.67}$$

For the case of a uncoated truncated spherical particle with $s = 1$ (as studied in this chapter) the potential $\psi_0^{(3)}$ is given as

$$\begin{aligned}
&\psi_0^{(3)} = \\
&\frac{1}{\sqrt{4\pi}} \Bigg\{ \sum_{\ell'=|m|}^{\ell'\neq 0} \zeta_{0\ell'}^0 R_s^{-\ell'-1} \left[M_{0\ell';\,1}^{0;\,(1)}[-\ell'-1](t_r)\, A_{\ell'0}^{(1)} \right] + \sum_{\ell'=|m|}^{\ell'\neq 0} \zeta_{0\ell'}^0 R_s^{\ell'} \left[M_{0\ell';\,1}^{0;\,(1)}[\ell'](t_r)\, B_{\ell'0}^{(3)} \right] \\
&\qquad + \sqrt{\frac{4\pi}{3}} E_0 R \cos\theta_0 \left[\frac{\varepsilon_2 - \varepsilon_1}{\varepsilon_2} \left\{ \sqrt{3} t_r \left[1 - \zeta_{00}^0 I_{00}^0[0|0](t_r) \right] + \zeta_{01}^0 I_{01}^0[0|0](t_r) \right\} \right] \Bigg\}.
\end{aligned} \tag{3.68}$$

This result is consistent with the expressions of the constant term b_0 given by Simonsen and co-workers in [46].

Summary of the calculations

Combining the relations given in Eqs. (3.64)-(3.68) and inserting them into Eq. (3.63), we finally obtain the linear system of equations that can be used to determine the set of multipole expansion coefficients $\{A_{\ell m}^{(i)}, B_{\ell m}^{(i)}\}$ for $i = 1, 3$. It is convenient to multiply Eq. (3.63a) by $1/R_s$ to obtain the final form of this linear system. This has been done in writing the linear matrix system in Eq. (3.32) for the truncated uncoated sphere.

Chapter 4

The GranFilm software

The GranFilm software is designed to efficiently calculate the optical properties of thin films [57] containing supported islands whose typical dimensions (size/spacing) are much smaller than the wavelength. In this chapter, we discuss the software architecture and give a user guide to launch a GranFilm simulation. The additional functionality of automatic correction of the material's bulk dielectric function with respect to finite-size and surface effects, and the algorithm used to fit experimental data will be described. Finally, to illustrate the potential of GranFilm, we present and comment on some simulation results.

Contents

Figure 4.1 A flowchart of the most important steps in a GranFilm simulation. The definition of the system geometry and the allocation of arrays are performed in the initialization process. Next, all the required micro- and macroscopic quantities are calculated in the step Run_GranFilm. The finalization process writes the simulation result to files. If fitting of experimental data is required, the model parameters are adjusted in the step Run_GranFilm until a χ^2-minimization criterion is reached.

4.1 Software architecture

The success of GranFilm as a simulation tool for the optical properties of supported granular films is its capability to connect the micro- and macroscopic properties of a system at a low computational cost. As discussed in Chs. 2-3, the mathematical foundation of GranFilm is based on an effective boundary condition approach. Originally the formalism was developed by Bedeaux and Vlieger in the first half of the 1970s [41]. Since the publication of this seminal work, with the help of several other authors, they have further refined and extended the formalism [37, 46, 48–50]. Much of these efforts are collected in the book *Optical Properties of Surfaces* authored by Bedeaux and Vlieger. It was published in its second edition in 2004 [5].

I. Simonsen and R. Lazzari developed the first version of the software package GranFilm. It was published in 2002; the code dealt with truncated spherical and spheroidal nanoparticles placed on a substrate [56]. Since 2010, its original authors have implemented a complete and more efficient version through several common projects and master thesis works.

As of today, the code written in Fortran consists of several thousand lines of code. The package can treat interacting truncated coated spherical and spheroidal supported particles. Extra features like calculating the electrostatic potential around an island, automatic corrections of the bulk dielectric function with respect to finite-size and surface effects, and fit of experimental data have been integrated into the original framework. For better user experience, a GranFilm Python interface with tutorials has been developed.

A flowchart of the most prominent steps in a GranFilm simulation is presented in

Fig. 4.1. The calling sequence in a typical GranFilm simulation starts with the definition of the system geometry, given by a set of input parameters. These parameters are sent to the code via the namelist functionality of Fortran. All physical parameters are internally made dimensionless before the calculation starts. When the GranFilm object has been properly allocated, the integrals over the particle surface, given in Eqs. (3.59)-(3.61), are evaluated using the QAG-routine from the QUADPACK library. This set of routines implement an adaptive Gauss-Kronrod quadrature algorithm with an automatic sub-interval division to reduce the overall error above a given threshold. The default of accepted values of the relative and absolute error of the integrals are 1.0e−5 and 1.0e−4, respectively. Since the integrals depend on the geometry of the system (mainly the truncation of particles), they have to be recalculated for spheres, spheroids, and coated particles. Hence, this step is among the most time-consuming calculation process in GranFilm.

Next, the dimensionless multipole coefficients are calculated by solving the linear system of equations in Eq. (3.63) to a given finite multipole order M. The corresponding linear system of equations implicitly depends on the dielectric functions of the different materials. The linear system of equations are solved with routines in the LAPACK library. The CGETRF/ZGETRF (single/double precision) routines are used for *lower-upper* (LU) decomposition and the CGETRS/ZGETRS routines for the back substitution. Thereupon, the island polarizabilities are obtained from the multipole coefficients as stated in Eq. (3.35). The obtained polarizabilities can latter be corrected to dipolar or quadrupolar order from the island-island interactions and/or averaged over a given size/shape distribution by looping over the previous steps. From these average island polarizabilities, the island film layer's surface susceptibilities can be obtained from the expressions in Eq. (3.36). Finally, physical observables deriving from the Fresnel coefficients Eq. (2.27) (*e.g.* transmissivity, reflectivity, differential reflectivity) can be obtained.

Once the multipole coefficients have been calculated, the electrostatic potential in any region inside and outside of the particle can be obtained through the relation in Eq. (3.13) (applications of this functionality will be given in Ch. 5). The eigenvalues and/or eigenvalues of the equation matrix system are then found with the CGEEV/ZGEEV (single/double precision) routines in LAPACK. With this functionality, the near-field behavior can be studied over a grid of points specified by the user in an additional input file.

Beyond the convergence of the polarizabilities themselves, the electrostatic potential can be used to control the accuracy of BCs on both sides of an interface. One should keep in mind that a build-up of the matrix system is based on a projection of the continuous BC over the complete basis of spherical/spheroidal harmonics; its truncation to a given multipolar order is merely a numerical issue.

Before concluding, one should always make sure that increasing the value of M does not alter the simulation results in a significant manner. In particular, the speed of convergence depends critically on the target quantity. Typically, far field quantities like Fresnel coefficients (and incidentally the polarizabilities), converge more rapidly than near field quantities like the potential close to the particle.

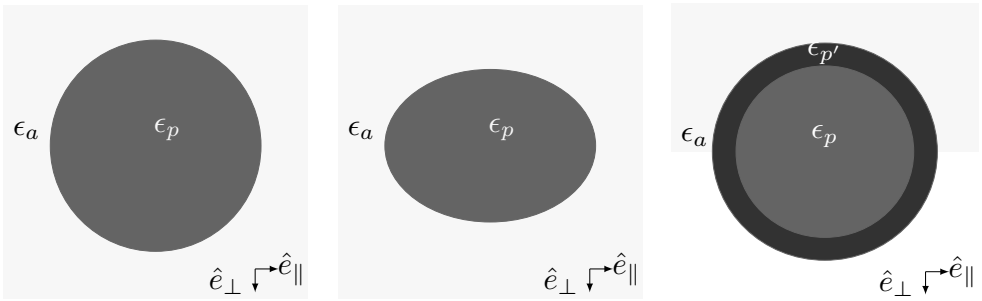

(a) Sphere. **(b)** Spheroid. **(c)** Coated particle.

Figure 4.2 Supported geometries in GranFilm. The particles can be shaped like either a sphere (a) or spheroid (b) with an eventual layer(s) of concentric coating(s) (c).

4.2 A user guide

This section is meant as a short user guide for the needed know-how to run a GranFilm simulation. We will discuss available geometries, the most important input parameters, the limitations of the software, and the GranFilm Python interface.

4.2.1 Accessible geometries

The underlying mathematics, described in detail in Chs. 2-3, restricts the shapes of the particles to truncated spheres or spheroids. The reason lies in the expansion of the Laplace's equation Eq. (3.12) in terms of a multipolar basis that is readily available for spheres and spheroids. In the new version of GranFilm, particles can also be coated with an arbitrary number of concentric layers of different materials. The particle geometries supported by GranFilm are illustrated in Fig. 4.2.

4.2.2 Input parameters

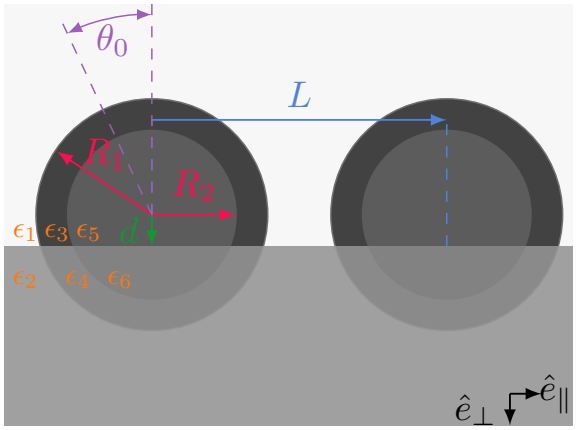

Figure 4.3 The most important parameters needed to define the system in a GranFilm simulation: angle of incidence θ_0, lattice constant L, radii R_i, distance to the substrate d, and materials ε_i.

The geometry of the islands, their arrangement on the surface of the substrate, their interaction with the nearest neighbors, and the values for parameters controlling how

the numerical calculations are performed are all part of the input parameters required by GranFilm. Default values are set if these parameters are not explicitly modified by the user in the input file (see the documentation for a complete description [57]).

An illustration of a typical system with the parameters required in a GranFilm simulation are presented in Fig. 4.3. A complete example of all the namespaces in the GranFilm Fortran input file is given in App. C.

The input parameters are organized into groups of Fortran namelists. These are named *Global*, *Source*, *Geometry*, *Interaction*, *Numerics*, and *Potential* and will be described in the following.

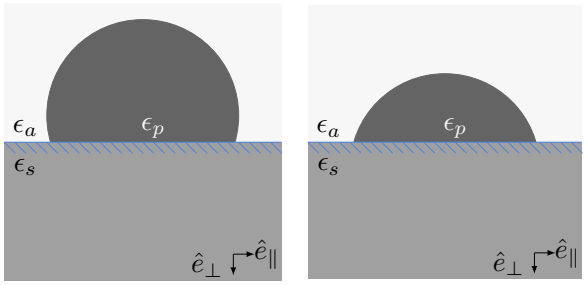

(a) $t_r > 0$. **(b)** $t_r < 0$.

Figure 4.4 The truncation ratio parameter, t_r, decides if the center of the particle is located (a) above or (b) below the surface of the substrate.

The *Global* namelist sets the needed paths to link the executable file with the database containing the experimental values of the bulk material permittivities. The *Source* group defines the angles of incidence θ_0, ϕ_0, the polarization state of light, and the energy range of interest.

The *Geometry* group defines the geometry of the isolated particle. Required parameters of this type are:

- The particle radii parallel $R_\parallel$ and perpendicular $R_\perp$ to the surface of the substrate. A spherical particle is modeled when $R_\parallel = R_\perp$. The spheroid and the sphere cases are treated with separate equation systems.
- The truncation ratio, t_r, characterizes how much of the island that is truncated by the substrate (see Fig. 4.4). In the range $0 < t_r < 1$ ($-1 < t_r < 0$, respectively) the center of the particle lies above (below, respectively) the surface of the substrate[1]. If $t_r = 0$, the particle has been truncated at the center. The distance d from the center of the particle to the substrate is derived from the relation $d = t_r R_\perp$.
- The dielectric functions ε_i of the materials in region i of the system (the superstrate, substrate, and particles etc.).

Furthermore, the *radius ratios* and the *broadening* are optional parameters of the geometry group.

To simulate the response of a particle with coatings, the thickness of each layer is defined by the (dimensionless) radius ratio $\chi^{(s)} = R_\perp^{(s)}/R_\perp^{(1)}$ where $s \in \{1, \ldots, S\}$.

[1] Please note that in the current version of the software the multipole position of the direct dipole must always be placed above the substrate

The numbering of the surfaces starts from the outermost one, for which $s = 1$ and $\chi^{(1)} = 1.0$. When all radius ratios are set, the radii and truncation ratio associated with the relevant surface s are defined as $R_{\perp}^{(s)} = \chi^{(s)} R_{\perp}^{(1)}$, $R_{\parallel}^{(s)} = \chi^{(s)} R_{\parallel}^{(1)}$, and $t_r^{(s)} = t_r^{(1)}/\chi^{(s)}$, respectively.

In a SDRS experiment, the particles will always be distributed in both size and shape (aspect ratio). The distribution of the particles will result in what is known as the *experimental broadening* of the plasmon resonance. A classical GranFilm simulation is preformed in a monodisperse system, *i.e.* all particles are identical. The broadening parameters σ_i, $i = \parallel, \perp$, are used to add an 'ad hoc' broadening of the plasmon resonance in the simulations. The broadening are added to the input-file with the keyword 'Broadening'. This inhomogeneous broadening of the monodisperse absorption peak $\mathrm{Im}\{\alpha_i(\omega)\}$ is accounted for by a convolution the monodisperse result with a Gaussian of width σ_i [42, 58]

$$\langle \mathrm{Im}\{\alpha_i\} \rangle = \frac{1}{\sigma_i \sqrt{2\pi}} \int_{\omega_1}^{\omega_2} \mathrm{d}\omega' \mathrm{Im}\{\alpha_i(\omega')\} \mathrm{e}^{-(\omega'-\omega)/2\sigma_i^2}, i = \parallel, \perp. \tag{4.1}$$

Several phenomena contribute to the experimental broadening. These will be discussed further in Ch. 6.

The parameters in the *Interaction* group control the particles' arrangement on the substrate and how they interact with each other. The distance between the particles is set with the lattice constant L. A GranFilm simulation will assume that the supported particles are arranged in either a *regular* or a *random two-dimensional* (2D) lattice. Currently, the types of regular lattices supported by the software package are *square* or *hexagonal* lattices. These have only one particle per unit cell. The random lattice is defined by an *equivalent* surface coverage Θ_{rand} as if the particles were organizes in a square or hexagonal lattice (see Sec. 3.5.2). This configuration has an average number of particles per unit surface area. Once the single particle polarizabilities, originating from the electrostatic interaction between the single particle and the substrate, have been calculated they are corrected (or not) by the island-island interactions of dipolar or quadrupolar order. To do so, the coupling is evaluated through the lattice sums or distribution integrals described in Sec. 3.5. The interaction is controlled at will by the *island-island interaction* parameter. It can be set to either *None*, *Dipole*, or *Quadrupole*.

The discretization in energy, the number of multipoles M, and the unitless position of the multipoles relative to the center of the reference particle, the multipole position ratio $\mu = z_{mp}/R_{\perp}$, are some of the parameters in the *Numerics* namelist. The parameters M and μ have the greatest impact on the convergence of the simulation result[2], although the contrasts of the different dielectric materials in the system also play a role.

[2] In Ch. 6 a polydispersity in the size/shape of the particles will be introduced. We will see that one must pay attention when choosing the multipole position ratio parameter if one wishes to compare the simulation results obtained in different systems.

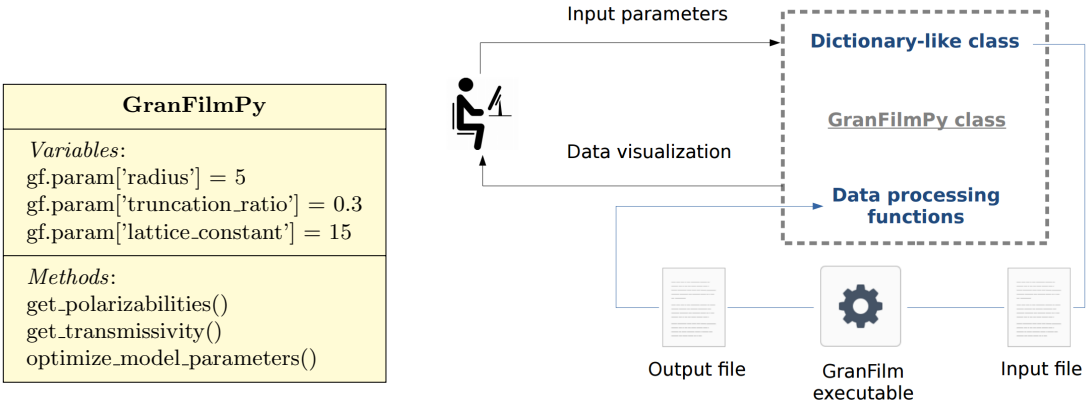

(a) A schematic of the GranFilmPy-class containing variables and functions for smooth user experience.

(b) Calling sequence between the Python interface and the Fortran code of GranFilm. In courtesy of Alexis Cvetkov-Iliev.

Figure 4.5 A schematic illustration of the GranFilmPy class (a) and the sequence to launch a GranFilm simulation from the Python interface (b).

4.2.3 Limitations of the software

Beyond numerical issues, the limitations of a GranFilm simulation are defined by the theoretical framework's approximations. Of these, the most critical one is the assumption that the island's size and the typical distance between the islands should remain much smaller than the wavelength of the incoming field. When these assumptions breakdown neither the *excess field* formalism nor the quasi-static approximation is valid [41].

If the wavelength of the incoming field is of the same order of magnitude as the distance L between the particles, the system may/will suffer from *second order scattering* or *diffraction* [59]. This phenomenon is not included in the present framework and other methods have to be used to account for them [60].

Also, the value of the surface density Θ, also known as the packing fraction of the particles, is limited because the island-island interaction is taken into account only to low order in GranFilm. Depending on geometry and dielectric functions, a discrepancy between dipolar and quadrupolar (or multipolar in the case of the full supported sphere [46]) interactions start appearing at a coverage above $\sim 50-60\%$. Anyway, in the case of random growth this threshold corresponds experimentally to the beginning of percolation. Where we know that the GranFilm approximations breakdown [53].

4.2.4 The GranFilm Python interface

To simplify the use and increase the potential number of users of GranFilm, a Python interface to the Fortran source code has been developed. For someone without a background in Fortran, the direct use and compilation of the GranFilm source code require some time investment. Fortran is a compiled imperative programming language that

```
system1 = GranFilmPy.GranFilm() # Initialize a new system.
# --- Configure the system
system1.param["radius"] = 6 # radius of the whole particle = 4 + 2 = 6 nm
system1.param["radius_ratios"] = [1, 4/6]
system1.param["lattice_constant"] = 15 # distance between 2 particles, in nanometers
system1.param["truncation_ratio"] = 0 # 0 for hemispheres
system1.param["media"] = ['air', 'zno', 'ag2o', 'zno', 'ag', 'zno'] # Materials used in the system
```

Figure 4.6 Setting the most important input parameters in the GranFilm Python interface. First, one initializes an instance of GranFilmPy (first line). The following lines demonstrate how the actual input parameter can be changed (or set) by calling the param-dictionary of the instance.

is not commonly used outside academia, in particular in the community of engineers. Moreover having a Python interface available for GranFilm also open up for scripting capabilities and making further analysis of the obtained simulation results more convenient. With this interface, a user can access the original functionality of the software without directly interacting with the Fortran code. The interface is essentially a Python class [see Fig. 4.5(a)], called GranFilmPy, with several variables and methods. A compiled executable of the GranFilm software[3] and installation of the GranFilmPy-class is all that is needed to run a simulation. The class methods take care of generating a valid input file, run the simulation, and automatically read the output files and save the results in the GranFilmPy instance. An illustration of the calling sequence used in the GranFilm Python interface is presented in Fig. 4.5(b).

All input parameters required to run a simulation with the GranFilm Python interface are set with Python dictionaries. An example of how the most important parameters can be set using the Python interface is given in Fig. 4.6. If the user does not explicitly change the input parameters, most of them will be given default values. A full tutorial with examples detailed in the notebooks *Tutorial_GranFilm.ipyb*, *Advanced_Functionalities.ipyb*, and *Theoretical_Aspects.ipyb* has been written to describe the use and capabilities of the Python interface of GranFilm. The GranFilm Python interface and documentation are currently available on demand.

4.3 Additional functionality

As GranFilm is designed to deliver fast and reliable simulations that can accompany the results of an experiment two additional functionalities are of great practical use. The following subsections will detail how material permittivity corrections and fitting of experimental data can be performed with GranFilm.

[3]This executable must be compatible with the user's operative system. Currently, the GranFilm software is compiled for Windows, Mac, and Linux.

Table 4.1 Skin depth ℓ_δ as a function of the photon energy and the bulk mean free paths l_∞ of the conduction electrons at 273 K [12, Table (2.3), Ch. 2].

Element	l_∞[nm]	ℓ_δ[nm]		
		2[eV]	3[eV]	4[eV]
Au	42	31	37	27
Ag	52	24	29	82

Table 4.2 Explicit units and typical values of the parameters for a hemisphere of a silver particle in Eqs. (4.2)-(4.4). Some of these variables are also input parameters to GranFilm (values for a silver hemisphere given in the last row).

Parameter	ε	$\hbar\omega_p$	$\hbar\Gamma_\infty$	$\hbar\omega$	Σ	B	A	V	$\hbar v_F$	D_{eff}	C
Unit	1	eV	eV	eV	eV^2	$\text{eV}^2\,\text{nm}$	nm^2	nm^3	eV nm	nm	1
Value	–	9.17	0.018	–	–	−1.13	–	–	0.91	–	0.6

4.3.1 Material permittivity corrections with GranFilm

In metals, the skin depth ℓ_δ is dependent on the energy of the incoming EM-field[4]. Furthermore, in the classical theory of free-electron metals, the damping frequency of the oscillating electrons in the bulk material Γ_∞ originates from the scattering with phonons and electrons, lattice defects, or impurities of the material. Due to the finite dimension of a granular thin film or a *nanoparticle* (NP), the damping of the electrons in the material become comparable to the electron mean free path l_∞. Thus, in cases where the material volume is limited the dielectric function is a subject of the so-called *intrinsic size effects* due to the changes of the atomic structure or the influence of NPs on the surface (increased localization of electrons). When ℓ_δ is of the order of the particle size, experimental results indicate that the direct use of the bulk permittivity breakdowns [12]. Table 4.1 reports the skin depth as a function of the photon energy compared to the bulk mean free path for gold and silver, two well-known plasmonic materials.

GranFilm does not model the bulk dielectric functions used in a simulation, but interpolates rather over the values taken from an experimental database[5]. A well-known solution to circumvent the issue of the finite sized particles is to apply correction on the bulk permittivity [58]. A specific routine has been added in the flow chart of the GranFilm software just after the initialization step (see Fig. 4.1). The correction types involve the *finite size correction* and the *surface correction*, as detailed below. A description of how to enables these corrections with the GranFilm Fortran input file is given in App. C, Sec. C.2.1.

[4] Remember from Ch. 1 that the skin depth is related to the imaginary part of the complex refractive index by the relation $\ell_\delta = 1/b$, $b = 4\pi\hat{k}(\omega)/\lambda$, $\hat{k}(\omega)$ provides the damping factor of a plane wave, traveling in the x-direction given as $\mathbf{E}(x,t) = E_0 e^{i[\omega\tilde{n}(\omega)x/c-\omega t]} e^{-(\omega\tilde{k}_x(\omega)x/c)}$

[5] See Appendix A for plots of the relevant bulk dielectric functions used in this work.

Finite size correction

A finite size correction of the permittivity is necessary when the skin depth of the incoming field is of the same order of magnitude as the bulk mean free path of conduction electrons. Because the scattering by the surface of the particle comes into play in the damping mechanism of the oscillating electrons, the correction consists in scaling the corresponding damping on an effective conduction length D_{eff} [12]. This finite size correction of the Drude part of $\varepsilon_B(\omega)$ in Eq. (1.25)
yields [12, Ch. 2, Eq. (2.53)] reads

$$\begin{aligned}\varepsilon_P^{FS}(\omega, D_{eff}) &= \varepsilon_B(\omega) - \varepsilon_D(\omega) + \varepsilon_D^{FS}(\omega, D_{eff}) \\ &= \varepsilon_B(\omega) - \left(1 - \frac{\omega_p^2}{\omega(\omega + i\Gamma_\infty)}\right) + \left(1 - \frac{\omega_p^2}{\omega(\omega + i\Gamma(D_{eff}))}\right) \\ &= \varepsilon_B(\omega) + \frac{\omega_p^2}{\omega(\omega + i\Gamma_\infty)} - \frac{\omega_p^2}{\omega(\omega + i\Gamma(D_{eff}))},\end{aligned} \tag{4.2}$$

where, again, ω_p denotes the co-called plasma frequency, and Γ_∞ is the damping frequency for the bulk material. The term $\Gamma(D_{eff})$ denotes the size dependent damping frequency and is determined from the relation

$$\begin{aligned}\Gamma(D_{eff}) &= \Gamma_\infty + \Delta\Gamma(D_{eff}), \\ &= \Gamma_\infty + C\frac{v_F}{D_{eff}}.\end{aligned} \tag{4.3}$$

The quantity C that appears in this expression is a dimensionless (Table 4.2) and theory dependent constant for a given metal[6] and v_F is the Fermi velocity of the *s*-electrons. Although this scattering effect of electrons at interfaces is highly anisotropic for a truncated and supported particle, only an isotropic correction is implemented in GranFilm. Appendix 4.A discusses how the effective length D_{eff} is defined for the different GranFilm geometries. The account of this effective length turns out to be essential in data analysis [58, 61] as it introduces a size-dependent broadening of the plasmon resonances.

Surface correction

Particularly in bulk silver, the free *sp*-conduction electrons are strongly screened by the more localized *d*-electrons. Therefore, the bulk plasma frequency is strongly downshifted from that of the Drude component of the dielectric function from around 9 eV to around 3.8 eV. But at surfaces, during the plasmon oscillation, this screening is reduced due to the spatial localization of *d*-electrons; *sp*-electrons recover their slightly Drude-like character. This effect, called *quantum blueshift*, depends on the ratio between surface and volume and, therefore, on the particle size. Again, starting with the bulk dielectric function, the Drude part of the dielectric function will be corrected

[6] The constant C often has a value that is close to one [12, Ch. 2, Eq. (2.53)].

as [58, 62, 63]:

$$\begin{aligned}\varepsilon_P^S(\omega,\Sigma) &= \varepsilon_B(\omega) - \varepsilon_D(\omega) + \varepsilon_D^S(\omega,\Sigma) \\ &= \varepsilon_B(\omega) + \frac{\omega_p^2}{\omega(\omega+i\Gamma_\infty)} - \frac{\omega_p^2}{\omega(\omega+i\Gamma_\infty)+\Sigma}.\end{aligned} \tag{4.4}$$

where $\Sigma = B(A/V)$ is a geometry dependent parameter, B is a material dependent constant, A and V are the surface and the volume of the particle. Appendices 4.B-4.C discuss how the particle volume and surface area are calculated for the different geometries. The units of the parameters as they must be given to GranFilm are presented in Table 4.2.

Finite size and surface correction

When the finite size and the surface corrections described in Eqs. (4.2)-(4.4) both are active, the combined corrections performed on the Drude part of the bulk permittivity given in Eq. (1.25) becomes [58, Sec. 3.4, Eq. (4)]

$$\begin{aligned}\varepsilon_P^{FS,S}(\omega,D_{eff},\Sigma) &= \varepsilon_B(\omega) - \varepsilon_D(\omega) + \varepsilon_D^{FS,S}(\omega,D_{eff},\Sigma) \\ &= \varepsilon_B(\omega) + \frac{\omega_p^2}{\omega^2+i\omega\Gamma_\infty} - \frac{\omega_p^2}{\omega\left(\omega+i\Gamma(D_{eff})\right)+\Sigma}.\end{aligned} \tag{4.5}$$

4.3.2 Fit of experimental data and parameter estimation with GranFilm

GranFilm simulations can be used to extract information regarding morphology from optical measurements. By comparing, *e.g.* a *Surface Differential Reflectivity Spectroscopy* (SDRS) measurement and a modeled differential reflectivity curve, one can extract detailed information about the evolution of size, shape, and density of particles all along a growth process [61]. Such nanoscale information is rather difficult to obtain from real-time microscopies.

A routine for fitting experimental data to the theoretical curves calculated with GranFilm has been integrated into the framework. This problem was recast into the minimization of a least-squares cost function with the *Levenberg-Marquardt* (LM) algorithm. We account for constraints on the model parameters via the *MINUIT* transformation. The obtained uncertainties on the model parameters are based on a linearization of the Hessian matrix.

The optimization feature is offered via a generic class structure around LMDIF, an optimization routine from the well-established MINPACK library written in Fortran [64]. The class structure handles the constraints on the model parameters and error estimation. The reason for choosing a Fortran implementation instead of a Python equivalent from the user interface is due to the significantly better numerical efficiency of the Fortran language. To obtain a fit of the experimental data the Run_GranFilm step in the calling sequence for GranFilm is looped over until a minimization criterion is reached [see Fig. 4.1]. The user must provide the experimental data set, an initial guess of the model parameters, and an observable type, like a reflection or transmission spectra. If the user does not provide the limits of the fitting parameters, a set of default values

Table 4.3 Parameters that can be fitted with the GranFilm software for a given experimental data set. The values specified for ℓ^{min} and ℓ^{max} correspond to the default values of the lower and upper bounds.

Parameter	ℓ^{min}	ℓ^{max}
$R_{\parallel}^{(1)}$	0	$L/2$
$R_{\perp}^{(1)}$	0	$3L$
$R_{\parallel}^{(s)}$, $s \in \{2, ..., S\}$	$R_{\parallel}^{(s+1)}$	$R_{\parallel}^{(s-1)}$
$R_{\perp}^{(s)}$, $s \in \{2, ..., S\}$	$R_{\perp}^{(s+1)}$	$R_{\perp}^{(s-1)}$
L	$2R_{\parallel}^{(1)}$	∞
t_r	-1	1
$\sigma_{\parallel}$	0	∞
$\sigma_{\perp}$	0	∞

consistent with the logic of the system geometry will be assumed. The possible fitting parameters and their default limits are presented in Table 4.3. An example of how to enable the fitting functionality with the GranFilm Fortran input file is given in App. C, Sec. C.2.3.

This section details the chosen solver and how to use the functionality within GranFilm. As optimization methods are a complex field in itself, we will mainly present the ideas behind the implementation rather than the full details of the chosen algorithm. For a detailed introduction to optimization routines, we invite the reader to look into the excellent texts in [65, 66].

Objective function

Given a known set of abscissa values with corresponding ordinates and uncertainties, respectively denoted $x_i, y_i = f(x_i)$, and σ_i, where $i \in \{1, ..., m\}$, we seek an optimal set of model parameters $\boldsymbol{\mathcal{P}} = \{p_j\}$, $j \in \{1, ..., n\}$ for which the model ordinate $\hat{f}(x_i|\boldsymbol{\mathcal{P}})$ fairly accurately reproduces the ordinate $y_i = f(x_i)$.

In the case of least-square optimization, the condition

$$\begin{aligned} \chi^2(\boldsymbol{\mathcal{P}}) &= \frac{1}{2}\sum_{i=1}^{m}\left[\frac{f(x_i) - \hat{f}(x_i|\boldsymbol{\mathcal{P}})}{\sigma_i}\right]^2 \\ &= \frac{1}{2}\sum_{i=1}^{m}\left[r_i(\boldsymbol{\mathcal{P}})\right]^2, \end{aligned} \tag{4.6}$$

where $r_i(\boldsymbol{\mathcal{P}})$ is a component in the residual vector $\mathbf{r}(\boldsymbol{\mathcal{P}}) = [r_1(\boldsymbol{\mathcal{P}}), ..., r_m(\boldsymbol{\mathcal{P}})]^{\mathrm{T}}$. Note that σ_i works as a weighting term for the residual r_i. Thus, Eq. (4.6) can equivalently be represented as

$$\chi^2(\boldsymbol{\mathcal{P}}) = \frac{1}{2}\mathbf{r}^{\mathrm{T}}(\boldsymbol{\mathcal{P}})\mathbf{r}(\boldsymbol{\mathcal{P}}). \tag{4.7}$$

The derivatives of Eq. (4.7) can be represented in terms of the Jacobian $\mathbb{J}(\boldsymbol{\mathcal{P}})$, which

is the $n \times m$ matrix of the first order partial derivatives of the residuals

$$\mathbb{J}(\boldsymbol{\mathcal{P}}) = \left[\frac{\partial r_i}{\partial p_j}\right]_{\substack{i=1,\dots,m \\ j=1,\dots,n}} = \begin{bmatrix} \boldsymbol{\nabla}_p r_1(\boldsymbol{\mathcal{P}})^{\mathrm{T}} \\ \boldsymbol{\nabla}_p r_2(\boldsymbol{\mathcal{P}})^{\mathrm{T}} \\ \vdots \\ \boldsymbol{\nabla}_p r_m(\boldsymbol{\mathcal{P}})^{\mathrm{T}} \end{bmatrix}, \tag{4.8}$$

where $\boldsymbol{\nabla}_p$ is the first order partial derivative with respect to the model parameters and each $\boldsymbol{\nabla}_p r_i(\boldsymbol{\mathcal{P}})$ is the gradient of $r_i(\boldsymbol{\mathcal{P}})$. The gradient of Eq. (4.7) can then be expressed as

$$\boldsymbol{\nabla}_p \chi^2(\boldsymbol{\mathcal{P}}) = \sum_{i=1}^{m} r_i(\boldsymbol{\mathcal{P}}) \left[\boldsymbol{\nabla}_p r_i(\boldsymbol{\mathcal{P}})\right] = \mathbb{J}^{\mathrm{T}}(\boldsymbol{\mathcal{P}}) \mathbf{r}(\boldsymbol{\mathcal{P}}). \tag{4.9}$$

Provided that there exists a minimum (local or global) such that Eq. (4.7) is minimized, the gradient in Eq. (4.9) equals zero. For the error analysis, the curvature of $\chi^2(\boldsymbol{\mathcal{P}})$ and therefore, its second derivative is required. The Hessian is a $n \times n$-matrix defined as

$$\begin{aligned} \mathbb{H}(\boldsymbol{\mathcal{P}}) = \boldsymbol{\nabla}_p^2 \left[\chi^2(\boldsymbol{\mathcal{P}})\right] &= \sum_{i=1}^{m} \left[\boldsymbol{\nabla}_p r_i(\boldsymbol{\mathcal{P}})\right] \left[\boldsymbol{\nabla}_p r_i(\boldsymbol{\mathcal{P}})^{\mathrm{T}}\right] + \sum_{i=1}^{m} r_i(\boldsymbol{\mathcal{P}}) \boldsymbol{\nabla}_p^2 r_i(\boldsymbol{\mathcal{P}}) \\ &= \mathbb{J}^{\mathrm{T}}(\boldsymbol{\mathcal{P}}) \mathbb{J}(\boldsymbol{\mathcal{P}}) + \sum_{i=1}^{m} r_i(\boldsymbol{\mathcal{P}}) \boldsymbol{\nabla}_p^2 r_i(\boldsymbol{\mathcal{P}}) \end{aligned} \tag{4.10}$$

With the Hessian on the form given in Eq. (4.10), it means that the first term can be obtained 'for free'. As long as the Jacobian in Eq. (4.9) is obtained one can evaluate the term without calculating any second order derivatives. As long as the Jacobian in Eq. (4.8) is calculated. In cases where $r_i(\boldsymbol{\mathcal{P}})$ is close to a minimum, or typically that the residual is relatively small the $\mathbb{J}^{\mathrm{T}}(\boldsymbol{\mathcal{P}})\mathbb{J}(\boldsymbol{\mathcal{P}})$ term will be the dominant one in Eq. (4.10). These properties of the Hessian are typically exploited by non-linear least-square algorithms to avoid the costly evaluation of the second order derivatives [65].

The Levenberg-Marquardt Algorithm

The LM algorithm, thoroughly described in Refs. 67, 68, is a popular and robust scheme for evaluating non-linear least-squares minimization problems, with objective functions on the form given in Eq. (4.6). The scheme combines the steepest descent with the Gauss-Newton method. The parameter estimates are updated iteratively using a linear solver. In cases where there exist multiple minima of the function, the LM algorithm is not guaranteed to converge towards the global minimum. A global minimum will only be identified if the initial guess happened to be sufficiently close to the optimal parameters.

To obtain a reliable estimate of the model parameters the number of experimental data points m must be (significantly) higher than the number of model parameters n. The parameters in the standard LM algorithm are all assumed to be unconstrained. This means that a given parameter p_j, $j \in \{1, ..., n\}$ may vary in the interval $-\infty < p_j < \infty$. Many physical parameters are naturally restricted to a certain range of values where values outside this range are deemed as non-physical. For instance, the radius of a spherical particle cannot be negative.

Constrained optimization

To perform constrained optimization, where one or several parameters have an upper and/or lower bound $\ell_j^{\min} < p_j < \ell_j^{\max}$, we will adopt the approach used by the *MINUIT* minimization package, well-known in particle physics [69].

With this approach, constrained optimization is achieved by first performing a particular parameter transformation so that after the transformation all the parameters are unconstrained. Once done, the original LM algorithm can be used to identify the optimal parameters in the transformed parameter space.

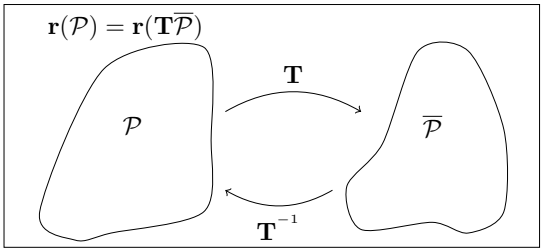

Figure 4.7 Illustration of the mapping between the sets of external, $\boldsymbol{\mathcal{P}}$, and internal parameters $\overline{\boldsymbol{\mathcal{P}}}$ via the transformations $\mathbf{T}$ and $\mathbf{T}^{-1}$.

The (forward) transformation defines a mapping between the sets of what we call external (bounded) parameters and internal (unbounded) parameters, denoted $\boldsymbol{\mathcal{P}}$ and $\overline{\boldsymbol{\mathcal{P}}}$, respectively (see Fig. 4.7). To verify that an updated set of model parameters are physical the inverse transformation $\mathbf{r}(\mathbf{T}^{-1}\overline{\boldsymbol{\mathcal{P}}}) = \mathbf{r}(\boldsymbol{\mathcal{P}})$ is called each time the algorithm has calculated a new set of internal parameters. If the bounded parameters are outside the legal interval, our framework will give an error message and the user should restart the optimization with a different set of initial values $\boldsymbol{\mathcal{P}}_0$. We will now detail how such transformations can be performed.

For a bounded p_j parameter with either a minimum $\ell_j^{\min}$, a maximum $\ell_j^{\max}$ or both limits given, and its unbounded counterpart $\overline{p}_j$, the *MINUIT*-transformation and it's inverse is defined as

$$\overline{p}_j = \begin{cases} \arcsin\left(2\frac{p_j - \ell_j^{\min}}{\ell_j^{\max} - \ell_j^{\min}} - 1\right) & \text{, both} \\ \sqrt{(p_j - \ell_j^{\min} + 1)^2 - 1} & \text{, only } \ell_j^{\min} \\ \sqrt{(\ell_j^{\max} - p_j + 1)^2 - 1} & \text{, only } \ell_j^{\max} \end{cases} \tag{4.11a}$$

$$p_j = \begin{cases} \frac{\ell_j^{\max} - \ell_j^{\min}}{2}\left[\sin\left(\overline{p}_j\right) + 1\right] + \ell_j^{\min} & \text{, both} \\ \ell_j^{\min} - 1 + \sqrt{\overline{p}_j{}^2 + 1} & \text{, only } \ell_j^{\min} \\ \ell_j^{\max} + 1 - \sqrt{\overline{p}_j{}^2 + 1} & \text{, only } \ell_j^{\max}, \end{cases} \tag{4.11b}$$

The derivatives of Eq. (4.11), needed for the error analysis, are

$$\frac{\partial \overline{p}_j}{\partial p_j} = \begin{cases} \frac{2}{(\ell_j^{\max}-\ell_j^{\min})} \frac{1}{\sqrt{1-\left(2\frac{p_j-\ell_j^{\min}}{\ell_j^{\max}-\ell_j^{\min}}-1\right)^2}} & \text{, both} \\ \frac{(p_j-\ell_j^{\min}+1)}{\sqrt{(p_j-\ell_j^{\min}+1)^2-1}} & \text{, only } \ell_j^{\min} \\ \frac{-(\ell_j^{\max}-p_j+1)}{\sqrt{(\ell_j^{\max}-p_j+1)^2-1}} & \text{, only } \ell_j^{\max} \end{cases} \tag{4.12a}$$

$$\frac{\partial p_j}{\partial \overline{p}_j} = \begin{cases} \frac{\ell_j^{\max}-\ell_j^{\min}}{2} \cos\left(\overline{p}_j\right) & \text{, both} \\ \frac{\overline{p}_j}{\sqrt{\overline{p}_j{}^2+1}} & \text{, only } \ell_j^{\min} \\ -\frac{\overline{p}_j}{\sqrt{\overline{p}_j{}^2+1}} & \text{, only } \ell_j^{\max}. \end{cases} \tag{4.12b}$$

If the limits are set to $\ell_j^{\min} = -\infty$ and $\ell_j^{\max} = \infty$, the parameter is considered to be unbounded and $p_j = \overline{p}_j$.

Error estimation

The uncertainties associated with a set of optimized model parameters $\boldsymbol{\mathcal{P}}^\star$, can be obtained from the covariance matrix. The standard error of an optimized parameter $p_j^\star$ is interpreted as the square root of the diagonal elements in the covariance matrix $\hat{\sigma}_j = \sqrt{C_{j,j}}$. For Gaussian distributed data the covariance matrix is found from the negative inverse of the Hessian

$$\begin{aligned} \mathbb{C}(\boldsymbol{\mathcal{P}}^\star) &= -\left[\mathbb{H}(\boldsymbol{\mathcal{P}}^\star)\right]^{-1} \\ &\approx -\left[\mathbb{J}^{\mathrm{T}}(\boldsymbol{\mathcal{P}}^\star)\mathbb{J}(\boldsymbol{\mathcal{P}}^\star)\right]^{-1}. \end{aligned} \tag{4.13}$$

In the last line of Eq. (4.13) only the first term in Eq. (4.10) has been used to approximate the Hessian. This is a valid conjecture, provided that the set of optimized model parameter give a residual close to zero, *i.e.* $r_i(\boldsymbol{\mathcal{P}}) = [f(x_i) - \hat{f}(x_i|\boldsymbol{\mathcal{P}}^\star)]/\sigma_i \approx 0$, $\forall i$. Since the Hessian is approximated by only a first derivative term this can result in a so-called ill-conditioned matrix, where the ratio between the largest and smallest singular values becomes big. In this case, our approximation of the standard deviation of the optimized parameters is not valid.

Since the optimized parameters essentially are calculated in internal parameters, $\overline{\boldsymbol{\mathcal{P}}}^\star$, a rescaling is needed to obtain the Jacobian for the external parameters. This rescaling is defined as

$$\begin{aligned} \overline{\mathbb{J}} &= \frac{\partial \mathbf{r}}{\partial \overline{\boldsymbol{\mathcal{P}}}^\star} \\ \overline{\mathbb{J}} &= \frac{\partial \mathbf{r}}{\partial \boldsymbol{\mathcal{P}}^\star} \frac{\partial \boldsymbol{\mathcal{P}}^\star}{\partial \overline{\boldsymbol{\mathcal{P}}}^\star} \\ \mathbb{J} &= \overline{\mathbb{J}} \left[\frac{\partial \boldsymbol{\mathcal{P}}^\star}{\partial \overline{\boldsymbol{\mathcal{P}}}^\star}\right]^{-1}, \end{aligned} \tag{4.14a}$$

or by the inverse transformation

$$\begin{aligned}\mathbb{J} &= \frac{\partial \mathbf{r}}{\partial \boldsymbol{\mathcal{P}}^{\star}} \\ &= \overline{\mathbb{J}} \frac{\partial \overline{\boldsymbol{\mathcal{P}}}^{\star}}{\partial \boldsymbol{\mathcal{P}}^{\star}}.\end{aligned} \tag{4.14b}$$

From stability tests performed on the model parameters in GranFilm we experience that the best choice is to approximate the Jacobian as in Eq. (4.14b).

It is warned against using the MINUIT-transformation in an optimization if the initial guess of a bounded parameter is close to a limit. If this is needed anyway, one should remove the limits and redo the error analysis when an estimate of optimized parameters has been obtained [69, 70].

4.4 Examples of GranFilm simulations: plasmon resonances in silver particles

In the previous sections, presentations of the most important input parameters, the corrections of the material permittivities, and the fit algorithm for experimental data were given. To conclude the discussion of the functionality offered by the GranFilm software, a series of simulations will be presented to illustrate the capabilities of GranFilm. Particular attention will be paid to the role of the geometry on the obtained results. Silver is used as a testbed material for the particles through out this thesis. Indeed, since interband transitions poorly damp its bulk plasmon oscillations, nanoparticles made from this metal show pronounced LSPRs in the visible region of the optical spectrum.

4.4.1 Connecting the micro and macro through polarizabilities

As discussed in Sec. 4.1, the interest of GranFilm as a simulation tool lies in its capability to connect the micro (polarizabilities) and macroscopic (Fresnel coefficients) properties of a layer of supported particles at reasonable computation times. An example related to a system consisting of hemispherical silver particles on alumina is presented in Fig. 4.8 for illumination at $\theta_0 = 45°$ by an s-polarized plane wave. The imaginary part of the polarizability and the reflection and transmission coefficients are presented as a function of the photon energy in Figs. 4.8(a)-(b). These results illustrate the connection between these quantities; the peak position of $\mathrm{Im}\{\alpha_{\parallel}\}$ is related to the positions of peaks (dips) in the reflectivity (transmission). This expected behavior lies in the fact that R_s depends only on the parallel surface susceptibility $\gamma \propto \alpha_{\parallel}$, like we discussed in Sec. 2.6.

Electrostatic potential maps may uncover what kind of resonance gives rise to the features observed in the Fig. 4.8. To make potential resonances more pronounced and get rid of the potential of the incoming field, it is useful to suppress the absorption in the metal particle partly. This is achieved by artificially reducing the imaginary part of the dielectric function of silver. Figures 4.8(c)-(d) presents contour plots of the imaginary part of the electrostatic potential in the xz plane of incidence. The

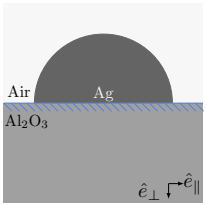

Parameter	Value
R [nm]	5.0
t_r	0.12
L [nm]	31.0
θ_0	45°
M	16

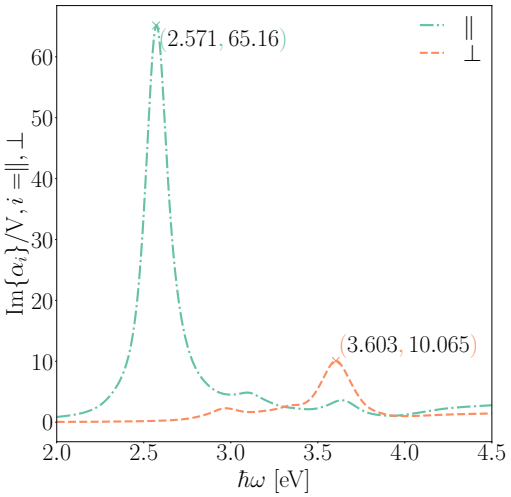

(a) $\mathrm{Im}\{\alpha_i\}$,$i = \parallel, \perp$.

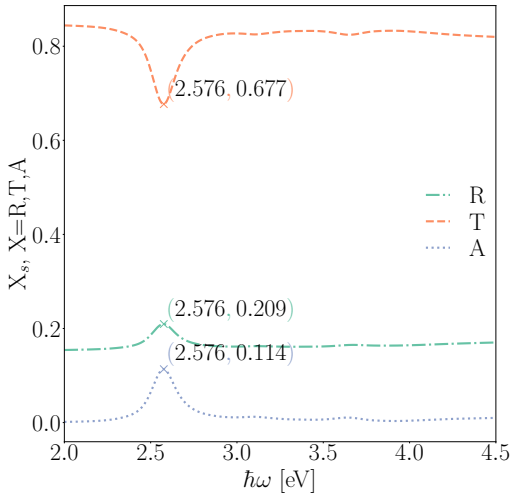

(b) Fresnel amplitudes; reflection, transmission and absorption.

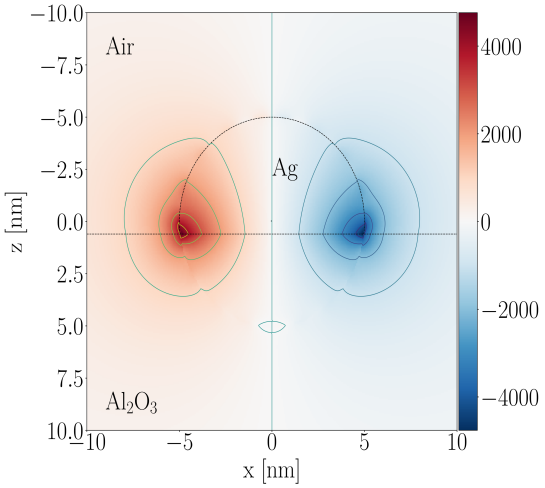

(c) $\hbar\omega = 2.57$ eV.

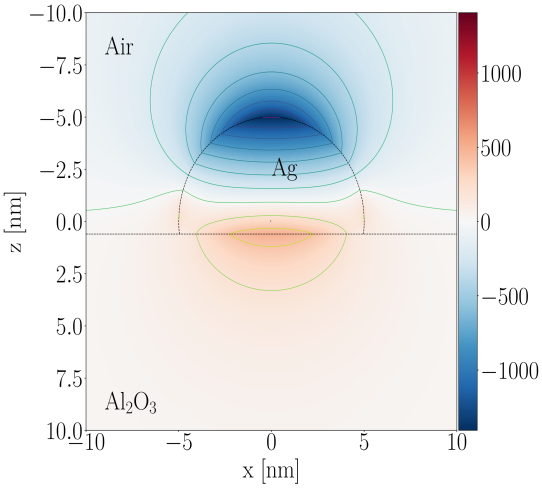

(d) $\hbar\omega = 3.60$ eV.

Figure 4.8 Examples of results from a typical GranFilm simulation of a hemisphere of silver on an alumina substrate. The energy position of the parallel polarizability, the highest peak in (a), and the reflection and transmission amplitudes for s-polarized light (b) are correlated. The electrostatic potential with the imaginary part of the dielectric function of silver reduced by a factor of 99% is plotted at the energies corresponding to the peaks of the parallel (c) and the perpendicular (d) polarizability. Simulation parameters are indicated on the top of the figure. The highest amplitude for each system in (a)-(b) is marked with (energy, amplitude).

imaginary part of the dielectric function of silver was reduced by 99% of the original value. Maps are plotted at photon energies of $\hbar\omega = 2.57\,\text{eV}$ [Fig. 4.8(c)] and $\hbar\omega = 3.60\,\text{eV}$ [Fig. 4.8(d)] corresponding to the main peaks of $\text{Im}\{\alpha_i\}$, $i = \parallel, \perp$. From the results in Figs. 4.8(c)-(d), one observes that both resonant modes display a dipole-like pattern of polarization with a charge accumulation at the interface [Fig. 4.8(c)] or above [Fig. 4.8(d)]. The dipole-like pattern of the polarization charges points in the opposite direction of each other. Chapter 5 will investigate the nature of these resonant modes in further detail.

4.4.2 The effect of simulation parameters

Sections 4.2-4.3.1 presented the most important input parameters and the possible types of corrections of the material permittivities that GranFilm supports. Among them, the *multipole order*, the type of *island-island interaction*, and the *correction of the bulk permittivity* turned out to have a significant influence on the simulation results.

Changing *the number of multipoles*, M, will drive the convergence of the simulation results. Shifts in the amplitudes and position of the peaks of the reflectivity curve in s-polarization are observed with increasing M Fig. 4.9(a). By changing from $M = 1$ to $M = 16$, the energy position of the highest amplitude in the plot is shifted around $0.063\,\text{eV}$ towards higher energies. The amplitude of the peak is also reduced by 0.101. Fortunately, above a given threshold, the obtained curves get closer; the lack of difference between $M = 16$ to $M = 22$ multipoles demonstrate that convergence was reached at $M = 16$.

Electrostatic interactions between neighbor particles do not drastically impact the single particle polarizability if $L \gg 2R$. However, when the particles come closer, the correction of the single particle polarizability leads to shifts of the resonances. As shown in Fig. 4.9(b), a shift of $0.091\,\text{eV}$ down words in energies is observed for the reflectivity curves in s-polarization between non-interacting particles and those interacting at dipolar/quadrupolar order. This redshift originates in the effect of the depolarization field induced by the neighbors [61]. Note that the overlap of the curves corresponding to dipolar and quadrupolar interactions between the particles gives some confidence in the validity of the interaction range. If it is found that the response calculated with quadrupole and dipolar interactions are not contiguous the island-island interaction should be performed to a higher order than quadrupole. This choice is currently not available in the GranFilm software.

As discussed in Sec. 4.3.1, the corrections of the bulk permittivity are needed to get reliable results from GranFilm when the skin depth of the metal is of the same order of magnitude as the mean free path of the electrons in the metallic nanoparticle. Figure 4.10 presents the impact of these corrections on the experimental bulk value of the dielectric function of silver. As expected, for the chosen energy range, the impact of the corrections is most prominent for the smallest particles. The finite size effect increases the imaginary part of the dielectric function in the low energy regime, as compared to the experimental bulk values, while the real part is moderately affected. This corresponds to enhanced damping. Moreover, Fig. 4.10(b) demonstrates that the

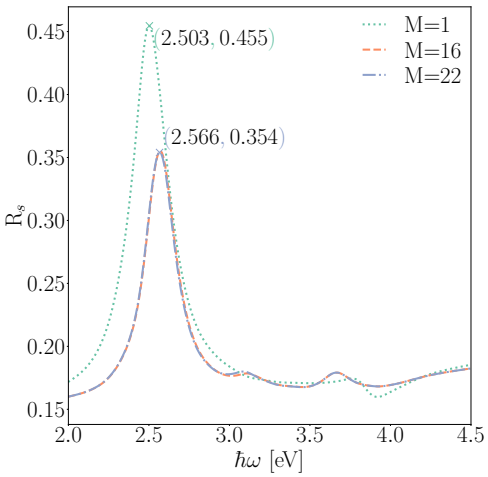

(a) Different number of multipoles M.

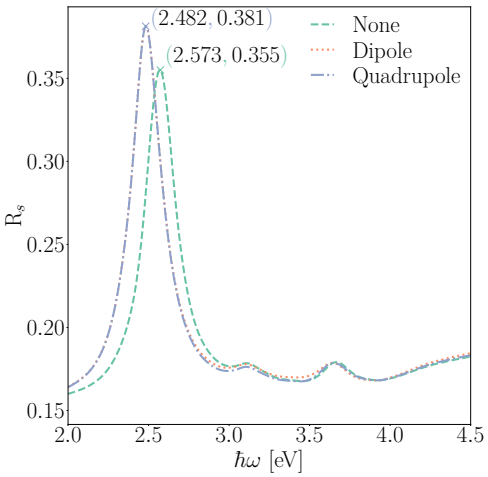

(b) Different type of island-island interactions.

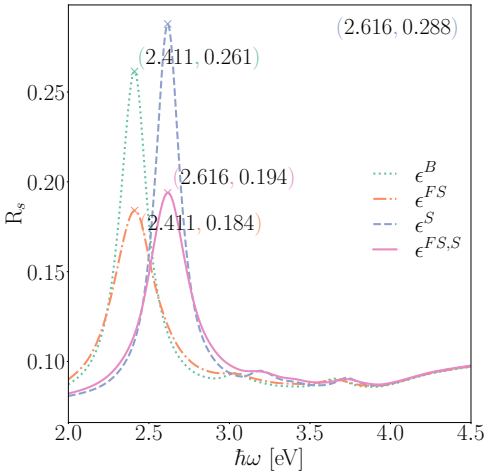

(c) Different types of corrections (surface correction ε^S, finite size correction ε^{FS} and both $\varepsilon^{FS,S}$) of the experimental bulk permittivity of silver ε^B .

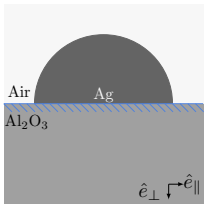

Parameter	Value
R [nm]	5.0
t_r	0.12
L [nm]	15.0
θ_0	45°
M	16

Figure 4.9 Examples of how certain parameter values affect the reflectivity coefficient in s-polarization of a GranFilm simulation: the number of multipoles (a), the type of island-island interaction (b), or the type of correction of the bulk permittivity (c). Simulation parameters are indicated in the lower right of the figure. The highest amplitude for each system response is marked with (energy, amplitude).

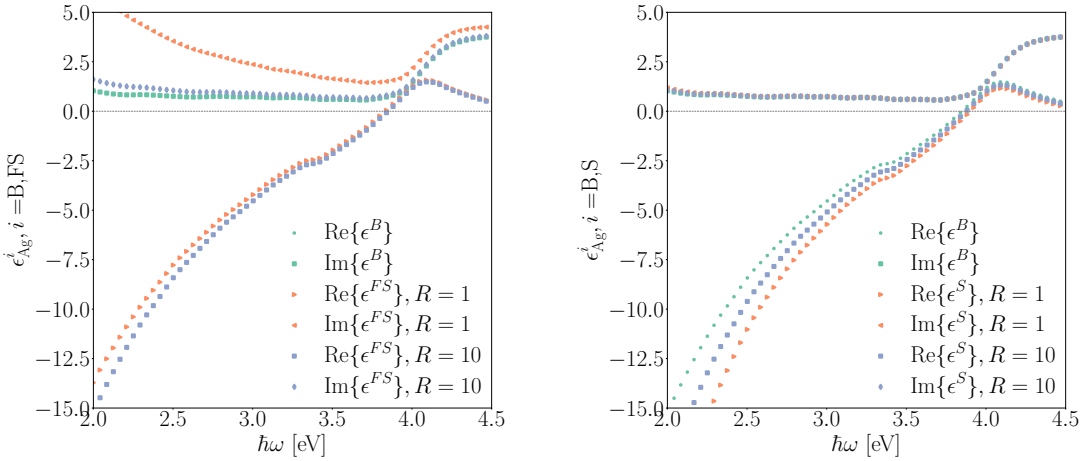

(a) Finite size correction. **(b)** Surface correction.

Figure 4.10 The bulk dielectric functions of silver, compared to corrected values by the finite size effect (a) and the surface effect (b) for small and middle sized particles.

Table 4.4 Values used for input parameters necessary to perform finite-size and surface correction for a hemisphere of a silver particle in a GranFilm simulation [58].

Parameter	$\hbar\omega_p$	$\hbar\Gamma_\infty$	B	$\hbar v_F$	C
Ag	9.17 eV	0.018 eV	$-1.13\,\mathrm{eV}^2\,\mathrm{nm}$	0.91 eV nm	0.6

surface effect tends to blueshift the real part of the dielectric function and, therefore, the position of the cross-over. This corresponds to a shift of the plasmon resonance.

Figure 4.9(c) presents the reflectivity curve calculated with GranFilm for a s-polarized plane wave at an incident angle of $\theta_0 = 45°$. Changing between the experimental bulk permittivity via a finite size correction, a surface correction, or both shifts and broadens the resonances. On one hand, finite size correction tends to broaden and decrease the amplitude of the resonance mainly at low energy as expected from the increase of the imaginary part of the dielectric function. On the other hand, the surface correction shifts the same peak towards higher energies. The used values of the input parameters needed to perform finite-size, surface, or the combination of the two corrections of the bulk dielectric function for the studied geometry are given in Table 4.4.

Varying the shape

Figure 4.11 illustrates how the different correction types of the experimental bulk dielectric function of silver affect the imaginary part of the direction dependent polarizability as a function of truncation ration.

Firstly, Figs. 4.11(a)-(b) shows how the imaginary part of the polarizability normalized

by the volume is blue-shifted for the parallel and red-shifted for the perpendicular components for increasing truncation ratio without any corrections. The amplitudes of the curves are also changed for both directions. Increasing the truncation ratio yields a decrease in the amplitude of the parallel component as opposed to an increase of the amplitudes in the perpendicular response. These shifts are related to the fact that a changing truncation ratio changes both the volume and the aspect ratio of the particles. As the truncation ratio is increased, the parallel part of the particle in contact with the substrate, is brought further away, and the amplitude is decreased. In contrast to this, the amount of perpendicular matter is increased because a higher value of the truncation ratio yields more matter in this direction.

Applying the finite-size or the surface correction on the experimental bulk dielectric function of silver also displays a different impact on the two direction dependent polarizabilities. The curves for a system of changing truncation ratio with finite-size and surface corrections are respectively given in Figs. 4.11(c)-(d) and Figs. 4.11(e)-(f).

The impact of the corrections of the bulk experimental dielectric function of silver is generally greater the smaller the oscillation path of the electrons or the ratio of surface/volume in the particle is. Thus, as the truncation ratio is increased, the impact on the parallel component of the imaginary part of the polarizabilities will be more and more prominent [Fig. 4.11(c), Fig. 4.11(e)]. In contrast, the perpendicular component of the imaginary part of the polarizability will be less and less prominent for a higher value of the truncation ratio [Fig. 4.11(d), Fig. 4.11(f)].

One could also combine the two correction types. The result would then be similar to what we already saw for the reflectivity coefficient in Fig. 4.9(c).

4.4.3 Fitting the experimental reflectivity curve

Section 4.3.2 presented the algorithm used by GranFilm to perform a fit of experimental data, like reflectivity measurements. Now we will illustrate how the fitting routine can be used to investigate a system of silver particles on an $Al_2O_3(0001)$ substrate.

The green dots in Fig. 4.12(a) represent the differential reflectivity curve for p-polarized light at $\theta_0 = 45°$ collected in a SDRS measurement during the vapor-deposition of silver on alumina. This data set displays two pronounced resonances that will be of importance when the model parameters are optimized. Optimization of the parameters $\boldsymbol{\mathcal{P}} = \{L, R, t_r, \sigma_\parallel, \sigma_\perp\}$, with default values as listed in Fig. 4.12(b), was performed. To improve agreement with experiments, the inherent size/shape distribution that broadens the resonance was treated with the 'ad hoc' broadening like presented in Eq. (4.1). Each time a set of the model parameters $\boldsymbol{\mathcal{P}}^{(n)}$ were estimated, the single particle direction dependent polarizabilities were convoluted with Gaussians of standard deviations $\sigma_\parallel^{(n)}, \sigma_\perp^{(n)}$ along the parallel and perpendicular direction. A better account of these effects will the topic of Ch. 6.

Minimization was performed starting from reasonable initial values (or guesses) (last column of Fig. 4.12(b)). The $\Delta R_p/R_p$ curve that corresponds to those parameters is presented as a blue dotted line in Fig. 4.12(a). The optimization process was performed by minimizing the $\chi^2(\boldsymbol{\mathcal{P}})$-function by the use of the LM-algorithm as described

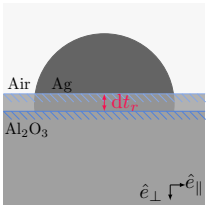

Parameter		Value
R	[nm]	5.0
t_r		dt_r
L	[nm]	31.0
θ_0		45°
M		16

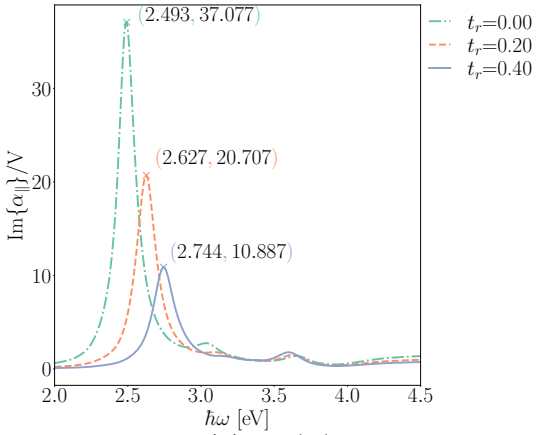

(a) $\alpha_\parallel(t_r)$.

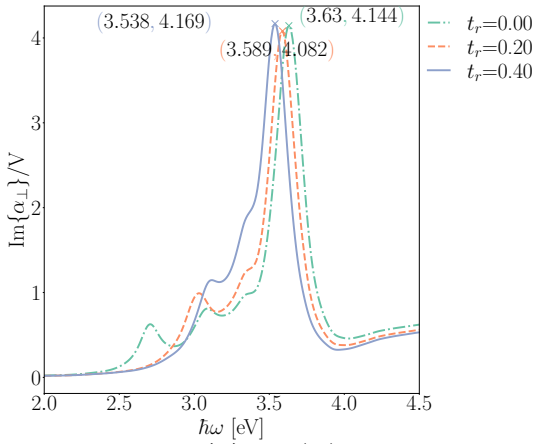

(b) $\alpha_\perp(t_r)$.

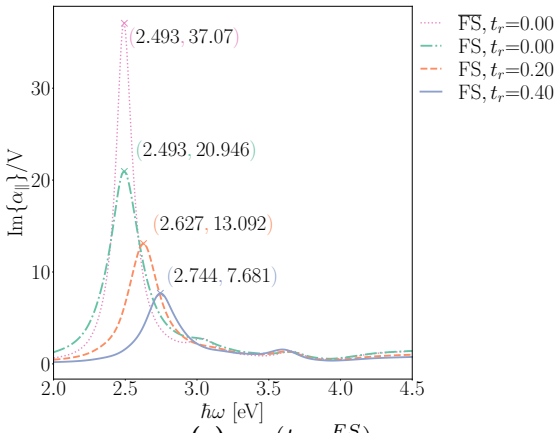

(c) $\alpha_\parallel(t_r, \varepsilon^{FS})$.

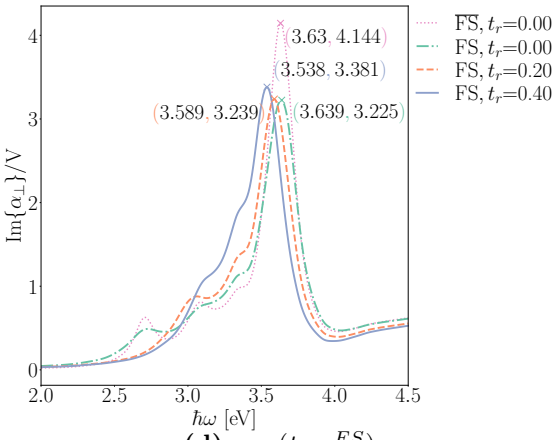

(d) $\alpha_\perp(t_r, \varepsilon^{FS})$.

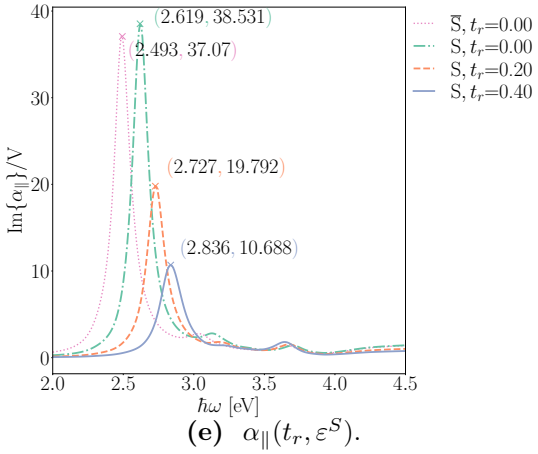

(e) $\alpha_\parallel(t_r, \varepsilon^{S})$.

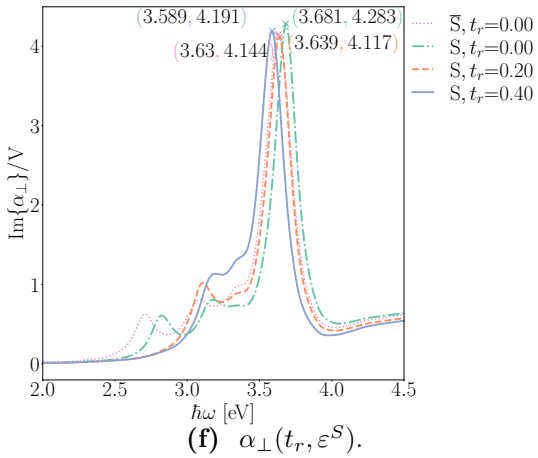

(f) $\alpha_\perp(t_r, \varepsilon^{S})$.

Figure 4.11 The imaginary part of the direction dependent polarizability induced in particles as a function of different truncation ratios without (a)-(b), with finite size (c)-(d), and with surface (e)-(f) corrections of the experimental bulk dielectric function. Simulation parameters are indicated on the top of the figure. The highest amplitude for each system response is marked with (energy, amplitude).

previously in Sec. 4.3.2. After convergence, the set of optimized parameters $\boldsymbol{\mathcal{P}}^{\star}$ (second column of Fig. 4.12(b)) was used to calculate a theoretical differential reflectivity $\Delta R_p/R_p$ curve presented as a solid orange line in Fig. 4.12(a). The good agreement with the experiment gives some degree of confidence in the fitted parameters. Beyond that, the real-time capability of SDRS combined with the fitting of experimental curves are interesting to access the time evolution of the experiments. An 'average' island radius, density, and aspect ratio can be compared to the expectation from the physics of nucleation, growth, and coalescence [61]. Such detailed information about the evolution of the film morphology is not trivial to obtain by other non-invasive methods.

4.5 Conclusion

This chapter was dedicated to the GranFilm software itself. First, we presented the software architecture and a short user guide with the needed know-how to launch a GranFilm simulation (Sections 4.1-4.2). The new functionalities like correction of the material permittivity with respect to the finite-size and the surface correction and fit of experimental data via the LM algorithm were described in Section 4.3. The chapter ended with a brief presentation of the capabilities of the software in Sec. 4.4. Through examples, we have shown how some input parameters potentially impact the simulation results. Also, an example of model parameter estimation of the data from a reflectivity measurement was given.

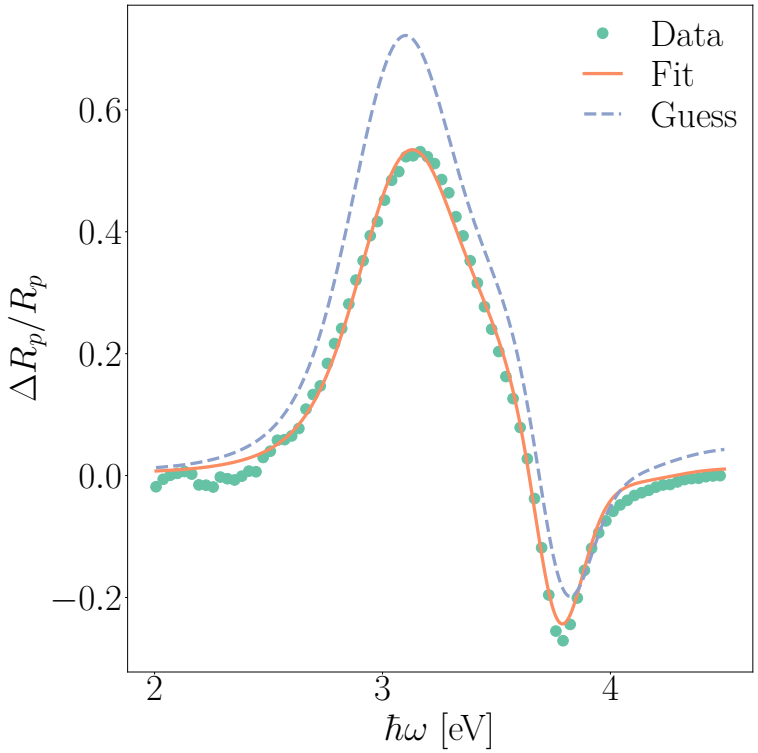

(a) The fit of an experimental p-polarized ($\theta_0 = 45°$) SDRS spectrum for silver particles grown on alumina. Data points are compared to a GranFilm simulation with initial guess parameters and optimized ones.

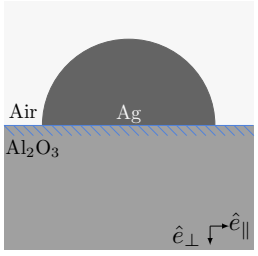

Parameter	Optimization	Guess
L [nm]	7.31 ± 0.020	6.76
R [nm]	2.3 ± 0.000021	2.3
t_r	0.67 ± 0.00000029	0.67
$\sigma_\parallel$ [nm]	0.15 ± 0.0040	0.15
$\sigma_\perp$ [nm]	0.061 ± 0.0025	0.075

(b) The values of the optimized model parameters with absolute error and initial guess.

Figure 4.12 A result of fitting a data set from a SDRS experiment given in (a), together with the resulting values of the model parameters, (b). Finite-size and surface correction of the bulk permittivity of silver were used in the optimization process. Number of multipoles where $M = 16$. The particles were arranged in a hexagonal lattice. The island-island interaction was taken into account to dipolar order.

4.A The effective oscillation length in a particle

The effective oscillation length D_{eff} of the s-electrons inside a spheroidal nanoparticle is taken as the smallest distance between the emerging part of the particle and the in-plane radius seen from above. The values are given by the spheroidal parametrization

$$\frac{x^2+y^2}{a^2}+\frac{z^2}{c^2}=1. \tag{4.15}$$

with $a=R_{\parallel}$ and $c=R_{\perp}$ and the definition of truncation or the distance from spheroid center to substrate $d=R_{\perp}|t_r^{(s)}|$. They read:

$$\begin{aligned} D_{eff,\perp}^{(s)} &= \begin{cases} R_{\perp}^{(s)}\left(1+t_r^{(s)}\right) & \left|t_r^{(s)}\right|\leq 1, \\ 2R_{\perp}^{(s)} & \left|t_r^{(s)}\right|>1, \end{cases} \\ D_{eff,\parallel}^{(s)} &= \begin{cases} 2R_{\parallel}^{(s)} & t_r^{(s)}\geq 0, \\ 2R_{\parallel}^{(s)}\sqrt{1-\left(t_r^{(s)}\right)^2} & -1\leq t_r^{(s)}\leq 0, \end{cases} \end{aligned} \tag{4.16}$$

where $t_r^{(s)}=\left(\dfrac{d}{R_{\perp}^{(s)}}\right)$. For the special case of a spherical particle, $R_{\perp}^{(s)}=R_{\parallel}^{(s)}=R^{(s)}$.

For a coated particle

The effective oscillation length inside the coating of a particle's surface s is chosen as

$$\Delta D_i=D_i^{(s)}-D_i^{(s+1)}, i=\parallel,\perp \tag{4.17}$$

where $D_i^{(s)}-D_i^{(s+1)}$ is defined as the difference in length between the surfaces s and $s+1$ given by Eq. (4.16).

4.B The volume of a particle

Starting from the equation of the spheroid the volume of a truncated spheroidal particle above the substrate is given by integrating the area of a single disk $A(z)$ along the $z-$axis

$$
\begin{aligned}
V_{above} &= \int_{z_1}^{z_2} A(z)dz \\
&\overset{①}{=} \pi a^2 \int_{z_1}^{z_2} \left[1 - \left(\frac{z}{c}\right)^2\right] dz \\
&= \pi a^2 \left[z - \frac{1}{3}\frac{z^3}{c^2}\right]_{z_1}^{z_2} \\
&\overset{②}{=} \frac{1}{3}\pi \left(R_{\parallel}^{(s)}\right)^2 R_{\perp}^{(s)} \left[3t_r^{(s)} - \left(t_r^{(s)}\right)^3 + 2\right] \quad \left|t_r^{(s)}\right| \leq 1.
\end{aligned}
\tag{4.18}
$$

① The area of an infinitesimal circle in an ellipsoidal particle is $A(z) = \pi \left(r_{\parallel}\right)^2 = \pi a^2 \left[1 - \left(\frac{z}{c}\right)^2\right]$.

② In the geometry of GranFIlm: $z_1 = -R_{\perp}^{(s)}, z_2 = d, t_r^{(s)} = \frac{d}{R_{\perp}^{(s)}}, c = R_{\perp}^{(s)}, a = R_{\parallel}^{(s)}$.

4.C The surface area of a particle

The total surface area of the given layer of a particle is $A_{particle}^{(s)} = A_{bottom}^{(s)} + A_{cap}^{(s)}$. $A_{bottom}^{(s)}$ is the surface area of the circle in the bottom of the spheroidal/sphere is defined as

$$
\begin{aligned}
A_{bottom}^{(s)} &= 2\pi x^2 \\
&= 2\pi \left(R_{\parallel}^{(s)}\right)^2 \left(1 - (t_r^{(s)})^2\right) \quad \left|t_r^{(s)}\right| < 1.
\end{aligned}
\tag{4.19}
$$

A_{cap} is found by chopping the particle in infinitesimal rings of thickness ds, and then integrating them along the z-axis

$$
\begin{aligned}
A_{cap}^{(s)} &= \int_{z_1}^{z_2} 2\pi x ds \\
&\overset{①}{=} 2\pi a \int_{z_1}^{z_2} \sqrt{1-\left(\frac{z}{c}\right)^2}\sqrt{\frac{1+\frac{1}{c^2}\left[\left(\frac{a}{c}\right)^2+1\right]z^2}{1-\left(\frac{z}{c}\right)^2}}dz \\
&\overset{②}{=} 2\pi a \int_{z_1}^{z_2} \sqrt{1+\xi z^2}dz \\
&\overset{③}{=} \begin{cases}
\pi a\left[z_2\sqrt{1+\xi z_2^2}-z_1\sqrt{1+\xi z_1^2}+\dfrac{1}{\sqrt{-\xi}}\left(\arcsin\left(z_2\sqrt{-\xi}\right)-\arcsin\left(z_1\sqrt{-\xi}\right)\right)\right], & (\xi<0,\alpha>0)\\
2\pi a\left[z_2-z_1\right], & (\xi=0)\\
\pi a\left[z_2\sqrt{1+\xi z_2^2}-z_1\sqrt{1+\xi z_1^2}+\dfrac{1}{\sqrt{\xi}}\ln\left(\dfrac{z_2\sqrt{\xi}+\sqrt{1+\xi z_2^2}}{z_1\sqrt{\xi}+\sqrt{1+\xi z_1^2}}\right)\right], & (\xi>0),
\end{cases} \\
&\overset{④}{=} \begin{cases}
\pi R_\parallel^{(s)}R_\perp^{(s)}\left[t_r\sqrt{\left[\left(\frac{R_\parallel^{(s)}}{R_\perp^{(s)}}\right)^2-1\right](t_r^{(s)})^2+1}+\frac{R_\parallel^{(s)}}{R_\perp^{(s)}}+\left(\arcsin\left(t_r^{(s)}\sqrt{1-\left(\frac{R_\parallel^{(s)}}{R_\perp^{(s)}}\right)^2}\right)+\arcsin\left(\sqrt{1-\left(\frac{R_\parallel^{(s)}}{R_\perp^{(s)}}\right)^2}\right)\right)\right], & \text{Prolate},\\
2\pi(R^{(s)})^2\left[t_r^{(s)}+1\right], & \text{Sphere},\\
\pi R_\parallel^{(s)}R_\perp^{(s)}\left[t_r^{(s)}\sqrt{\left[\left(\frac{R_\parallel^{(s)}}{R_\perp^{(s)}}\right)^2-1\right](t_r^{(s)})^2+1}+\frac{R_\parallel^{(s)}}{R_\perp^{(s)}}+\frac{1}{\sqrt{\left(\frac{R_\parallel^{(s)}}{R_\perp^{(s)}}\right)^2-1}}\ln\left(\frac{t_r^{(s)}\sqrt{\left(\frac{R_\parallel^{(s)}}{R_\perp^{(s)}}\right)^2-1}+\sqrt{\left[\left(\frac{R_\parallel^{(s)}}{R_\perp^{(s)}}\right)^2-1\right](t_r^{(s)})^2+1}}{\frac{R_\parallel^{(s)}}{R_\perp^{(s)}}-\sqrt{\left(\frac{R_\parallel^{(s)}}{R_\perp^{(s)}}\right)^2-1}}\right)\right], & \text{Oblate}.
\end{cases}
\end{aligned}
$$

---

① The surface element is $ds=\sqrt{dx^2+dz^2}=\sqrt{1+\left(\frac{dx}{dz}\right)^2}dz$. The radii in our circles are $x=a\sqrt{1+\left(\frac{z}{c}\right)^2}$.

② $\xi=\dfrac{1}{c^2}\left[\left(\dfrac{a}{c}\right)^2-1\right]$.

③ Integral identity by [71, Sec.2.27, Eq. 2.271.3],

$$
\begin{aligned}
u &= \sqrt{\alpha+\beta x^2}\\
I_1 &= \begin{cases}
\dfrac{1}{\sqrt{\beta}}\ln\left(x\sqrt{\beta}+u\right), & \beta>0\\
\dfrac{1}{\sqrt{-\beta}}\arcsin\left(x\sqrt{\dfrac{-\beta}{\alpha}}\right), & \beta<0,\alpha>0,
\end{cases}\\
\int u dx &= \frac{1}{2}\left[xu+aI_1\right].
\end{aligned}
$$

④ In GranFilm $z_1=-R_\perp^{(s)}, z_2=d, t_r^{(s)}=\dfrac{d}{R_\perp^{(s)}}, c=R_\perp^{(s)}, a=R_\parallel^{(s)}$.

Chapter 5

The oscillation modes of non-coated and coated particles

By now, it should be well established that the features of a macroscopic observable like the SDRS-signal are directly linked to the microscopic properties of the system, *e.g.* direction-dependent polarizabilities. This chapter is aimed at describing the origin of the experimentally observed peaks and dips in terms of shape-driven eigen oscillation modes or LSPRs. The shifts in the intensities and energy positions of the resonances are investigated for truncated and coated particles. Interactions with the substrate and the neighbors are accounted for.

Contents

5.1 The origin of the oscillation modes in supported nanoparticles

In Ch. 1 we gave examples of how the dipolar model can explain qualitatively the changes in the LSPRs caused by the presence of a substrate [30, 31]. Typical results of GranFilm simulations were commented in Ch. 4. In particular the link between the theoretical differential reflectivity curves generated with GranFilm and the experimental SDRS-signals was stressed. In Figs. 4.8(c)-(d) we showed plots of the potential maps around the two main resonance energies in a system of truncated silver particles on alumina. In the following, we will discuss in greater details the origin of these modes.

The LSPRs studied in this work are induced by an incoming electric field. Its main effect is to polarize the metal's electron gas and potentially excite the collective oscillations [8]. In an isolated object with spherical symmetry, only one dipolar mode is optically active while for a spheroid, the degeneracy of the space directions is lifted off leading to one dipolar mode along each main axis.

However, for supported truncated particles, as described in this thesis, a double break of symmetry occurs even in the quasi-static approximation. This gives rise to the excitation of a potentially richer set of polarization modes:

- the first break of symmetry, even for a spherical particles, is induced by the presence of the substrate. After the constant incident field has created a dipole inside the metal particle, the substrate reacts by inducing an image dipole which in turn modifies the local field felt by the particle. The response of the is no more homogeneous. The image field excites a quadrupole mode in the particle and therefore an image quadrupole in the substrate, and so on. This cascade of polarization to a high multipolar order is naturally described by solving Laplace's equation for the geometry in question with proper BCs. As a result, the particle+substrate ensemble is able to sustain new oscillations modes that are present neither in the isolated object nor, of course, in the case of the flat surface. The determination of the strength and energies of the oscillations is obtained self-consistently by the solution of Laplace's equation.
- the truncation of the particle itself is an important break of symmetry, compared to the full spherical/spheroidal shape. It is well known that the particle shape is of paramount importance in defining the nature, the intensity and the energy of the observed resonances [1]. The most relevant geometrical parameter is the particle aspect ratio, defined as the ratio of sizes along the parallel and perpendicular substrate directions. In GranFilm this parameter is controlled by the truncation ratio of the spheres. As already shown in Fig. 4.11, it governs the resonance splitting and relative intensities along parallel/perpendicular directions.

Up to now in this work, no clear description of the nature of theses resonances was given. Lazzari *et al.* [20, 32, 72] gave a thorough discussion of the link between the experimental results obtained in a vapor deposition experiment of silver on alumina and the oscillation modes, their strengths, and their widths for a geometry of truncated

spherical particles. Following their approach, we will study the nature of the oscillation modes in the limit of undamped bulk dielectric functions. The question at hand is how these oscillation modes are changed with the presence of a substrate and a coating layer.

5.1.1 Identifying the multipolar modes with GranFilm

The formalism described in Ch. 3 for solving the Laplace's equation in the case of a supported truncated particle ended with a linear system of equations [Eqs. (3.64)-(3.67)] for the multipole expansion coefficients. By solving this linear set of equations to a given multipole order M, exemplified in Eq. (3.32), all the unknown multipolar coefficients of the scalar potential could be obtained. In a synthetic way, the set of equations reads:

$$\mathbb{M}(\omega,\kappa)\mathbf{X}(\omega,\kappa) = \mathbf{V}(\omega,\kappa), \tag{5.1}$$

where $\mathbb{M}(\omega,\kappa)$ is a matrix containing the frequency dependent integral definitions given in Eq. (3.63a), $\mathbf{X}(\omega,\kappa)$ is a column vector containing the unknown multipole coefficients
$V_{\ell m}(\omega,\kappa) = [A^{(i)}_{\ell m}(\omega,\kappa), B^{(i)}_{\ell m}(\omega,\kappa)]$ of dimension $\ell = 1,...,2M$, where M is the multipole order, and $m = \{0,\pm 1\}$. The vector $\mathbf{V}(\omega,\kappa)$ contains the terms of the field which excites the system either parallel, $m = \pm 1$, or normal, $m = 0$, to the surface of the substrate. Finally, κ is an *ad hoc* parameter used to scale the imaginary part of the experimental bulk dielectric functions $\varepsilon = \varepsilon_1 + i\kappa\varepsilon_2$ $(0 < \kappa \leq 1)$ of the media.

We found that the components of the polarizability tensor that drive the optical response of the system were proportional to the first multipole coefficients: [1]

$$\alpha_m(\omega,\kappa) \propto A_{1m}(\omega,\kappa) = X_{1m}(\omega,\kappa) = \left\{ [\mathbb{M}(\omega,\kappa)]^{-1} V(\omega,\kappa) \right\}_{1m}. \tag{5.2}$$

This writing shows that the LSPR modes will appear when the inverse of the matrix system is 'resonant'. This will occur at an angular frequency $\omega = \omega_r$, for which the matrix-system $\mathbb{M}(\omega,\kappa)\mathbf{X}(\omega,\kappa) = 0$ has non-trivial solutions [see Eq. (5.1)]. This is equivalent to saying that the matrix $\mathbb{M}(\omega = \omega_r,\kappa)$ is singular or that its determinant is zero.

Another way to understand the problem is to see the resonances as undamped eigen oscillations of the electrostatic potential. Once they have been excited, they do not need an external field to be maintained. This corresponds to the right-hand side of Eq. (5.1) being zero. For a non-trivial solution, this is the same as having a zero determinant for the matrix $\det \mathbb{M}(\omega = \omega_r,\kappa)$.

When absorption is present in the system, that is to say, when the dielectric functions has a non-vanishing imaginary part, this typically implies complex angular frequency for the eigenmode, where the imaginary part $\mathrm{Im}\{\omega\}$ is related to the lifetime of the mode. To determine the complex values of the angular frequency for which $\det \mathbb{M}(\omega,\kappa) = 0$ is a highly non-trivial and time-consuming task. In order to avoid dealing with the non-linear nature of the determinant function we will follow an alternative route, as described below.

[1] The relations between the multipole coefficients and the components of the polarizability tensor were discussed in Sec. 3.3.4 or, alternatively, see [5] for a detailed description.

5.1.2 The minima of the smallest eigenvalue in absolute value

We will seek for the minima of the smallest eigenvalue in absolute value of the matrix $\mathbb{M}(\omega, \kappa)$, as a function of the (real) angular frequency $\min_j |\lambda_j(\omega, \kappa)|$. Note that this procedure does not require a complex minimization of a highly non-linear function. Eigenmodes of the system will express themselves as peaks in the function $[\min_j |\lambda_j(\omega, \kappa)|]^{-1}$ vs. ω for a given damping $0 \leq \kappa < 1$. In the small damping limit, $\kappa \approx 0$, the mode-frequency ω satisfying $\det \mathbb{M}(\omega, \kappa) = 0$ is expected to have a vanishing or small imaginary part so that $\min_j |\lambda_j(\omega, \kappa)| \approx 0$ and, therefore, its inverse will show a peak at this value of $\mathrm{Re}\{\omega\}$ [20]. The corresponding eigenmode is obtained on the basis of the eigenvector of the matrix $\mathbb{M}(\omega, \kappa)$ (or any linear combination of the eigenvectors in case of a degenerate mode).

Thus, in a practical way, we will artificially reduce the imaginary parts of the dielectric functions, typically by 99% of their original values, to sharpen the oscillation modes. Once the relevant system of equations is defined, the eigenvalues are calculated with the ZGEEV routine in the Fortran library Lapack. The maxima of the inverse of the absolute value of $\mathbb{M}(\omega, \kappa)$ are obtained in a straightforward way as function of energy. The corresponding representation of the polarization modes are then given by the potential maps. The equipotential lines will surround the charges.

In the following, we try to gain some insight into the role of a coating layer on the polarization modes of the particles. To this end, new automatic plotting routines have been added to the GranFilm Python interface. As a reminder, the thickness of the coating is given by $(1-\chi^{(2)})R$, where $\chi^{(2)}$ is the second component of the radius ratio vector [2]. When $\chi^{(2)} \to 1^-$, the thickness of the coating goes to zero; on the other hand, when $\chi^{(2)} \to 0^+$ the coating layer disappears. We start the discussion with the oscillation modes of coated metallic particles in vacuum, before tackling the case of supported objects.

5.2 Oscillation modes in metallic nanoparticles in vacuum

To start the discussion of the effect of a coating layer, we begin with an unsupported object embedded in an homogeneous medium. This example also serves as a verification of the numerical implementations in GranFilm. Analytical formulas to calculate the LSPRs in NP within the quasi-static approximation are well-known [8, 10, 12].

Figure 1.11 in Sec. 1.3 presented a comparison of the imaginary part of the normalized polarizability of a non-coated and coated spherical particle in a homogeneous media, calculated for a Drude-like metal particle with the analytical formulas. Figure 5.1 presents the electrostatic potential plotted at the resonance energies in the xz-plane for:

- a free standing silver sphere;
- a silica coated silver sphere;

[2] See Ch. 4 for a description of the GranFilm Python interface and relevant parameter/variables in the software.

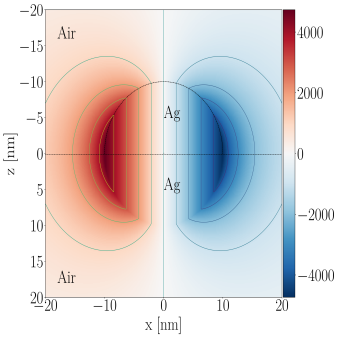

(a) $\hbar\omega = 3.53$.

Variable	Value
R [nm]	10.0
$\chi^{(2)}$	$\{0.8, 0.4\}$
κ	0.01
M	16

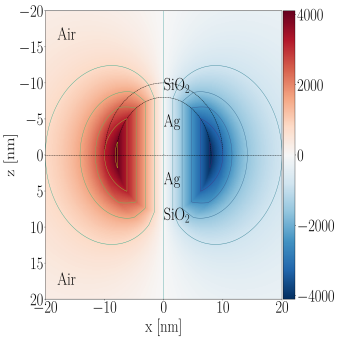

(b) $\hbar\omega = 3.29$, $\chi^{(2)} = 0.8$.

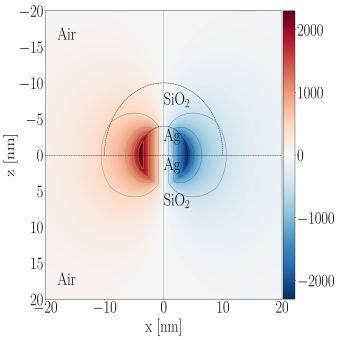

(c) $\hbar\omega = 3.07$, $\chi^{(2)} = 0.4$.

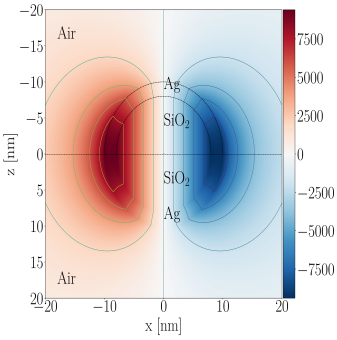

(d) $\hbar\omega = 2.42$, $\chi^{(2)} = 0.8$.

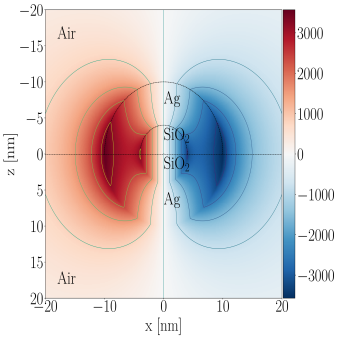

(e) $\hbar\omega = 3.34$, $\chi^{(2)} = 0.4$.

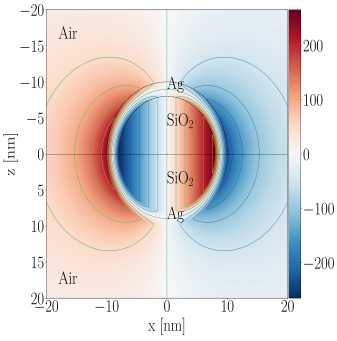

(f) $\hbar\omega = 3.82$, $\chi^{(2)} = 0.8$.

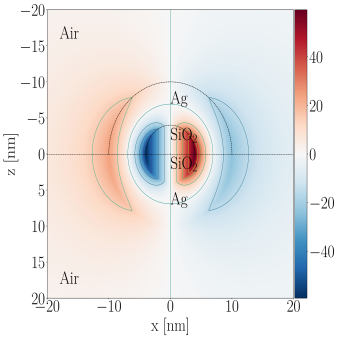

(g) $\hbar\omega = 3.74$, $\chi^{(2)} = 0.4$.

Figure 5.1 Contour plots in the xz-plane of the electrostatic potential calculated with GranFilm at the resonance energy of the polarizability of free-standing spheres or coated spheres in vacuum: a single silver sphere (a), a silver sphere with thin (b) and thick (c) dielectric coating, and a thin (d)/(f) and a thick (e)/(g) layer of metallic coating on a dielectric core (metallic nanoshell). The simulation parameters are indicated in the upper right corner of the figure. The imaginary part of the experimental bulk dielectric function of silver has been reduced to 1% of its original value.

- a silver coated silica sphere

in vacuum calculated with GranFilm and using the values in our dielectric database for the experimental bulk dielectric functions. The same value for the outer radius, $R = 10\,\text{nm}$, is used for all the objects. To obtain these results, the imaginary part of the experimental bulk dielectric function of silver $\text{Im}\{\varepsilon_{\text{Ag}}\}$ has been reduced to 1% of its original value. By doing this, the eigenmode peak is sharpened and the oscillation eigenmode is seen more clearly. The GranFilm truncated sphere morphology was used by setting the substrate to air, $\varepsilon_{\text{Air}} = 1 + i0$, and choosing the 'buried' part of the sphere to be silver.

The calculated resonant frequency for the free standing sphere at $\hbar\omega = 3.53\,\text{nm}$ [Fig. 5.1(a)] matches with to the value we would expect form the Frölich condition [8,73]. A clear dipolar spreading of the polarization charges is observed.

Assuming a constant outer radius, we now turn to a silver particle coated with silica. The presence of the dielectric coating has two effects, dependent on its thickness [Fig. 5.1(b)/Fig. 5.1(c)]. The first observation is an obvious decrease of the the amplitude of the electrostatic potential [Fig. 5.1(b)/Fig. 5.1(c)], caused by the smaller metallic core. Indeed, as observed from the location of the 'hot-spots' of the potential [Fig. 5.1(c)], polarization happens only at the surface of the metallic object. Furthermore, the resonance's energy position is red-shifted compared to the non-coated NP due to a screening by the dielectric shell. A similar shift would be observed at the limit of an infinite dielectric shell *i.e.* by embedding the metallic core in pure silica. At last, the dipolar form of the polarization charges is the same as for the non-coated particle.

We now turn to the more intersting case of metallic nano-shells with dielectric cores. Two resonances are observed for both the thin [Fig. 5.1(d)/Fig. 5.1(f)] and the thick [Fig. 5.1(e)/Fig. 5.1(g)] metallic shell. These two different resonance modes have been explained by a quantum mechanical *hybridization approach* for plasmons [17,74,75] in nanoshells. The energies for which the plasmon resonances occur in such structures are sensitive to the metal shell's inner and outer radii. The resonances in the nanostructure arise from the mixing of resonances of the sphere (outer surface of the metallic layer) and the cavity (inner surface of the metallic layer) [75]. Observing the maps of the electrostatic potential, we realize that there are two different types of modes: (i) an *inner mode* where the oscillation charges are placed inside the coating which is down-shifted in energy (red-shifted) as compared to the non-coated particle and (ii) the antisymmetric mode, called an *inner-outer mode*, which is up-shifted (blue-shifted) in energy as compared to the non-coated sphere. The oscillation charges are placed on the outer and inner surface of the metallic shell. As the thickness of the metallic layer increases, the deviation in energy from the full silver sphere decays; both modes become progressively degenerated.

5.3 Truncated coated supported particles

In order to perform a detailed analysis of the combined effect of coating, substrate and island-island interaction, we have defined three test cases:

- *System 1* is the 'classical' test bed used throughout this thesis: truncated silver particles on an alumina substrate.
- *System 2* consists in truncated NPs with a dielectric silica coating and a metallic silver core on an alumina substrate.
- *System 3* is a the reverse geometry with respect to that of *System 2*, namely a silica core and a silver nanoshell supported by alumina.

For all the systems, the outer radius of the (untruncated) spherical particles $R = 10\,\text{nm}$ is assumed to be constant, if not stated. Regarding the inter-particle interaction, particles are organized on a square lattice with a lattice constant $L = 31\,\text{nm}$.

As already discussed in Ch. 1, the structure of the SDRS-curves are governed by the plasmon oscillation modes. To link the macroscopic and microscopic observables in these systems, we have systematically compared the theoretical SDRS curves generated with GranFilm without ($\kappa = 1$) and with the reduced damping ($\kappa = 0.01$) of the experimental bulk dielectric function, and the inverse of the absolute value of smallest eigenvalue of the matrix system. All following figures will show how the SDRS-signal for both s and p polarization is intimately related to the eigenvalues of the left-hand-side matrix of the linear system defined in Eq. (5.1). In order to be able to distinguish the modes which are close in energy, the imaginary part of the experimental bulk dielectric function of silver is reduced, typically to 1% of its original value. Furthermore, when $\kappa \neq 1$ we will mark the three most intense modes in the plot by (energy, intensity) to compare the shifts of the modes in the different systems.

System 1

As a reference, we start the analysis with the response of System 1 at truncation ratio $t_r = 0.01$ and polar angle of incidence $\theta_0 = 45°$. The SDRS-spectra for s- and p-polarized incident light are displayed in Figures 5.2(a)-(b), respectively, for non-modified imaginary part of bulk dielectric function ($\kappa = 1$). Figures 5.2(c)-(d) present the corresponding SDRS signal obtained with reduced damping ($\kappa = 0.01$) on silver dielectric function on the right y-axis, while one over the smallest eigenvalue in absolute value for $m = 0$ and $m = 1$ is displayed on the left y-axis. For both polarizations, the most prominent peaks in the $(\Delta R/R)_\nu$-curves are marked with their energy position and their amplitude (or intensity).

The electric field in the plane of the substrate for s-polarization, $(\Delta R/R)_s$ is only driven by the $m = 1$ modes. At the opposite, for p-polarization, both eigenvalues $m = 0$ and $m = 1$ contribute to the response. For both polarizations, the inverse of the absolute value of the smallest eigenvalues and the computed SDRS-curve display a complex structure for energy values higher than 3.6 eV due to the close proximity of several modes.

As one could expect, by comparing the results presented in Figs. 5.2(c)-(d) peaks in the $(\Delta R/R)_\nu$-curves are accompanied by a feature at the same energy for $\min|\lambda_j|^{-1}$-curves for $m = 0$ or $m = 1$ or, in other words, when the matrix system is resonant. One should notice from the same figures that the inverse is not necessarily false; the existence of an eigenmode (a resonance) for the system is not necessarily

Variable	Value
R [nm]	10.0
t_r	0.01
N_{energy}	10000
κ	0.01
L [nm]	31.0
θ_0	45°
M	16

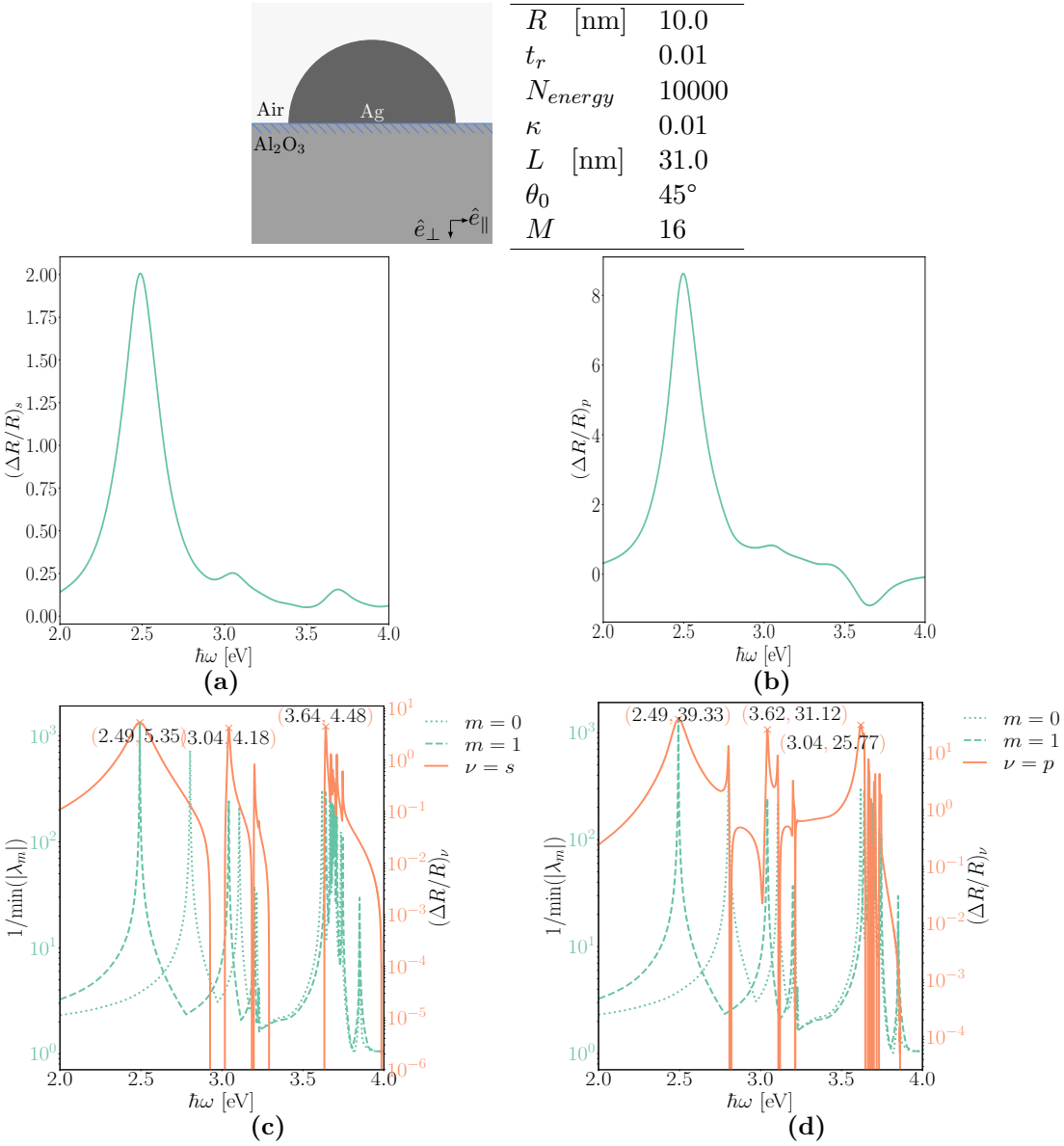

Figure 5.2 System 1: SDRS-curves calculated in s (a) and p (b) polarized light with bulk dielectric function ($\kappa = 1$) compared, at reduced damping ($\kappa = 0.01$), to the inverse of the absolute value of the smallest eigenvalue (left scale; $m = 0, 1$) and SDRS-signal (right scale) (c)-(d). In (c)-(d) the three most intense peaks are marked by (energy, intensity). Simulation parameters are given above the figure.

associated with a feature in the corresponding $(\Delta R/R)_\nu$-curve. For this to be the case, the incident field must strongly couple into the resonance, and that may, or may not, be the case.

Finally, when the damping increases, the various resonances broaden in intensity which causes an overlap between the modes. As a consequence, the modes are not anymore properly defined and will mix. Nevertheless, the most prominent features can still be assigned to distinct oscillation modes that will be described later on.

System 2

For System 2 (the dielectric shell configuration), several SDRS-curves are displayed in Figs. 5.3(a)-(b) for different thicknesses of the shell. As the thickness of the shell decrease all the curves are red-shifted, as expected, from a simple screening effect. Of course, the intensity scales with the size of the core, that is to say, with the amount of polarizable metal. As the core size increases, the SDRS curve approaches the ones found for System 1 [Figs. 5.2(a)-(b)]. The overall shape of the curves is poorly affected by the change in coating thickness. This suggests that the dielectric coating is simply shielding the plasmonic response of the metallic core.

The same analysis of eigenmodes as for System 1 was performed. The resulting SDRS-signal (solid orange lines) are then plotted for a thicker [$\chi^{(2)} = 0.4$, (e)/(c)] and a thinner [$\chi^{(2)} = 0.8$, (e)/(c)] dielectric shell. Compared to the non-coated case, the behavior of System 2 appears more complex, with an energy shift of main resonances being more prominent for the larger core.

System 3

The SDRS-curves for different core sizes for System 3 are displayed in Fig. 5.4. For a thick core (*i.e.* a thin metallic coating), the main peak in the SDRS-signal for the actual metal dielectric function ($\kappa = 1$) is red-shifted outside the energy range of our tabulated experimental bulk dielectric functions. Beside an overall shift in energy, the shape of the curves do not seem to be impacted by the core radiuses [Figs. 5.4(a)-(b)].

Switching from a truncated sphere to a shell geomtetry for the metallic part dramatically alters the SDRS-signal in terms of a shift in the energy position of the highest peak and its amplitude. Also, the set of eigenmodes seem to be richer. As for the coated particle in homogeneous media [Figs. 5.1(d)-(g)], the thinner the coating, the more prominent is the effect.

5.4 The oscillation modes

According to the excess field formalism, the reflection and transmission amplitudes [Eq. (2.27)] are driven only by the surface susceptibilities, parallel to the surface component, γ, in s-polarization, and by both the parallel and perpendicular components, both γ and β, in p-polarization. As these quantities are directly connected to the

Variable	Value
R [nm]	10.0
$\chi^{(2)}$	$\{0.4, 0.6, 0.8\}$
t_r	0.01
N_{energy}	10000
κ	0.005
L [nm]	31.0
θ_0	45°
M	16

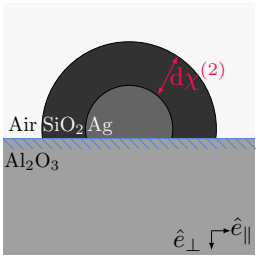

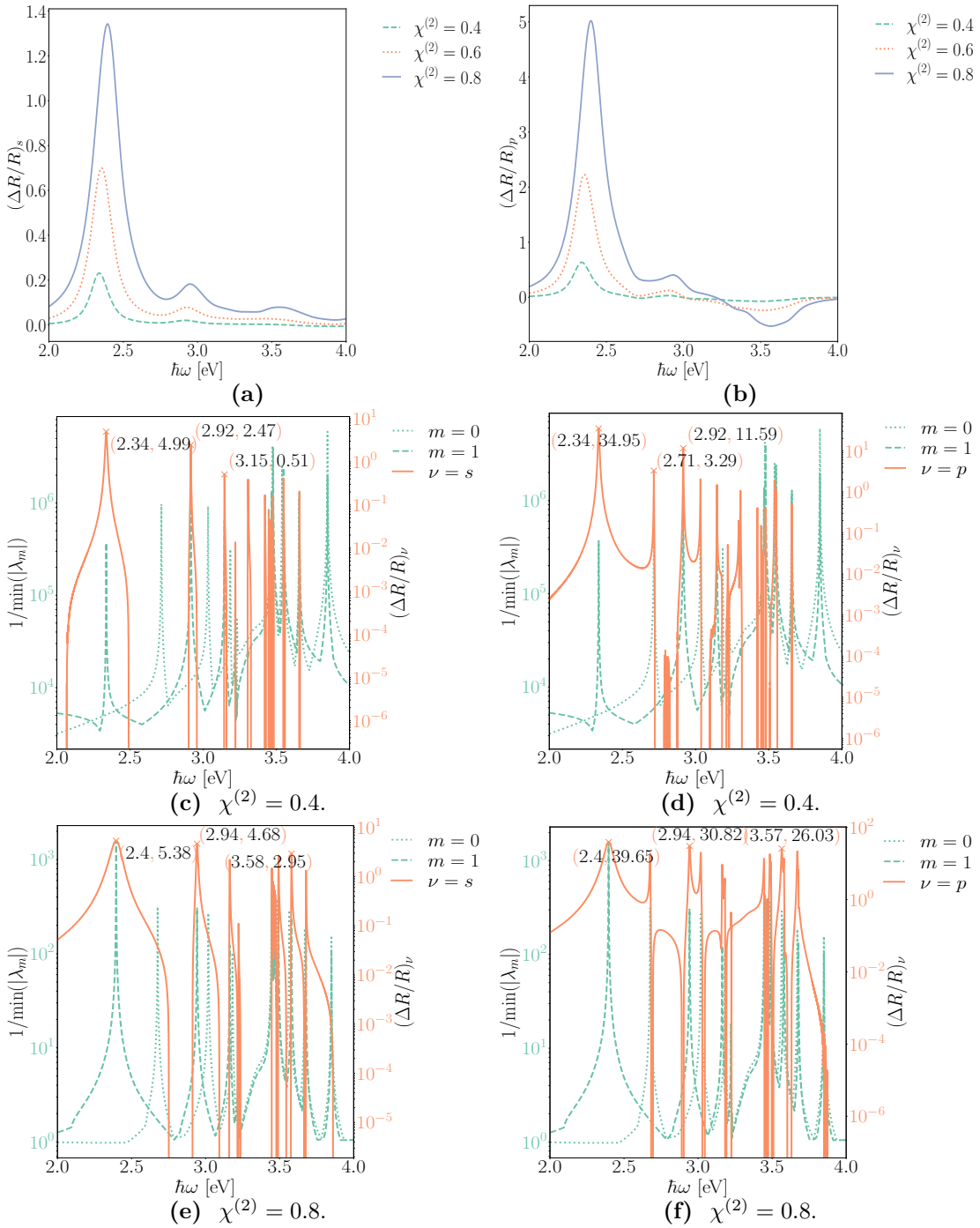

Figure 5.3 Same figure as Fig. 5.2 but for a dielectric silica shell on a silver core. SDRS-curves are calculated in s (a) and p (b) for the indicated core size. Calculations at reduced damping are performed for two dielectric shell thicknesses: $\chi^{(2)} = 0.4$ (thick) and $\chi^{(2)} = 0.8$ (thin).

Variable	Value
R [nm]	10.0
$\chi^{(2)}$	$\{0.4, 0.6, 0.8\}$
t_r	0.01
N_{energy}	10000
κ	0.01
L [nm]	31.0
θ_0	45°
M	16

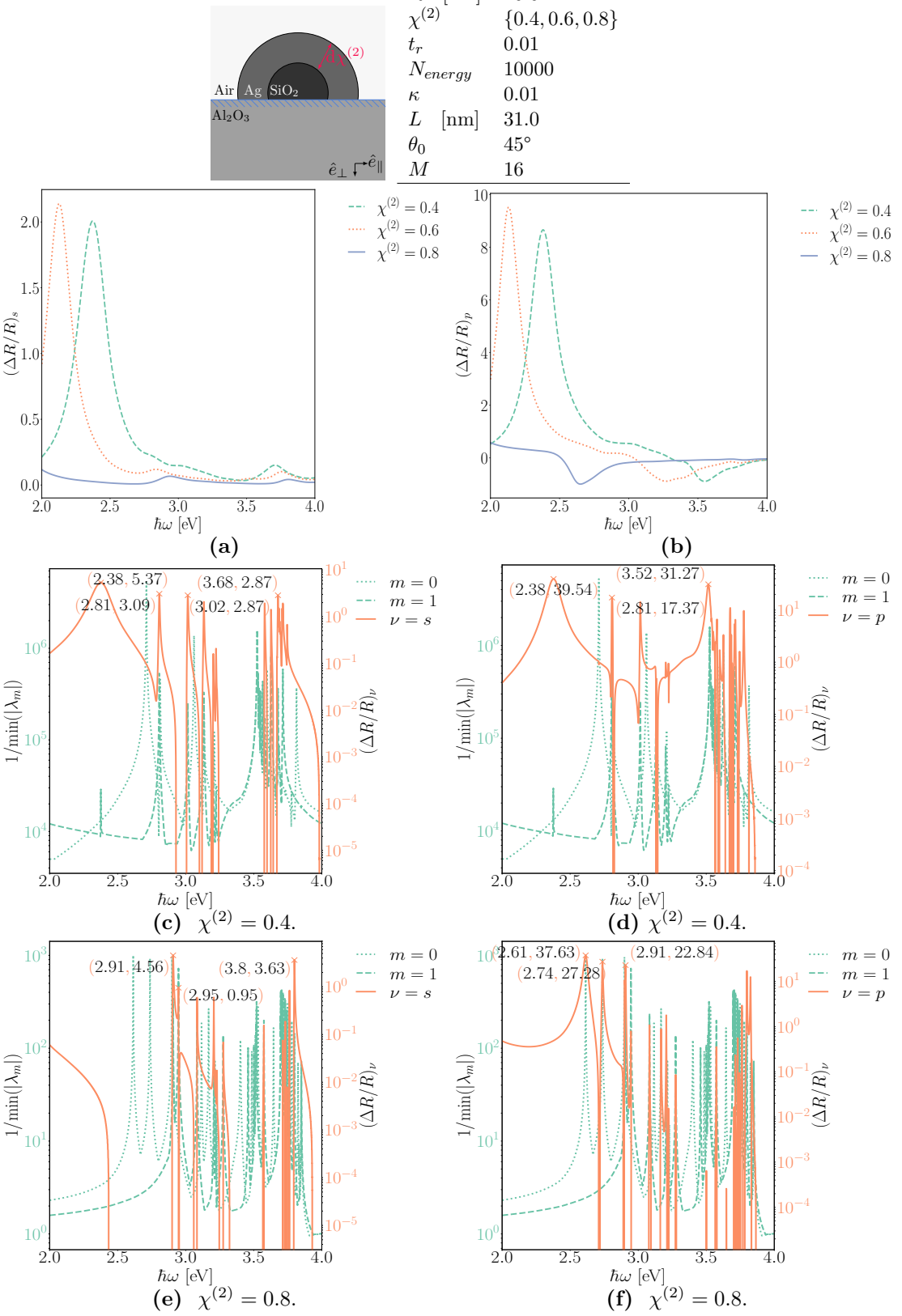

Figure 5.4 SDRS-curves calculated in s (a) and p (b) polarized light for changing core radius and a comparison of these with the inverse of the absolute value of the smallest eigenvalue (c)-(f) of System 3. In (c)-(f) the three most intense peaks are marked by (energy, intensity), scaling of $\mathrm{Im}\{\varepsilon^{\mathrm{Ag}}\}$ was used. Simulation parameters are given above the figure.

particle polarizabilities, we will analyze the form of the direction-dependent polarizabilities for the previous described *i.e.* Systems 1, 2, and 3, to further study the link between the micro- and macroscopic properties for the system. This link is even more transparent in the long wavelength approximation of the SDRS-signal [Eq. (2.30)]. In this case, the SDRS-curves are directly driven by $\mathrm{Im}\{\gamma\}$ and $\mathrm{Im}\{\beta\}$ [20, 41, 42], and therefore the absorption in the particles.

In the following, we will present plots of the imaginary part of the polarizabilities normalized by the particle volume (solid orange lines) together with one over the smallest eigenvalue of the matrix system in absolute value (green dashed/dotted lines). The three most intense values of the direction dependent polarizability will be marked with (energy, intensity) in each plot. To study also the polarization charges, the electrostatic potential will be mapped at the energy of the corresponding resonance. It should be kept in mind that parallel modes ($m = 1$) have a plane of symmetry perpendicular to the page ($x = 0$ plane) and perpendicular modes ($m = 0$) have a rotational symmetry along the $z-$axis. The former is excited by the component of the electric field parallel to the surface and appears in $\mathrm{Im}\{\alpha_{\parallel}\}/V$. The latter is excited by the electric field normal to the surface and appears in $\mathrm{Im}\{\alpha_{\perp}\}/V$. All relevant system parameters of the simulations will be indicated on the top of each figure.

System 1

To establish a reference, we start again with the discussion of System 1, the basic configuration. The imaginary part of the normalized direction-dependent polarizabilties and contour plots of the electrostatic potential in the xz-plane are presented in Fig. 5.5.

Two main modes are clearly singled out: one at $\hbar\omega = 2.49\,\mathrm{eV}$ for the parallel component of the polarizabilities [Fig. 5.5(a)] and one at $\hbar\omega = 3.62\,\mathrm{eV}$ for the perpendicular component [Fig. 5.5(b)]. The corresponding contour maps in the xz-plane of the potential are presented in Fig. 5.5(c), and Fig. 5.5(h), respectively. The distribution of the oscillation charges associated with those modes with the highest intensities resemble dipoles oriented in the directions parallel and perpendicular to the substrate. In line with the case of a free standing sphere, we will refer to these modes as *dipole modes*. We already saw this form of the oscillation charges in Figs. 4.8(c)-(d), but for a different geometry configuration of the system.

Note that for energies $\hbar\omega > 3.8\,\mathrm{eV}$, neither in the parallel ($m = 1$) nor the perpendicular ($m = 0$) directions match with a peak in the eigenmodes. The observed peak in $\mathrm{Im}(\alpha_i)/V$ is assigned to bulk absorption through interband transitions in silver.

More interestingly, for both directions, the truncation of the particle and the introduction of the substrate have introduced 'exotic' modes as compared to what we could observe for a free standing sphere. These modes are placed at $\hbar\omega = 3.01\,\mathrm{eV}$ [Fig. 5.5(d)] and $\hbar\omega = 3.64\,\mathrm{eV}$ [Fig. 5.5(e)] for the parallel polarizability, and at $\hbar\omega = 2.81\,\mathrm{eV}$ [Fig. 5.5(f)] and $\hbar\omega = 3.10\,\mathrm{eV}$ [Fig. 5.5(g)] for perpendicular one. The pattern of the oscillation charges can not be identified directly as a dipole. For instance, in the mode shown in Fig. 5.5(e), despite a strong dipolar character, the polarization charges are

Variable	Value
R [nm]	10.0
t_r	0.01
N_{energy}	10000
κ	0.01
L [nm]	31.0
M	16

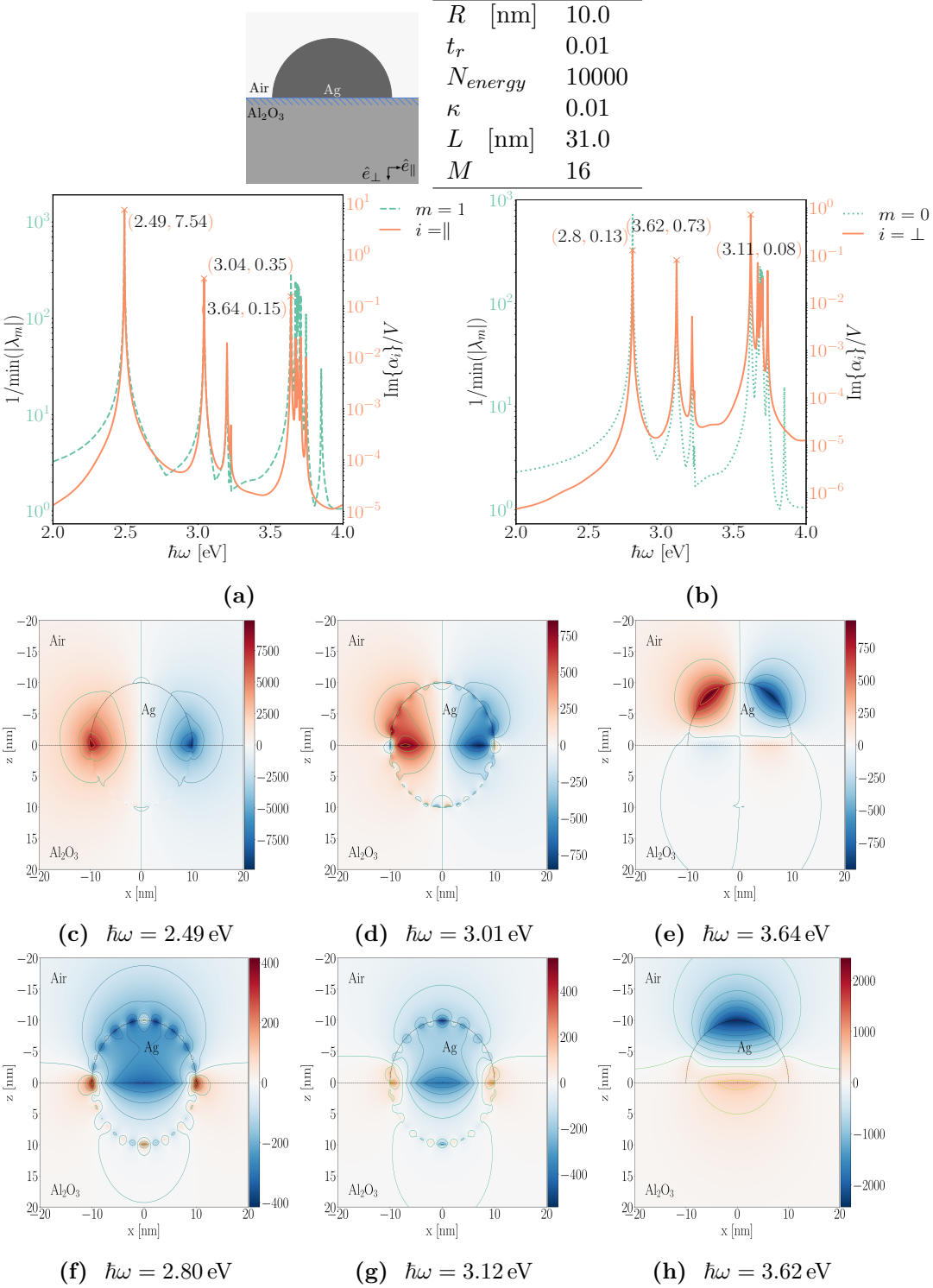

Figure 5.5 The normalized imaginary part of the polarizabilities plotted with the inverse of the absolute value of the smallest eigenvalue parallel (a) and perpendicular (b) to the substrate. The three most intense peaks are pinpointed, and the corresponding part of the potential are mapped for the parallel (c)-(e) and perpendicular (f)-(h) directions. Simulation parameters are given above the figure.

shifted to the top of the particle. This mode also involves some weaker polarization at the interface with the substrate. It has a quadrupole character. A similar mode shown in Fig. 5.5(f) has a dipole character due to a ring of charge at the interface and an isolated charge at the top of the particle.

After close inspection of the form of the potentials in Figs. 5.5(c)-(h), two types of polarization charge patterns are identified: those arising at the interface between the sphere and the substrate [(c), (d), (f), (g)], and those arising at the interfaces between either the particle surface or the substrate [(e), (h)].

All of these modes have already been discussed thoroughly and linked to experimental spectra obtained in a vapor deposition experiment by Lazzari *et al.* in Refs. 20, 32. They have been shown to be 'universal', *i.e.* driven by the shape of the particle. They appear at given values of the real part of the metal dielectric function. It is interesting to see how these modes will change in terms of polarization patterns, positions in energy and strengths when a coating layer is introduced in the system.

System 2

The same kind of plots for the imaginary part of the polarizabilities and for the electrostatic potential at the same value of the truncation ratio are presented in Fig. 5.6 for System 2. Notice that the artificial damping of the experimental bulk dielectric function of silver was reduced to 0.5% to clearly see the oscillation modes. Because of this further reduced damping, as compared to System 1, all intensities are increased as compared to the non-coated case.

The 'dipolar' peaks are red-shifted from $\hbar\omega = 2.49\,\text{eV}$ to $\hbar\omega = 2.40\,\text{eV}$ for the direction parallel to the surface [Fig. 5.6(a)], and from $\hbar\omega = 3.62\,\text{eV}$ to $\hbar\omega = 3.57\,\text{eV}$ for the perpendicular [Fig. 5.6(b)] direction, as compared to the non-coated truncated particle. Again, for energy values higher than $\hbar\omega > 3.8\,\text{eV}$, eigenmodes are absent for both directions. As compared to System 1, the set of peaks in the polarizabilities around $\hbar\omega = 3.8\,\text{eV}$ are shifted slightly downwards in energy, as expected. This global red-shift results from the screening of the silica layer.

Inspecting the electrostatic potential maps, the oscillation pattern corresponding to the highest peak in the parallel direction follows the well-known dipole form [Fig. 5.6(c)]. Interestingly, the potential pattern corresponding to the most intense peak in the perpendicular direction has 'changed' from a clear dipolar form as seen in System 1 [Fig. 5.5(h)], to a different form [Fig. 5.6(h)]. However, despite some differences, a parallel can be drawn between the non-coated [Fig. 5.6] and silica coated [Fig. 5.6] patterns of polarization charge; the dielectric coating do not drastically affect the physics of the polarization of the metallic particle core.

System 3

As already mentioned, we expect different and more complex oscillation patterns for System 3 (the metallic shell configuration) than for the two other systems. Thus, we have chosen to study separately the effect of shell thickness and truncation ratio on the imaginary part of the direction-dependent polarizability and the oscillation patterns.

Variable	Value
R [nm]	10.0
$\chi^{(2)}$	0.8
t_r	0.01
N_{energy}	10000
κ	0.005
L [nm]	31.0
M	16

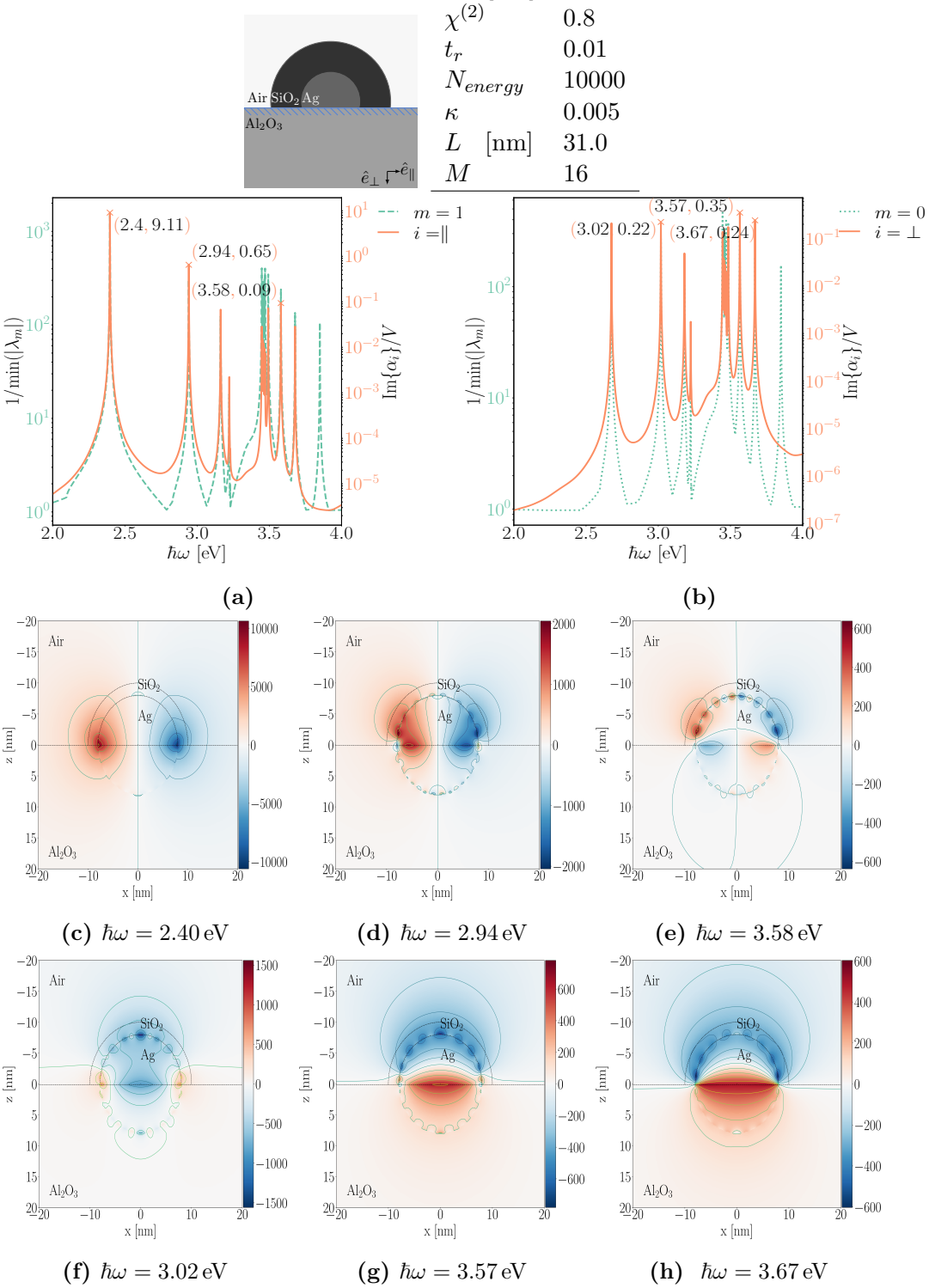

Figure 5.6 Same as Fig. 5.5 but for a silver core coated by a thin silica layer.

Varying the shell thickness

The types of modes observed in System 3 for a thick and thin shell are displayed in Fig. 5.7 and Fig. 5.8, respectively. The simulation results obtained for these configurations indicate, once again, that one can observe inner-outer and inside polarization patters for System 3.

For a thick shell, $\chi^{(2)} = 0.4$, the parallel 'dipolar' mode is blue-shifted $\hbar\omega = 2.38\,\text{eV}$ [Fig. 5.7(c)] relative to the same mode in System 1 [Fig. 5.5(c)]. For a configuration with a thinner shell, the mode with the highest amplitude is shifted to $\hbar\omega = 2.91\,\text{eV}$ [Fig. 5.8(a)]. Looking at the shape of the electrostatic potential, it appears that also the oscillation pattern has changed along this direction. The most intense mode in the thick shell configuration had charges at the substrate/sphere interface [Fig. 5.7(c)]. This seems to be replaced by a mode with charges only at the sphere interface [Fig. 5.8(c)] for a thinner shell.

The 'dipolar' mode in the direction perpendicular to the substrate is red-shifted in energy when changing from a thicker to a thinner shell. The most intense mode in the case of the thicker shell is observed at $\hbar\omega = 3.52\,\text{eV}$ [Fig. 5.7(b)]. For the configuration with the thinner shell, the most intense mode is observed at $\hbar\omega = 2.61\,\text{eV}$ [Fig. 5.8(b)]. The tendency of a shift of the main peak out of the range of accessible energy values was also observed for System 3 in SDRS-curves in Fig. 5.4.

Varying the truncation ratio

We already know that increasing the truncation ratio (or descreasing the aspect ratio) of the particles in an non-coated system will induce a strong blue-shift in energy and decrease in the amplitude of the parallel polarizability, and a weaker red-shift for the perpendicular polarizability [see Figs. 4.11(a)-(b)]. Interestingly, the trends when changing truncation ratio in System 3 seem to be more complex.

The parallel oscillation pattern for the dipolar mode in this configuration of System 3 with $t_r = 0.6$ [Fig. 5.9(c)] is not the same as observed for $t_r = 0.01$ [Fig. 5.7(c)]. Still, some similarities can be observed. The perpendicular dipolar mode is now shifted to $\hbar\omega = 2.35\,\text{eV}$ [Fig. 5.9(f)]. Inner-outer modes of similar pattern that were observed at $t_r = 0.01$ are found again at higher energy for the parallel [Fig. 5.8(e) $\rightarrow$ Fig. 5.9(e)] and lower energy for the perpendicular [Fig. 5.8(h) $\rightarrow$ Fig. 5.9(h)] direction.

In this configuration of System 3 there are modes which appear in both the parallel [Fig. 5.9(d)] and perpendicular [Fig. 5.9(g)] directions at the same energy value $\hbar\omega = 2.70\,\text{eV}$. Thus, the electrostatic potential appears as a combination of these two modes, and there will be no well-defined symmetry or anti-symmetry with respect to the plane $x = 0$ for the whole system.

5.5 Maps of polarizabilities versus truncation ratio and shell-thickness

The study of the imaginary part of the polarizabilities and the corresponding potential maps of the electrostatic potential at the resonance energies for different configurations

Variable	Value
R [nm]	10.0
$\chi^{(2)}$	0.4
t_r	0.01
N_{energy}	10000
κ	0.01
L [nm]	31.0
M	16

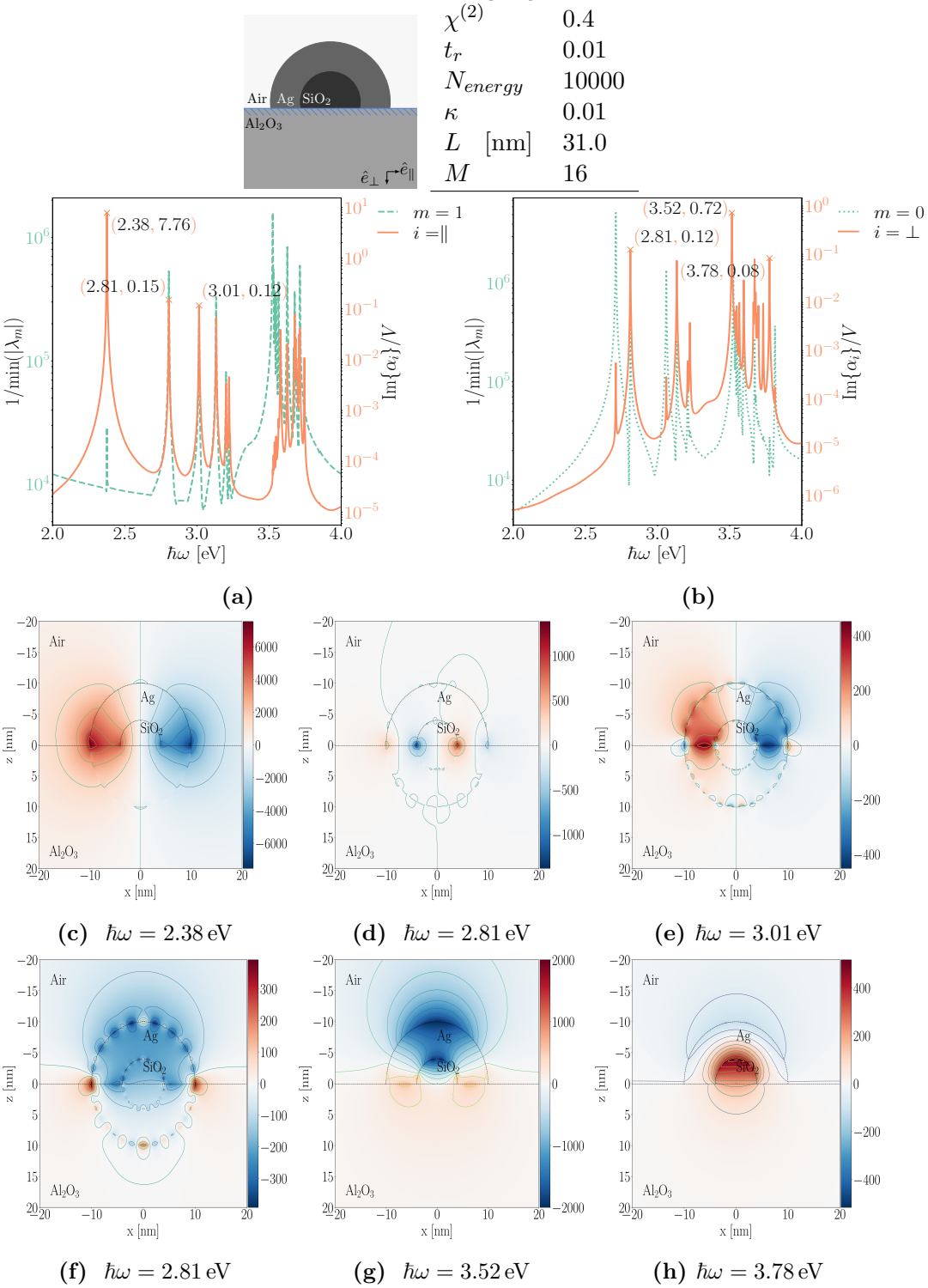

Figure 5.7 Same as Fig. 5.5 but for a thick silver layer ($\chi^{(2)} = 0.4$) on a silica core.

Variable	Value
R [nm]	10.0
$\chi^{(2)}$	0.8
t_r	0.01
N_{energy}	10000
κ	0.005
L [nm]	31.0
M	16

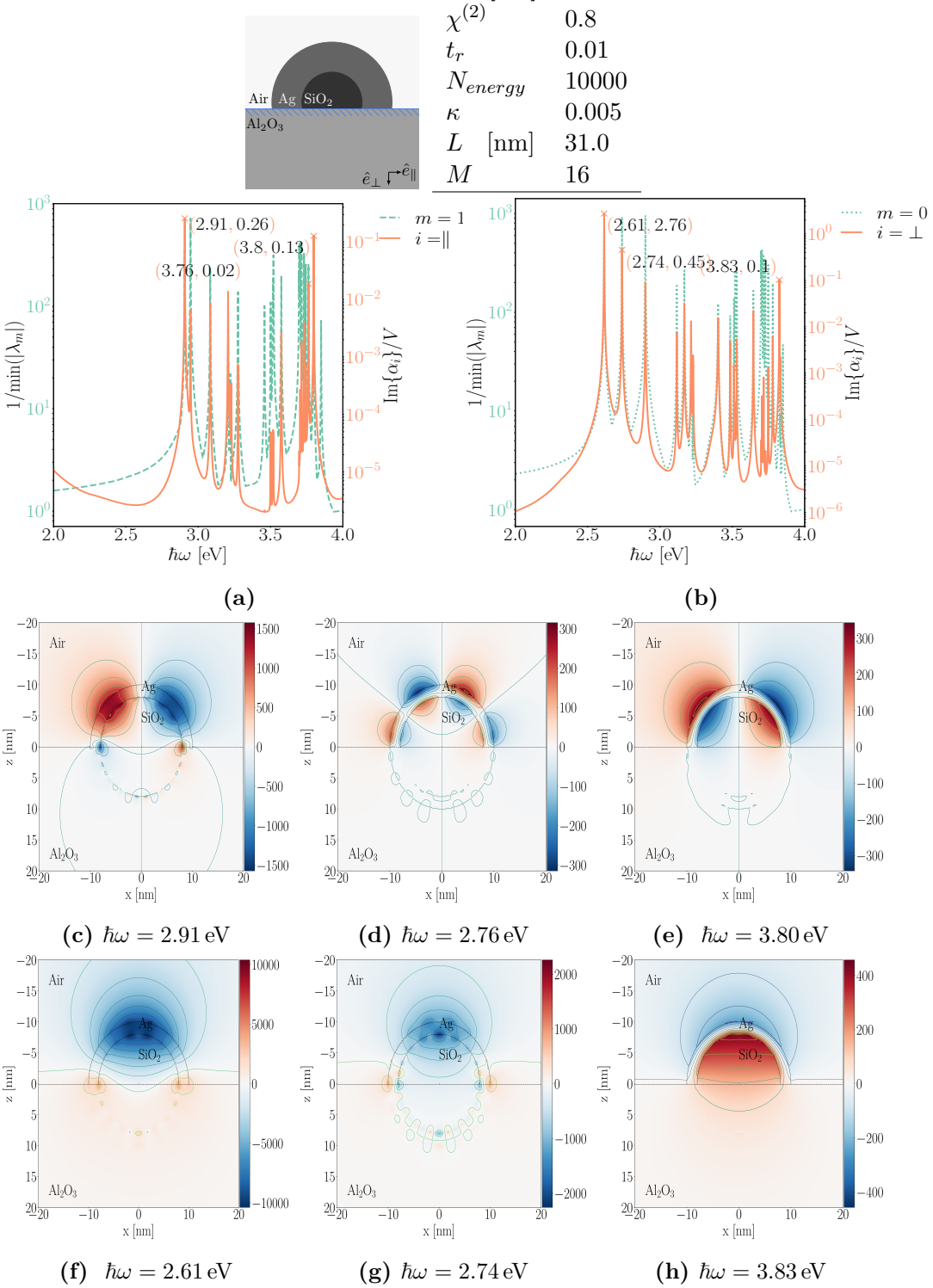

(a) **(b)**

(c) $\hbar\omega = 2.91\,\text{eV}$ **(d)** $\hbar\omega = 2.76\,\text{eV}$ **(e)** $\hbar\omega = 3.80\,\text{eV}$

(f) $\hbar\omega = 2.61\,\text{eV}$ **(g)** $\hbar\omega = 2.74\,\text{eV}$ **(h)** $\hbar\omega = 3.83\,\text{eV}$

Figure 5.8 Same as Fig. 5.5 but for a thin silver layer ($\chi^{(2)} = 0.8$) on a silica core.

Variable	Value
R [nm]	10.0
$\chi^{(2)}$	0.8
t_r	0.60
N_{energy}	10000
κ	0.005
L [nm]	31.0
M	16

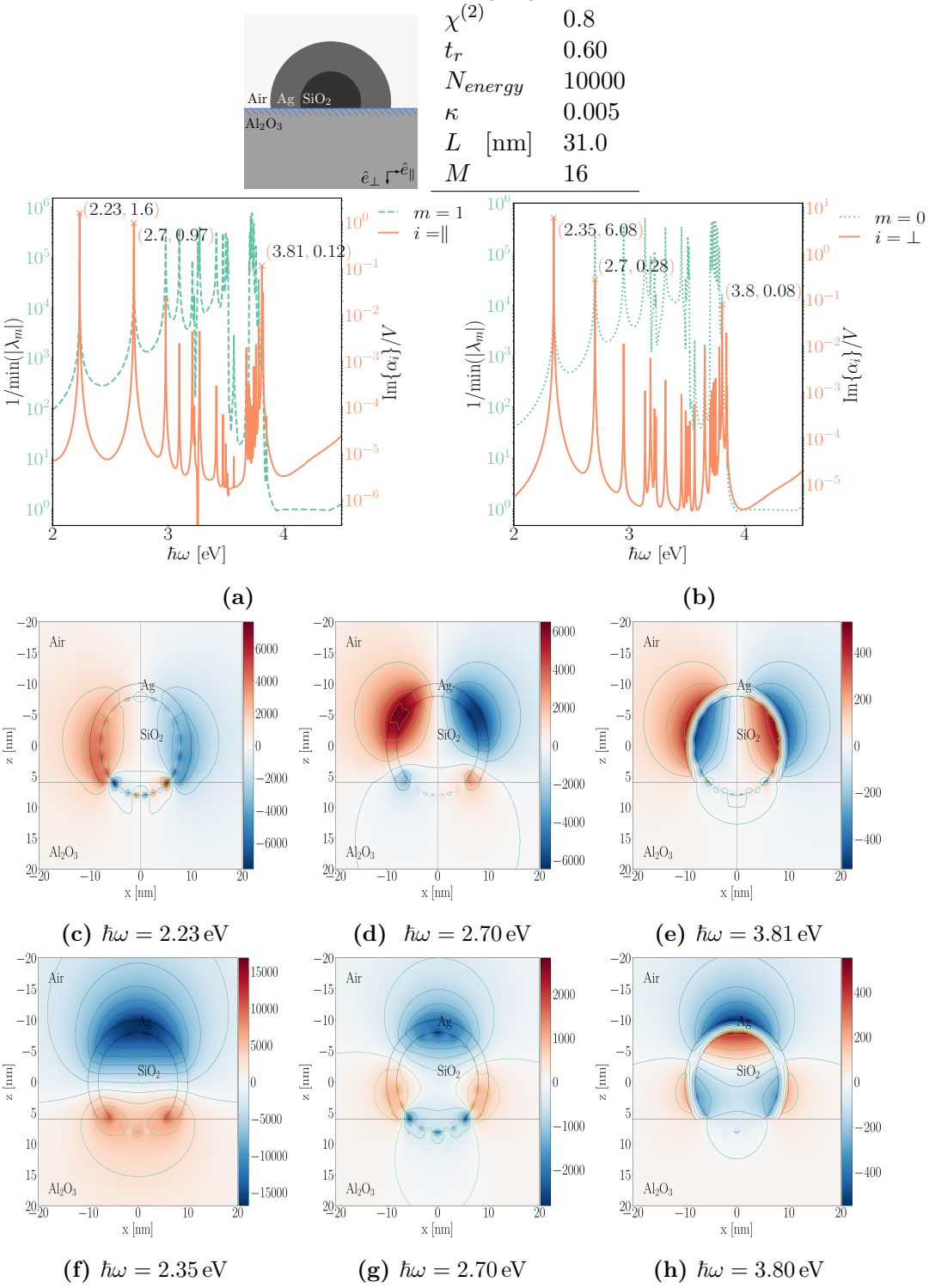

Figure 5.9 Same as Fig. 5.8 but for a truncation of $t_r = 0.6$.

(Systems 1-3) have taught us that the oscillation modes are sensitive to both the core radius and the aspect ratio of the particles. Furthermore, the most intense, the 'dipolar', mode of the various systems displayed different oscillation patters of the charges. For instance, see the difference of the oscillation patterns between Fig. 5.5(c) (System 1), and Fig. 5.8(c) and Fig. 5.9(c) (System 3).

In an attempt to track the energy positions and the intensities of the oscillation eigenmodes, maps of the imaginary part of the direction-dependent polarizabilities have been generated as a function of energy for a changing truncation ratio t_r or a changing thickness of the coating layer, *i.e.* changing core thickness for a constant outer radius $\chi^{(2)}$. To compare the results, the same reduction factor ($\kappa = 0.001$) of the experimental bulk dielectric function of silver has been used. As the impact of the island-island interaction is crucial, as shown by the red-shifts in the reflectivity curves in *s*-polarization [see Fig. 4.9(b)], all the potential maps in this section are generated for a system without and with island-island interaction of dipolar order. To clearly see the difference with and without the island-island interaction the lattice constant of the systems was reduced to 21.1 nm. In what follows, the systems without island-island interaction will be displayed to the left, [subfigures (a) and (c)], whereas the systems with island-island interaction at dipolar order will be displayed to the right [subfigures (b) and (d)]. Each contour plot represents simulations for 250 different sample geometries.

5.5.1 Dependence of the *truncation ratio*

For the three previously introduced systems, maps of the imaginary part of the parallel and perpendicular polarizabilities have been generated for a changing truncation ratio in the interval $t_r = 0.01 - 0.79$ (Figs. 5.10-5.12). Above or below this range, convergence issues in the simulation results are encountered [46].

System 1

At truncation ratio $t_r = 0.01$, three eigenmodes are clearly singled out in Fig. 5.10, in the parallel direction located at energies $\hbar\omega = 2.49, 3.01, 3.64\,\text{eV}$ [Fig. 5.10(a)], and the perpendicular direction at energies $\hbar\omega = 2.81, 3.10, 3.62\,\text{eV}$ [Fig. 5.10(c)]. The dipolar modes with the highest intensities stand out as red curves in the map. Upon increasing t_r and getting closer to the full sphere configuration, the different modes tend progressively towards the same energy. This results from the well-known trend of splitting of resonant modes upon flattening [1, 8, 20].

When the island-island interaction is taken into account, a strong red-shift of the low-energy parallel mode and a blue-shift of the high-energy perpendicular mode are found. This is, as expected, on the basis of dipole-dipole coupling arguments. For instance, the mode at $\hbar\omega = 2.50\,\text{eV}$ [Fig. 5.10(a)] shifts to $\hbar\omega = 2.15\,\text{eV}$ [Fig. 5.10(b)]. For the modes observed at higher-energy values, $\hbar\omega > 3.60\,\text{eV}$, the imaginary part of the normalized perpendicular polarizabilities is slightly blue-shifted [Fig. 5.10(d)]. For $t_r = 0.45$ a mode crossing at $\hbar\omega = 3.6\,\text{eV}$ is observed. The red intensity curves

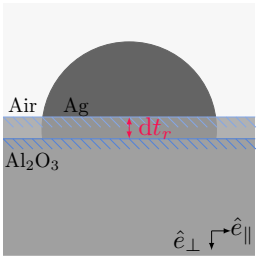

Variable	Value
R [nm]	10.0
t_r	dt_r
N_{energy}	10000
κ	0.001
L [nm]	21.0
M	16

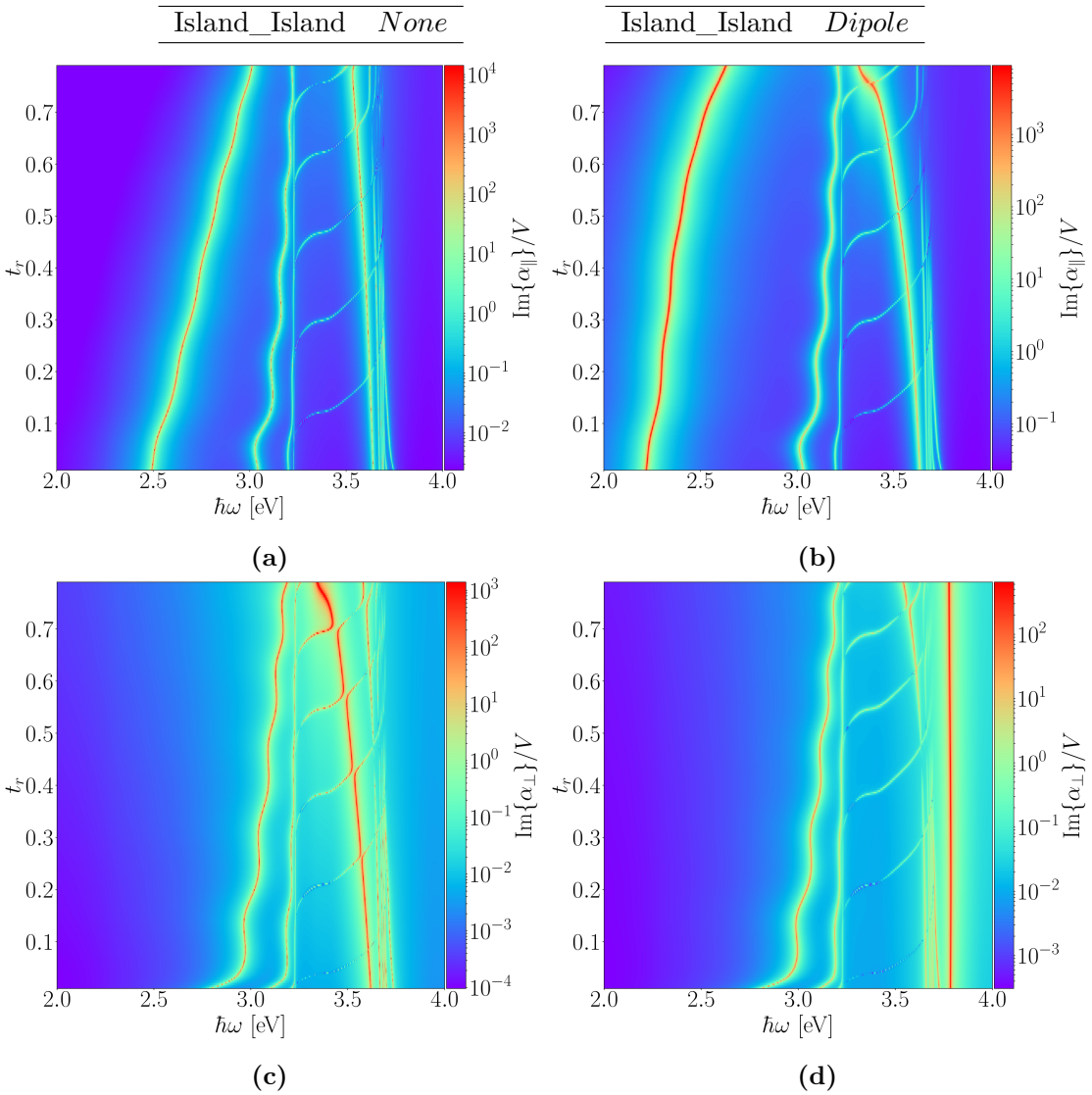

Figure 5.10 Maps of the imaginary part of the direction-dependent polarizabilities of System 1 when changing truncation ratio in the interval $t_r = 0.01 - 0.79$ without [(a)/(c)] and with [(b)/(d)] island-island interaction at dipolar order. Simulation parameters are indicated at the top of the figure.

meet at one point before they split again. This phenomenon is not clearly observed anymore if the island-island interaction is taken into account [Fig. 5.10(c)].

System 2

The maps generated with a variable truncation ratio for System 2 without the island-island interaction [Fig. 5.11(a) and Fig. 5.11(c)] are slightly red-shifted as compared to the non-coated case. Except for a clearer distinction between the modes at higher energies $\hbar\omega > 3.5\,\text{eV}$, the overall evolution for $t_r < 0.40$ is similar to the non-coated case. At higher values of the truncation ratio $t_r > 0.40$, the pattern becomes more intricate. Furthermore, the logarithmic scale in the color maps are one order of magnitude lower than what we found in the non-coated case, an obvious effect of the reduction of the metal volume. The tracking of the dipolar modes are still possible to do over the whole range of chosen truncation ratio values.

The global effect for System 2 for changing truncation ratio with island-island interaction to dipolar order [Fig. 5.11(b) and Fig. 5.11(d)] is the same as for non-interacting particles [Fig. 5.11(a) and Fig. 5.11(c)] except for the blue-shift of the dipolar perpendicular mode starting at $\hbar\omega = 3.5\,\text{eV}$ around $t_r = 0.4$. In general, also in this system, the position of the low-energy mode in the parallel mode map is red-shifted. The position of high-energy mode in the perpendicular mode map is blue-shifted, but at a smaller amount than the shifts observed in System 1 while including the island-island interaction to dipolar order [Fig. 5.10(b) and Fig. 5.10(d)].

System 3

Again, as shown by the maps Fig. 5.12(a) and Fig. 5.12(c), the evolution for System 3 is more complex and the mode structure is richer than what we saw in the contour maps for System 1 and 2. As for the previous configurations, the three most intense peaks for the parallel direction at $\hbar\omega = 2.91, 3.76, 3.80\,\text{eV}$ and the perpendicular direction at $\hbar\omega = 2.61, 2.74, 3.83\,\text{eV}$ for truncation ratio $t_r = 0.01$ are consistent with the peaks seen in Figs. 5.8(a)-(b).

Apart from the modes around $\hbar\omega \geq 3.6\,\text{eV}$, it is not possible to track a single eigenmode over the total truncation ratio interval. This was already indicated by the observed shifts of the direction-dependent polarizabilities and the potential maps discussed in Figs. 5.8-5.9. The energy positions of the high energy eigenmodes, (in the potential maps these modes were identified as the inner-outer type of modes), for both the parallel and perpendicular direction are nearly constant close to $\hbar\omega \approx 3.8\,\text{eV}$, even for a rather big change in the truncation ratio. This was already noticed in the maps of the electrostatic potential when changing truncation ratio from $t_r = 0.01$ to $t_r = 0.60$ [Fig. 5.8(e)→Fig. 5.9(e) and Fig. 5.8(h)→Fig. 5.9(h)].

The perpendicular symmetric dipolar mode which was blue-shifted from $\hbar\omega = 2.61\,\text{eV}$ to $\hbar\omega = 2.35\,\text{eV}$ with increasing truncation ratio [Fig. 5.8(f)→Fig. 5.9(f)] is not continuously connected in the maps Fig. 5.12(c). This indicates the existence of mode crossings. It appears that the spectral superposition of parallel and perpendicular

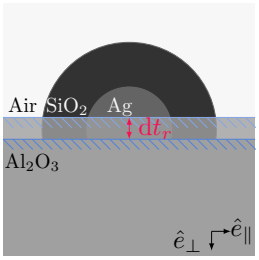

Variable	Value
R [nm]	10.0
$\chi^{(2)}$	0.8
t_r	dt_r
N_{energy}	10000
κ	0.001
L [nm]	21.0
M	16

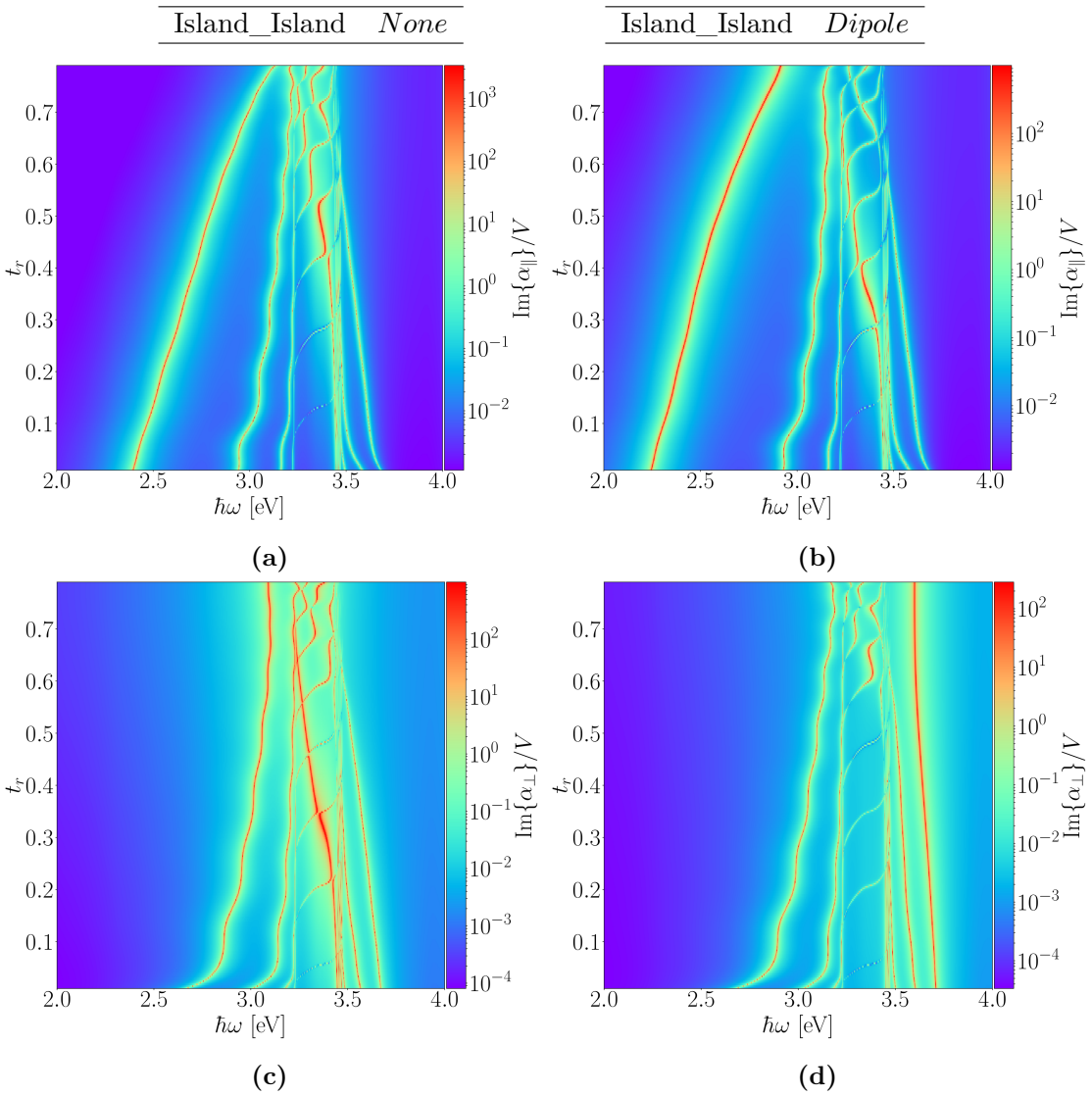

Figure 5.11 Same as Fig. 5.10 but for System 2, *i.e* a silica shell on a silver core.

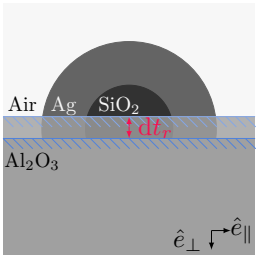

Variable	Value
R [nm]	10.0
$\chi^{(2)}$	0.8
t_r	dt_r
N_{energy}	10000
κ	0.001
L [nm]	21.0
M	16

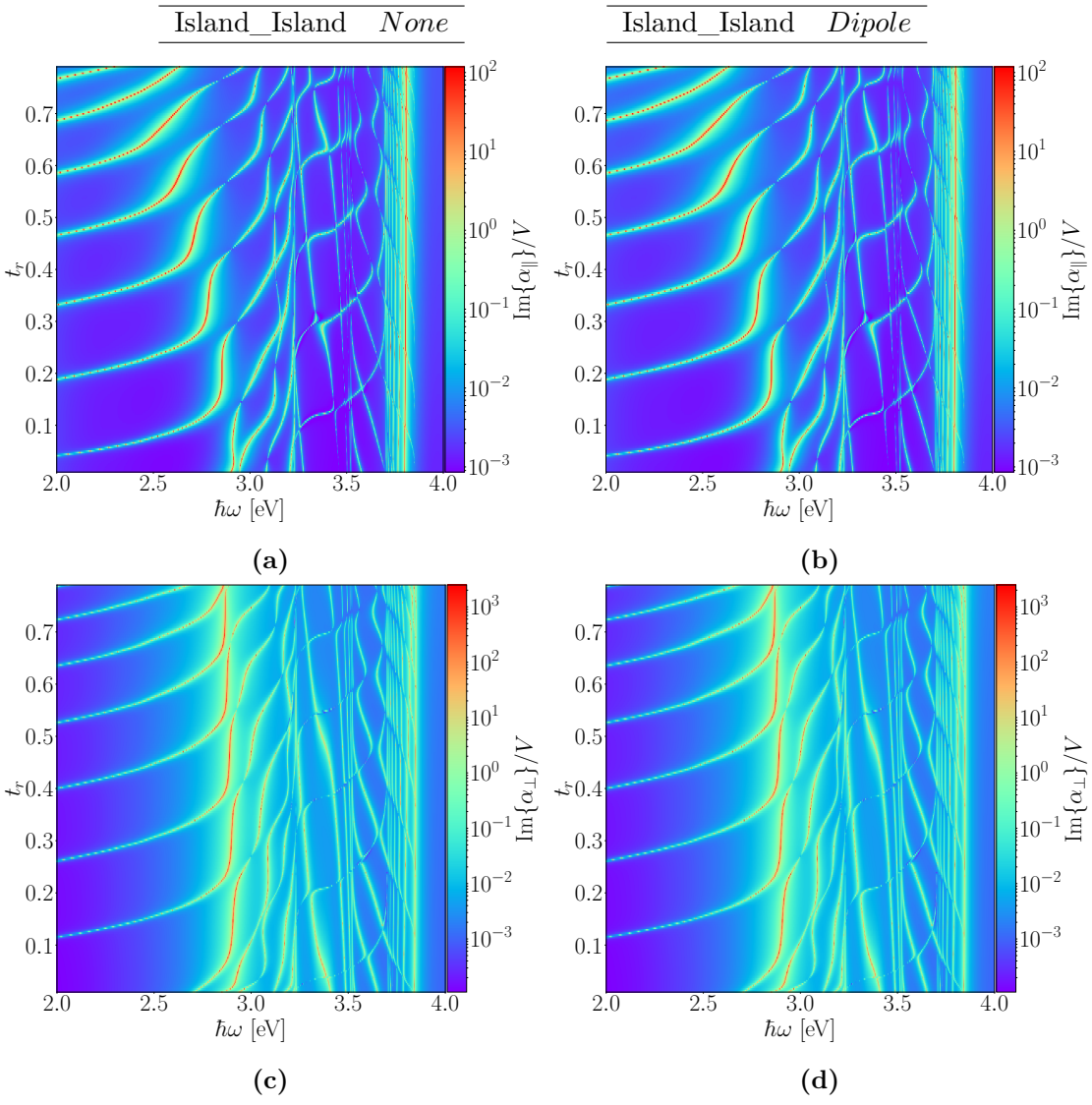

Figure 5.12 Same as Fig. 5.10 but for System 3, *i.e* a silver shell on a silica core.

modes, such as the 'mixed' mode that was observed at $\hbar\omega = 2.70\,\text{eV}$ in both the parallel [Fig. 5.9(d)] and perpendicular [Fig. 5.9(g)] direction for $t_r = 0.6$ in System 3, also appear at other truncation ratios such as 0.07, 2.0 etc. [see Fig. 5.12(a) and Fig. 5.12(c)] for parallel and perpendicular directions, respectively].

After a thorough inspection of the impact of island-island interactions to dipolar order in System 3, we observe a slight red-shift in energy in the parallel map [Fig. 5.12(b)] and a blue-shift in the perpendicular one [Fig. 5.12(c)]. But, the impact of the dipolar interaction between the particles is considerably smaller than what we have seen in Systems 1 and 2.

5.5.2 Dependence on the thickness of the *coating layer*

Maps of the imaginary part of the direction-dependent normalized polarizabilities for changing coating thickness, *i.e.* inner core radius is changed $\mathrm{d}\chi^{(2)}$, of the dielectric/metallic coating for System 2/System 3 without and with island-island interaction to dipolar order are displayed in Figs. 5.13-5.14. To have a clear contrast on the log-scale, the big coating thickness for System 2 are not displayed in Fig. 5.13. Again, the mirror systems behave fundamentally differently.

System 2

As the dielectric shell becomes thinner in System 2, the lowest energy mode in map for the parallel direction is slightly blue-shifted [Fig. 5.13(a)], while the lowset-energy mode in map for perpendicular direction is slightly red-shifted Fig. 5.13(c)]. The peaks at higher energy in the interval $3.25\,\text{eV} \leq \hbar\omega \leq 3.8\,\text{eV}$ merge at a large core size $\chi^{(2)} > 0.7$. For $\chi^{(2)} = 0.8$, 6 distinct modes are observed both in the parallel and perpendicular directions. These correspond to the eigenmodes we observed in System 2 for $t_r = 0.01$ [Fig. 5.10(a) and Fig. 5.10(c)]. Also the chaotic behavior with many peaks appearing as one around $\hbar\omega = 3.5\,\text{eV}$ is seen again as a slightly thicker line.

Considering the same system where the island-island interaction to dipolar order has been included, the shifts are more prominent in the parallel [Fig. 5.13(b)] than the perpendicular [Fig. 5.13(d)] direction. Also, the geometries with the thinner shell, $\chi^{(2)} > 0.7$, are more affected by the island-island interaction than the geometries with a thicker shell, as expected because the dipole-dipole interaction scales with the amount of polerizable matter [20].

System 3

The maps with changing shell thickness in System 3 display a general red-shift for the eigenmodes in the lower part of the energy spectra $\hbar\omega < 3.6\,\text{eV}$, and a blue-shift for the high-energy eigenmodes $\hbar\omega > 3.7\,\text{eV}$ in both parallel and perpendicular direction [Fig. 5.14]. The number of distinct peaks increase with a thinner shell thickness. Again, this is consistent with what we have already seen for a thicker [Figs. 5.7(a)-(b)] and thinner [Figs. 5.8(a)-(b)] metallic coating on a dielectric core.

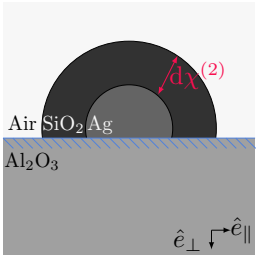

Variable	Value
R [nm]	10.0
$\chi^{(2)}$	$\mathrm{d}\chi^{(2)}$
t_r	0.01
N_{energy}	10000
κ	0.001
L [nm]	21.0
M	16

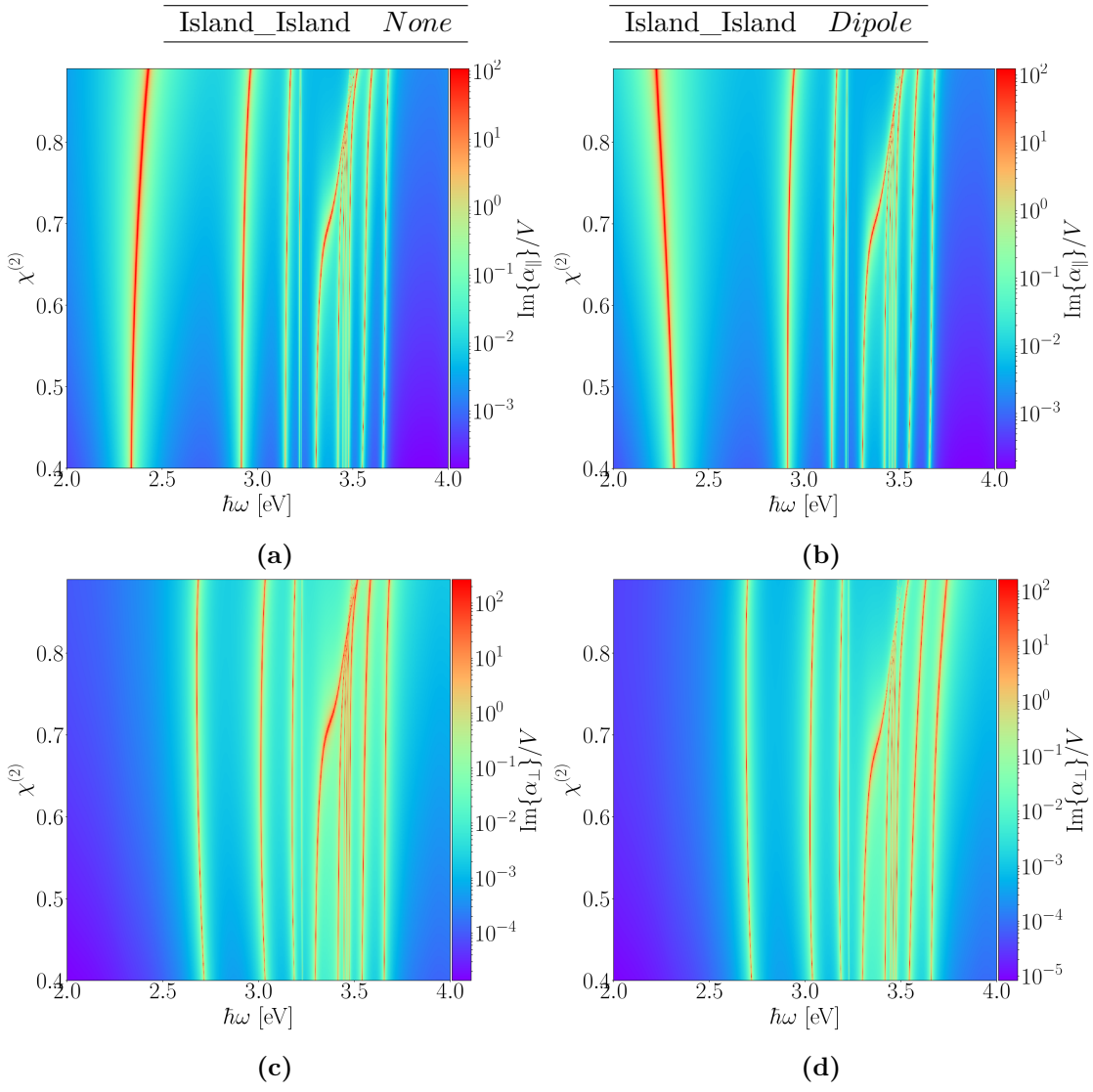

Figure 5.13 Maps of the imaginary part of the direction-dependent polarizabilities in System 2 as function of energy and shell thickness in the interval $\chi^{(2)} = 0.4 - 0.89$ without [(a)/(c)] and with [(b)/(d)] island-island interaction to dipolar order. Simulation parameters are indicated on the top of the figure.

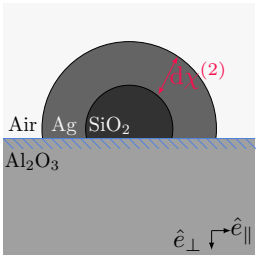

Variable	Value
R [nm]	10.0
$\chi^{(2)}$	$\mathrm{d}\chi^{(2)}$
t_r	0.01
N_{energy}	10000
κ	0.01
L [nm]	21.0
M	16

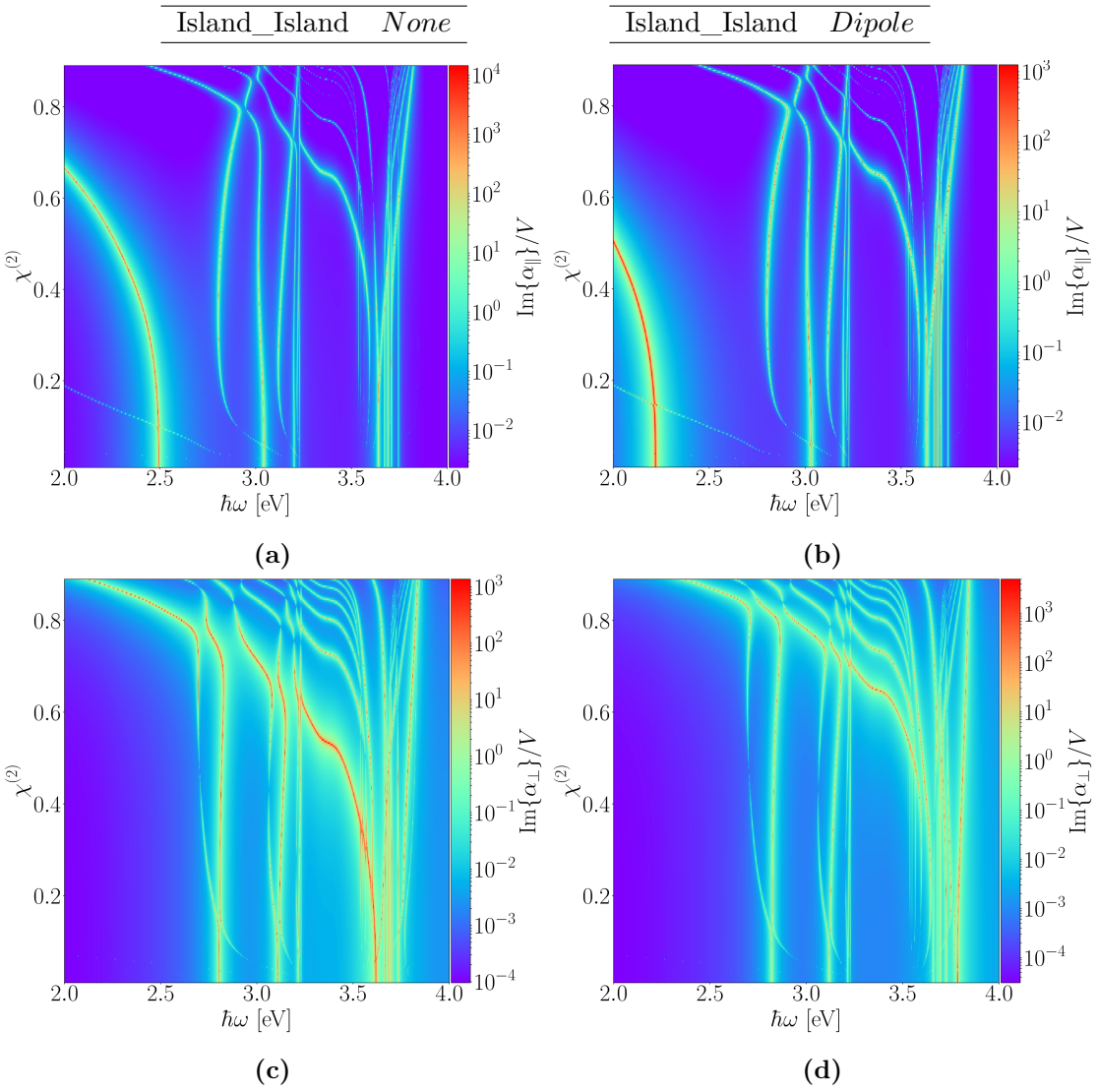

Figure 5.14 Same as Fig. 5.13 but for metallic silver shell on a silica core.

The dipolar mode in the parallel direction shifts out of the available energy range around $\chi^{(2)} = 0.65$ [Fig. 5.14(a)]. This was also observed for the main peak in the SDRS-signal [Figs. 5.4(a)-(b)]. The perpendicular dipolar mode observed at $\hbar\omega = 3.52\,\text{eV}$ in Fig. 5.7(g), and then at $\hbar\omega = 2.61\,\text{eV}$ in Fig. 5.8(f) can be traced in the map [Fig. 5.14(c)], but it does not follow a continuous trend for changing shell thickness.

Again, as compared to the non-interacting case [Fig. 5.14(a) and Fig. 5.14(c)], we observe the general trend of a red-shift for the parallel and blue-shift for the perpendicular response.

5.5.3 General trends of the polarization modes in coated particles

The results presented in the maps of Figs. 5.10-5.14 have attempted to investigate how the oscillation modes are affected by changing the truncation ratio, the shell thickness, the shell material and if the island-island interaction of dipolar order is included or not.

The authors of Refs. 20, 32 have showed that the features observed in experimental SDRS-spectra of silver on alumina obtained during vapor deposition can be explained by the excitation of several multipolar resonances in the truncated sphere, as previously described. By reformulating the oscillation conditions of the matrix system Eq. (5.1) into a spectral representation of the polarizability, they could show that the island-island interactions at dipolar order give rise to a shift in the energy position, either blue- or red-shift, depending on the direction-dependent polarizability. The shift is proportional to the the intensity of the considered oscillator. The figures described in the latter sections indicate that the same type of dependence is also valid for the case of the coated particle. Therefore, the most intense dipolar modes are generally more affected by the island-island interaction. On the contrary, the energy positions of the high energy modes, $\hbar\omega > 3.6\,\text{eV}$ are more or less constant. Compared to the contour maps shown in Fig. 5.10(a) and Fig. 5.10(c), it appears that System 3 of the chosen geometries is least affected by the island-island interaction to dipolar order.

However, the truncation ratio of the particle, the presence of the substrate and of the coating introduce a variety of modes which are not observed for non-coated and coated spherical particles in a homogeneous media. By bringing in a new break of symmetry, the metallic shells display the most exotic and complex optical response among the geometries studied in this chapter. In principle, the discussion could be extended by introducing several coatings/shells and spheroidal prolate/oblate particles as GranFilm's capabilities also cover these geometries. With recent advances in preparation techniques at the nanoscale, such geometries are achievable: nanorice (coated prolats), nanoeggs (coated oblates) and nanomatryushkas (dielectric core, metallic shell, dieletric layer, etc.) [74, 75].

5.6 Conclusion

While the effect of a coating on a spherical/spheroidal particle in an homogeneous media is known analytically (see Fig. 5.1), the combined effect on the plasmonic response

of the presence of both a coating layer and a dielectric substrate are not fully understood. The optical response of coated supported truncated metallic nanoparticles originates from the excitation of multipolar absorption modes caused by the breaks of symmetry introduced by the presence of the substrate, the truncation of the particle, and the coating layer. This chapter was devoted to the understanding of the type of modes excited in such systems.

The oscillation eigenmodes were investigated via a multipolar expansion of the potential outside and inside the island as implemented in the GranFilm software [56]. To do so, the mimima of the eigenvalue of the matrix system for the multipolar coefficients were scrutinized to locate the resonances. Maps of potential at the corresponding frequencies helped deciphering the nature of the modes. Their shifts in energy were systematically investigated and compared to the case of objects without coating for changing particle geometries [20]. While the dielectric shell poorly affect the nature of the modes and mainly red-shifts their frequency through screening, a much richer polarization pattern was observed in the case of a metallic shell. Both complex mixing and splitting of the eigenmodes were observed for this geometry [17].

Chapter 6

Broadening of the plasmon resonances

Until now, in this manuscript, the considered system has consisted of identical NPs organized in regular or random arrays and supported by the planar surface of a dielectric substrate. The physical system encountered in *e.g.* deposition experiments, will always display a certain degree of dispersity in the size and shape of the particles due to the random nature of the growth process. This chapter deals with the main phenomena behind the so-called *experimental broadening* that can be observed in the plasmon resonances of supported aggregates of metallic NPs. The discussion of the origin of this phenomenon will be divided into two sources; *intrinsic* sources, related to the nanoscale; and *extrinsic* sources that are related to the size and shape distribution of the individual particles.

Contents

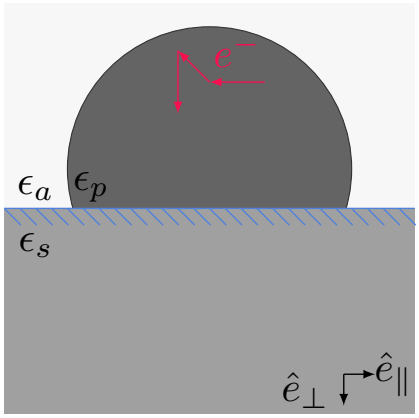

(a) Schematic illustration of the finite-size effect in a metallic NP. The surface of the particle restricts the movement of the free electrons, e^-.

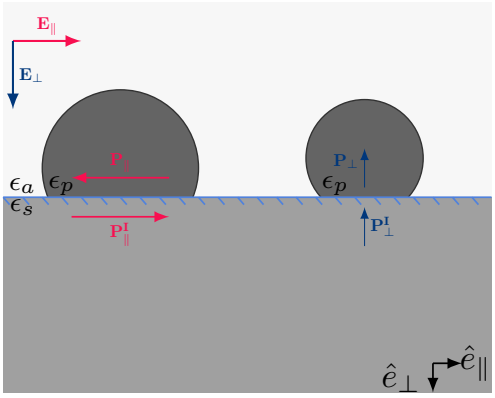

(b) Figurative illustration of the direction dependent and different sized dipoles caused by the components of the incoming electric field.

Figure 6.1 The two main contributors to the broadening of the plasmon resonance caused by intrinsic (a) and extrinsic (b) sources.

6.1 Origins of the broadening of the plasmon resonances

A classical GranFilm simulation is performed on a system of identical particles organized in either a lattice (square/hexagonal) or in a random array[1]. For the random array configuration, one must define a particle-particle correlation function and the surface coverage. When comparing the results obtained for a lattice (an ordered array) and a random array, one has to make sure that the two configurations correspond to the same surface coverages of the lattice, this quantity is derived from the lattice constant.

As we saw in Chapter 3 the calculation of the polarizability is done in two main steps. First, the single particle polarizabilities are calculated taking its shape (truncated sphere or spheroid) and its electrostatic interaction with the substrate into account. Second, the electrostatic coupling between the NPs are computed to dipolar or quadrupolar order. Depending on the array type, this correction is for the single particle polarizability calculated with the use of lattice sums (ordered array) or distribution integrals (random array).

In Ch. 4, we saw that the experimental bulk dielectric function of the metallic NPs had to be modified to take into account specific phenomena on the nanoscale. Here we consider two such corrections terms: the finite-size and the surface corrections. The finite-size correction originates from the reduced mean free path of the free electrons in small volumes of metal. It leads to an enhancement of the imaginary part of the dielectric function of the metallic NPs which results in an increased damping that

[1]See Ch. 3 for a refreshment of the definitions of the given systems.

broadens the width of the plasmon resonance. The surface correction, on the other hand, is related to a change in the electronic structure close to the surface of the NP due to a decrease in the screening of the conduction electrons. Both these effects contribute to a shift in position and/or a change in the resonance peak width. Generally, the smaller particles are affected more than the bigger particles by these corrections. Since these corrections originate from the physical system itself, the broadening they induce is called *intrinsic*. Figure 6.1(a) gives a schematic illustration of the origin of the finite-size effect in a NP.

During the growth of NPs on a surface, in particular, by vapor or sputtering depositions, some degree of dispersity in particle size and shape will always be present due to the random character of the growth process [76]. This dispersity will impact the plasmonic response of the system and, as a consequence, the optical properties [77,78]. Indeed, as we saw in Ch. 1, the polarizabilities scale with the volume of the particle and the resonance frequencies shift with the truncation ratio, or more generally, with the aspect ratio of the particles. The resulting effect is an overall complex broadening that we call *extrinsic*. A sketch of the size and direction dependent dipoles caused by the incoming field in a polydisperse system is illustrated in Fig. 6.1(b).

In principle, the resonances of a system display simultaneously both extrinsic and the intrinsic broadening. Until now, the broadening of the resonance peaks were treated pragmatically by a simple convolution of the polarizabilities in the monodisperse case with a somehow arbitrary Gaussian envelope [42, 58]. In the case of a *low coverage polydisperse* (LCP) system the island-island interaction between the neighboring particles can be neglected. Extrinsic broadening results simply from an ensemble average over sizes and shapes of the particles. However, for a higher surface density of particles, in a *finite coverage polydisperse* (FCP) system, the shifts induced by the island-island interaction will depend on the local environment of each particle. The aim of this chapter is to treat both limits, in particular, the finite coverage limit within the mean field approximation.

In the following, we will give a systematic analysis of these intrinsic and extrinsic effects as sources of plasmon resonance broadening. We start by a description of the impact of the intrinsic broadening in a LCM system. The impact of the size and shape distributions in LCP and FCP systems are then considered.

The optical properties of a system containing metallic NPs are, to a great extent, driven by the polarizabilities of the metallic NPs. Since the energy position of the direction dependent polarizabilities of supported NPs calculated with GranFilm is independent of the angle of incidence of the incident field, these observables will be chosen to illustrate all the effects that can occur in the different cases. Because the absorption in the substrate is directly linked to the imaginary part of the polarizability, we will use this observable in our discussion [8]. The imaginary parts of the polarizabilities will always be normalized by a proper average volume term to single out the broadening/shift effects. The test case of silver particles (Ag) on an alumina substrate (Al_2O_3) will be used.

6.2 Broadening caused by intrinsic effects

The simulation results discussed in Sec. 4.4 showed some general trends of the reflectivity curves [Fig. 4.9(c)], caused by a finite-size correction of the bulk dielectric function of the metal. This section illustrates the effect on the polarizabilities upon a change of particle size in a *low coverage monodisperse* (LCM) or *finite coverage monodisperse* (FCM) system.

Figure 6.2 displays the imaginary part of the parallel and perpendicular polarizabilities normalized by the volume of the particle in a monodisperse system, for different values of the radius parameter. The presented curves follow similar trends when changing the size of the particle.

Firstly, as depicted in Figs. 6.2(a)-(b), without correction of the experimental bulk dielectric function of the metal, the polarizabilities scaled by the volume of the particle yield identical results. A well-known result from plasmonics [8].

Secondly, the finite-size and surface corrections impact the polarizabilities in a different way [Figs. 6.2(c)-(d) and Figs. 6.2(e)-(f)]. Generally, a reduction of the electron mean free path simply broadens [Figs. 6.2(c)-(d)] the peaks and reduce their amplitudes, as compared to the cases without corrections. The spectral shift is negligible in this case. Of course, for both directions, the smaller the particle, the larger the effect.

The surface correction applied to LCM and FCM systems do not cause broadening of the resonance peak. Instead, this type of correction results in a shift of the peak. As this effect becomes important for a distribution over size and shape the results for the monodisperse case are given in Figs. 6.2(e)-(f). Applying the surface correction on the experimental bulk dielectric function, the positions of the peaks are all shifted towards higher energies (blue-shifted) for both the parallel and perpendicular directions with a negligible broadening and a small shift in the amplitude. Again, the smallest particles are those most affected.

6.3 Broadening caused by extrinsic effects

In the monodisperse system, the polarizabilities of each particle are identical. For a polydisperse system with a distribution over the size, the shape or both, it is possible to show that the surface susceptibilities should be calculated from the spatial averages of the relevant polarizabilities [5, 79]

$$\gamma = \rho \left\langle \alpha_{\parallel} \right\rangle \tag{6.1a}$$

$$\beta = \frac{\rho}{\varepsilon_a^2} \left\langle \alpha_{\perp} \right\rangle \tag{6.1b}$$

$$\tau = -\rho \left\langle \alpha_{\parallel}^{10} \right\rangle \tag{6.1c}$$

$$\delta = -\frac{\rho}{\varepsilon_a} \left[\left\langle \alpha_{\perp}^{10} \right\rangle + \left\langle \alpha_{\parallel}^{10} \right\rangle \right], \tag{6.1d}$$

where $\langle \cdot \rangle$ denotes spatial average[2].

[2]See Ch. 2 for a reminder of the definitions of the electrical surface susceptibilities.

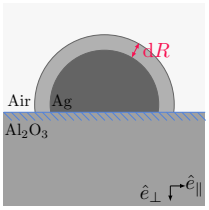

Parameter		Value
R	[nm]	dR
t_r		0.0
L	[nm]	31.0
M		16

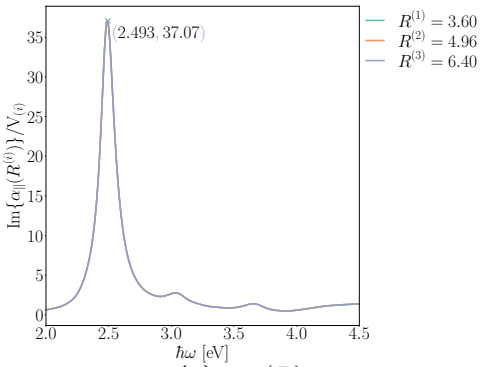

(a) $\alpha_\parallel(R)$.

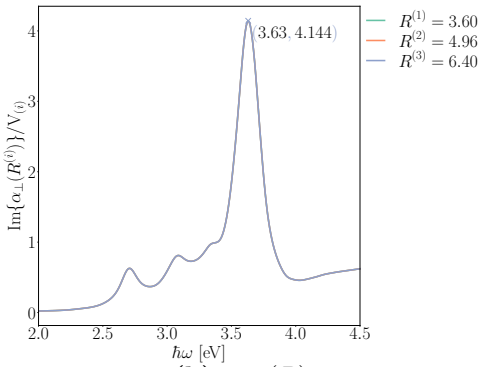

(b) $\alpha_\perp(R)$.

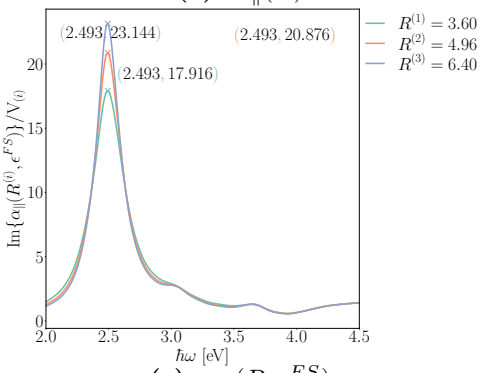

(c) $\alpha_\parallel(R, \varepsilon^{FS})$.

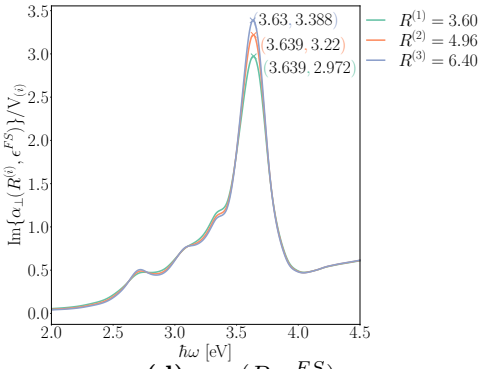

(d) $\alpha_\perp(R, \varepsilon^{FS})$.

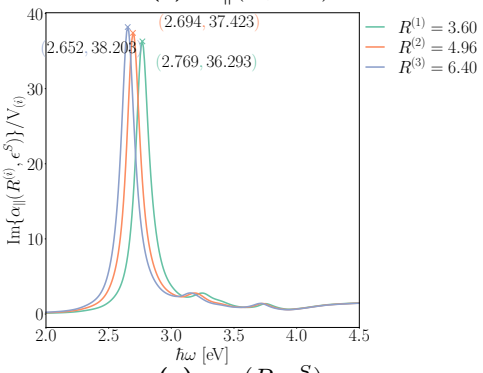

(e) $\alpha_\parallel(R, \varepsilon^{S})$.

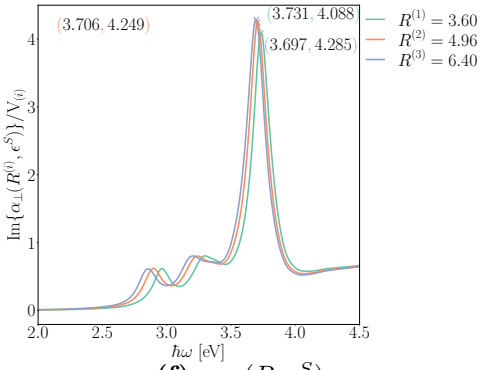

(f) $\alpha_\perp(R, \varepsilon^{S})$.

Figure 6.2 Imaginary parts of the parallel/perpendicular polarizabilities normalized by the volume as a function of different radii without (a)-(b), with a finite size (c)-(d) and with a surface (e)-(f) correction of the experimental bulk dielectric function. Parameters of the modeled system are reminded on the top of the figure.

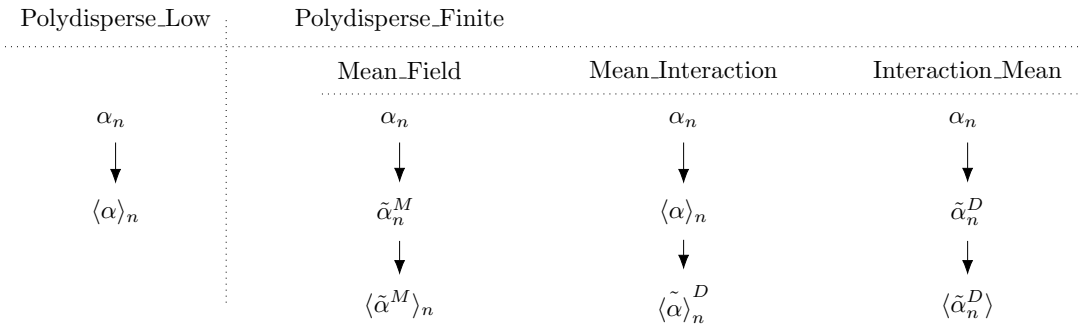

Figure 6.3 A scheme for the calculation of the average polarizability for the different types of polydisperse systems accounted for in GranFilm.

To describe the effect of polydispersity from a statistical point of view, we need to introduce the size and shape *probability density function* (PDF) of the particles. Moreover, handling the spatial average requires to take into account properly the electrostatic coupling between the particles and therefore to distinguish, as done for the monodisperse system, between the low and the finite coverage limits. Theoretically, four cases should be distinguished for the polydisperse system:

- the low coverage limit for which the island-island interaction is negligible and the spatial average is solely an average over the sizes and shapes times the PDFs of the particles. This configuration of particles is a LCP system.
- the finite coverage limit for the polydisperse system. In this limit, the local variations of the depolarization field due to island-island interactions should be taken into account. The system in this limit is a FCP system. We have three different ways to account for the island-island interaction for such a configuration:
  - in the *Mean Field Theory* (MFT) approximation the island-island interaction ignores the fluctuation of the dipole moments around their mean values.
  - The theoretical case of an ensemble average of monodisperse domains, called the *interaction mean* (IM) system. The island-island interaction is taken into account to dipolar order for the single particle polarizability in the monodisperse system before the ensemble average is computed.
  - The theoretical case of calculating the average particle response before the island-island interaction of dipolar order is computed for the average monodisperse response, called *mean interaction* (MI).

A summary of the different ways to calculate the average polarizabilities for a set of particles n in FCP is illustrated in Figure 6.3. Note the difference between including the island-island interaction before or after the mean is computed. Examples of polydisperse systems in the LCP and FCP limits are given in Fig. 6.4.

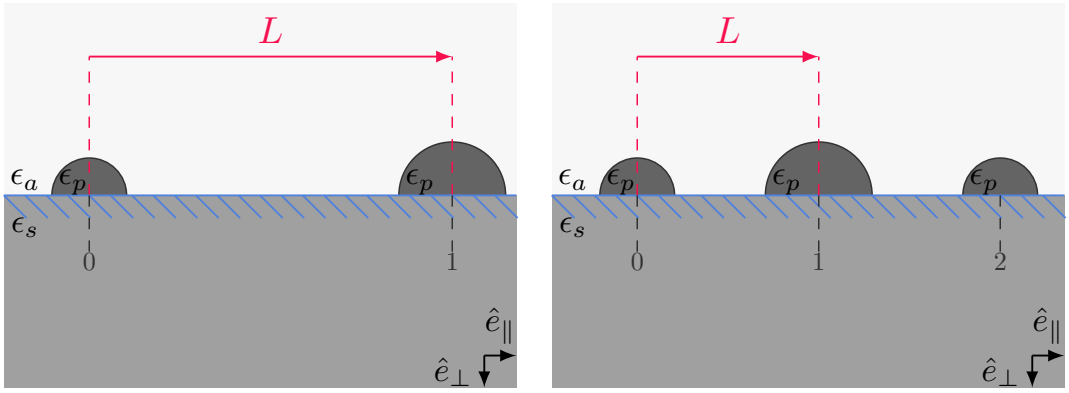

(a) Low coverage. **(b)** Finite coverage.

Figure 6.4 A schematic illustration of a system containing polydisperse particles in low (a) and finite (b) coverage.

6.3.1 Working with polydisperse particles in GranFilm

Several changes in the calling structure of GranFilm had to be performed in order to enable the calculation of observables related to the polydisperse system. In Appendix C Sec. C.2.2, an example of the updated input file for GranFilm is given.

The distribution parameter namelist

Firstly, the reading of the input file and the logic related to setting consistent parameters for the size and shape distribution had to be handled[3]. An additional keyword 'Size_Distribution' was added to the Geometry nml-namelist to decide if GranFilm should simulate a polydisperse or monodisperse system. Valid options for this keyword are 'None' or 'Size_Distribution'. If the keyword 'Size_Distribution' is given, the optional 'Size_Distribution' namespace will be read.

To construct the PDF polydispersity over a parameter we have chosen to give the user the possibility to set the mean value of the wanted distribution μ_n, the standard deviation σ_n, and the lower and upper limits, respectively, a_n and b_n, where the distributed parameter n is one or all in the set $\{R_\parallel, R_\perp, t_r\}$ is the set of geometrical parameters possible to introduce as the input in a GranFilm simulation. As always in the case of a spherical particle $R_\parallel = R_\perp = R$. The reading of the input file, and the checking of the logic for several of the variables are now properly taken into account by the software. The joint size and shape PDF characterizing the polidispersity of the particles in the system is assumed to be constructed from products of marginal *truncated normal distributions* for each of the geometrical parameters of the particles that can vary ($\{R_\parallel^{(n)}, R_\perp^{(n)}, t_r^{(n)}\}$).

[3]See a full description of the most crucial input parameter of GranFilm in Sec. 4.2.

The truncated normal distribution

For the sake of simplicity, the set of parameter $\{R_{\parallel}^{(n)}, R_{\perp}^{(n)}, t_r^{(n)}\}$ that the size/geometry parameters we can construct a PDF for in a polydisperse system we have chosen the truncated normal distribution.

The *normal distribution* with mean μ and variance σ^2, denoted $\phi(\mu, \sigma^2; x)$ for a random variable x, is formally defined as [80]

$$\phi(\mu, \sigma^2; x) = \frac{1}{\sigma\sqrt{2\pi}} \mathrm{e}^{-\frac{(x-\mu)^2}{2\sigma^2}}. \tag{6.2}$$

Its *cumulative distribution function* (CDF) is given by

$$\Phi(\mu, \sigma^2; x) = \int_{-\infty}^{x} \mathrm{d}t \frac{1}{\sigma\sqrt{2\pi}} \mathrm{e}^{-\frac{(t-\mu)^2}{2\sigma^2}}, \tag{6.3}$$

which can be rewritten

$$\Phi\left(\mu, \sigma^2; x\right) = \frac{1}{2}\left(1 + \mathrm{erf}(x/\sqrt{2})\right), \tag{6.4}$$

where $\mathrm{erf}(x)$ denotes the related error function.

The PDF associated with the truncated normal distribution is, in fact, defined as a normal distribution with the parameters μ and σ^2, but only given in a limited range $(a < x < b)$ for a random variable x. Outside this range, the PDF is set equal to zero. As any PDF, the truncated normal distribution should be normalized to 1. Therefore, if we denote by the truncated normal distribution by $f(\mu, \sigma, a, b; x)$, where μ and σ^2 are the mean and the variance of the 'parent' normal distribution as defined in Eq. (6.2) and by the range (a, b) where $-\infty \leq a < b \leq \infty$, then the PDF is defined as

$$f(x, \mu, \sigma, a, b) = \begin{cases} 0 & -\infty < x \leq a \\ \frac{1}{\sigma} \frac{\phi\left(\frac{x-\mu}{\sigma}\right)}{\Phi\left(\frac{b-\mu}{\sigma}\right) - \Phi\left(\frac{a-\mu}{\sigma}\right)} & a < x < b \\ 0 & b \leq x < \infty \end{cases} \tag{6.5}$$

where

$$\phi\left(\frac{x-\mu}{\sigma}\right) = \frac{1}{\sqrt{2\pi}} \exp\left[-\frac{1}{2}\left(\frac{x-\mu}{\sigma}\right)^2\right], \tag{6.6}$$

is the PDF of the standard normal distribution defined by the parameters μ_0 and $\sigma = 1$, and $\Phi(\cdot)$ is the corresponding standard CDF.

For the sake of simplicity, in the case of distribution over more than one parameter at the time, we will model the joint probability distribution function as a product of the marginal probability distribution of each parameter (*e.g.* radius, truncation, spheroid flattening etc...) *i.e.*, independent distributions. Each of these independent distributions has a distinct number of islands $\mathcal{N} \in \{N_{R_{\parallel}}, N_{R_{\perp}}, N_{t_r}\}$.

The average polarizability

With a known form of the PDF(s) and assuming the eventual joint probability distribution to be independent for the different random variables, the mean polarizability given by a set of random variables $\langle\alpha(\mathcal{P})\rangle$ can be calculated.

The parameters are taken from the set $\mathcal{P} \in \{R_{\parallel}^{(n)}, R_{\perp}^{(n)}, t_r^{(n)}\}$, $n = 1, ..., N$ with the smaller and bigger limits of the individual parameters respectively taken from the sets $\mathcal{A} \in \{a_{R_{\parallel}}, a_{R_{\perp}}, a_{t_r}\}$ and $\mathcal{B} \in \{b_{R_{\parallel}}, b_{R_{\perp}}, b_{t_r}\}$. Approximating the integral with quadrature integration and the (naive) midpoint rule for sampling, the average (expectation value) of the polarizability becomes

$$\begin{aligned}\langle\alpha(\mathcal{P})\rangle &\approx \int_{\mathcal{A}}^{\mathcal{B}} \mathrm{d}\mathcal{P}\mathrm{pdf}(\mathcal{P})\alpha(\mathcal{P}) \\ &\approx \sum_{n=1}^{N} \Delta\mathcal{P}\mathrm{pdf}(\mathcal{P}_n)\alpha(\mathcal{P}_n), \qquad \mathcal{P}_n = \mathcal{A} + \left[n - \frac{1}{2}\right]\Delta\mathcal{P} \\ &\approx \left(\frac{\mathcal{B}-\mathcal{A}}{N}\right)\sum_{n=1}^{N} \mathrm{pdf}(\mathcal{P}_n)\alpha(\mathcal{P}_n), \end{aligned} \tag{6.7}$$

where N is the total number of unique islands in the distribution and $\Delta\mathcal{P}_n = \frac{\mathcal{B}-\mathcal{A}}{N}$ the length of each subinterval.

The error term when approximating an integral with the midpoint rule in s-dimensions will scale as $Error_{midt} \propto \mathcal{O}(n^{-1/s})$ [81]. This is an important fact to consider when calculating an average quantity for higher order distributions.

6.3.2 Modified calling sequence in GranFilm

The original calling sequence in the GranFilm software has been adapted to integrate the possibility of treating systems that contain polydisperse particles. The final code has readable and accessible structure for the calculations of relevant observables for both the mono- and polydisperse case. Figure 6.5 displays a flowchart of the most significant changes made to the original structure we displayed in Fig. 4.1.

Firstly, the distribution is sampled, and all geometry parameters of the individual islands are set. A loop over the number of individual islands to calculate the single particle polarizabilities is then performed. In this loop, the (potential) evaluation of the corrections of the experimental bulk dielectric function is performed each time a new island configuration $p_n = \{R_{\parallel}^{(n)}, R_{\perp}^{(n)}, t_r^{(n)}\}$ is chosen. To save the computation time, the integrals over the spherical surface of the particles are evaluated only if the value of the truncation ratio has changed from the previous to the next iteration. The multipole coefficients are calculated, and the single particle polarizabilities evaluated. At this stage, the code will include the island-island interaction correction of the single particle polarizabilities if required by the user (in the IM limit).

When the single particle polarizabilities of the total number of islands in the ensemble or the wanted error term in the calculation is reached, the loop over island types is ended. In the case of FCP in the MF or MI limit one correct the single particle

polarizabilities before the average is computed. In the IM limit, the correction of the single particle polarizabilities is performed already in the loop over island types. If one uses the LCP configuration, the mean polarizability of the system will be calculated directly. Finally, from the obtained average (potentially renormalized) polarizabilities, the surface susceptibilities and the physical observables can be calculated as before.

The bottleneck of the calculation is again the evaluation of the integrals over the spherical surfaces of the particles; this was discussed in Ch. 4. A significant speed up is expected if hash or lookup-tables (a technique of mapping data keys) could be deployed to tabulate the integrals over the spherical surfaces [82]. Due to the time limitation of the thesis, this aspect is not to be further considered here.

We will now detail how the average polarizabilities calculation is performed and comment on the simulation results for the LCP and FCP limits.

6.4 Polydispersity in the low coverage regime

The LCP regime [see Fig. 6.4(a)] corresponds to a size-distributed sample where the particles are arranged in such a way that the electrostatic coupling between them can safely be ignored.

6.4.1 Sampling rule

There are two obvious methods to sample the island distributions to obtain the average polarizability. One could either choose a quadrature technique as proposed in Eq. (6.7), or to obtain the average by a *Monte Carlo* (MC) integration technique.

Monte Carlo integration

For this latter method, the MC integration scheme suggests that an estimate of the average of the polarizability is given by

$$\langle \bar{\alpha} \rangle_N = \frac{1}{N} \sum_n^N \alpha(x_n), \tag{6.8}$$

where $\alpha(x_n)$ is calculated for a random variable (or set of variables), x_n is drawn from the joint size and/or shape distribution function in question. This random variable can be generated from the inverse CDF of the truncated normal distribution and with the rejection method [80]. The great advantage of the MC technique is that the estimate of the average always can be given with a known error. A final assessment of the average polarizability with an error estimate calculated with this method is

$$\begin{aligned} \langle \alpha \rangle &\approx \langle \bar{\alpha} \rangle_N \pm \sigma_{\bar{\alpha}} \\ &\approx \langle \bar{\alpha} \rangle_N \pm \frac{\sigma\left[\{\bar{\alpha_n}\}_{n=1}^N\right]}{\sqrt{N}} \\ &\approx \langle \bar{\alpha} \rangle_N \pm \frac{\sqrt{\langle |\bar{\alpha}|^2 \rangle_N - |\langle \bar{\alpha} \rangle_N|^2}}{\sqrt{N}}, \end{aligned} \tag{6.9}$$

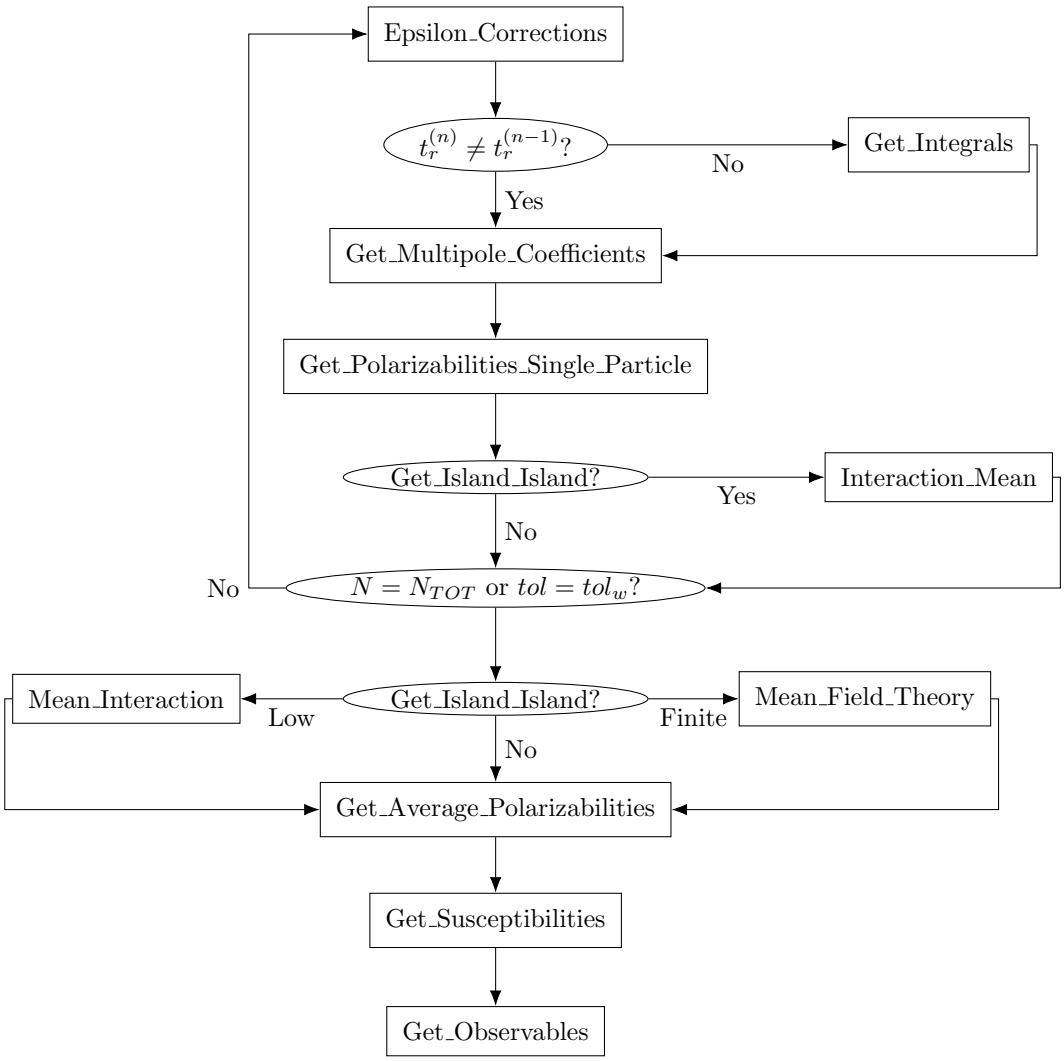

Figure 6.5 An updated flowchart of the most crucial steps in a Gran-Film simulation for a polydisperse system. The (potential) evaluation of the corrections of the experimental bulk dielectric function is performed each time a new island configuration is chosen. To save computation time during the computation of the average polarizabilities, the evaluation of the integrals over the spherical surface is only performed if the truncation ratio is changed between the current and the previous iteration. The multipole coefficients are then calculated, and the single particle polarizabilities evaluated. At this stage, polarizabilities can be corrected from island-island interaction, assuming the IM limit. When the polarizabilities for the wanted number of islands or the required tolerance of calculation is reached, the loop over island types is ended. In the case of the MF or MI limits, the renormalization of the single particles are computed before the average is calculated. Finally, from the obtained average (potentially renormalized) polarizabilities, the surface susceptibilities and the physical observables can be calculated as before.

where N is the number of terms added to calculate the average and $\sigma_{\bar{\alpha}}$ is the standard deviation of the estimator. It should be remarked that for MC integration the error estimate scales as $Error_{MC} \propto \mathcal{O}(n^{-1/2})$, independent of the order of the integral [81].

Calculating the average polarizabilities with the Monte Carlo technique

All the relevant equations in the GranFilm software (described in Ch. 3) are given in dimensionless forms. Thus, special attention has to be paid to the normalization of the estimator $\langle\bar{\alpha}\rangle_N$. Denoting the dimensionless direction dependent polarizability as

$$\hat{\alpha}_i^{\ell,0} = \frac{\alpha_i^{\ell,0}}{R_\perp^{\ell+2}}, \qquad i = \{\parallel, \perp\}, \quad \ell = \{0, 1\}, \tag{6.10}$$

where the subscript i denotes the direction and the subscript ℓ the order of the polarizability. The estimate of the average polarizability $\langle\bar{\alpha}\rangle_N$ for a distribution over either the radii or the truncation ratio parameters is defined as

$$\begin{aligned}\frac{\langle\alpha_i^{(\ell,0)}\rangle_N}{\left(\tilde{R}_\perp\right)^{\ell+2}} &\approx \frac{1}{N}\sum_{n=1}^{N}\frac{1}{\left(\tilde{R}_\perp\right)^{\ell+2}}\alpha_i^{(\ell,0,n)}\left(R_\parallel^{(n)}, R_\perp^{(n)}, t_r^{(n)}\right)\\ &= \frac{1}{N}\sum_{n=1}^{N}\left[\frac{R_\perp^{(n)}}{\tilde{R}_\perp}\right]^{\ell+2}\hat{\alpha}_i^{(\ell,0,n)}\left(R_\parallel^{(n)}, R_\perp^{(n)}, t_r^{(n)}\right),\end{aligned} \tag{6.11}$$

where the term $\tilde{R}_\perp$ is the chosen normalization of the polarizability. If there is a distribution over the perpendicular radius $\tilde{R}_\perp = \mu_{R_\perp}$, if not $\tilde{R}_\perp = R_\perp^{(1)}$ as usual. For a proper normalization during the MC integration scheme, the sum Eq. (6.11) can be recast into

$$\frac{\langle\alpha_i^{(\ell,0)}\rangle_{N-1}}{\left(\tilde{R}_\perp\right)^{\ell+2}} \approx \frac{1}{N-1}\sum_{n=1}^{N-1}\left[\frac{R_\perp^{(n)}}{\tilde{R}_\perp}\right]^{\ell+2}\hat{\alpha}_i^{(\ell,0,n)}\left(R_\parallel^{(n)}, R_\perp^{(n)}, t_r^{(n)}\right), \tag{6.12}$$

and we can rewrite Eq. (6.11) as the sum of two terms

$$\begin{aligned}\frac{\langle\alpha_i^{(\ell,0)}\rangle_N}{\left(\tilde{R}_\perp\right)^{\ell+2}} &\approx \frac{1}{N}\left(\sum_{n=1}^{N-1}\left[\frac{R_\perp^{(n)}}{\tilde{R}_\perp}\right]^{\ell+2}\hat{\alpha}_i^{(\ell,0,n)}\left(R_\parallel^{(n)}, R_\perp^{(n)}, t_r^{(n)}\right)\right.\\ &\quad\left.+\left[\frac{R_\perp^{(N)}}{\tilde{R}_\perp}\right]^{\ell+2}\hat{\alpha}_i^{(\ell,0,N)}\left(R_\parallel^{(N)}, R_\perp^{(N)}, t_r^{(N)}\right)\right)\\ &= \frac{N-1}{N}\frac{\langle\alpha_i^{(\ell,0)}\rangle_{N-1}}{\left(\tilde{R}_\perp\right)^{\ell+2}} + \frac{1}{N}\left[\frac{R_\perp^{(N)}}{\tilde{R}_\perp}\right]^{\ell+2}\hat{\alpha}_i^{(\ell,0,N)}\left(R_\parallel^{(N)}, R_\perp^{(N)}, t_r^{(N)}\right).\end{aligned} \tag{6.13}$$

The average volume $\langle V\rangle_N$ for the islands in the ensemble is calculated in a similar manner.

Choosing the integration method

The basis of the quadrature and the MC methods for numerically evaluating the integrals are fundamentally different, both in the sampling routine and the obtained error estimate. For quadrature integration, the size of the error term will decrease with a smaller step size in the discretization of the parameter. For integration in higher-dimensions, the number of points required to a have a small error quickly becomes significant.

In the MC method, the error term itself is of probabilistic nature. It's estimate lies within one standard deviation of the true value. Both of our two sampling techniques have great potential for improvement. Important sampling techniques for the MC method or a smarter quadrature than the midpoint sampling is expected to speed up the simulation results [81].

For our needs, the computational speed is the most essential requisite. Time estimates of our software's calculations shows that the computational speeds when using the two integration methods to evaluate one-dimensional integrals to calculate the average polarizabilities essentially are the same. However, for a multivariate size and shape distributions the MC method is the fastest of the two. The user can choose the kind of integration method. For quadrature integration, the number of points for each parameter that should be distributed must be given as input. For the MC integration the user can set the required tolerance of the error of the estimator of the standard deviation. The software will then chose the requested number of islands in the integration routine.

6.4.2 The effect of polydispersity in the low coverage regime

Figure 6.6 and Fig. 6.7 summarize the trends observed in simulations of the direction-dependent polarizability of a polydisperse system when choosing a truncated normal distribution over the radius (Fig. 6.6) and over the truncation ratio (Fig. 6.7) parameters where the average polarizability is calculated with the deterministic quadrature method. The effect of varying the widths of the various size and shape distributions is illustrated by the results presented in Figs. 6.8-6.9.

Radius versus truncation distributions

Figure 6.6(a) and Fig. 6.7(a) display the PDF for the chosen distribution, respectively, for the radius and truncation ratio parameter. The final results for the average values appear in Figs. 6.6(b)-(c) and Figs. 6.7(b)-(c) with the dotted pink curve given by the TOT parameter (right y-axis) together with three different values in the distribution times the probability of the variable (left y-axis). To highlight the effect of averaging, as given by Eq. (6.13), the central value μ and two values of equal probabilities $\mu \pm \sigma$ are pinpointed for each of the distributions. The other parameters defining the systems are given in the upper right corner of the figure.

In Fig. 6.6(b) and Fig. 6.7(b) the actual value of the PDF is multiplied by the imaginary part of the parallel polarizability for the given random variable scaled by the average volume factor $\langle V \rangle$, which is also computed according to the relation Eq. (6.7)

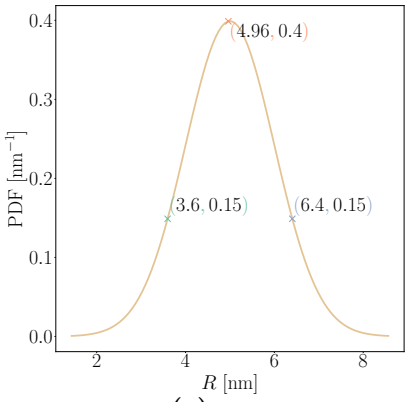

(a)

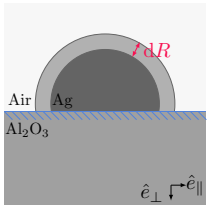

Parameter	Value
μ_R [nm]	5.0
σ_R [nm]	1.0
$\min_R$ [nm]	1.4
$\max_R$ [nm]	8.6
N_R	100
t_r	0.0
L [nm]	31.0
M	16

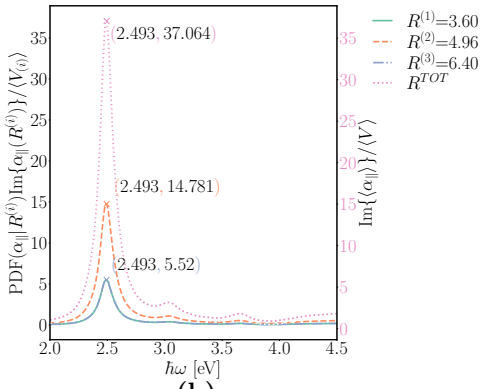

(b)

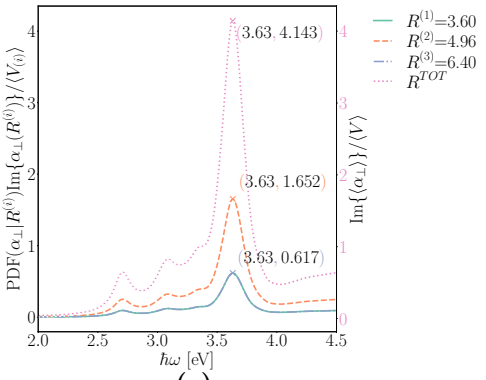

(c)

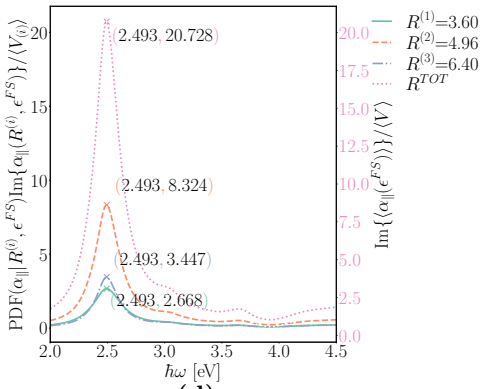

(d)

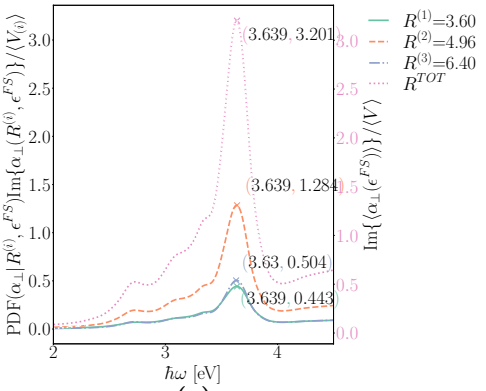

(e)

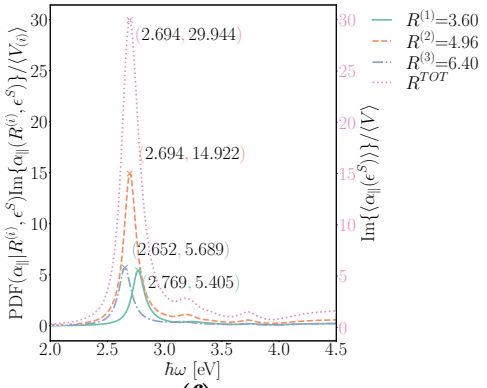

(f)

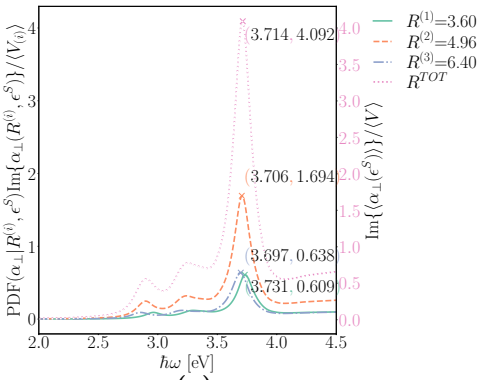

(g)

Figure 6.6 Effect of polydispersity for a truncated normal distribution over the radius parameter (a) on the imaginary parts of the parallel polarizability (b), including for the corrections of the experimental bulk function ε^{FS} (d), ε^{S} (f). The perpendicular counterparts of the polarizability are given, respectively, in (c),(e), (g) polarizabilities. Simulation parameters are given in the upper right corner of the figure.

for either a radius or truncation ratio[4] variable. The corresponding perpendicular polarizabilities are illustrated in Fig. 6.6(c) and Fig. 6.7(c).

In the case where the particle radius is varied, within a scaling factor, the same curve is observed for $R^{(1)}, R^{(2)}$ and $R^{(3)}$ since the polarizabilities of the truncated particle of the same aspect ratio will simply scale with the particle volume. The calculation of the average polarizabilities is just that of the average volume. A trivial case. But, of course, when size-dependent dielectric functions are introduced, the combined effect of broadening by intrinsic and extrinsic effects will be more complex, and the averaging finds all its interest. The results obtained for distributions over the radius parameter with a correction of either the bulk dielectric function as the finite size or the surface correction are shown in Figs. 6.6(d)-(e) and Figs. 6.6(f)-(g) respectively.

The finite-size effect will again broaden the response. Because of the probabilistic nature of the polydispersity it is the orange dashed line for the middle sized radius, and not the blue dashed-dotted line for the largest radius, which has the highest amplitude.

We observe that in contrast to the monodisperse case with the surface correction of the bulk dielectric function [Figs. 6.2(e)-(f)] the polydisperse case with the same type of correction will i) work differently on the different sizes of the particles in the distribution, effecting more the smaller than the bigger particles, ii) result in a slightly broadened peak [Figs. 6.6(f)-(g)] as compared to the effect of the distribution itself [Figs. 6.6(b)-(c)].

As for the distribution over the truncation ratio parameter, the trend of the response is more interesting as it reflects the sensitivity of the plasmon resonances to the aspect ratios of the particles which is changed through the truncation ratio parameter in GranFilm. The plasmon resonance's energy position is blue-shifted for the parallel polarizability with increasing truncation ratio value [Fig. 6.7(b)] and red-shifted for the perpendicular polarizability [Fig. 6.7(c)]. Note that not only the volume of the particle is changed with the truncation ratio of the particle, but also the oscillator strength of the parallel/perpendicular resonances (normalized by the volume) that will increase/decrease.

Once multiplied by the probability of having a given truncation ratio, the conjunction of those effects give rise to a complex effect. We observe an apparent broadening of the peaks which is more important for the parallel than the perpendicular direction. The reason for this behavior is found in the higher sensitivity to the aspect ratio of the particle for the parallel resonance than for the perpendicular one. Although, as a general rule of thumb, this effect depends on the underlying modes of polarization that show different dispersion with truncation[5]. A side effect of the truncation ratio distribution is also an asymmetry of the peaks and a slight shift of its maximum value away from that of the central component of the truncation distribution [see in particular Fig. 6.7(b)].

[4]The general formula to calculate the volume of a particle was discussed in App. 4.B.
[5]See Ch. 5 for a discussion of the nature of the resonance peaks.

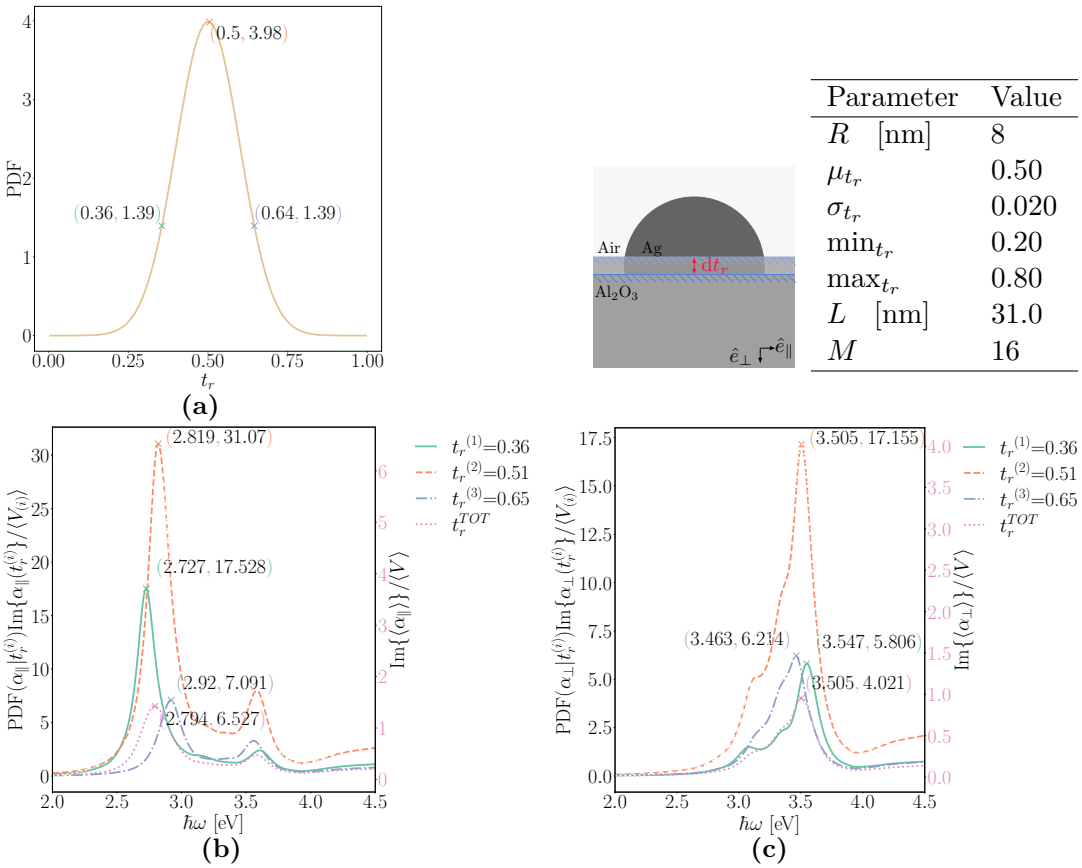

Parameter	Value
R [nm]	8
μ_{t_r}	0.50
σ_{t_r}	0.020
$\min_{t_r}$	0.20
$\max_{t_r}$	0.80
L [nm]	31.0
M	16

Figure 6.7 Effect of polydispersity on the imaginary parts of the parallel (b) and perpendicular (c) polarizabilities for a truncated normal distribution over the truncation ratio (a) parameter. Simulation parameters of the system are given in the upper right corner of the figure.

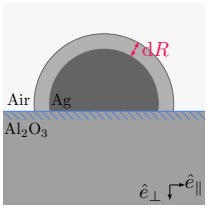

Parameter	Value
R [nm]	$\mu_R = 3.0, \sigma_R = \mathrm{d}\sigma_R, \min_R = 0.00001, \max_R = 6.0$
tol_{MC}	0.05
t_r	0.45
L [nm]	31.0
M	16

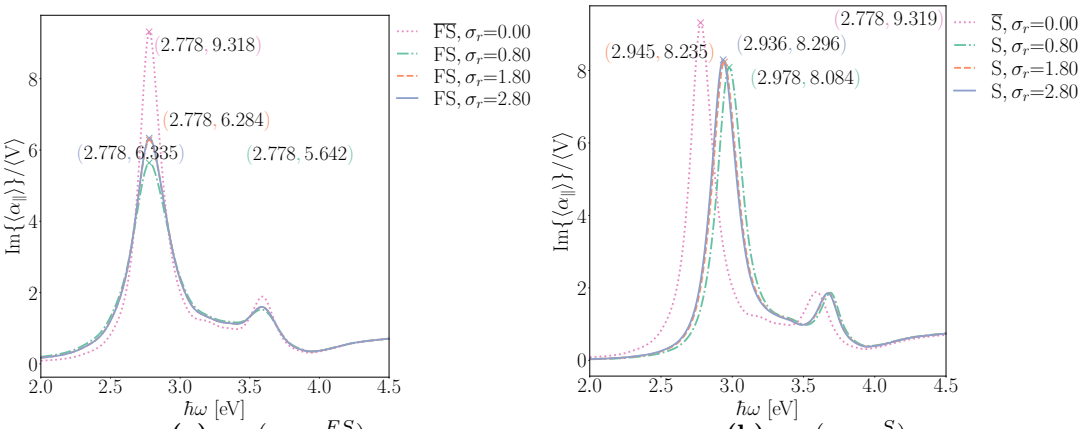

(a) $\alpha_\parallel(\sigma_R, \varepsilon^{FS})$. **(b)** $\alpha_\parallel(\sigma_R, \varepsilon^{S})$.

Figure 6.8 Effect of polydispersity on the normalized imaginary parts of the parallel polarizability of changing distribution widths with the finite-size (a) and the surface (b) corrections of the bulk dieletric function. Simulation parameters are reminded above the figure.

The impact of the width of the distributions

The impact of the width of the size and shape distributions are investigated by varying their variance σ^2. As demonstrated earlier, only changing the width of the PDF for the radius parameter is of limited interest without also correcting of the experimental bulk dielectric functions of the metal since otherwise the resulting polarizabilities, when divided by the volume of the particle, will be identical.

Combining both types of corrections of the bulk dielectric function and broader distributions over the radius parameter yields interesting results. As the distributions become broader the effects of the polydispersity and the corrections of the bulk experimental dielectric functions are competing. Again, the effect of the averaging is such that the broadening related to the surface correction of the experimental bulk dielectric function is more prominent, as compared to the monodisperse case. In Figs. 6.8(a)-(b) it is no longer only the distributions with the overall smallest particles that are most impacted by the corrections. The dash-dotted green line represents the overall smallest particles with a narrow distribution. For the two wider distributions we can see that the dashed orange line appears to be affected in the same way as the broader distribution represented by a solid blue line. This indicates that it is the smallest particles in the distribution that contributes most significantly to the broadening. The perpendicular polarizabilities show a similar behavior, but the results are not shown here in order to limit the number of figures.

When increasing the width of the truncation ratio distribution σ_{tr}, as already discussed for more moderate values, the polarizabilities get broader and more asymmetric. A

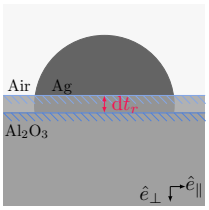

Parameter	Value
R [nm]	3.0
t_r	$\mu_{t_r} = 0.45, \sigma_{t_r} = \mathrm{d}\sigma_{t_r}, \min_{t_r} = 0.0, \max_{t_r} = 1.0$
tol	0.05
L [nm]	31.0
M	16

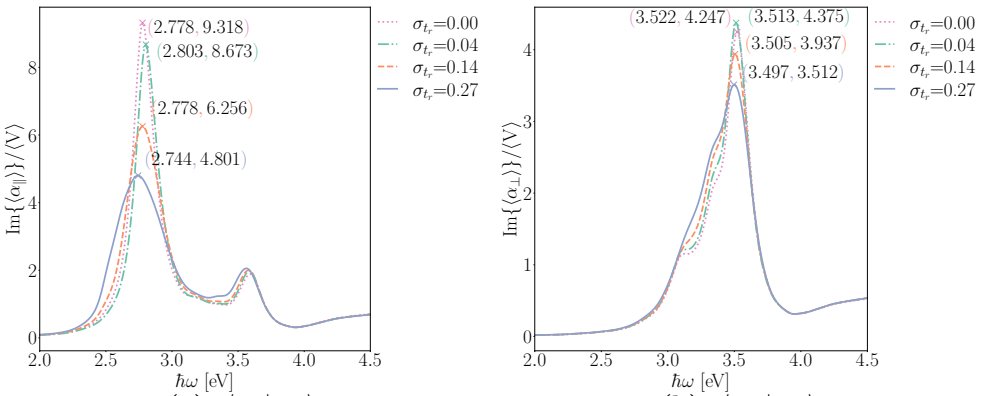

(a) $\langle\alpha_\parallel|\sigma_{tr}\rangle$. **(b)** $\langle\alpha_\perp|\sigma_{tr}\rangle$.

Figure 6.9 Effect of polydispersity on the normalized imaginary parts of the parallel (a) and perpendicuar (b) polarizabilities for a distribution over the truncation ratio parameter with varying widths. Simulation parameters are given above the figure.

spectral shift of the peak is also observed, and it is more pronounced for the parallel than for the perpendicular direction, as illustrated in Figs. 6.9(a)-(b). The asymmetry and the shift in energy towards the red (lower energies) in case of the parallel resonance peaks mean that the increase of oscillator strength more than compensates for the decrease in the particle volume when the truncation ratio is decreased.

Observed trends in the low coverage polydisperse limit

The discussion of a LCP system is terminated by drawing some conclusions from the results presented so far in this section.

- A radius distribution alone, does change the amplitudes of the polarization peaks in both the parallel and the perpendicular directions. When the effect of the averaging is combined with the effect of the corrections of the bulk dielectric functions both the finite-size and the surface correction will contribute to the broadening of the plasmon resonance peaks. The surface correction also shifts the energy position of the peak.
- A distribution over the truncation ratio parameter alone will produce broader peaks due to the energy shift of plasmon resonance caused by the modification of the aspect ratio. Again, it is clear that the wider distribution results in the broader peak. In contrast to a distribution over the radius parameter.

The investigations of varying both the radius and truncation ratio parameter for other

substrates (MgO, ZnO), have been performed. The results are similar to the ones reported for Al_3O_2 and will, therefore, not be given in this manuscript.

6.5 Polydispersity in the finite coverage regime

The FCP system [see Fig. 6.4(b)] corresponds to a size and shape distribution in the NPs were the island-island interaction matters. In contrast to the monodisperse case, the local field felt by a particle will depend both on its neighbors of different sizes/shapes and the distances between the particles. The calculation of the spatial average of this fluctuating quantity requires to account for the correlation between the particles in a proper way. Following the idea of Barrera *et al.* [83], a first solution is obtained in the *Mean Field Theory* (MFT) limit. Furthermore, with the idea proposed by Gazzillo *et al.* [84] we will apply a scaling approximation of the monodisperse RDF to approximate the polydisperse RDF. Our approach will be restricted to dipolar interaction but can, in principle, be generalized to quadrupolar interaction.

6.5.1 The average polarizability calculated in the mean field theory

Let's assume a polydisperse (size/shape) collection of particles. Since we are interested only in their dipolar interactions, each particle is replaced by its direct dipole located at position $\mathbf{r}_i$ and its images located at $\bar{\mathbf{r}}_i$. Figure 6.10 displays the relevant sizes for the considered geometry. All particles in the system will have an individual geometry decided by the set of parameters $\{R_\mu, d_\mu, z^\mu_{mp}, z^\mu_{\bar{m}p}\}$. The truncation ratio is (as always) defined as the distance from the center of the sphere to the surface of the substrate $t^\mu_r = d_\mu/R_\mu$.

The system that we consider consists of an infinite set of polydisperse particles that are supported by a dielectric substrate. In the following, it will be assumed that the geometry of a particle is fully specified by the index ξ that we will refer to as the *particle geometry* (or geometrical type of the particle). For instance, collectively this symbol specifies the radius, truncation ratio and the aspect ratio of the particle in question or any other parameter needed to characterize the size and shape of the particle. It can even be used to distinguish different particle types, for instance, if the particle is coated or not, or its coating thickness or even the material that the coating consists of. Figure 6.10 displays the relevant sizes for the considered geometry.

When such a system is illuminated by a planar EM wave, for which the electric field component has the form

$$\mathbf{E}(\mathbf{r}, t) = \mathbf{E}_0 \exp\left[i\mathbf{k}\cdot\mathbf{r} - i\omega t\right] = \mathbf{E}_0(\mathbf{r}) \exp\left[-i\omega t\right], \tag{6.14}$$

a dipole will be induced inside each of the particles of the system as we have seen previously. Here $\mathbf{E}_0(\mathbf{r}) = \mathbf{E}_0 \exp\left[i\mathbf{k}\cdot\mathbf{r}\right]$ with $\mathbf{E}_0$ being a constant vector and we will neglect the time-harmonic dependence from now onward. Furthermore, to keep the notation simple, we will suppress any explicit reference to the angular frequency ω for the relevant quantities of interest. If we assume that one of these induced dipoles is located at the spatial position $\mathbf{r}_i = \mathbf{r}_\parallel + z_{mp}\hat{\mathbf{z}}$ and that the particle at this position

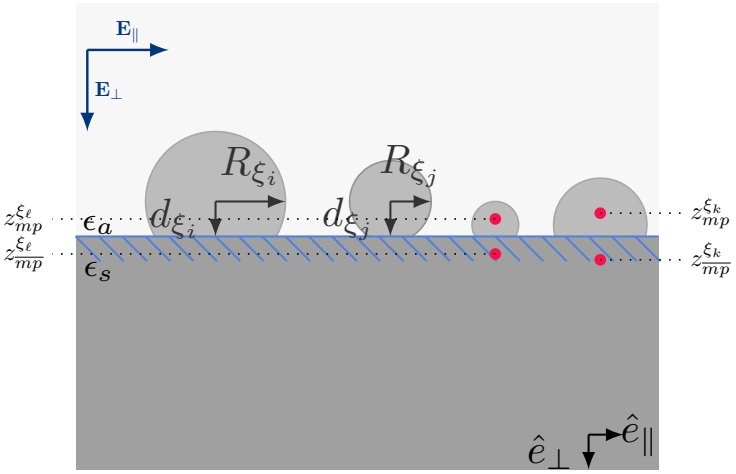

Figure 6.10 Principal sketch of a FCP system. Each particle in the ensemble is specified by their individual geometry. To keep the sketch clear the geometry parameters (R, d) and the direct/image multipoles $(z_{mp}/z_{\overline{mp}})$ are marked in two different pair of particle geometries $\{\xi_i, \xi_j\}$ and $\{\xi_\ell, \xi_k\}$.

has the geometrical type ξ_i, then the induced dipole moment at this position will be

$$\mathbf{p}_i(\mathbf{r}_i, \xi_i) = \overleftrightarrow{\boldsymbol{\alpha}}(\xi_i)\, \mathbf{E}_{\text{loc}}(\mathbf{r}_i) \tag{6.15}$$

Here $\overleftrightarrow{\boldsymbol{\alpha}}(\xi_i)$ denotes the polarizability tensor of the ith particle that is of geometry ξ_i and $\mathbf{E}_{\text{loc}}(\mathbf{r}_i)$ is the *local* electric field at $\mathbf{r}_i$ in the medium of incidence (the host medium) when the particle is *absent*. This field receives contributions from both the incident wave but also from the neighboring particles and from the substrate, that is, from the immediate surroundings of the particle.

To satisfy the required BCs on the planar surface of the substrate, we used the method of images for the monodisperse case (see Ch. 3). For the polydisperse system it is practical to do the same. Therefore, for the dipole at $\mathbf{r}_i$ and of dipole moment $\mathbf{p}_i(\mathbf{r}_i, \xi_i)$ given by Eq. (6.15), there is an associated image dipole of moment

$$\bar{\mathbf{p}}_i(\bar{\mathbf{r}}_i, \xi_i) = \overleftrightarrow{\boldsymbol{M}}\, \mathbf{p}_i(\mathbf{r}_i, \xi_i) \tag{6.16a}$$

with

$$\overleftrightarrow{\boldsymbol{M}} = \frac{\varepsilon_2 - \varepsilon_1}{\varepsilon_2 + \varepsilon_1}\, \text{diag}(-1, -1, 1). \tag{6.16b}$$

Here ε_1 and ε_2 denote the dielectric functions of the ambient and the substrate, respectively. The position vector of the image dipole is defined as $\bar{\mathbf{r}}_i = \mathbf{r}_\parallel + z_{\overline{mp}}\hat{\mathbf{z}}$.

It is now time to specify the local electric field that appears in Eq. (6.15). It can be

written in the form[6]

$$\mathbf{E}_{\text{loc}}(\mathbf{r}_i) = \mathbf{E}_0(\mathbf{r}_i) + \sum_{j\neq i} \mathbf{E}_j(\mathbf{r}_i) + \sum_{j\neq i} \overline{\mathbf{E}}_j(\mathbf{r}_i). \tag{6.17}$$

Here $\mathbf{E}_j(\mathbf{r}_i)$ represents the (direct) electric dipole field at $\mathbf{r}_i$ that is due to the jth dipole of moment $\mathbf{p}_j(\mathbf{r}_j, \xi_j)$ located at $\mathbf{r}_j$. Similarly, $\overline{\mathbf{E}}_j(\mathbf{r}_i)$ is the corresponding field from the jth image dipole of moment $\bar{\mathbf{p}}_j(\bar{\mathbf{r}}_j, \xi_j)$ that is placed in the substrate at $\bar{\mathbf{r}}_j$. The physical interpretation of Eq. (6.17) is the following: The first term on the right-hand-side of this equation represents the contribution to the local electric field from the incident field[7]; the second term represents the direct contribution to the field in the ambient medium from the neighboring particles (note that $i \neq j$ in the sum); while the third and last term in Eq. (6.17) is the contribution due to scattering at the planar surface of the substrate of the dipole fields originating from the induced dipoles located above the surface of the substrate (note that the term $i = j$ here is included in the sum since we want to include the reflected dipole field from the ith dipole).
Here we will assume that the interaction between the particles primarily is of near-field character. Under this assumption the electric dipole field from the jth induced dipole has the form [6, 85] (when using the cgs unit system with Lortenz-Heaviside formalism[8])

$$\mathbf{E}_j(\mathbf{r}_i) = \frac{1}{4\pi\varepsilon_1} \frac{3[\mathbf{p}_j \cdot \hat{\mathbf{r}}_{ij}]\,\hat{\mathbf{r}}_{ij} - \mathbf{p}_j}{r_{ij}^3}, \tag{6.18}$$

where we have defined the distance vector

$$\mathbf{r}_{ij} = \mathbf{r}_i - \mathbf{r}_j \tag{6.19}$$

from the jth dipole (located above the substrate) to the point $\mathbf{r}_i$ where the field is evaluated; to simplify the notation we have suppressed the arguments of the dipole moment so that $\mathbf{p}_j \equiv \mathbf{p}_j(\mathbf{r}_j, \xi_j)$. A caret over a vector means that it is a unit vector, and $r_{ij} = |\mathbf{r}_{ij}|$. In a similar way we have

$$\overline{\mathbf{E}}_j(\mathbf{r}_i) = \frac{1}{4\pi\varepsilon_1} \frac{3[\bar{\mathbf{p}}_j \cdot \hat{\bar{\mathbf{r}}}_{ij}]\,\hat{\bar{\mathbf{r}}}_{ij} - \bar{\mathbf{p}}_j}{\bar{r}_{ij}^3}, \tag{6.20}$$

[6] It should be noted that there is some ambiguity as to if the term $j = i$ should be included, or not, in the last sum on the right-hand-side of Eq. (6.17). Whether it should be included depends on the definition of the polarizability $\overleftrightarrow{\boldsymbol{\alpha}}(\xi_i)$ that appears in Eq. (6.15). If the single-particle polarizability already includes the effect of the substrate, then the term $j = i$ should be excluded from the sum; on the other hand, if $\overleftrightarrow{\boldsymbol{\alpha}}(\xi_i)$ does not include the effect of the substrate, the term $j = i$ has to be included in order to account for the response of the substrate. Here we have chosen to exclude the term $j = i$ since the single-particle polarizabilities calculated with GranFilm automatically will include the effect of the substrate.

[7] It should be noticed that if the incident medium is polarizable, not vacuum as we assume here, this term has to be multiplied by the dielectric function of the incident medium and the wave vector $\mathbf{k}$ of the incident medium.

[8] This choice of units is consistent with the already developed formalism in Chs. 2-3. Remember that we took the vacuum permittivity equal to one $\varepsilon_0 = 1$.

where $\mathbf{p}_j \equiv \bar{\mathbf{p}}_j(\bar{\mathbf{r}}_j, \xi_j)$ and we have defined the distance vector as

$$\bar{\mathbf{r}}_{ij} = \mathbf{r}_i - \bar{\mathbf{r}}_j \tag{6.21}$$

from the jth (induced) image dipole located in the substrate at $\bar{\mathbf{r}}_j$ to the field point $\mathbf{r}_i$. It should be noted that if the interaction is not only via the near field, as we have assumed here, the expressions in Eqs. (6.18) and (6.20) have to be replaced by the full expressions for the electric dipole field which includes, for instance, the contributions from radiation (see Refs. [6,85] for details).

To facilitate the coming analysis, it is practical to introduce the *dipole interaction tensors* $\overleftrightarrow{\boldsymbol{T}}_{ij}$ and $\overleftrightarrow{\bar{\boldsymbol{T}}}_{ij}$ that correspond to the jth dipole and its image dipole, respectively. They propagate the electric field of the dipoles located at $\mathbf{r}_j$ and $\bar{\mathbf{r}}_j$, respectively, to the observation point $\mathbf{r}_i$. They are implicitly defined by the relations

$$\mathbf{E}_j(\mathbf{r}_i) = \overleftrightarrow{\boldsymbol{T}}_{ij}\, \mathbf{p}_j, \tag{6.22a}$$

and

$$\bar{\mathbf{E}}_j(\mathbf{r}_i) = \overleftrightarrow{\bar{\boldsymbol{T}}}_{ij}\, \bar{\mathbf{p}}_j. \tag{6.22b}$$

Written out in explicit form one has for $i \neq j$

$$\overleftrightarrow{\boldsymbol{T}}_{ij} = \frac{1}{4\pi\varepsilon_1}\left[\frac{3\,\mathbf{r}_{ij}\otimes\mathbf{r}_{ij} - \overleftrightarrow{\mathbb{I}}}{r_{ij}^3}\right] = \frac{1}{4\pi\varepsilon_1}\begin{bmatrix} \frac{3\,x_{ij}^2}{r_{ij}^5} - \frac{1}{r_{ij}^3} & \frac{3\,x_{ij}y_{ij}}{r_{ij}^5} & \frac{3\,x_{ij}z_{ij}}{r_{ij}^5} \\ \frac{3\,y_{ij}x_{ij}}{r_{ij}^5} & \frac{3\,y_{ij}^2}{r_{ij}^5} - \frac{1}{r_{ij}^3} & \frac{3\,y_{ij}z_{ij}}{r_{ij}^5} \\ \frac{3\,z_{ij}x_{ij}}{r_{ij}^5} & \frac{3\,z_{ij}y_{ij}}{r_{ij}^5} & \frac{3\,z_{ij}^2}{r_{ij}^5} - \frac{1}{r_{ij}^3} \end{bmatrix}, \tag{6.23}$$

where $\otimes$ is the tensor product (outer product) and $\mathbf{r}_{ij} = (x_{ij}, y_{ij}, z_{ij})$; for reasons of later convenience, we will also set $\overleftrightarrow{\boldsymbol{T}}_{ii} = 0$ (note that when $i = j$ the distance $\mathbf{r}_{ii} = 0$). The explicit form of $\overleftrightarrow{\bar{\boldsymbol{T}}}_{ij}$ is obtained from Eq. (6.23) by replacing $\mathbf{r}_{ij}$ with $\bar{\mathbf{r}}_{ij} = (\bar{x}_{ij}, \bar{y}_{ij}, \bar{z}_{ij})$.

If Eq. (6.17) is multiplied from the left by the polarizability tensor of the ith dipole, $\overleftrightarrow{\boldsymbol{\alpha}}(\xi_i)$, and the resulting expression is combined with Eqs. (6.15) and (6.22), one is lead to

$$\mathbf{p}_i(\mathbf{r}_i, \xi_i) = \overleftrightarrow{\boldsymbol{\alpha}}(\xi_i)\left[\mathbf{E}_0(\mathbf{r}_i) + \sum_j \overleftrightarrow{\boldsymbol{T}}_{ij}\, \mathbf{p}_j(\mathbf{r}_j, \xi_j) + \sum_j \overleftrightarrow{\bar{\boldsymbol{T}}}_{ij}\, \bar{\mathbf{p}}_j(\bar{\mathbf{r}}_j, \xi_j)\right]. \tag{6.24}$$

In writing this equation, we have for reasons of convenience also included the term $j = i$ in the sums since they do not contribute due to the way the dipole interaction tensors were defined. To get a closed set of equations, we take advantage of results in Eq. (6.16) to obtain

$$\mathbf{p}_i(\mathbf{r}_i, \xi_i) = \overleftrightarrow{\boldsymbol{\alpha}}(\xi_i)\left[\mathbf{E}_0(\mathbf{r}_i) + \sum_j \overleftrightarrow{\boldsymbol{V}}_{ij}\, \mathbf{p}_j(\mathbf{r}_j, \xi_j)\right], \tag{6.25a}$$

where we have defined the dyad

$$\overleftrightarrow{\boldsymbol{V}}_{ij} = \overleftrightarrow{\boldsymbol{T}}_{ij} + \overleftrightarrow{\boldsymbol{T}}_{ij}\,\overleftrightarrow{\boldsymbol{M}}. \tag{6.25b}$$

If the system consists of an infinite and regular array of monodisperse particles, then all the induced dipole moments $\mathbf{p}_i$ (now without the dependence on the geometrical type index) will have the same magnitude, say p; the relative phase change from dipole-to-dipole is due to the spatial variation of the oscillation electric field. By introducing $\mathbf{p}_i = \mathbf{p}\exp[i\mathbf{k}\cdot\mathbf{r}_i]$ and a similar expression for $\mathbf{p}_j$, the substitution of these expressions into Eq. (6.25a), one is lead to an equation that can be readily solved for each of the components of the common dipole moment $\mathbf{p}$ that is corrected for the interaction between the particles. By defining $\mathbf{p} = \overleftrightarrow{\boldsymbol{\alpha}}'\,\mathbf{E}_0$, where $\overleftrightarrow{\boldsymbol{\alpha}}'$ denotes the polarizability renomalized for the interaction of the particles. Without going into the technical details of this calculation, it suffices to mention that the results will contain the lattice-sums, and the parallel and perpendicular components for the renormalized polarizabilities $\overleftrightarrow{\boldsymbol{\alpha}}'$ will be given by the expression presented previously in Eq. (3.44).

We now turn to the more interesting case of a polydisperse system for which the induced dipole moments $\mathbf{p}_i(\mathbf{r}_i, \xi_i)$ no longer are the same for all particles. To obtain them, one needs to solve Eq. (6.25a) for a set of particle geometries but, in general, this is a highly non-trivial task. Below we will obtain a solution of this equation within the so-called mean field approximation. However, before presenting this solution we introduce some necessary concepts.

In principle, there are infinitely many particle geometries ξ_i in the polydisperse system of our interest. However, Eq. (6.25a) can only be solved for a finite number of unknowns. To overcome this, we start by restricting ourselves to a large area S of the planar surface of the substrate which consists of N_S particles in total. Next we introduce a set of predefined particle geometries $\Omega_N = \{\nu_i\}_{i=1}^{N}$ that has a large but finite number of elements N and which will represents the size and shape probability distribution function that characterizes the particles of the system. In some sense, Ω_N can be seen as a discretization of the size and shape PDF of the system. Now we make the approximation that any particle geometry in the system, ξ_i, is well approximated as an element of the set Ω_N of particle geometries. Furthermore, for a given particle geometry $\nu \in \Omega_N$ we define a set $\mathcal{P}(\nu)$ consisting of *all* the particle numbers of those particles which are characterize by the geometrical type ν.

Now, one may ask for the averaged dipole moment for particles of a given geometry ν, a quantity that we defined as

$$\langle \mathbf{p}_i(\nu)\rangle_{\mathbf{r}_i|\nu} = \frac{1}{N_\nu}\sum_{i\in\mathcal{P}(\nu)} \mathbf{p}_i, \tag{6.26}$$

where N_ν is the cardinality (or number of elements) of the set $\mathcal{P}(\nu)$ (that is $N_\nu = |\mathcal{P}(\nu)|$). The dipole moment averaged over all particles of the system, that is, averaged over both position and particle geometry, is defined as

$$\langle \mathbf{p}_i\rangle_i = \frac{1}{N_S}\sum_i \mathbf{p}_i = \frac{1}{N_S}\sum_{\nu=\nu_1}^{\nu_N}\sum_{i\in\mathcal{P}(\nu)} \mathbf{p}_i = \frac{1}{\rho}\sum_\nu \rho_\nu \langle \mathbf{p}_i(\nu)\rangle_{\mathbf{r}_i|\nu}\,, \tag{6.27}$$

where $\rho = N_S/S$ is the surface coverage of *all* particle in the system and $\rho_\nu = N_\nu/S$ is the surface coverage of *only* particles of geometry ν. In writing this equation we have used that $\sum_i = \sum_{\nu=\nu_1}^{\nu_N} \sum_{i\in\mathcal{P}}(\nu)$ and in the following we will suppress the limits on the ν-summation to simplify the notation; from the context it should be apparent that we sum over all particles geometries. Note from Eq. (6.27) that the global average $\langle \mathbf{p}_i \rangle_i$ can be written as a weighted average of $\langle \mathbf{p}_i(\nu) \rangle_{\mathbf{r}_i|\nu}$ with weights ρ_ν/ρ (note that $\rho = \sum_\nu \rho_\nu$).

To obtain a solution of Eq. (6.25a) within the mean field approximation, we will follow Barrera *et al.* [83] and first define the fluctuations around the mean of the dipole moment of a particle of geometrical type $\xi_j = \nu' \in \Omega_N$ as

$$\Delta\mathbf{p}_j(\mathbf{r}_j, \nu') = \mathbf{p}_j(\mathbf{r}_j, \nu') - \left\langle \mathbf{p}_j(\nu') \right\rangle_{\mathbf{r}_j|\nu'}, \tag{6.28}$$

and when it is introduced into the right-hand side of Eq. (6.25a), we obtain

$$\mathbf{p}_i(\mathbf{r}_i, \xi_i) = \overleftrightarrow{\boldsymbol{\alpha}}(\xi_i) \left[\mathbf{E}_0(\mathbf{r}_i) + \sum_{\nu'} \sum_{j\in\mathcal{P}(\nu')} \overleftrightarrow{\boldsymbol{V}}_{ij} \left\langle \mathbf{p}_j(\nu') \right\rangle_{\mathbf{r}_j|\nu'} + \sum_{\nu'} \sum_{j\in\mathcal{P}(\nu')} \overleftrightarrow{\boldsymbol{V}}_{ij}\, \Delta\mathbf{p}_j(\mathbf{r}_j, \nu') \right]. \tag{6.29}$$

The fluctuating dipole moment (for type ν') that appears in the last term on the right-hand side of this equation is difficult to calculate as it depends on the local arrangement of particles. To perform such a calculation, one is required to determine and use higher order position-position pair correlation functions for the system at hand [83]. This is a challenging task since detailed information and analysis of the particle morphology is required.

A more appealing approach, from a practical point of view, is to adapt the so-called *mean field approximation*. Here one simply neglects the fluctuating dipole moment in Eq. (6.29), that is, one sets $\Delta\mathbf{p}_j(\mathbf{r}_j, \nu') = 0$ in this equation. This is equivalent to treat each dipole of type ν as if it was embedded in the mean field exerted by the other particles. In order to proceed, we define a renomalized polarizability $\overleftrightarrow{\widetilde{\boldsymbol{\alpha}}}(\nu)$ for particles of geometrical type ν by the relation

$$\langle \mathbf{p}_i(\nu) \rangle_{\mathbf{r}_i|\nu} = \overleftrightarrow{\widetilde{\boldsymbol{\alpha}}}(\nu)\, \mathbf{E}_0. \tag{6.30}$$

This renomalized polarizability includes the effect of the interaction with neighboring dipoles (and image dipoles). However, it is important to realize that this polarizability only gives the response of an average particle of geometry ν. Depending on the immediate neighborhood of such a particle, and in particular what kind of particles that surrounds it, the dipole moments of these particles of geometrical type ν will vary; such variations are not captured by $\overleftrightarrow{\widetilde{\boldsymbol{\alpha}}}(\nu)$.

To obtain the equation satisfied by the renomalized polarizability $\overleftrightarrow{\widetilde{\boldsymbol{\alpha}}}(\nu)$ within the mean field approximation we start by setting $\Delta\mathbf{p}_j(\mathbf{r}_j, \nu') = 0$ and $\xi_i = \nu \in \Omega_N$ in Eq. (6.29). Next, we apply the spatial average $\langle \cdot \rangle_{\mathbf{r}_i|\nu}$ to the resulting equation;

then we introduce the results from Eq. (6.30) and cancel a common amplitude of the incident electric field. In this way we obtain

$$\overleftrightarrow{\widetilde{\boldsymbol{\alpha}}}(\nu) = \overleftrightarrow{\boldsymbol{\alpha}}(\nu) + \overleftrightarrow{\boldsymbol{\alpha}}(\nu) \sum_{\nu'} \sum_{j\in\mathcal{P}(\nu')} \left\langle \overleftrightarrow{\boldsymbol{V}}_{ij} \right\rangle_{\mathbf{r}_i|\nu} \overleftrightarrow{\widetilde{\boldsymbol{\alpha}}}(\nu'), \tag{6.31}$$

where we have used that the average $\langle\cdot\rangle_{\mathbf{r}_i|\nu}$ commutes with the sums over ν'. This equation is the tensorial equation for the determination of the renomalized polarizability $\overleftrightarrow{\widetilde{\boldsymbol{\alpha}}}(\nu)$. Alternatively one may write Eq. (6.31) in the more compact form

$$\sum_{\nu'=\nu_1}^{\nu_N} \overleftrightarrow{\boldsymbol{\mathcal{M}}}(\nu|\nu') \overleftrightarrow{\widetilde{\boldsymbol{\alpha}}}(\nu') = \overleftrightarrow{\boldsymbol{\alpha}}(\nu), \tag{6.32a}$$

where we have defined

$$\overleftrightarrow{\boldsymbol{\mathcal{M}}}(\nu|\nu') = \overleftrightarrow{\mathbb{I}} - \overleftrightarrow{\boldsymbol{\alpha}}(\nu) \left\langle \sum_{j\in\mathcal{P}(\nu')} \overleftrightarrow{\boldsymbol{V}}_{ij} \right\rangle_{\mathbf{r}_i|\nu} \tag{6.32b}$$

with $\overleftrightarrow{\mathbb{I}}$ denoting the unit dyad. In Appendix 6.A it is shown explicitly that the $\overleftrightarrow{\boldsymbol{\mathcal{M}}}(\nu|\nu')$ is a diagonal tensor of the form $\overleftrightarrow{\boldsymbol{\mathcal{M}}} = \mathrm{diag}(\mathcal{M}_\parallel, \mathcal{M}_\parallel, \mathcal{M}_\perp)$.

Due to the isotropy of the system in the plane of the surface of the substrate, the polarizability tensors are diagonal for the coordinate system that we assume such that

$$\overleftrightarrow{\boldsymbol{\alpha}}(\nu) = \begin{bmatrix} \alpha_\parallel(\nu) & 0 & 0 \\ 0 & \alpha_\parallel(\nu) & 0 \\ 0 & 0 & \alpha_\perp(\nu) \end{bmatrix} \tag{6.33}$$

and a similar relation for $\overleftrightarrow{\widetilde{\boldsymbol{\alpha}}}(\nu)$. For this reason, the components of the polarizability tenors that are parallel and perpendicular to the surface of the substrate are not coupled in Eq. (6.32a) and, therefore, one can write

$$\sum_{\nu'=\nu_1}^{\nu_N} \mathcal{M}_\parallel(\nu|\nu')\, \widetilde{\alpha}_\parallel(\nu') = \alpha_\parallel(\nu) \tag{6.34a}$$

and

$$\sum_{\nu'=\nu_1}^{\nu_N} \mathcal{M}_\perp(\nu|\nu')\, \widetilde{\alpha}_\perp(\nu') = \alpha_\perp(\nu), \tag{6.34b}$$

where $\nu, \nu' \in \Omega_N$. One should note that Eq. (6.34) should be satisfied for any particle geometry ν in Ω_N. To solve these two systems, we evaluate Eq. (6.34) for $\nu = \nu_m$ with $m = 1, \ldots, N$ to get an $N \times N$ linear system of equations (in the space of particle geometries) of the form

$$\mathbb{A}\mathbf{x} = \mathbf{b}, \tag{6.35a}$$

where the matrix and vector elements of system (6.34a) are

$$[\mathbb{A}]_{mn} = \mathcal{M}_{\parallel}(\nu_m|\nu_n) \qquad [\mathbf{x}]_n = \widetilde{\alpha}_{\parallel}(\nu_n) \qquad [\mathbf{b}]_m = \alpha_{\parallel}(\nu_m). \tag{6.35b}$$

For system (6.34b) the elements are defined in an equivalent manner. Once the linear system (6.35a) is solved by standard methods, the renormalized polarizabilities $\widetilde{\alpha}_{\parallel}(\nu_n)$ and $\widetilde{\alpha}_{\perp}(\nu_n)$ for all $\nu_n \in \Omega_N$ are known. Hence, these results can be used to obtain, within the mean-field approximation, the renormalized polarizability tensor averaged over the polydispersity of the system. This average polarizability is defined in accordance with Eq. (6.26) as

$$\left\langle \overleftrightarrow{\widetilde{\boldsymbol{\alpha}}} \right\rangle = \sum_{\nu=\nu_1}^{\nu_N} \frac{\rho_\nu}{\rho} \overleftrightarrow{\widetilde{\boldsymbol{\alpha}}}(\nu) \tag{6.36}$$

and it includes the effect of the (dipole) interaction with the neighboring particles as well as the effect of the substrate. It is the elements of this tensor, $\left\langle \widetilde{\alpha}_{\parallel} \right\rangle$ and $\langle \widetilde{\alpha}_{\perp} \rangle$, that enter into the calculation of the surface suceptibilities γ and β that are used in calculating the reflectivity of the system; see Eq. (6.1) for details.

It should be noticed that the ratio ρ_ν/ρ that appears in Eq. (6.36) is not know *a priori*. However, for a sufficiently large surface area S it can be obtained in terms of the size and shape probability distribution function that one has assumed. For the sake of argument, let us assume that this function $pdf(R)$ only depends on the (outer) radius R of spherical particles. Hence, the set of particle geometries used to calculate $\left\langle \widetilde{\alpha}_{\parallel} \right\rangle$ and $\langle \widetilde{\alpha}_{\perp} \rangle$, for instance, will be of the form $\Omega_N = \{R_n\}_{n=1}^N$ with $R_n = R_1 + (n-1)\Delta R$ where ΔR is the (constant) radial sampling interval. Under these assumptions, we can make the approximation $\rho_{\nu_n}/\rho \approx p(R_n)\Delta R$.

The scaling approximation of the radial distribution function

In the calculation of the tensor elements in Eq. (6.32) we needed to evaluate the integrals given in Eq. (6.46). These included the function $g_{\nu\nu'}(r_{ij,\parallel})$ which is the partial pair correlation function for particles of geometrical types ν and ν' separated by an in-plane distance $r_{ij,\parallel}$ [83]. This function is needed to give a microscopic description of the morphology of the system.

Already for a system of monodisperse particles where the interaction was approximated as hard-disks in 2D, the form of the RDF was non analytical. A generalization to the polydisperse case is far from trivial. A part of the difficulty in approximating these functions lies in the *excluded volumes* around the particles.

In the literature one can find several attempts of approximate these functions. Here the *dipole approximation* [86] and the *local monodisperse approximation* [87] represent important contributions.

We deal with this problem by following Gazzillo *et al.* 84. These authors suggested a 'scaling approximation' to express the partial RDFs for polydisperse nonionic collodial fluids, where the RDF for a mixture is approximated according to

$$g_{\nu\nu'}(r_{ij,\parallel}) \approx \hat{g}(\lambda_{\nu\nu'}\tilde{r}_{ij,\parallel}), \tag{6.37}$$

where $\hat{g}(\lambda_{\nu\nu'}\tilde{r}_{ij,\parallel})$ is an approximately equal RDF for a monodisperse system. With the choice of scaling parameters as

$$\lambda_{\nu\nu'} = \frac{D}{D_{\nu\nu'}} \tag{6.38a}$$

$$D_{\nu\nu'} = R_{\parallel}^{\nu} + R_{\parallel}^{\nu'}, \tag{6.38b}$$

where D is the diameter for the monodisperse system and $D_{\nu\nu'}$ is the additive diameter of the particle ν and ν' in the polydisperse system. Furthermore, since $\lambda_{\nu\nu'}\tilde{r}_{ij,\parallel} = \tilde{r}_{ij,\parallel}^{\nu\nu'}$ with the definition $\tilde{r}_{ij,\parallel}^{\nu\nu'} = r_{ij,\parallel}/D_{\nu\nu'}$ and write a scaling approximation as

$$\begin{aligned} g_{\nu,\nu'}(r_{ij,\parallel}) &\approx \hat{g}(\tilde{r}_{ij,\parallel}^{\nu\nu'}), \\ &= \hat{g}(r_{ij,\parallel}/D_{\nu\nu'}), \end{aligned} \tag{6.39}$$

Although the scaling approximation of Gazzillo *et al.* 84 incorrectly assumes that at contact all values of the RDF are equal, the results obtained on the basis of this approximation are still satisfactory.

The different forms for the RDF implemented in the GranFilm software are listed in Appendix B in the case of a monodisperse ensemble of non-overlapping particles.

6.5.2 Implementation of the mean field theory in GranFilm

The calculation of the renormalized polarizabilities $\overleftrightarrow{\tilde{\alpha}}$ in the MFT limit as described in Sec. 6.5.1 has been implemented into the GranFilm software. The main steps to perform this calculation are detailed in Fig. 6.5. First, the single particle polarizabilities are calculated for a given number of different island types in the chosen distributions. Then, the island-island interaction is calculated with MFT before the average polarizabilities are obtained. The samples in the distribution(s) are calculated according to the midpoint rule given in Eq. (6.7). Using the MC integration technique to compute the average in Eq. (6.36) is not possible in this limit as we need the dimensions of the matrices to compute the renormalized polarizabilities.

To compute the matrix elements in Eq. (6.34) the evaluation of the RDF is needed several times. With the two more realistic models of this function, namely the $g_{exp}(r_{ij})$ and the $g_{hard}(r_{ij})$ models, calling these functions adds a considerable amount of computational time to the simulation. To optimize the speed of the calculations the chosen RDF model is only evaluated once in the beginning of the calculation. When it is needed later, it uses the Akima spline algorithm to interpolate when needed again [57, 88].

Consistency check of the mean field code

As there exist no exact solutions we can compare our results with, a precise test to check the presented implementation is not obvious. However, some relevant and interesting limiting behavior does exist.

When the width of the size distribution tends towards zero the MFT results should approach the case of a random array given in Eq. (3.44) for monodisperse particles. If the distance from the direct multipole to the substrate $d^{\nu}_{mp} = (t_r^{(\nu,1)} - \mu^{(\nu,1)})R_{\perp}^{(\nu,1)} \approx 0$ the form of Eq. (3.44) and Eq. (6.46) becomes approximately equal. This test can be performed if one choses a narrow size distribution over the radius parameter and $t_r^{(\nu,1)} \approx \mu^{(\nu,1)}$.

A summary of tests comparing the MF code with a narrow distribution over the radius for different truncation ratios and surface coverage are displayed in Fig. 6.11. The distribution of the spherical particles in the MFT part of the code was chosen to be $\sigma_R = 0.1\,\text{nm}$ so the ensemble contains almost identical particles. It was sampled over a large $N_R = 100$ number of points. Figures 6.11(a)-(b) show an almost perfect overlap between the two limits for several truncation ratios and a non-overlapping particles at a surface coverage of $\Theta = 0.42$.

The same comparison for different surface coverages of particles with the RDF form corresponding to the hard-disk model is presented in Figs. 6.11(c)-(d). In this case, the truncation ratio was taken to $t_r = 1.0\text{e}{-4}$ and the multipole position ratio was set to $\mu = 9.0\text{e}{-6}$ for both the random array and for the MFT. The imaginary part of the average parallel polarizability [Fig. 6.11(c)], the overlap with the random array and the MF limit, although quite satisfactory, become significantly worse for the increased surface coverage. The effect of the local environment of each particle becomes more pronounced. The difference between the imaginary part of the average perpendicular polarizability [Fig. 6.11(d)] is smaller than on the parallel counterpart. This is related to a lower oscillator strength along the perpendicular direction, and therefore, a worse sensitivity to the induced shifts.

6.5.3 The effect of polydipersity in the finite coverage regime

In this subsection, we will present the main trends of calculations made in the FCP limit. We will start by describing the role of the RDF model in the MF code before we compare the different results of the more rigorous MF code with the (only theoretical) IM and MI models.

The role of the radial distribution function in the mean field model

Figure 6.12 investigates the role of the different RDF models for a changing surface coverage calculated with the MF code. A broader width of the distribution $\sigma_R = 1.5\,\text{nm}$ is chosen to see the real effect of the polydispersity in this limit. The lattice constant is taken from the set $L \in \{15, 12\}$, thus the surface coverage of the particle is changed. The rest of the simulation parameters are indicated above the figure. Figures 6.12(a)-(b) display, respectively, the imaginary part of the normalized average parallel and perpendicular polarizability.

For both the directions and coverages, the curves which are modeled with the $g_{step}(r)$-model as the RDF give a distinct response from the two other (more realistic) models. The results of a simulation with the step-model (turquoise dotted line and the green

Parameter	Value
R [nm]	$\mu_R = 5, \sigma_R = 0.1, \min_R = 4.9, \max_R = 5.1$
N_R	100
t_r	$\{0.1, 0.4\}$
μ	$\{0.0090, 0.39\}$
L [nm]	15.0
Θ	0.42
$g_x(r)$	*hard*
M	16

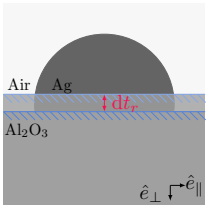

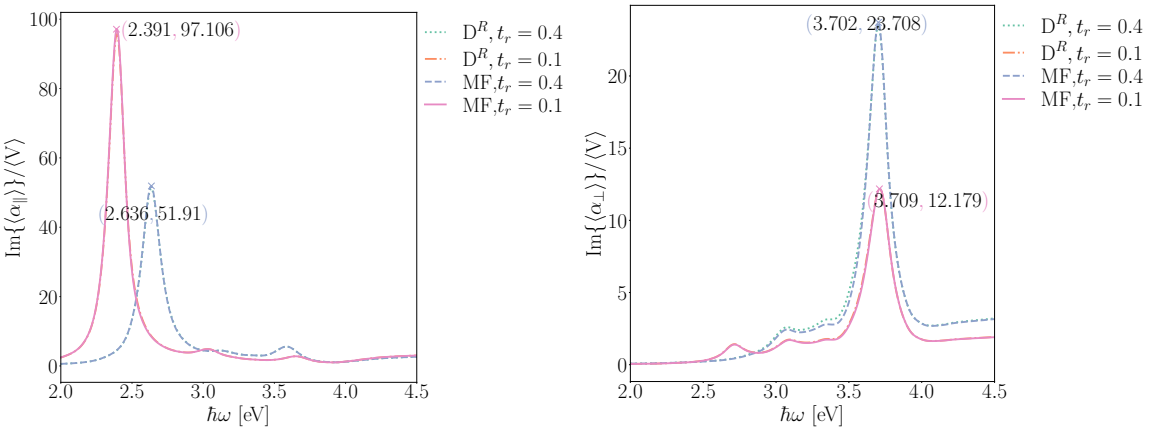

(a) $\mathrm{Im}\langle\alpha_\parallel(t_r)\rangle$. **(b)** $\mathrm{Im}\langle\alpha_\perp(t_r)\rangle$.

Parameter	Value
R [nm]	$\mu_R = 5, \sigma_R = 0.1, \min_R = 4.9, \max_R = 5.1$
N_R	100
t_r	0.0001
μ	0.00009
L [nm]	$\{15.0, 12.0\}$
Θ	$d\Theta$
$g_x(r)$	*hard*
M	16

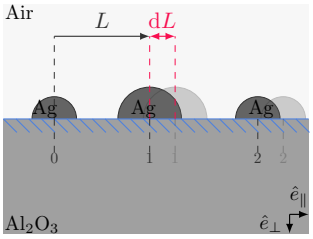

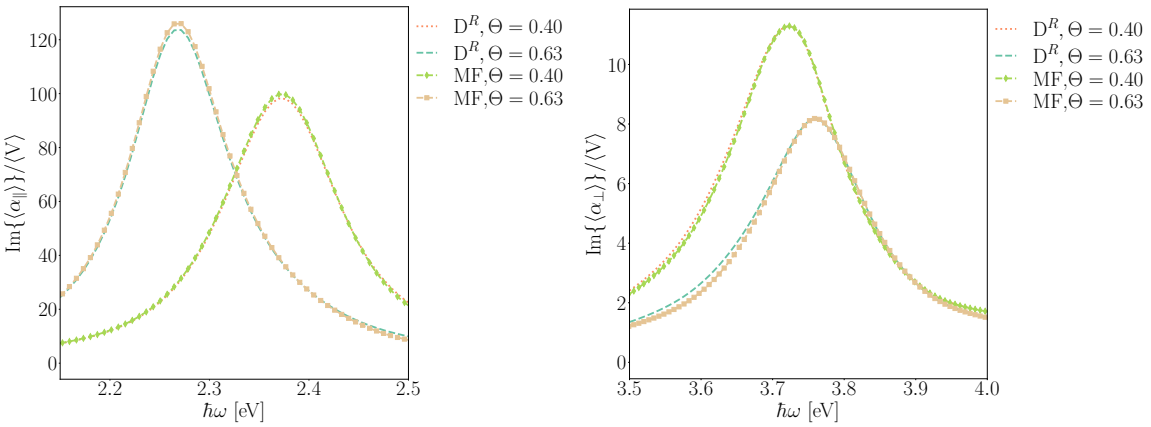

(c) $\mathrm{Im}\langle\alpha_\parallel(g(r), \Theta)\rangle$. **(d)** $\mathrm{Im}\langle\alpha_\perp(g(r), \Theta)\rangle$.

Figure 6.11 A comparison between the result of MF and the random array code for in the imaginary part of the average parallel and the perpendicular polarizabilities: (a)-(b) for a small size distribution and several truncation ratio parameters at fixed coverage, and (c)-(d) for different surface coverages. The used parameters are reminded on top of each subfigure.

solid line), are blue-shifted for the parallel polarizability and red-shifted for the perpendicular polarizability. As this model only is not physical, but taken into the discussion to test theoretical limits of the simulation models it is expected that the results will deviate from the two other models.

The agreement between the results for the polarizabilities obtained when RDF is assumed to be either $g_{exp}(r)$ and $g_{hard}(r)$ is rather good for low values of surface coverage. As the surface coverage is increased, the difference between the results obtained when assuming these two forms for the RDF becomes more pronounced, both in amplitude and energy of the peak for the parallel and perpendicular components of the polarizabilities. Again, the difference is largest for the parallel component.

As we know from the discussion of the RDF (see Appendix B), the first peak of the RDF is related to the first order neighbors, the next peak to the second order neighbors and so on. The higher the amplitude, the more pronounced is the short-range order of the lattice. The amplitude of the $g_{exp}(r)$-model is chosen to match the amplitude of the $g_{hard}(r)$-model for the same coverage. It seems that for a system where the coverage of particles is around $\Theta \leq 0.40$ the contributions from the higher (mainly the second) order neighbors are less critical than for the first order one. As the coverage increases, the short-range order in the system increases, and the contribution of the second-order neighbor in the RDF-model becomes more important.

The table below Figs. 6.12(a)-(b) displays typical computation times of one simulation for the discussed systems. If the running times are taken into account, it is evident that the $g_{hard}(r)$-model is at least one order of magnitude more time-consuming than the two other models.

The role of the electrostatic coupling

To investigate the qualitative impact of the MF code we have compared how the plasmon resonances are shifted for the three configurations; that is, for the LCM, the FCM, and the LCP systems.

Figures 6.13(a)-(b) display the imaginary part of the normalized parallel and perpendicular components of the polarizability averaged over a radius (or size) distribution function. The LCM and FCM results are illustrated with the dashed-dotted green line and the dotted orange line, respectively. The particles were organized in a random array and the single particle polarizability was corrected with the distribution integrals to dipolar order as given by Eq. (3.44). For the system where the electrostatic coupling is calculated (orange dotted line) the peak is red-shifted in the parallel [Fig. 6.13(a)] and blue-shifted in the perpendicular [Fig. 6.13(b)] direction. The LCP (blue dashed line) response shifts the amplitude, but not the position of the peaks. A result that we already commented on in Sec. 6.4.

The difference in positions of energies for the parallel and perpendicular response for the FCM (dotted orange line) and FCP (solid pink line) where the island-island interaction in the first case has been calculated with the distribution integrals for the monodisperse system and the second case with MFT for the polydisperse system are

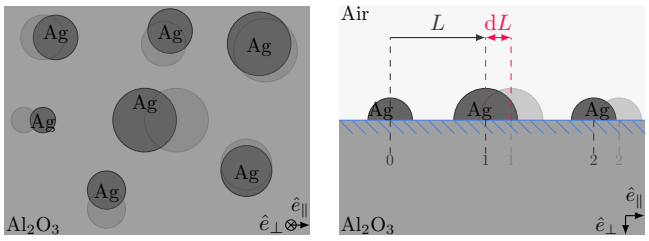

Parameter	Value
R [nm]	$\mu_R = 4.0, \sigma_R = 1.5, \min_R = 1.0, \max_R = 7.0$
N_R	100
t_r	0.0
L [nm]	$\{15.0, 12.0\}$
Θ	$\mathrm{d}\Theta$
$g_x(r)$	$\mathrm{d}g_x(r)$
M	16

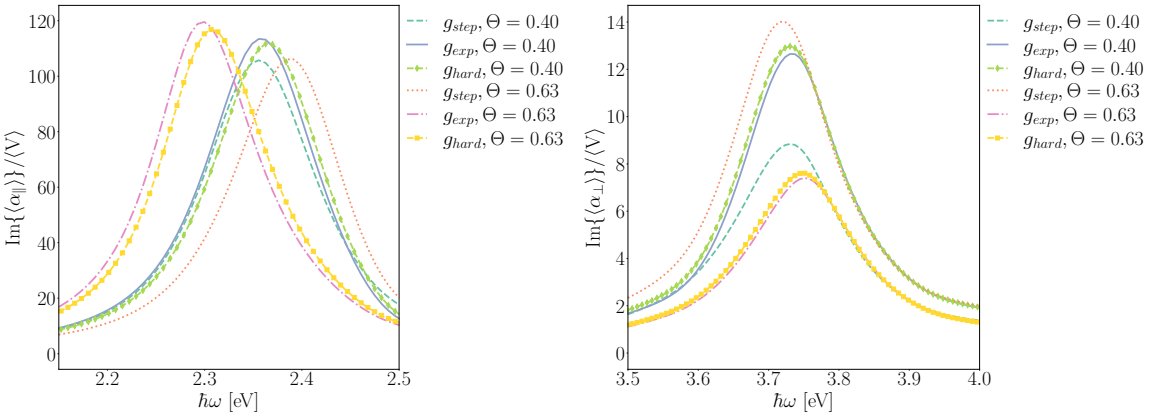

(a) $\mathrm{Im}\langle\alpha_\parallel(t_r)\rangle$. **(b)** $\mathrm{Im}\langle\alpha_\perp(t_r)\rangle$.

Θ	$g_x(r)$	Simulation time [s]
0.40	*step*	21
0.40	*exp*	24
0.40	*hard*	345
0.63	*step*	22
0.63	*exp*	24
0.63	*hard*	435

Figure 6.12 The imaginary parts of the normalized average parallel (a) and the perpendicular (b) polarizabilities for different values of the surface coverage and forms of the RDF. The parameters assumed in performing the simulations are given on top of the figure. A table displaying the running times for each system is shown below the figure.

surprisingly good. On the other hand, the amplitudes of the different limits are not the same.

Figures 6.13(c)-(d) display the imaginary part of the normalized and direction dependent polarizability averaged over a shape distribution. In contrast to the size distribution the effect of averaging tends to bring the amplitude of the polydisperse system lower than what was observed in the corresponding monodisperse case.

The agreement in energy position of the peaks within the different systems are surprisingly good for all cases except for a slight difference between the finite coverage result of the parallel polarizability [Fig. 6.13(a)/Fig. 6.13(c)] where the MF curve (solid pink line) is slightly red-shifted as compared to the orange dotted line. On the other hand, the amplitudes of the different limits are not the same except for the perpendicular polarizability corrected from the island-island interaction for a distribution over the truncation ratio parameter [Fig. 6.13(d)].

Different ways to calculate the average polarizability in the finite coverage polydisperse limit

In the FCP limit we had three different ways to calculate the average polarizability [see Fig. 6.3 for a review of the differences between them], namely the MF, the IM, and the MI limits. Figure 6.14 displays the imaginary part of the average normalized polarizabilities for a distribution over size [Figs. 6.14(a)-(b)] and shape [Figs. 6.14(c)-(d)]. The MF limit is displayed with the green dashed line, the IM with the orange dotted line, and the MI with the blue dashed-dotted line. The two latter simulations have been computed with the MC integration scheme.

Again, we observe the general trend that it is the parallel polarizability [Fig. 6.14(a)/Fig. 6.14(c)] which is most affected by the different ways to compute the average polarizability in terms of the energy position and the amplitude of the resonance peak. For the parallel direction relative to the substrate it is obvious that the order of the averaging and accounting for the island-island interaction between the particles matter in terms of the obtained result. The MF limit curve (dashed tourquise line) is blue-shifted for the size distribution [Fig. 6.14(a)] and red-shifted for the shape distribution [Fig. 6.14(c)].

In the perpendicular direction for a distribution over size [Fig. 6.14(b)] the difference between the two theoretical limits are smaller, but they do not approach the result of the MF limit. This curve (dashed turquoise line) lies higher in amplitude than the two others. For a distribution over shape [Fig. 6.14(d)] the MI (dashed-dotted blue line) and the MF (dashed turquoise line) are almost imposed. The result calculated in the IM limit has the same position in energy, but not amplitude.

Observed trends in the finite coverage polydisperse limit

The qualitative shifts of the imaginary part of the direction dependent average normalized polarizability discussed in this subsection have shown us how the three different methods in the FCP limit differ. Some conclusions can be drawn:

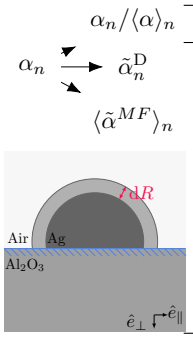

Parameter	Value
R_{poly} [nm]	$\mu_R = 5.0, \sigma_R = 1.5, \min_R = 2.5, \max_R = 7.5$
$N_{R_{poly}}$	100
R_{mono} [nm]	5.0
t_r	0.0
L [nm]	15.0
$g_x(r)$	*hard*
M	16
Island_Island	{None, D, MF}

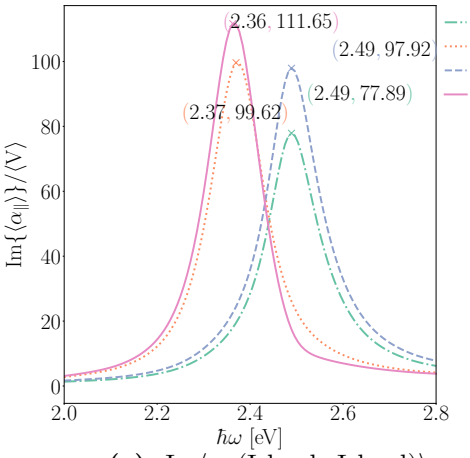

(a) $\mathrm{Im}\langle\alpha_\parallel(\mathrm{Island\_Island})\rangle$.

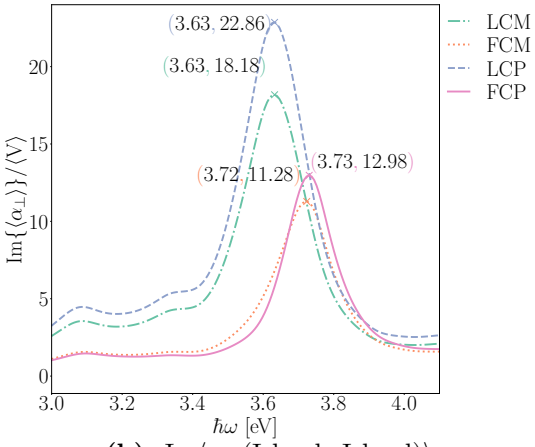

(b) $\mathrm{Im}\langle\alpha_\perp(\mathrm{Island\_Island})\rangle$.

Parameter	Value
R [nm]	5.0
t_r^{mono}	0.45
t_r^{poly}	$\mu_{t_r} = 0.45, \sigma_{t_r} = 0.135, \min_{t_r} = 0.3, \max_{t_r} = 0.6$
$N_{t_r^{poly}}$	100
L [nm]	15.0
$g_x(r)$	*hard*
M	16
Island_Island	{None, D, MF}

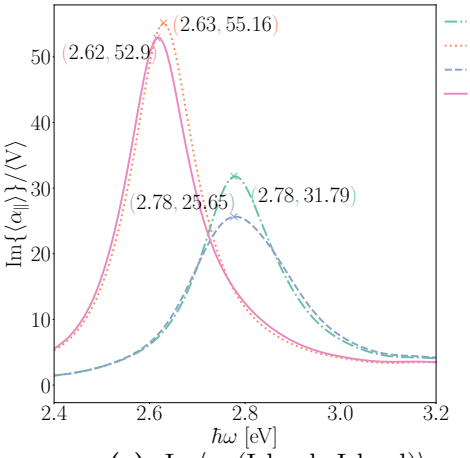

(c) $\mathrm{Im}\langle\alpha_\parallel(\mathrm{Island\_Island})\rangle$.

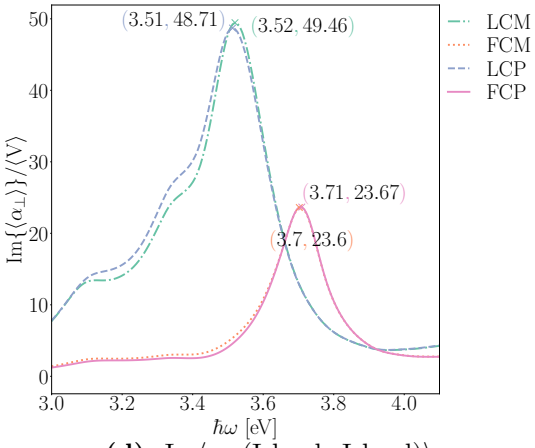

(d) $\mathrm{Im}\langle\alpha_\perp(\mathrm{Island\_Island})\rangle$.

Figure 6.13 A comparison between the result of the normalized average polarizability in the parallel (a)/(c) and perpendicular (b)/(d) direction for a random array of mono- and polydisperse system for a distribution over the radius/truncation ratio parameter. The Island_Island interaction is varied with 'None' (for LCM and LCP), 'D^R' for FCM and 'MF' for FCP. Simulation parameter are given above each subfigure.

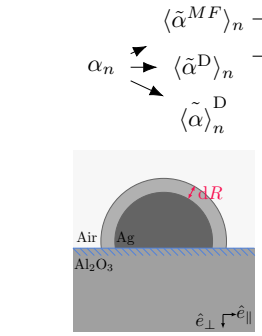

Parameter	Value
R [nm]	$\mu_R = 5.0, \sigma_R = 1.5, \min_R = 2.5, \max_R = 7.5$
$N_{R_{\mathrm{MF}}}$	100
$tol_{\mathrm{IM/MI}}$	0.02
t_r	0.0
L [nm]	15.0
$g_x(r)$	*hard*
Island_Island	{MF, IM, MI}
M	16

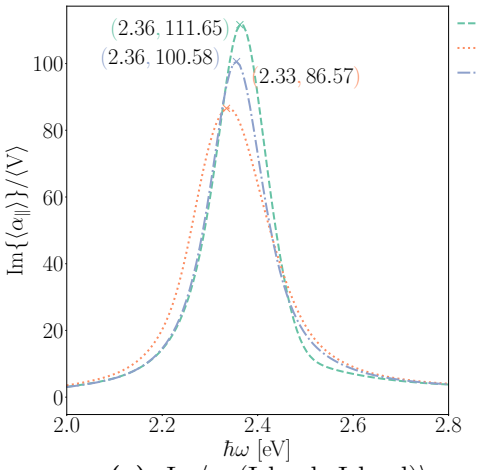

(a) $\mathrm{Im}\langle\alpha_\parallel(\mathrm{Island\_Island})\rangle$.

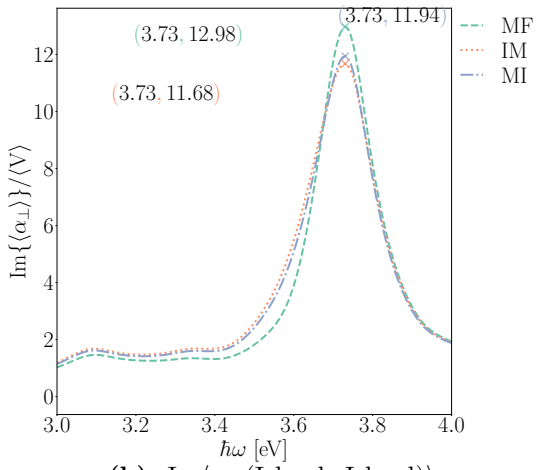

(b) $\mathrm{Im}\langle\alpha_\perp(\mathrm{Island\_Island})\rangle$.

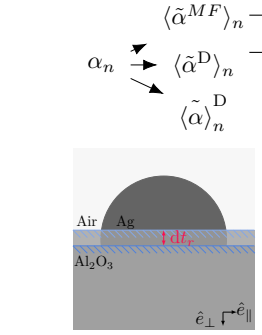

Parameter	Value
R [nm]	5.0
t_r	$\mu_{t_r} = 0.45, \sigma_{t_r} = 0.135, \min_{t_r} = 0.30, \max_{t_r} = 0.50$
$N_{t_r^{\mathrm{MF}}}$	100
$tol_{\mathrm{IM/MI}}$	0.02
L [nm]	15.0
$g_x(r)$	*hard*
Island_Island	{MF, IM, MI}
M	16

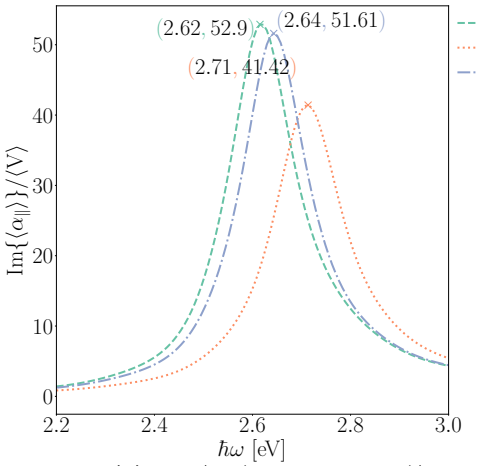

(c) $\mathrm{Im}\langle\alpha_\parallel(\mathrm{Island\_Island})\rangle$.

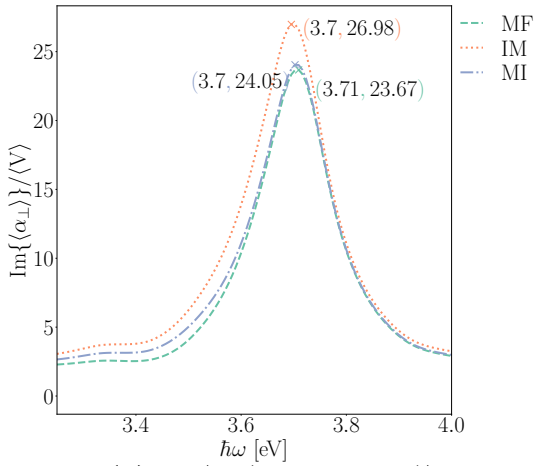

(d) $\mathrm{Im}\langle\alpha_\perp(\mathrm{Island\_Island})\rangle$.

Figure 6.14 A comparison between the results in the FCP limit for the average normalized parallel (a)/(c) and perpendicular (b)/(d) polarizabilities for a size/shape distribution calculated with the island_island interaction taken as MF, IM, and MI. The simulation parameters are given above each subfigure.

- The implementation of the MF limit has passed certain limit case tests, which have given consistent results.
- The simulation results for a FCP system are sensitive to the choice of RDF model. When the software is used, one should take into account the simulation time. For low surface coverage ($\Theta \leq 0.40$), a system where one uses the naive $g_{exp}(r)$-form seems to give satisfactory results.
- The overlap between the energy position of the resonances for the MF (rigorous) and MI (naive) results is surprisingly good.

The real part of the average polarizabilities follows similar trends to what we have observed for the imaginary part of the same polararizabilities. To limit the length of this manuscript, these results were not included since they do add little additional information to the discussion.

6.6 Conclusion

This chapter tackled the question of the origins of plasmon resonance broadening. This phenomenon has been divided into (i) intrinsic and (ii) extrinsic sources. The former source is related mainly to the finite-size effects and to the reduction of the electron mean free path of the electrons impacting the dielectric constants of metals at the nanoscale. The extrinsic source of broadening is inherent to the size and shape distributions, in other words, to the polydispersity of the particles. Of course, a coupling between these two sources do exist. To fully conclude several systematic simulations should be done. Even though the figures shown in the latter sections have given us some general trends that we can give a first conclusion of.

Polydispersity was handled in the low and finite coverage limits. For non-interacting objects at low coverage the resonances, as shown by the imaginary part of the polarizabilities, are broadened in a complex and intertwined way because of their dependence to the system parameters, such as

- sensitivity of their positions to aspect ratio (or truncation) and to surface effects
- sensitivity of their intensities to flattening, total volume and finite-size effects.

Nevertheless, as it is well-known in plasmonics, the dominating effect comes from the distribution of aspect ratio.

At finite surface coverage, the shifts of the plasmons resonance peaks induced by island-island electrostatic coupling lead to an extra source of broadening. Indeed, because of the fluctuations of the local environment of each object and of its size and shape, fluctuating shifts of the peaks exist across the surface. A framework was proposed to deal this effect within the MFT at dipolar order. The MFT assumes that each particle is embedded in the average dipolar electric field generated by all the other particles (all neighbors). However, this effect is treated as a function of the type (size/shape) of particles. To do so, a deep knowledge of the statistical description of the morphology is required; to overcome this, a scaling approximation for their RDF was introduced as a simplification.

The dispersion was firmly investigated in a polydisperse system. Aside from a full implementation in GranFilm, a comparison between the LCP and FCP was given. The new part of the code has passed the tests of certain limit cases and shows promising results for far. Some conclusions can be drawn:

- Generally, a distribution over sizes of the particles increase the amplitudes of the plasmon resonances as compared to the monodisperse system consisting of particles of the average radius. When the corrections of the experimental bulk dielectric function of the metal is performed on the polydisperse system, the smaller particles in the ensemble dominate the response. Because of the probabilistic nature of the averaging, both the finite-size and the surface corrections potentially have a broadening effect on the average polarizability.
- A distribution over the shape tends to bring the amplitude of the resonances down and broaden the peak, as compared to the monodisperse case. The broader the shape distribution is, the broader is the plasmon resonances observed in the average polarizabilities.
- The average parallel polarizability is more sensitive to the corrections in the FCP limit than the average perpendicular polarizability.
- The results of the average polarizabilities are sensitive to the chosen model of the RDF. The higher the surface coverage of particles is, the more important the short-range interactions in the system become.
- A 'full simulation' in the MF limit is time consuming. For coverages $\Theta \approx 0.40$ (in the limit where the short-range in the system is quickly decreasing) simulation time can be saved by choosing the exponential model.
- The MFT results and the an average particle interacting with the monodisperse correction (MI) seems to overlap fairly well.

Furthermore, the real part of the normalized average polarizability displays the same trends as the imaginary part. Figures containing plots for these observables have not been added to this thesis since they do not add any new points to the discussion.

There are still several interesting paths that have not (yet) been investigated. All the simulations discussed in this chapter were made for systems of spheres. It would be interesting to see how spheroidal particles in the MF limit are affected by the renormalized theory [89].

6.A Average of the dipole-dipole interaction

In this Appendix we aim at calculating the elements of the tensor $\overleftrightarrow{\boldsymbol{\mathcal{M}}}(\nu|\nu')$ that appear in the matrix-system in Eq. (6.32a). It is defined in Eq. (6.40) as

$$\overleftrightarrow{\boldsymbol{\mathcal{M}}}(\nu|\nu') = \overleftrightarrow{\mathbb{I}} - \overleftrightarrow{\boldsymbol{\alpha}}(\nu)\overleftrightarrow{\boldsymbol{\mathcal{V}}}(\nu|\nu') \tag{6.40}$$

where we for later convenience have introduced the averaged dipole-interaction tensor defined as

$$\overleftrightarrow{\boldsymbol{\mathcal{V}}}(\nu|\nu') = \left\langle \sum_{j\in\mathcal{P}(\nu')} \overleftrightarrow{\boldsymbol{V}}_{ij} \right\rangle_{\mathbf{r}_i|\nu} = \frac{1}{N_\nu} \sum_{i\in\mathcal{P}(\nu)} \sum_{j\in\mathcal{P}(\nu')} \overleftrightarrow{\boldsymbol{V}}_{ij}. \tag{6.41}$$

In the last transition, we have introduced the meaning of the average $\langle\cdot\rangle_{\mathbf{r}_i|\nu}$ as defined by Eq. (6.26). We also recall that the tensor $\overleftrightarrow{\boldsymbol{V}}_{ij}$ is defined by Eq. (6.25b) and explicit expressions for the various elements of it can be obtained with the use of the results in Eq. (6.23).

With the use of the partial pair-pair correlation function discussed in Appendix B, all elements of the dipole interaction tensor $\overleftrightarrow{\boldsymbol{\mathcal{V}}}(\nu|\nu')$ can be calculated. First we will address the 11-element of this tensor. It is given as

$$\begin{aligned}\left[\overleftrightarrow{\boldsymbol{\mathcal{V}}}(\nu|\nu')\right]_{11} &= \frac{1}{N_\nu} \sum_{i\in\mathcal{P}(\nu)} \sum_{j\in\mathcal{P}(\nu')} \left[\overleftrightarrow{\boldsymbol{V}}_{ij}\right]_{11} \\ &= \frac{1}{4\pi\varepsilon_1} \frac{1}{N_\nu} \frac{N_\nu}{S} \frac{N_{\nu'}}{S} \int_S \mathrm{d}^2\mathbf{r}_{i,\parallel} \int_S \mathrm{d}^2\mathbf{r}_{j,\parallel}\, g_{\nu\nu'}(r_{ij,\parallel}) \left[\left(\frac{3x_{ij}^2}{r_{ij}^5} - \frac{1}{r_{ij}^3} \right) \right. \\ &\qquad \left. - \frac{\varepsilon_2 - \varepsilon_1}{\varepsilon_2 + \varepsilon_1} \left(\frac{3\bar{x}_{ij}^2}{\bar{r}_{ij}^5} - \frac{1}{\bar{r}_{ij}^3} \right) \right],\end{aligned} \tag{6.42}$$

where the 3D-distances from (i) the direct dipole at $\mathbf{r}_j$ and (ii) the image dipole at $\bar{\mathbf{r}}_j$ to the point $\mathbf{r}_i$ are, respectively, given by

$$r_{ij} = |\mathbf{r}_i - \mathbf{r}_j| = \left[r_{ij,\parallel}^2 + z_{ij,\parallel}^2 \right]^{1/2} \tag{6.43a}$$

and

$$\bar{r}_{ij} = |\mathbf{r}_i - \bar{\mathbf{r}}_j| = \left[r_{ij,\parallel}^2 + \bar{z}_{ij,\parallel}^2 \right]^{1/2}, \tag{6.43b}$$

with

$$r_{ij,\parallel} = \sqrt{x_{ij}^2 + y_{ij}^2}. \tag{6.43c}$$

Here S is the area of a large but finite region of the planar surface of the substrate over which the spatial average is made and N_ν [$= |\mathcal{P}(\nu)|$] is the number of particles of geometrical type ν inside this region.

In writing the expression in Eq. (6.42) one has used that given we have a particle of geometrical type ν at position $\mathbf{r}_i$, then $(N_\nu/S)(N_{\nu'}/S)\, g_{\nu\nu'}(r_{ij,\parallel})\mathrm{d}^2\mathbf{r}_{i,\parallel}\mathrm{d}^2\mathbf{r}_{j,\parallel}$ is the probability to finding a particle of geometrical type ν' an in-plane distance $r_{ij,\parallel}$ away [at $\mathbf{r}_j$] [90]. The function $g_{\nu\nu'}(r_{ij,\parallel})$ denotes the partial pair correlation function for particles of geometrical types ν and ν' separated by an in-plane distance $r_{ij,\parallel}$ [83]. For given explicit forms of the partial pair correlation function the integrals that appear in Eq. (6.42) can be evaluated, at least by numerical means, to obtain the tensor-element $\mathcal{V}_{11}(\nu|\nu')$.

The 22-element of the tensor in Eq. (6.41) is obtained by from the right-hand side of Eq. (6.42) by replacing x_{ij} with y_{ij}. It is readily shown that the 11-element and the 22-element are equal, and for later convenience we define

$$\mathcal{V}_\parallel(\nu|\nu') = \frac{1}{2}\left[\overleftrightarrow{\boldsymbol{\mathcal{V}}}(\nu|\nu')\right]_{11} + \frac{1}{2}\left[\overleftrightarrow{\boldsymbol{\mathcal{V}}}(\nu|\nu')\right]_{22}. \tag{6.44}$$

Due to the isotropy of the system in the plane of the substrate, the two integrals that appear in Eq. (6.42) are most easily evaluated by the introduction of polar coordinates. Hence, for a general scalar function $f(\cdot)$ one has

$$\begin{aligned}\int \mathrm{d}^2\mathbf{r}_{i,\parallel} \int \mathrm{d}^2\mathbf{r}_{j,\parallel}\, f(r_{ij,\parallel}) &= \int \mathrm{d}^2\mathbf{u}_\parallel \int \mathrm{d}^2\mathbf{r}_{j,\parallel}\, f(u_\parallel) \\ &= S\int_0^{2\pi}\mathrm{d}\theta \int_0^\infty \mathrm{d}u_\parallel\, u_\parallel f(u_\parallel) \\ &= 2\pi S\int_0^\infty \mathrm{d}u_\parallel\, u_\parallel f(u_\parallel),\end{aligned}$$

where we have made the coordinate transformation $\mathbf{u}_\parallel = \mathbf{r}_{i,\parallel} - \mathbf{r}_{j,\parallel}$ with $u_\parallel = |\mathbf{u}_\parallel|$ and used the fact that $\mathrm{d}^2\mathbf{u}_\parallel = \mathrm{d}^2\mathbf{r}_{i,\parallel}$. one should note that $u_\parallel = r_{ij,\parallel}$.

Finally one obtains when these results are introduced into the expression that result from substituting the expressions for $\mathcal{V}_{11}(\nu|\nu')$ [Eq. (6.42)] and $\mathcal{V}_{22}(\nu|\nu')$ into Eq.(6.44)

$$\begin{aligned}\mathcal{V}_\parallel(\nu|\nu') = \frac{1}{\varepsilon_1}\frac{1}{4}\frac{N_{\nu'}}{S}\int_0^\infty \mathrm{d}u_\parallel\, u_\parallel g_{\nu\nu'}(u_\parallel) \Bigg[&\left(\frac{3u_\parallel^2}{\left(u_\parallel^2+z_{ij}^2\right)^{5/2}} - \frac{2}{\left(u_\parallel^2+z_{ij}^2\right)^{3/2}}\right) \\ &-\frac{\varepsilon_2-\varepsilon_1}{\varepsilon_2+\varepsilon_1}\left(\frac{3u_\parallel^2}{\left(u_\parallel^2+\bar{z}_{ij}^2\right)^{5/2}} - \frac{2}{\left(u_\parallel^2+\bar{z}_{ij}^2\right)^{3/2}}\right)\Bigg] \\ = \frac{1}{4}\frac{\rho_{\nu'}}{\varepsilon_1}&\left[G_{\nu\nu'} - \frac{\varepsilon_2-\varepsilon_1}{\varepsilon_2+\varepsilon_1}\overline{G}_{\nu\nu'}\right],\end{aligned} \tag{6.45}$$

where $\rho_{\nu'} = N_{\nu'}/S$ and we have defined the following two classes of integrals

$$G_{\nu\nu'} = \int_0^\infty \mathrm{d}u_\parallel\, g_{\nu\nu'}(u_\parallel)\frac{u_\parallel\left(u_\parallel^2 - 2z_{ij}^2\right)}{\left(u_\parallel^2+z_{ij}^2\right)^{5/2}} \tag{6.46a}$$

and

$$\overline{G}_{\nu\nu'} = \int_0^\infty \mathrm{d}u_\parallel \, g_{\nu\nu'}(u_\parallel) \frac{u_\parallel \left(u_\parallel^2 - 2\bar{z}_{ij}^2\right)}{\left(u_\parallel^2 + \bar{z}_{ij}^2\right)^{5/2}}. \tag{6.46b}$$

The result expressed by Eq. (6.45) is the final result for the parallel component of the average dipole interaction tensor.

The 33-element of the tensor $\overleftrightarrow{\boldsymbol{\mathcal{V}}}(\nu|\nu')$, that we in the following will call $\mathcal{V}_\perp(\nu|\nu')$, is obtained in a manner that is equivalent to how we obtained $\mathcal{V}_\parallel$. The result of an explicit calculation gives

$$\begin{aligned}
\mathcal{V}_\perp(\nu|\nu') &= \frac{1}{4\pi\varepsilon_1}\frac{1}{N_\nu}\frac{N_\nu}{S}\frac{N_{\nu'}}{S}\int_S \mathrm{d}^2\mathbf{r}_{i,\parallel}\int_S \mathrm{d}^2\mathbf{r}_{j,\parallel}\, g_{\nu\nu'}(r_{ij,\parallel})\left[\left(\frac{3z_{ij}^2}{r_{ij}^5} - \frac{1}{r_{ij}^3}\right) + \frac{\varepsilon_2-\varepsilon_1}{\varepsilon_2+\varepsilon_1}\left(\frac{3\bar{z}_{ij}^2}{\bar{r}_{ij}^5} - \frac{1}{\bar{r}_{ij}^3}\right)\right] \\
&= \frac{1}{2}\frac{\rho_{\nu'}}{\varepsilon_1}\int_0^\infty \mathrm{d}u_\parallel \, u_\parallel g_{\nu\nu'}(u_\parallel)\left[\frac{2z_{ij}^2 - u_\parallel^2}{\left(u_\parallel^2 + z_{ij}^2\right)^{5/2}} + \frac{2\bar{z}_{ij}^2 - u_\parallel^2}{\left(u_\parallel^2 + \bar{z}_{ij}^2\right)^{5/2}}\right] \\
&= -\frac{1}{2}\frac{\rho_{\nu'}}{\varepsilon_1}\left[G_{\nu\nu'} + \frac{\varepsilon_2-\varepsilon_1}{\varepsilon_2+\varepsilon_1}\overline{G}_{\nu\nu'}\right].
\end{aligned} \tag{6.47}$$

This is the final expression for the average interaction tensor in the perpendicular direction.

What remains to obtain are the off-diagonal elements of $\overleftrightarrow{\boldsymbol{\mathcal{V}}}(\nu|\nu')$. In fact, they all vanish but we will not here go into great detail to show it. Instead we here simply mention that it is a result of the following averages $\langle x_{ij}\rangle$, $\langle y_{ij}\rangle$, $\langle x_{ij}y_{ij}\rangle$, etc. vanishing.

To conclude, we have in this appendix shown that the average interaction tensor $\overleftrightarrow{\boldsymbol{\mathcal{V}}}(\nu|\nu')$ is a diagonal tensor of the form $\overleftrightarrow{\boldsymbol{\mathcal{V}}} = \mathrm{diag}(\mathcal{V}_\parallel, \mathcal{V}_\parallel, \mathcal{V}_\perp)$ When this result is substituted into the expression for $\overleftrightarrow{\boldsymbol{\mathcal{M}}}(\nu|\nu')$, defined in Eq. (6.40), it is found that also this tensor is diagonal. It can be expressed in the form

$$\overleftrightarrow{\boldsymbol{\mathcal{M}}} = \mathrm{diag}\left(\mathcal{M}_\parallel, \mathcal{M}_\parallel, \mathcal{M}_\perp\right), \tag{6.48a}$$

where

$$\mathcal{M}_\parallel(\nu|\nu') = \delta_{\nu\nu'} - \alpha_\parallel(\nu)\,\mathcal{V}_\parallel(\nu|\nu') \tag{6.48b}$$

and

$$\mathcal{M}_\perp(\nu|\nu') = \delta_{\nu\nu'} - \alpha_\perp(\nu)\,\mathcal{V}_\perp(\nu|\nu') \tag{6.48c}$$

In obtaining these results we have used that the tensor $\overleftrightarrow{\boldsymbol{\alpha}}(\nu)$ also is diagonal and of the form given in Eq. (6.33).

Chapter 7

General conclusion and further work

In this thesis we have studied the optical properties of granular thin films, mainly from a theoretical and numerical point of view. In this chapter we will state the general conclusions and comment on some directions of further work.

Contents

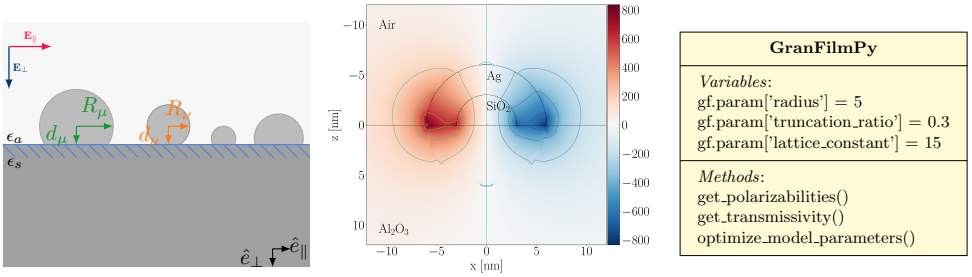

(a) Polydisperse system. **(b)** Oscillation modes in a coated particle. **(c)** Schematic of the GranFilm Python-class.

Figure 7.1 Most important deliverables from the thesis; the introduction of polydispersity (a), the discussion of the oscillation modes in a coated particle (b), and the development of the GranFilm Python interface (c).

7.1 General conclusions

The three most important outcomes of the work performed during the period of this thesis are summarized in Fig. 7.1. They are:

1. The introduction of polydispersity over the size and shapes of the particles has extended the accessible geometries one can study with the GranFilm software [see Fig. 7.1(a)].
2. The analysis of the physical origin of the oscillation modes (eigenmodes) in the context of coated and truncated particles has demonstrated that the combined effect of a coating layer and the substrate can be studied with the GranFilm software [see Fig. 7.1(b)].
3. The update and further development of the GranFilm Python interface is an important contribution in order to make GranFilm more easily accessible for new users [see Fig. 7.1(c)].

7.2 Summary

In the previous chapters, the optical properties of granular thin films containing truncated and supported spherical and spheroidal islands have been discussed in depth from a theoretical point of view. Below we summarize the main conclusions of each chapter.

We started in **Ch. 1** by discussing the general properties of plasmonics needed to understand the LSPRs observable in metallic NPs. With a series of examples provided by analytical formulas for the polarizabilities of simple systems (sphere/spheroid/dipolar interaction with a substrate), we learned how the shape of the particle, a coating layer, the embedding medium and the presence of a substrate or of neighboring islands strongly affect the optical response of the system. By changing one of these parame-

ters, one can tune drastically the energy position of the resonance and its amplitude (or intensity).

In **Ch. 2**, we explained how the EF-formalism could be used to describe the EM properties of non-sharp interfaces. The definitions of the so-called excess quantities and the surface susceptibilities were the formalism's key concepts. It was shown that the surface susceptibilities, in the case of truncated particles supported by the substrate, are linked to particle polarizabilities parallel and perpendicular to the substrate. The chapter ended by stating the formulas for a set of modified Fresnel amplitudes for a non-sharp interface. These amplitudes were used to define the *differential reflectivity*, an observable which is measured in a SDRS experiment.

Chapter 3 illustrated how the polarizabilities, to the first or second order, of truncated and supported particles can be obtained in the quasi-static approximation. The calculation method was valid for particles that were symmetric along the z-axis. It is based on a solution of the Laplace equation through a multipolar expansion of the expansion supplemented by the image charge technique to account for the electrostatic coupling with the substrate. A weak formulation of the boundary conditions at the surface of the sphere leads to a linear system of equations for the multipolar coefficients. Its solution gives access to the polarizabilities (the first term in the expansion) and the mapping of the electrostatic potential. The analysis was detailed primarily for the case of a truncated sphere. Guidelines to the generalization to coated objects, as well as the case of spheroidal particles, were given. The chapter ended with a discussion of the island-island interactions and how it influences the optical properties of island films containing supported particles. Expressions for the polarizabilities renormalized by the island-island interactions were introduced for particles organized in regular or random arrays.

The GranFilm software itself was thoroughly introduced in **Ch. 4**. We gave a detailed description of the input file and commented on some of the new functionalities. The development of the GranFilm Python interface was the most important contribution in order to increase the number of users. Simulation results for typical systems were discussed. Through examples, we showed how some input parameters could greatly impact the results produced by the software. Also, an example of model parameter estimation based on a differential reflectivity curve was given.

Chapter 5 was devoted to the understanding of the type of oscillation modes which can be excited in a system where the particles experience the combined effect of the presence of a coating layer and the substrate. A methodology to track them as function of a given parameter (truncation/shell thickness) was proposed; it consists of identifying the nearly singular points of the matrix system at low damping. While the case of a dielectric shell poorly affected the nature of the modes and mainly red-shifted their frequency through screening, richer polarization patterns were observed in the case of a supported metallic shell. For such systems complex mixing and splitting of the eigenmodes, as a function of the geometry were observed.

Finally, in **Ch. 6** we address the origin of the broadening of the plasmon resonance peaks. This phenomenon was divided into (i) intrinsic and (ii) extrinsic sources. The former is mainly related to finite-size effects and to the reduction of the mean free

path of the electrons at the nanoscale. This latter effect is inherent to size and shape distributions, in other words, to the polydispersity of the particles. Of course, a coupling exist between both. The case of polydispersity was handled in the low and finite coverage limits.

For non-interacting objects at *low coverage* the resonances were broadened in a complex and intertwined. The positions of the resonance peaks were shifted because of their sensitivity to the aspect ratio (or truncation) of the particles and to surface effects. The amplitude of the peaks were linked to flattening, total volume, and the finite-size effects. At *finite coverage*, the shift of the peaks induced by island-island electrostatic coupling leads to an additional source of broadening. A framework to treat this effect in the MFT and at dipolar order was proposed and implemented. The model assumed that each particle is embedded in the average dipolar field generated by all the (polydisperse) neighbors. A scaling approximation for the particles' RDF was introduced as a way to tackle the issue of the statistical description of the particle morphology.

The dispersion was firmly investigated in a polydisperse system. Aside from a full implementation in GranFilm, a comparison between the LCP and FCP was given. The new part of the code has passed a number of consistency checks and for certain limiting geometries the produced results are promising. The new functionalities model the polydispersity of real systems, encountered in *e.g.* deposition experiments, in a more realistic manner.

7.3 Directions for further work

Although this thesis has made progress towards including a broader set of geometries into the GranFilm software package, several issues still remain open.

Does our model for the polydisperse systems better match the experimental results than the results obtained for a corresponding monodisperse system? In the classical GranFilm configuration the 'experimental broadening' was accounted for by simply broadening the monodisperse absorption peak with a convolution of a Gaussian of width σ_i [42, 58]. It would be very interesting to see if the MF code can produce realistic results during parameter optimization. For this to be feasible, one would need a considerable speed up of the new branches of the code. Also, the effect of the polydispersity for the spheroidal geometries have not been investigated. The results are expected to follow similar trends to what we saw for the system consisting of polydisperse and truncated spheres.

When are our systems definitely out of the quasi-static approximation? We know that the relevant sizes of the particles simulated with our software must be in the quasi-static approximation. Furthermore, we also know that the agreement between the results produced with the dipolar and quadrupolar island-island interactions is satisfactory for surface coverage as high as 60 % [56]. But, it has not yet been tested carefully when, for instance, the full set of reduced Rayleigh equations have to be solved to obtain a physical result were retardation is included. The work described

in the thesis by J-P Banon [91], is an interesting starting point for performing a comparison to the similar results obtained by GranFilm simulations.

Is it feasible to combine the speed of GranFilm with other methods? In a study conducted by Alvarez *et al.* [92] a combination of GranFilm and other simulation methods were used to model the response of a truncated spheroid placed on a thin film and a substrate with promising results. Such and similar approaches should definitely be studied further in the future.

Chapter A

The experimental bulk dielectric functions

This appendix contains plots of all the experimental bulk dielectric functions that were used in the different GranFilm simulations displayed in this thesis.

Contents

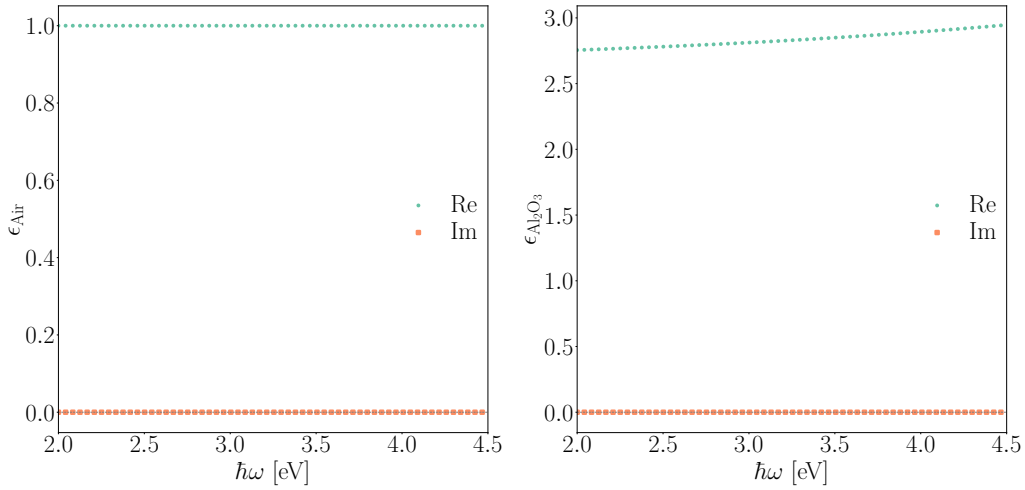

(a) Air. **(b)** Al_2O_3.

Figure A.1 The experimental bulk dielectric functions of the system materials relevant for this work.

A.1 Materials of the surrounding system

In this work, all the simulations made with GranFilm the dielectric function of the ambient material is chosen to be air [see Fig. A.1(a)] and the substrate is taken as alumina [see Fig. A.1(b)] as the substrate. Respectively denoted $\varepsilon_1/\varepsilon_a$ and $\varepsilon_2/\varepsilon_s$.

A.2 Materials of the particles

The materials of the particles and the eventual coatings for the simulations made with GranFilm in this work are either silver [see Fig. A.2(a)] or silica [Fig. A.2(b)].

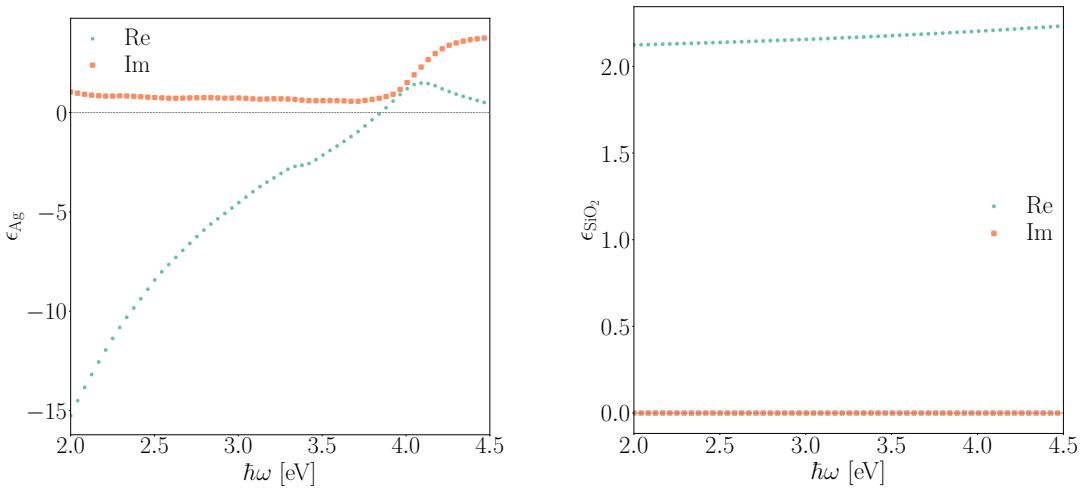

(a) Ag. **(b)** SiO_2.

Figure A.2 The experimental bulk dielectric functions of the materials used in the particles relevant for this work.

Chapter B

The radial distribution function

In the cases when the organization of the particles is not regular (a so-called random lattice configuration), the electrostatic interaction between particles can not anymore be described through lattice sums that are based on the periodic (square or hexagonal) arrangement of similar objects. They should be replaced by their continuous integral counterparts (Sec. 3.5 based on the particle-particle or two-point pair correlation function. When the particles organized in a random 2D lattice, reasonable analytical models of these correlation functions do not exist [93]. In the following, a precise definition of this function is presented as well as approximate expression in the particular case of hard-core interacting (*i.e.* non-overlapping) objects. In the case of polydispersed objects, the modeling of the average polarizabilities in the mean-field approximation (Sec. 6.5) requires similar functions, but for particles of different types, the so-called partial pair correlation functions. For this case a scaling approximation of the point-point pair correlation of the monodisperse assembly of NPs is used.

Contents

B.1 Statistical description of amorphous materials

When our particles are organized in what we call herein a random lattice, their arrangement does not follow regular patterns. Typically we will have some kind of local order between the first few neighbors. Thus, we speak of *short-range* order in contrast to the *long-range* order of lattices. Following Refs. [90, 94, 95], we define the *radial distribution function* (RDF), universally denoted by $g(r)$. The framework around determining the RDF deploys techniques from statistical mechanics to model the distribution of objects.

Historically, the first experimental studies of the RDF is credited to J. D. Bernal. In his work carried out in the 1930s, he tried to explain the observed short-range order of x-ray diffraction patterns [90] of amorphous or glassy media. By the 1960s, the theoretical framework of statistical mechanics was developed to allow a more formal description of the RDF in the case of particles interacting through a given potential in a fluid or gas. The idea is to link the properties of the underlying potential from the spatial distribution of particles. Among the most famous theories to determine $g(r)$, are the Ornestin-Zernike equation and the integral equation of Percus-Yevick. Also, the thermodynamic quantities like the potential energy, pressure, and compressibility can be directly linked to the RDF [90].

A probabilistic formulation

To give a complete description of the arrangement of all the particles in a system, we need to specify the n-body correlation function. The n-particle PDF $\rho_n(\mathbf{r}_1, ..., \mathbf{r}_n)$, is defined by stipulating that the probability that the volumes $\mathrm{d}\mathbf{r}_1$ around $\mathbf{r}_1$, $\mathrm{d}\mathbf{r}_2$ around $\mathbf{r}_2$, *etc.*, contains only one atom can be given by

$$\mathrm{d}P_n(\mathbf{r}_1, ..., \mathbf{r}_n) = \rho_n(\mathbf{r}_1, ..., \mathbf{r}_n)\mathrm{d}\mathbf{r}_1, ..., \mathrm{d}\mathbf{r}_n. \tag{B.1}$$

In a disordered system, where a large number of atomic configurations are possible, the n-particle PDF is determined by taking the average over all configurations to give a complete description. In practice, it is sufficient to know the one- and two-particle distribution functions to give a satisfactory description of the system. These latter quantities can also be determined from experiments [90].

Equivalent representations can give the correlation functions with the average of delta-functions or with the integral over the phase space and partition functions. We choose the first representation.

A delta-function representation

Considering a system containing N particles in the volume V, the first-order correlation function is

$$\rho^{(1)}(\mathbf{r}) = \left\langle \sum_{i=1}^{N} \delta(\mathbf{r}_1 - \mathbf{r}_i) \right\rangle, \tag{B.2}$$

where the δ-is the delta function and $\mathbf{r}_i$ denotes the center of the i^{th} particle. Similarly, we can define the second-order correlation function as

$$\rho^{(2)}(\mathbf{r}_1, \mathbf{r}_2) = \left\langle \sum_{i=1}^{N} \sum_{\substack{j=1 \\ j \neq i}}^{N} \delta(\mathbf{r}_1 - \mathbf{r}_i)\delta(\mathbf{r}_2 - \mathbf{r}_j) \right\rangle. \tag{B.3}$$

With the definitions of probability densities,

$$\int_V \mathrm{d}\mathbf{r}^n \rho^{(n)}(\mathbf{r}^{(n)}) = \frac{N!}{(N-n)!}, \tag{B.4}$$

where n is the order of the correlation function, V the volume of the system, and N the total number of particles in the system.

The n-particle probability distribution function is obtained by dividing the n-particle density function by the one-particle densities

$$g(\mathbf{r}_1, ..., \mathbf{r}_n) = \frac{\rho_N(\mathbf{r}_1, ..., \mathrm{d}\mathbf{r}_n)}{\rho(\mathbf{r}_1), ..., \rho(\mathbf{r}_n)}. \tag{B.5}$$

By assuming

$$N(N-1)/V^2 \approx N^2/V^2 = \rho^{-2}, \tag{B.6}$$

the two-particle probability distribution function can be re-written as

$$\begin{aligned} g^{(2)}(\mathbf{r}_1, \mathbf{r}_2) &= \frac{\rho^{(2)}(\mathbf{r}_1, \mathbf{r}_2)}{\rho(\mathbf{r}_1)\rho(\mathbf{r}_2)} \\ &= \rho^{-2} \left\langle \sum_{i=1}^{N} \sum_{\substack{j=1 \\ j \neq i}}^{N} \delta(\mathbf{r}_1 - \mathbf{r}_i)\delta(\mathbf{r}_2 - \mathbf{r}_j) \right\rangle \\ &= \rho^{-1} \left\langle \sum_{i=1}^{N} \sum_{\substack{j=1 \\ j \neq i}}^{N} \delta(\mathbf{r}_1 - \mathbf{r}_2 + \mathbf{r}_j - \mathbf{r}_i) \right\rangle. \end{aligned} \tag{B.7}$$

With the coordinate transformation $\mathbf{r} = \mathbf{r}_1 - \mathbf{r}_2$ we can rewrite Eq. (B.7) as

$$g^{(2)}(\mathbf{r}) = \rho^{-1} \left\langle \sum_{i=1}^{N} \sum_{\substack{j=1 \\ j \neq i}}^{N} \delta(\mathbf{r} - \mathbf{r}_i + \mathbf{r}_j) \right\rangle. \tag{B.8}$$

In an isotropic system (as assumed in this work), the two-particle distribution function depends only on the distance between the particles $g(\mathbf{r}) = g(|\mathbf{r}|) = g(r)$. This quantity is what we call the RDF. Formally, it measures the probability to find a particle j at a distance r from the reference particle i relative to the average density of particles j.

If we select the center of one particle as the origin, the number of particles in the spherical shell of radius r and thickness $\mathrm{d}r$ is

$$n(r)\mathrm{d}r = 2\pi\rho g(r) r \mathrm{d}r. \tag{B.9}$$

The limiting behavior of the radial distribution function

Due to the impenetrability of two particles, RDF must be equal to zero when the distance between the centers of any two particles in the system is less than their diameter D_0. This means that $\lim_{r<D_0} g(r) = 0$.

When the particles are separated by distances greater than the particle diameter the behavior of the RDF is highly non-trivial. If there is only short-range order present in the system the joint probability distribution becomes a product between two independent distributions

$$\frac{\rho^{(2)}(\mathbf{r}_1, \mathbf{r}_2)}{\rho^{(1)}(\mathbf{r}_1)\rho^{(1)}(\mathbf{r}_2)} = \frac{\rho^{(1)}(\mathbf{r}_1)\rho^{(1)}(\mathbf{r}_2)}{\rho^2} = 1, \tag{B.10}$$

and therefore the limit $\lim_{r\to\infty} g(r) = 1$ should hold for the RDF. It is common practice to separate this term to define *the pair correlation function* [90]

$$h(r) = g(r) - 1. \tag{B.11}$$

To summarize, the behavior of RDF in the two most relevant limits are

$$\lim_{r<D_0} g(r) = 0, \qquad \lim_{r\to\infty} g(r) = 1. \tag{B.12}$$

The structure factor and the radial distribution function

In X-ray diffraction and/or neutron experiments the spatial FT, universally known as the structure factor denoted $S(k)$, rather than the RDF is obtained. For an isotropic 2D fluid, these two quantities are related by [90]

$$S(k) = 1 + 2\pi\rho \int_0^\infty \mathrm{d}r r g(r) \frac{\sin kr}{kr}, \quad k \neq 0. \tag{B.13}$$

B.2 Models of the pair-correlation function

The analytical forms of these functions do not exist in 2D. Nevertheless, an approximate form in the case of hard-core interacting particles, can be defined. As a test of our model of the particle-particles electrostatic coupling, we used different approximations for the RDF. Although, even if particles on a substrate do not overlap, they do not interact through a potential. Their spatial arrangement results from the complex interplay between growth phenomena that can not be accounted for by a simple potential.

B.2.1 The step-function

In the *ideal gas*-model, the positions of the atoms are random. Thus, from the previous sections we know that the absolute simplest form of the RDF that fulfills the behavior

in the limits proposed in Eq. (B.12) will a step function

$$g_{step}(r) = \begin{cases} 0, r \leq D_0 \\ 1, r > D_0. \end{cases} \tag{B.14}$$

This first model is useful only for testing the different limits of our implementations, as the considered systems are certainly not equal to those of the ideal gas.

B.2.2 A damped exponential

A more realistic model is some function that is properly normalized. A naive function that also respects the limits given in Eq. (B.12) is

$$g_{exp}(r) = \begin{cases} 0, r < D_0 \\ 1 + C\mathrm{e}^{-\frac{r-D_0}{a_0}}, r \geq D_0, \end{cases} \tag{B.15}$$

where the two terms C and a_0 are positive constants that result from the normalization of the pair-correlation function. The normalization constant a_0 can be determined from the integral over the pair-correlation function

$$\begin{aligned} 2\pi\rho \int_0^\infty \mathrm{d}r r h(r) &= -2\pi\rho \int_0^{D_0} \mathrm{d}r r g(r) + 2\pi\rho \int_{D_0}^\infty \mathrm{d}r r C\mathrm{e}^{-\frac{r-D_0}{a_0}} \\ &= \left(-\int_0^{D_0} \mathrm{d}r r + C \int_{D_0}^\infty \mathrm{d}u (u + D_0)\mathrm{e}^{-\frac{u}{a_0}} \right) \\ &= -\frac{D_0^2}{2} + CD_0a_0 + Ca_0^2 \\ &= 0, \end{aligned} \tag{B.16}$$

where the change of variables $u = r - D_0$ was used in the second step of Eq. (B.16). Solving the second order equation and choosing only the positive solution we find

$$a_0 = \frac{1}{2}\left(-C + \sqrt{C(C+2)} \right). \tag{B.17}$$

The second constant C is the amplitude of $g_{\mathrm{exp}}\,(r)|_{r=D_0}$.

B.2.3 The hard disk model

A more rigorous approach, but still approximate RDF for hard-core interacting objects has been obtained by Baus and Colot [93] from thermodynamic considerations. They derived accurate expressions for the thermodynamic and structural properties of a fluid of hard D-spheres for even and odd values of D. By rescaling the low density expressions of the equation of state and *the direct correlation function* $c(r, \Theta)$, they obtained a satisfying overlap with the well-known result of the integral equation of Percus-Yevick for hard interacting disks ($D = 2$). The dimensionless packing fraction[1] Θ, is the only needed input for this model.

[1] The packing fraction is called *coverage* in the GranFilm software.

Following the formalism of Ref. 93, our implementation for $D = 2$-spheres first calculates a dimensionless structure factor from the relation

$$S(q, \Theta) = [1 - c(q, \Theta)]^{-1}, \tag{B.18}$$

where $c(q, \Theta)$ is the spatial FT of the direct correlation function $c(r, \Theta)$ and given as

$$c(q, \Theta) = -\Theta \frac{\partial}{\partial \Theta} [\Theta z(\Theta)] \left[(1 - a^2\Theta) 2^2 f_1(q) + a^2 \Theta \left\{ (a f_1(aq/2))^2 + H_2(q; a) \right\} \right], \tag{B.19}$$

where $z(\Theta)$ is a central quantity related to the equation of states, the term $f_1(.)$ an auxiliary function related to the Bessel functions, and $H_2(q; a)$is an one-dimensional integral. Also, a dimensionless wave number $q = kD_0$ and a rescaling of the diameter a have been introduced.

The RDF of the hard disk model then determined from the dimensionless structure factor

$$g_{hard}(r') = 1 + \frac{1}{2\pi\rho'} \int_0^\infty \mathrm{d}q J_0(qr') r' \left(S(qr') - 1 \right), \tag{B.20}$$

where $r' = r_\parallel / D_0$ and $\rho' = \rho / D_0$ are, respectively, a dimensionless distance and density, the term $J_0(qr_\parallel)$ is the zeroth order Bessel function of the first kind. To deal with the oscillating behavior of the Bessel function during the computations we deploy *the epsilon algorithm* of Wynn [96].

Because the calculation of the inverse of the spatial FT of the static structure to the given order is a time-consuming process, the calculation of RDF is performed once for a given coverage of particles. The result of this calculation is then stored and interpolated to obtain the required value needed during a simulation.

B.3 Examples

In all configurations, the RDF is calculated for a unitless radial distance r' calculated from the relationship between the diameter and the radial distance between the neighboring particles.

An illustration of a typical result for the different choices of the RDF is given in Fig. B.1 for a coverage of $\Theta = 0.403$. The exponential and hard disk model of the RDF as introduced in Eqs. (B.15)-(B.20), are respectively shown with an orange dotted line and a solid blue line. The free parameter controlling the amplitude of $g_{exp}(r')$ is chosen to match $g_{hard}(r')$ at $r' = r_\parallel / D_0$.

In the limit where the coverage of particles is small, $\Theta \to 0$, the hard disk would approach an exponential-like behavior before reaching the dilute limit described by the step function. The first amplitude of the exponential and the hard disk model represents the ring of first neighbors.

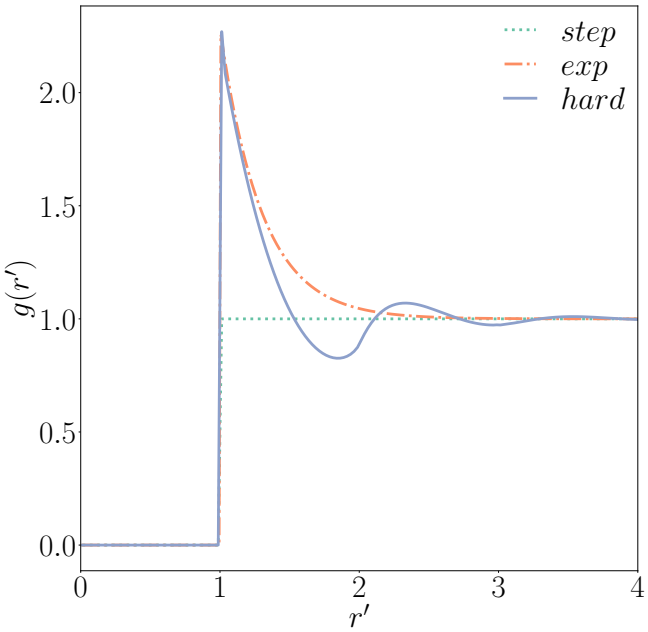

Figure B.1 Examples of the three approximations of the RDF of hard disks. The coverage is $\Theta = 0.403$. The parameter controlling the amplitude of $g_{exp}(r')$ (orange dotted line) is chosen so it matches the amplitude of $g_{hard}(r')$ (solid blue line).

In all the three models, the demanded limit behavior of the RDF is as stated in Eq. (B.12). Furthermore, the hard disk model displays an oscillator behavior. The underlying partial short-range order is rapidly lost at greater distances. As indicated by the solid blue line approaching one after the second peak in Fig. B.1. However, the number of peaks and their amplitudes would increase at a higher coverage of particles until reaching the RDF of a perfect hexagonal lattice. An example of how the oscillations and amplitudes of the hard disk model change for a different coverage of particles $d\Theta$ is presented in Fig. B.2.

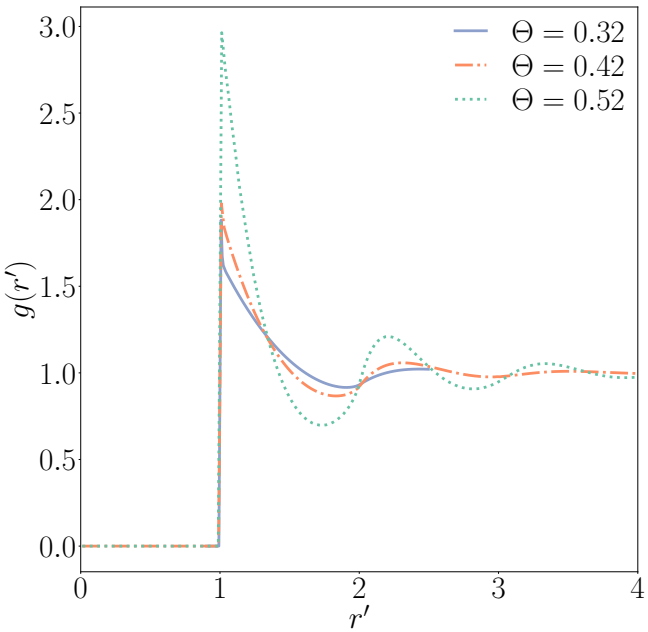

Figure B.2 Examples of how the amplitudes and oscillations of the hard disk model change with a different coverage of particles.

Chapter C

The GranFilm Fortran input file

This appendix will explain all the nml-namespaces which can be given in a GranFilm Fortran input file. See Ch. 4 and Ch. 6 for a description of the relation between the different parameters for the different simulation types.

Contents

A Fortran-namespace begins with the &-symbol and is followed by the name of the namelist. All variables left of the equal sign are taken as keyword-names. The scalars and vectors of integers, reals, and strings to the right of the equal sign are the values of the keyword. In cases where there are several possible input values these are given behind the exclamation mark in parenthesis. In cases where the units of the parameters are needed, these are indicated with square brackets. In Fortran, the comment command is !, *i.e.* keywords with a ! in front are ignored when the input file is read by the Fortran code. Some keywords with a ! is added in the following to exemplify the different configurations.

C.1 Required parameters

These parameters are required to successfully run a GranFilm simulation in the default configuration of the software, for a system of identical truncated spheres.

C.1.1 Global

```
! This namelist is in the file param.sif
 &Global
  Title         =  "Parameters to run GranFilm"
  EPSILON_ROOT  = '/home/usr/local/path_to_DataBase_for_epsilon_values/'
 /
```

The path to the values of the experimental values of the bulk dielectric functions for the materials used in the simulations are given with the keyword EPSILON_ROOT.

C.1.2 Source

```
! This namelist is in the file param.sif
 &Source
  Theta0        =     45           ![deg]
  Phi0          =     0            ![deg]
  Polarization  =    's'           !(s,p)
  Energy_Range  =    1.5, 5        ![eV]
 /
```

The chosen interval of the Energy_Range must match with the values in the experimental database.

C.1.3 Geometry

```
! This namelist is in the file param.sif
 &Geometry
  Radius              = 5                    ! [nm] Sphere
  ! Radius            = 5, 3                 ! [nm] Oblate
  Truncation_Ratio    = 0.0
  Media               = 'air','mgo','ag','mgo'
  Radius_Ratios       = 1.
```

```
  Broadening          = 0.17                  ! [nm]
  Distribution        = 'None'                ! ( None, Size_Distribution)
 /
```

If a sphere geometry is chosen, the Radius-keyword will have one value. In the case of a spheroidal geometry, the Radius-keyword must have two values. If the inhomogeneous broadening is wanted the number of components of in the Radius- and Broadening-keywords must match. The first component is always the parallel radius, the second the perpendicular radius.

To run a configuration with a polydispersity over the size or shape the Distribution-keyword must be set to 'Size_Distribution'. The additional namespace '&Size_Distribution' is then read.

Furthermore, with the Media-keyword the reading routine will automatically search for namespaces which match the media to decide if corrections of the bulk dielectric functions should be performed (see optional namelist under corrections).

C.1.4 Interaction

```
! This namelist is in the file param.sif
 &Interaction
  Arrangement               =  'Lattice ! (Lattice, Random_Array)
  Lattice_Type              =  'Square' ! (Square, Hexagonal)
  Lattice_Constant          =  31       ! [nm]
  Island_Island_Interaction = 'None'    ! (None, Dipole, Quadrupole, Mean_Field)
  Pair_Correlation_Type     = 'Step'    ! (Step, Exponential, Hard_Disk)
 /
```

The Pair_Correlation_Type-keyword is only needed when Arrangement=Random_Array arrangement of the monodisperse particles, or in the case of a polydisperse system where the Island_Island_Interaction= Mean_Field.

C.1.5 Numerics

```
! This namelist is in the file param.sif
 &Numerics
  Multipole_Order             = 16
  Multipole_Position_Ratio    = 0.00
  No_Energy_Points            = 500
 /
```

C.2 Extra parameters

These are considered extra as they are not needed to be set for the default configuration in a GranFilm simulation.

C.2.1 Correction of the bulk dielectric function

```
! This namelist is in the file param.sif
 &ag
  Material             = 'ag'
  Correction           = 'Surface'! ('Scaling','Surface','Finite-Size')
  Epsilon_Scaling      = 1, 0.01
  Plasma_Frequency     = 9.17     ! [eV]
  Damping_Frequency    = 0.018    ! [eV]
  Fermi_Velocity       = 0.91     ! [eVnm]
  Finite_Size_Constant = 0.6
  Plasmon_Shift        = -1.13    ! [eV^2nm]
 /
```

The name of this namelist, *i.e.* &ag, must match with at least one of the materials in the Media-keyword given in the Geometry-namelist. The parameter in the Material-keyword must match with one of the members in the database of the bulk dielectric function.

C.2.2 Polydisperse systems

```
! This namelist is in the file param.sif
 &Size_Distribution
  PDF                   = 'Truncated_Gaussian_NonCorr'
  Sigma_Radius          = 2.1                ! [nm]
  Min_Radius            = 0.1                ! [nm]
  Max_Radius            = 7.4                ! [nm]
  Samples_of_Radius     = 100
  !Tolerance_Dipole     = 0.02
  !Tolerance_Quadrupole = 0.009
  !Interaction_Sequence = 'Mean-Interaction' ! ('Mean-Interaction',
 /
```

The polydispersity is enabled when the keyword Distribution=Size_Distribution in the &Geometry namespace. The name of the parameter after the underscore for the keywords Sigma, Min and Max decides which parameter the distribution should be taken over, here the radius of a sphere.

In cases where the *Monte Carlo* (MC) integration is performed also the required tolerance of the estimate of the average polarizability must bee given. In this case, the keyword Samples_of_X is not needed.

If the Island_Island_Interaction = 'Dipole' or 'Quadrupole' in the &Interaction namespace also the sequence indicating the order of averaging and correcting for the island-island interaction can be decided.

If the Radius-keyword in &Geometry has two components (spheroidal geometry) one indicates the one that should be distributed by adding an index to the end of the Radius-keyword, *i.e.* Sigma_Radius(2) and Tolerance_Dipole(2) indicated a distribution and required tolerance for the perpendicular component.

C.2.3 Parameter estimation

```
! This namelist is in the file fit.sif
 &Fitting
   Experimental_Data  = 'experimental_data.dat'
   Mode               = 'dR/R'
   ! Tolerance        = 1.0E-06
   ! Radius_Ratios(2) = 0.4, 0, 100            ! [nm]
   Radius             = 3.50, 2.1, 6           ! [nm]
   Truncation_Ratio   = 0.62, 0.00001, 0.99
   Lattice_Constant   = 20, NaN, 25            ! [nm]
   ! Broadening(2)    = 0.13                   ! [nm]
 /
```

To be able to perform a series of parameter optimizations efficiently through 'scripting' the &Fitting-namelist must be placed inside the file fit.sif. The Mode-keyword sets the type of observable the parameter optimization should be performed for. The Tolerance-keyword is used to set the size of the relative error of the sum of squares the wanted in the optimization.

To enable a model parameter for an optimization the name of the keyword must be given with one or three values. The first value is interpreted as the initial guess of the parameter. If one wishes to perform constrained optimization of the given model parameter two additional numbers must be given. The first one is taken as the lower and the second one as the upper limit of the model parameter. If one wish that only one of the limits should be constrained in the optimization the 'NaN' value should be chosen on the other limit.

If the Radius-keyword in the &Geometry has two components (spheroidal geometry) or there are present a number of coatings on the particle the right component of the model parameter to be optimized are chosen by adding an index to the actual keyword, *i.e.* Radius_Ratios(2) and Broadening(2). The logic of the chosen model parameters which should be optimized are automatically checked against the values in the param.sif file.

REFERENCE LIST

[1] C Noguez. Surface plasmons on metal nanoparticles: the influence of shape and physical environment. *The Journal of Physical Chemistry C*, 111(10):3806–3819, 2007. 2, 19, 20, 22, 104, 122

[2] E Ozbay. Plasmonics: merging photonics and electronics at nanoscale dimensions. *science*, 311(5758):189–193, 2006. 2

[3] H A Atwater. The promise of plasmonics. *Scientific American*, 296(4):56–63, 2007. 2

[4] O Stenzel. *The physics of thin film optical spectra*. Springer, 2005. 2

[5] D Bedeaux and J Vlieger. *Optical properties of surfaces*. Imperial College Press, London, 2 edition, 2004. 3, 21, 22, 23, 27, 29, 36, 37, 38, 40, 45, 54, 56, 58, 59, 60, 62, 76, 105, 136

[6] D J Griffiths. *Introduction to Electrodynamics*. Prentice-Hall, 3rd edition, 1999. 3, 5, 20, 42, 44, 153, 154

[7] L Novotny and B Hecht. *Principles of nano-optics*. Cambridge university press, 2012. 5, 7

[8] S A Maier. *Plasmonics: Fundamentals and Applications*. Springer, 2007. 6, 8, 9, 15, 16, 104, 106, 108, 122, 135, 136

[9] S V Gaponenko. *Introduction to nanophotonics*. Cambridge University Press, 2010. 7

[10] C F Bohren and D R Huffman. *Absorption and Scattering of Light by Small Particles*. Wiley-VCH, 2004. 7, 14, 15, 16, 106

[11] Drude model parameters to fit the dielectric function of free electron metals. http://www.wave-scattering.com/drudefit.html. Retrieved 11:34, July 20, 2020. 10

[12] U Kreibig and M Vollmer. *Optial Properties of Metal Clusters*. Springer, 1 edition, 1995. 11, 16, 83, 84, 106

[13] I Freestone, N Meeks, M Sax, and C Higgitt. The lycurgus cup—a roman nanotechnology. *Gold bulletin*, 40(4):270–277, 2007. 11

[14] D J Barber and I C Freestone. An investigation of the origin of the colour of the lycurgus cup by analytical transmission electron microscopy. *Archaeometry*, 32(1):33–45, 1990. 11

[15] J C Maxwell Garnett. Xii. colours in metal glasses and in metallic films. *Philosophical Transactions of the Royal Society of London. Series A, Containing Papers of a Mathematical or Physical Character*, 203(359-371):385–420, 1904. 11

[16] G Mie. Beiträge zur optik trüber medien, speziell kolloidaler metallösungen. *Annalen der physik*, 330(3):377–445, 1908. 11

[17] E Prodan, C Radloff, N J Halas, and P Nordlander. A hybridization model for the plasmon response of complex nanostructures. *Science*, 302(5644):419–422, 2003. 16, 17, 108, 131

[18] M Quinten. *Optical properties of nanoparticle systems: Mie and beyond*. John Wiley & Sons, 2010. 16

[19] M A Van Dijk, J G H Joosten, Y K Levine, and D Bedeaux. Dielectric study of temperature-dependent aerosol ot/water/isooctane microemulsion structure. *The Journal of Physical Chemistry*, 93(6):2506–2512, 1989. 16

[20] R Lazzari, S Roux, I Simonsen, J Jupille, D Bedeaux, and J Vlieger. Multipolar plasmon resonances in supported silver particles: The case of ag/α- al 2 o 3 (0001). *Physical Review B*, 65(23):235424, 2002. 19, 40, 104, 106, 114, 116, 122, 127, 130, 131

[21] A Moores and F Goettmann. The plasmon band in noble metal nanoparticles: an introduction to theory and applications. *New Journal of Chemistry*, 30(8):1121–1132, 2006. 19, 49

[22] J Z Zhang and C Noguez. Plasmonic optical properties and applications of metal nanostructures. *Plasmonics*, 3(4):127–150, 2008. 19, 20

[23] R Malureanu and A Lavrinenko. Ultra-thin films for plasmonics: a technology overview. *Nanotechnology Reviews*, 4(3):259–275, 2015. 19

[24] B T Draine and P J Flatau. Discrete-dipole approximation for scattering calculations. *Josa a*, 11(4):1491–1499, 1994. 20

[25] M A Yurkin and A G Hoekstra. The discrete dipole approximation: an overview and recent developments. *Journal of Quantitative Spectroscopy and Radiative Transfer*, 106(1-3):558–589, 2007. 20

[26] LinLin Zhao, K Lance Kelly, and George C Schatz. The extinction spectra of silver nanoparticle arrays: influence of array structure on plasmon resonance wavelength and width. *The Journal of Physical Chemistry B*, 107(30):7343–7350, 2003. 20

[27] K L Kelly, E Coronado, L L Zhao, and G C Schatz. The optical properties of metal nanoparticles: the influence of size, shape, and dielectric environment, 2003. 20

[28] T C Choy. *Effective medium theory: principles and applications*, volume 165. Oxford University Press, 2015. 20

[29] D M Wood and N W Ashcroft. Effective medium theory of optical properties of small particle composites. *Philosophical Magazine*, 35(2):269–280, 1977. 20

[30] T Yamaguchi, S Yoshida, and A Kinbara. Optical effect of the substrate on the anomalous absorption of aggregated silver films. *Thin solid films*, 21(1):173–187, 1974. 20, 104

[31] T Yamaguchi, S Yoshida, and A Kinbara. Anomalous optical absorption of aggregated silver films. *Thin solid films*, 18(1):63–70, 1973. 20, 104

[32] R Lazzari, J Jupille, R Cavallotti, and I Simonsen. Model-free unraveling of supported nanoparticles plasmon resonance modes. *The Journal of Physical Chemistry C*, 118(13):7032–7048, 2014. 22, 104, 116, 130

[33] R Lazzari. *Vers la maitrise de la croissance de couches minces: une etude par spectroscopie optique et d'electrons*. PhD thesis, Université Paris-Sud, 2000. 22

[34] P A Letnes, I Simonsen, and D L Mills. Plasmonic resonances at interfaces patterned by nanoparticle lattices. *arXiv preprint arXiv:1208.1911*, 2012. 22, 59

[35] A M Albano, D Bedeaux, and J Vlieger. On the description of interfacial properties using singular densities and currents at a dividing surface. *Physica A: Statistical Mechanics and its Applications*, 99(1-2):293–304, 1979. 28, 30, 35

[36] A M Albano, D Bedeaux, and J Vlieger. On the description of interfacial electromagnetic properties using singular fields, charge density and currents at a dividing surface. *Physica A: Statistical Mechanics and its Applications*, 102(1):105–119, 1980. 28, 30, 35

[37] D Bedeaux and J Vlieger. *Optical properties of surfaces*. Imperial College Press, London, first edition, 2002. 31, 32, 33, 34, 36, 39, 42, 45, 47, 55, 59, 61, 76

[38] U Kocks, C N Tomé, and H-R Wenk. *Texture and anisotropy: preferred orientations in polycrystals and their effect on materials properties*. Cambridge university press, 1998. 35

[39] D Bedeaux, G J M Koper, E A vd Zeeuw, J Vlieger, and M Wind. The definition and use of optical invariants for thin island films. *Physica A: Statistical Mechanics and its Applications*, 207(1-3):285–292, 1994. 36

[40] M T Haarmans and D Bedeaux. Optical properties of thin films up to second order in the thickness. *Thin Solid Films*, 258(1-2):213–223, 1995. 38, 59

[41] D Bedeaux and J Vlieger. A phenomenological theory of the dielectric properties of thin films. *Physica*, 67(1):55–73, 1973. 40, 76, 81, 114

[42] S Grachev, M De Grazia, E Barthel, E Søndergård, and R Lazzari. Real-time monitoring of nanoparticle film growth at high deposition rate with optical spectroscopy of plasmon resonances. *Journal of Physics D: Applied Physics*, 46(37):375305, 2013. 40, 80, 114, 135, 176

[43] A Bagchi, R G Barrera, and A K Rajagopal. Perturbative approach to the calculation of the electric field near a metal surface. *Physical review B*, 20(12):4824, 1979. 40

[44] Alan H Barr. The einstein summation notation. *An Introduction to Physically Based Modeling (Course Notes 19), pages E*, 1, 1991. 42

[45] M Zhan. *Electromagnetic field theory: a problem solving approach*. Krieger Publishing Company, Malabar, Florida, 3 edition, 2003. 44

[46] I Simonsen, R Lazzari, J Jupille, and S Roux. Numerical modeling of the optical response of supported metallic particles. *Physical Review B*, 61(11):7722, 2000. 44, 47, 52, 55, 74, 76, 81, 122

[47] M M Wind, P A Bobbert, J Vlieger, and D Bedeaux. The polarizability of truncated spheres and oblate spheroids on a substrate: comparison with experimental results. *Thin Solid Films*, 164:57–62, 1988. 45

[48] M M Wind, J Vlieger, and D Bedeaux. The polarizability of a truncated sphere on a substrate i. *Physica A: Statistical Mechanics and its Applications*, 141(1):33–57, 1987. 47, 54, 76

[49] M M Wind, P A Bobbert, J Vlieger, and D Bedeaux. The polarizability of a truncated sphere on a substrate ii. *Physica A: Statistical Mechanics and its Applications*, 143(1-2):164–182, 1987. 47, 76

[50] P A Bobbert and J Vlieger. The polarizability of a spheroidal particle on a substrate. *Physica A: Statistical Mechanics and its Applications*, 147(1-2):115–141, 1987. 56, 76

[51] R Lazzari, I Simonsen, D Bedeaux, J Vlieger, and J Jupille. Polarizability of truncated spheroidal particles supported by a substrate: model and applications. *The European Physical Journal B-Condensed Matter and Complex Systems*, 24(2):267–284, 2001. 56, 58

[52] H Feshbach, P M Morse, and M Michio. *Methods of theoretical physics*. Dover Publications, 2019. 56

[53] M T Haarmans and D Bedeaux. The polarizability and the optical properties of lattices and random distributions of small metal spheres on a substrate. *Thin Solid Films*, 224(1):117–131, 1993. 59, 61, 62, 81

[54] C Noguez and R G Barrera. Multipolar and disorder effects in the optical properties of granular composites. *Physical Review B*, 57(1):302, 1998. 59

[55] G A Niklasson, P A Bobbert, and H G Craighead. Optical properties of square lattices of gold nanoparticles. *Nanostructured Materials*, 12(5-8):725–730, 1999. 59

[56] R Lazzari and I Simonsen. Granfilm: a software for calculating thin-layer dielectric properties and fresnel coefficients. *Thin Solid Films*, 419(1-2):124–136, 2002. 60, 71, 76, 131, 176

[57] I Simonsen and R Lazzari. Granfilm: Optical properties of granular thin films, 2003. 75, 79, 159

[58] R Lazzari and J Jupille. Quantitative analysis of nanoparticle growth through plasmonics. *Nanotechnology*, 22(44):445703, 2011. 80, 83, 84, 85, 94, 135, 176

[59] N Stefanou and A Modinos. Scattering of light from a two-dimensional array of spherical particles on a substrate. *Journal of Physics: Condensed Matter*, 3(41):8135, 1991. 81

[60] N Stefanou, V Karathanos, and A Modinos. Scattering of electromagnetic waves by periodic structures. *Journal of Physics: Condensed Matter*, 4(36):7389, 1992. 81

[61] R Lazzari and J Jupille. Growth kinetics and size-dependent wetting of ag/α-al2o3 (0001) nanoparticles studied via the plasmonic response. *Nanotechnology*, 23(13):135707, 2012. 84, 85, 92, 97

[62] A Liebsch. Surface-plasmon dispersion and size dependence of mie resonance: silver versus simple metals. *Physical Review B*, 48(15):11317, 1993. 85

[63] Y Borensztein, P De Andres, R Monreal, T Lopez-Rios, and F Flores. Blue shift of the dipolar plasma resonance in small silver particles on an alumina surface. *Physical Review B*, 33(4):2828, 1986. 85

[64] M Newville, T Stensitzki, D B Allen, and A Ingargiola. LMFIT: Non-Linear Least-Square Minimization and Curve-Fitting for Python¶, September 2014. 85

[65] J Nocedal and S Wright. *Numerical optimization*. Springer Science & Business Media, 2006. 86, 87

[66] Boyd and L Vandenberghe. *Convex optimization*. Cambridge university press, 2004. 86

[67] K Madsen, H B Nielsen, and O Tingleff. *Methods for non-linear least squares problems*. 1999. 87

[68] H Gavin. The levenberg-marquardt method for nonlinear least squares curve-fitting problems. *Department of Civil and Environmental Engineering, Duke University*, pages 1–15, 2011. 87

[69] F James. Minuit function minimization and error analysis: reference manual version 94.1. Technical report, 1994. 88, 90

[70] F James. MINUIT User's Guide (Old). *Unpublished*, page 50, 1994. 90

[71] A Jeffrey and D Zwillinger. *Table of integrals, series, and products*. Elsevier, seventh edition, 2007. 101

[72] R Lazzari, I Simonsen, and J Jupille. Onset of charge localisation on coupling multipolar absorption modes in supported metal particles. *EPL (Europhysics Letters)*, 61(4):541, 2003. 104

[73] G J Hyland. *Herbert Fröhlich: a physicist ahead of his time*. Springer, 2015. 108

[74] H Wang, D W Brandl, P Nordlander, and N J Halas. Plasmonic nanostructures: artificial molecules. *Accounts of chemical research*, 40(1):53–62, 2007. 108, 130

[75] C Radloff and N J Halas. Plasmonic properties of concentric nanoshells. *Nano letters*, 4(7):1323–1327, 2004. 108, 130

[76] R Lazzari, G Renaud, C Revenant, J Jupille, and Y Borensztein. Adhesion of growing nanoparticles at a glance: surface differential reflectivity spectroscopy and grazing incidence small angle x-ray scattering. *Physical Review B*, 79(12):125428, 2009. 135

[77] H Hövel, S Fritz, A Hilger, U Kreibig, and Michael Vollmer. Width of cluster plasmon resonances: bulk dielectric functions and chemical interface damping. *Physical Review B*, 48(24):18178, 1993. 135

[78] J Sancho-Parramon. Surface plasmon resonance broadening of metallic particles in the quasi-static approximation: a numerical study of size confinement and interparticle interaction effects. *Nanotechnology*, 20(23):235706, 2009. 135

[79] J Vlieger and D Bedeaux. A statistical theory for the dielectric properties of thin island films. *Thin Solid Films*, 69(1):107–130, 1980. 136

[80] J Burkardt. The truncated normal distribution. *Department of Scientific Computing Website, Florida State University*, 2014. 140, 142

[81] P L DeVries. *A first course in computational physics*. John Wiley & Sons, 1994. 141, 144, 145

[82] W H Press, S A Teukolsky, B P Flannery, and William T Vetterling. *Numerical recipes in Fortran 77: volume 1, volume 1 of Fortran numerical recipes: the art of scientific computing*. Cambridge university press, 1992. 142

[83] R G Barrera, P Villasenor-Gonzalez, W L Mochán, and G Monsivais. Effective dielectric response of polydispersed composites. *Physical Review B*, 41(11):7370, 1990. 151, 156, 158, 170

[84] D Gazzillo, A Giacometti, R Guido D V, E Venuti, and F Carsughi. A scaling approximation for structure factors in the integral equation theory of polydisperse nonionic colloidal fluids. *The Journal of chemical physics*, 111(16):7636–7645, 1999. 151, 158, 159

[85] J D Jackson. *Classical electrodynamics*. John Wiley & Sons, 2007. 153, 154

[86] M Kotlarchyk and S-H Chen. Analysis of small angle neutron scattering spectra from polydisperse interacting colloids. *The Journal of chemical physics*, 79(5):2461–2469, 1983. 158

[87] J S Pedersen. Determination of size distribution from small-angle scattering data for systems with effective hard-sphere interactions. *Journal of applied crystallography*, 27(4):595–608, 1994. 158

[88] C de Boor. *A practical guide to splines*. Springer, 2 edition, 2001. 159

[89] R G Barrera, J Giraldo, and W L Mochán. Effective dielectric response of a composite with aligned spheroidal inclusions. *Physical Review B*, 47(14):8528, 1993. 168

[90] B Bagchi. *Statistical Mechanics for Chemistry and Materials Science*. CRC Press, 2018. 170, 184, 186

[91] J-P Banon. *On the Simulation of Electromagnetic Wave Scattering by Periodic and Randomly Rough Layered Structures based on the Reduced Rayleigh Equations: Theory, numerical analysis and applications*. PhD thesis, Norges teknisk-naturvitenskapelige universitet (NTNU), 2018. 177

[92] A Alvarez-Fernandez, G Fleury, V Ponsinet, P M Walmsness, and M Kildemo. Formation and optical response of self-assembled gold nanoparticle lattices on oxidized silicon synthesized using block copolymers. *Journal of Vacuum Science & Technology B, Nanotechnology and Microelectronics: Materials, Processing, Measurement, and Phenomena*, 38(1):013601, 2020. 177

[93] M Baus and J-L Colot. Thermodynamics and structure of a fluid of hard rods, disks, spheres, or hyperspheres from rescaled virial expansions. *Physical Review A*, 36(8):3912, 1987. 183, 187, 188

[94] Y Waseda. The structure of non-crystalline materials. *Liquids and Amorphous Solids*, 1980. 184

[95] J Sólyom. *Fundamentals of the Physics of Solids: Volume 1: Structure and Dynamics*, volume 1. Springer Science & Business Media, 2007. 184

[96] P Wynn. The epsilon algorithm and operational formulas of numerical analysis. *Mathematics of Computation*, 15(74):151–158, 1961. 188